Stepping Dynamics of the Bacterial Flagellar Motor and F_1-ATPase

Ashley L. Nord

Balliol College

University of Oxford

Michaelmas 2013-2014

ABSTRACT

Stepping Dynamics of the Bacterial Flagellar Motor and F_1-ATPase

Ashley L. Nord

Balliol College

Thesis submitted for the degree D.Phil. in Physics

University of Oxford

Michaelmas 2013-2014

Rotary molecular motors are protein complexes which convert chemical or electrochemical energy from the environment into mechanical work in the form of rotary motion. The work in this thesis examines two of these motors: the F_1 portion of F_1F_O-ATP synthase, which is responsible for ATP production in bacteria and eukaryotes, and the bacterial flagellar motor (BFM), which rotates the flagella of a bacterium, enabling locomotion. The aim of these investigations was to measure the stepping dynamics of these motors, in order to further elucidate details of the stepping mechanism, the mechanism of rotation, and the mechanochemical cycle. A back-scattering laser dark field microscope of unprecedented resolution was designed and constructed to observe the rotation of gold nanoparticles attached to fixed motors. This microscope is capable of sub-nanometer and $20\mu s$ resolution.

The protocols and algorithms to collect and analyze high resolution rotational data developed for these experiments have yielded novel discoveries for both F_1 and the BFM. While most of the previous single-molecule work has been done on F_1 from the thermophilic *Bacilus* PS3 (TF$_1$), only mitochondrial F_1 has been well characterized by high-resolution crystal structures, and single-molecule studies of mesophilic F_1 are lacking. This thesis presents evidence that mesophilic F_1 from *E. coli* and wild type yeast F_1 from *S. cerevisiae* are governed by the same mechanism as TF$_1$ under laboratory conditions. Experiments with yeast F_1 mutants allow a direct comparison between single-molecule rotation studies and high resolution crystal structures. A data set of unprecedented size and resolution was acquired of high speed, low load BFM rotation, enabling the first observation of steps in the BFM under physiological conditions. Preliminary results from this analysis question previously published results of the dependence of speed on stator number at low load and provide novel hypotheses necessitating new models of BFM rotation.

DECLARATION

The work in this thesis was undertaken at the University of Oxford, in the Clarendon Laboratory, Department of Physics. Work was performed from October 2009 to January 2014 under the supervision of Dr R. M. Berry. All the work in this thesis is my own unless stated and has not been submitted for a degree at this or any other university.

Acknowledgments

I have spent the last four years and three months working on a project that has been intensely interesting, boggling, exhilarating, frustrating, humbling, panic inducing, and different combinations thereof. Overall, however, it has been very rewarding, and I have many to thank for this experience.

Much of my gratitude goes to my supervisor, Dr. Richard Berry, and I thank him for taking a chance on and maintaining confidence in me. I have an immense amount of respect for Richard as a scientist and as a person, and I have been inspired by, among other things, his enthusiasm and approach to science. He is generous with his guidance, patience, and time, and he is never lacking in helpful ideas and methods. He has granted me the academic freedom to chose my own lines of inquiry and the personal freedom to escape periodically into the mountains. From all of these things, I have benefited greatly.

I was lucky to be welcomed into a friendly environment, and I would like to thank those that have moved on from the Berry Lab, including Dr. Bradley Steel, Dr. Mostyn Brown, Dr. Matt Baker, Dr. Richard Branch, Dr. Wei Ho, and Dr. Murray Tipping for their support and help during the first few years. I owe the current lab members, including Dr. James Flewellen, Dr. Irwin Zaid, Dr. Robert Ishmukhametov, Dr. Nick Delalez, Aidan Russell, Ren Lim, Bas Leerkotte, Dewei Jia, and Diana di Paolo, for many fruitful and interesting discussions on science and for (almost as many) amusing distractions. In particular, I owe a huge thank you to Dr. Bradley Steel. Bradley is a remarkable scientist and teacher, and his patience is inexhaustible. He was a source of joy both inside the lab and out, and I particularly enjoyed his company during the long days and nights building microscopes. He has helped me through every stage of the last few years, including providing valuable input on this thesis, for which I am incredibly grateful.

Abbreviations

ADP	adenosine diphosphate
APD	avalanche photo diode
ATP	adenosine triphosphate
BIC	Bayesian information criterion
BFM	bacterial flagellar motor
CCD	charged coupled device
CMOS	complementary metal-oxide semiconductor
GFP	green-fluorescent protein
IMF	ion motive force
MLE	maximum likelihood estimation
MB	motility buffer
NA	numerical aperture
PMF	proton motive force
QPD	quadrant photo-diode
SMF	sodium motive force
TIRF	total internal reflection fluorescence
TB	tryptone broth

NATURE! We are surrounded and embraced by her: powerless to separate ourselves from her, and powerless to penetrate beyond her.

Without asking, or warning, she snatches us up into her circling dance, and whirls us on until we are tired, and drop from her arms.

She is ever shaping new forms: what is, has never yet been; what has been, comes not again. Everything is new, and yet nought but the old.

We live in her midst and know her not. She is incessantly speaking to us, but betrays not her secret. We constantly act upon her, and yet have no power over her.

The one thing she seems to aim at is Individuality; yet she cares nothing for individuals. She is always building up and destroying; but her workshop is inaccessible.

Her life is in her children; but where is the mother? She is the only artist; working-up the most uniform material into utter opposites; arriving, without a trace of effort, at perfection, at the most exact precision, though always veiled under a certain softness.

Each of her works has an essence of its own; each of her phenomena a special characterisation: and yet their diversity is in unity.

She performs a play; we know not whether she sees it herself, and yet she acts for us, the lookers-on.

Incessant life, development, and movement are in her, but she advances not. She changes for ever and ever, and rests not a moment. Quietude is inconceivable to her, and she has laid her curse upon rest. She is firm. Her steps are measured, her exceptions rare, her laws unchangeable.

- from Goethe's *Aphorisms on Nature*
Translated by T. H. Huxley

Contents

Preface

Controlled movement is everywhere in life, both on the macroscopic and microscopic level, and it is necessary for the maintenance thereof. On the microscopic level, this movement is dominated by molecular motors, working either individually or collectively. In fact, these motors contribute to most of the biological functions that allow life, such as cellular organization, response, adaptation, reproduction, and metabolism.

To live is to move, and to move is to generate force. At the microscopic level the physics of force generation is dominated not by inertia but by intermolecular forces and Brownian motion. Single molecule biophysics has provided tools to manipulate and measure the forces and motions of motors on an individual basis, rather than using bulk studies. These tools have greatly enhanced our understanding of how these amazing machines function.

The focus of this thesis is the only two known rotating motors in nature, F_1F_O-ATPsynthase and the bacterial flagellar motor. The goal of this work has been to measure the stepping dynamics of these two motors in order to elucidate the mechanism of rotation. Chapter 1 gives an overview of the field of rotary molecular motors and the current understanding of their characteristics. Chapter 2 describes some of the single molecule tools that have previously been used to study these motors and explains the methods of investigation used in this thesis. This includes a description

of the construction of a dark field microscope used for some of the experiments in Chapters 3 and 4. Chapter 3 describes an analysis of the stepping kinetics of two types of mesophilic F_1-ATPase, and Chapter 4 describes experiments and analysis of stepping of the bacterial flagellar motor. Immediate conclusions are provided within each chapter, with broader implications of this work provided in Chapter 5.

Chapter 1

Introduction

1.1 Molecular Motors

A motor is a device that takes external energy and converts it into mechanical work. Molecular motors are protein complexes that transform chemical or electrochemical energy of the environment into mechanical work, thus enabling directed motion on both a microscopic and macroscopic scale. Like macroscopic motors, molecular motors are constructed of multiple smaller components. In the case of molecular motors, these components are the main functional elements of molecular biology: proteins. Proteins are polypeptide chains which have folded into an elaborate three-dimensional structure, and the function of a protein depends upon that structure. Once folded, many proteins are only marginally stable, allowing them to fluctuate between multiple meta-stable conformations. It is often the case that these conformational changes determine the mechanism of the protein.

Motor proteins use conformational transformations to generate force. As these transformations use chemical energy from the environment to do mechanical work,

they are called mechanochemical transitions. Molecular motors are complexes containing multiple motor proteins, and of those molecular motors that occur in nature, we can categorize them into two types by the nature of their movement: linear motors and rotary motors. Motors within the myosin, dynein, and kinesin families are examples of linear molecular motors, moving in a specific direction along actin filaments or microtubules. The bacterial flagellar motor, F_O and F_1ATPases, V-ATPases, and A-ATPases are examples of rotary molecular motors where one part of the motor rotates around another. The work in this thesis concentrates solely on rotary molecular motors.

Unlike macroscopic motors where molecular energies are negligible, molecular motors are small and exist in an environment where thermal fluctuations dominate. As molecular motors operate at energies only slightly above the surrounding thermal bath, thermal fluctuations are a crucial component of the environment and potentially the motor mechanism. It is possible that molecular motors do work only by biasing these fluctuations.

Work is coupled to energy, and there are two types of free energy utilized by molecular motors: chemical energy from the hydrolysis of adenosine triphosphate (ATP) and electrochemical energy from the transit of ions across a membrane. The second law of thermodynamics states that the entropy of an isolated system can not decrease. The Gibbs free energy of a reaction, the maximum amount of work that can be extracted from a closed system at constant pressure and temperature, is given by the enthalpic change minus the temperature weighted entropic change:

$$\triangle G = \triangle H - T \triangle S \qquad (1.1)$$

The Second Law tells us that the total $\triangle G$ of a closed system must be negative for a process to occur. Thus, molecular motors harness the free energy of chemical

or electrochemical reactions, and this energy is consumed when the motor performs mechanical work.

Molecular motors function at energy levels comparable to the thermal energy of their environment, $k_B T$, where k_B is the Boltzmann constant and T is the temperature of the aqueous environment. As most molecular motors function near room temperature, denoted T_0, it is sensible to speak of the relevant energies in units of $k_B T_0$. A ion transit across a cell membrane yields about $6k_B T_0$, whereas the hydrolysis of a single molecule of ATP yields about $20 k_B T_0$. In SI units, $1 k_B T_0$ is 4×10^{21}J, and is equivalent to 4pNnm of work.

1.1.1 Rotary molecular motors

Rotary molecular motors transform chemical or electrochemical energy into work in the form of rotary motion. There are two known families of rotary motors in nature: the F, V, and A-ATPases, and the bacterial flagellar motor [1]. The ATPases are structurally rather different from the bacterial flagellar motor, and the two classes do not appear to have a common ancestry (though an ATPase drives the export of proteins which constitute the flagella of the BFM [2]). Thus, while nature has not made much use of the wheel, she has invented it at least twice. The work in this thesis concentrates on the F_1 portion of ATP synthase and the bacterial flagellar motor.

1.2 F_1-ATPase

$F_1 F_O$-ATP synthase is a rotary molecular motor responsible for the adenosine triphosphate (ATP) production in bacteria and eukaryotes. When ATP is broken up into adenosine diphosphate (ADP) and free phosphate, it releases energy that is harnessed for many cellular processes. F-ATPases are ubiquitous in the inner membranes of mitochondria and chloroplasts, for animals and plants respectively, and in the cyto-

plasmic membranes of bacteria. Whatever the source, F-ATPases are all remarkably similar in structure and function, and at only about 20nm in size, they are one of the most evolutionarily conserved enzymes [3–5]. Rotation of part of the enzyme was predicted to be necessary for the production of ATP [6, 7]; this hypothesis was first reinforced by high resolution crystal structures [8], and later confirmed by single molecule techniques [9].

Driven by an electrochemical gradient across the membrane, F_1F_O-ATP synthase is composed of two coaxial motors, F_1 ($\sim$380kDa) and F_O ($\sim$120kDa), which share a common rotor. A flux of ions (usually H^+) through F_O, which is embedded in the membrane, powers ATP production in F_1, which is soluble and located in the cytoplasm. The motor is also capable of functioning in reverse where ATP hydrolysis and rotation in F_1 cause proton pumping in F_O [10, 11]. Rotation has been directly observed in F_1 in both the ATP synthesis and ATP hydrolysis directions. The rotation of F_O has been observed in F_1F_O both under ATP hydrolysis conditions [12–14] and under ATP synthesis conditions [15–17].

The overall structure of F_1F_O-ATP synthase was obtained from low resolution cryo-electron microscopy studies of enzymes from yeast mitochondria [18], bovine mitochondria [19], and *E. coli* [20]. X-ray crystallography has been used to obtain many structures of the F_1 portion, a small number of structures of the F_O portion, and the peripheral stalk [21]. These atomic structures have been docked into the cryo-electron microscopy structures from bovine mitochondrial F_1F_O-ATP synthase [22] and have been combined with the results from numerous biochemical studies [23]. The schematic structure of F_1F_O-ATP synthase is shown in Figure 1.1. When placed in low-ionic strength medium, the two motors separate. On its own, F_1 is decoupled from the electrochemical potential and is unable to synthesize ATP. Instead, it behaves as an ATP hydrolyzing enzyme, turning the γ subunit in the opposite direction. In this condition, it is referred to as F_1-ATPase. The work in this thesis is concerned with

the rotation of F$_1$-AT   *accharomyces*

cerevisiae (YF$_1$). A   tion of F$_1$ is

provided below.

Figure 1.1: A schematic model of *E. coli* F$_1$F$_O$-ATP synthase. F$_1$F$_O$-ATP synthase is composed to two coaxial motors that share a common rotor (C$_{12}$,$\gamma\epsilon$). F$_1$ is located mostly in the cytoplasm and F$_O$ mostly in the membrane. The PMF powers the rotation of F$_O$, which drives the rotation of the γ subunit within the $\alpha_3\beta_3$ hexamer of F$_1$. This enables the synthesis of ATP from ADP and Pi. Figure from Fillingame, 1999 [24].

1.2.1   Structure

The first high resolution crystal structure of F$_1$-ATPase was obtained from bovine

mitochondria in 1994 [8]. Since then, high resolution crystal structures have also been

obtained from yeast [25,26], and chloroplasts [27], and low resolution crystal structures

have been obtained from *E. coli* [28,29]. For ease of reference, I adopt the following

nomenclature when referring to F$_1$-ATPase from different organisms: thermophilic

bacteria, TF$_1$, bovine mitochondria, MF$_1$, *E. coli*, EF$_1$, and yeast, YF$_1$. Regardless

of the source, the structures of F$_1$ are remarkably similar. EF$_1$, the simplest of the

enzymes, and MF_1, the enzyme with the most detailed crystal structure, are described and compared below.

EF_1 and MF_1 are composed of five and six separate subunits with stoichiometry $\alpha_3\beta_3\gamma\delta\epsilon$ and $\alpha_3\beta_3\gamma\delta\epsilon OSCP$, respectively. The $\alpha_3\beta_3\gamma$ subunits make up the central part of the enzyme, with ATP synthesis and hydrolysis occurring in the $\alpha_3\beta_3$ hexamer. This hexamer is formed of alternating subunits and is known as the head piece. The three catalytic nucleotide binding sites are located on the β subunits at the interface of the α subunits. Three more non-catalytic nucleotide binding sites are located on the α subunits at the interface with the β subunits. The γ subunit is a right-handed coiled-coil structure that occupies a cavity in the middle of the headpiece, and extends outside the hexameric structure to form the main stalk. It rotates with respect to $\alpha_3\beta_3$, either driving synthesis or being driven by hydrolysis. In EF_1, the δ subunit rests on top of the headpiece, where it may interact with either the α [30] or β [31,32] subunits, forming part of the peripheral stalk. The ϵ subunit is located near the base of the γ subunit. The ϵ subunit of EF_1 is homologous to the δ and ϵ subunits combined of MF_1, while the δ subunit in EF_1 is homologous to the oligomycin sensitivity conferring protein (OSCP) in MF_1. In MF_1, both the δ and ϵ subunits are located near the base of γ.

1.2.2 Mechanochemical cycle

Though there was much indirect evidence of the rotary nature of F_1-ATPase [6, 8, 33–35], part of which helped develop Boyer's famous proposal that the rotation of one or more subunits was intrinsic to catalysis [36–38], it was not until 1997 that single molecule experiments enabled the first direct observation of rotation in TF_1 [9]. In these experiments, $\alpha_3\beta_3$ TF_1 was immobilized on a coverslip and a fluorescent actin filament was attached to the γ subunit. In the presence of ATP, unidirectional rotation of the fluorescent actin filament was observed. From these experiments it was

determined that TF_1 exerts about 40pN nm rad^{-1} of torque during ATP hydrolysis at high load. Soon after, similar experiments confirmed the rotary nature of EF_1 [39–41], CF_1 [42], and YF_1[1] in the presence of ATP.

Due to its small size, the γ subunit can not be seen in an optical microscope and a probe is necessary to observe its rotation. Initially, this probe took the form of a fluorescently-tagged actin filament around 1-3μm in length, attached to the γ subunit of TF_1 [9, 43] and EF_1 [39, 40, 44, 45]. Subsequent probes, attached either to the γ subunit or the ϵ subunit have allowed for greater temporal resolution. This has included a single or pair of beads on TF_1 [46, 47], and EF_1 [48, 48–52], a fluorescent bead on TF_1 [53], or a FRET pair attached to the β subunit and either the γ or ϵ subunit of TF_1 [54] and EF_1 [55–57]. A more recent method measures F_1 rotation via the polarization of light scattered by gold nanorods on EF_1, though technical difficulties have thus far made angle recovery with this method ambiguous [14, 58, 59].

The γ subunit rotates CCW during ATP hydrolysis, when viewed from the F_O domain [9]. As the load of the probe on the γ subunit becomes small enough, somewhere around a 100nm bead pair, the motor rotation is no longer impeded by the load. With such a load, at saturating [ATP], TF_1 can reach a maximum speed of about 130Hz at room temperature [46]. As a comparison, an actin filament probe yields a speed of less than 7Hz [43]. However, EF_1 rotates at almost four fold the speed of TF_1 at room temperature [49], most likely due to the different *in vivo* conditions the species inhabit. Experiments have confirmed that the rotational behavior, including maximum speed, of TF_1F_O resembles that of TF_1, suggesting that the friction of F_O within a non-energized membrane during ATP driven rotation is negligible [12].

The reversibility of TF_1 has been demonstrated by the use of magnetic tweezers. When TF_1 was isolated and immobilized in femtoliter chambers [60], an external torque applied to the γ subunit forced it to rotate in the CW direction, causing ATP

---

[1]Manuscript in preparation; Steel BC, Nord AL, Wang Y, Pagadala V, Mueller DM, Berry RM

synthesis. Synthesized ATP was detected using a luciferase-luciferin reaction [61] or by switching the magnetic field off and measuring the speed of TF_1 rotation in the ATP hydrolysis direction [62].

A majority of the recent single molecule rotation work has used TF_1 from thermophilic *Bacillus* PS3 strain, a bacterial strain found in Japanese thermal springs, which operates optimally at 75°C [63,64]. It is highly stable, robust to denaturation, and is characterized by relatively slow kinetics at room temperature. Rotation rates of single surface-immobilized TF_1 molecules obey Michaelis-Menton type kinetics as a function of [ATP] [43,46,65]. The first observation of discrete 120° steps in F_1 used a fluorescent actin filament attached to the γ subunit observed in low [ATP] conditions. Three steps per revolution agrees nicely with the three fold symmetry of F_1. The first experiments to use gold beads also observed discrete 120° steps, but this time at high [ATP] [46]. It was later learned that each 120° step corresponded to the hydrolysis of one ATP molecule [61]. At intermediate [ATP], these steps were further resolved into 80° and 40° substeps [46,66]. Typical traces and steps are shown in Figure 1.2. The length of the dwell which occurs immediately prior to a particular site's binding of an ATP molecule has been demonstrated to be dependent on ATP concentration. The duration of this dwell becomes short at high [ATP], and it is thus commonly referred to as the ATP binding dwell. It has also been shown that ADP release occurs during this dwell [67–69]. The dwell after the 80° substep was demonstrated to be independent of substrate concentration, and this intermediate dwell (the 'catalytic dwell') has been assigned to ATP hydrolysis and inorganic phosphate (P_i) release [66,68,70].

The nature of the substeps is supported by an analysis of the distribution of times taken to rotate 120°. At low [ATP], the 80° substep takes longer than the 40°, as ATP binding is rate limiting. The dwell time distribution is well fit by a single exponential function with a rate constant directly proportional to [ATP] [66]. At saturating [ATP] the 40° substep is rate limiting, and the dwell time distribution is well fit with
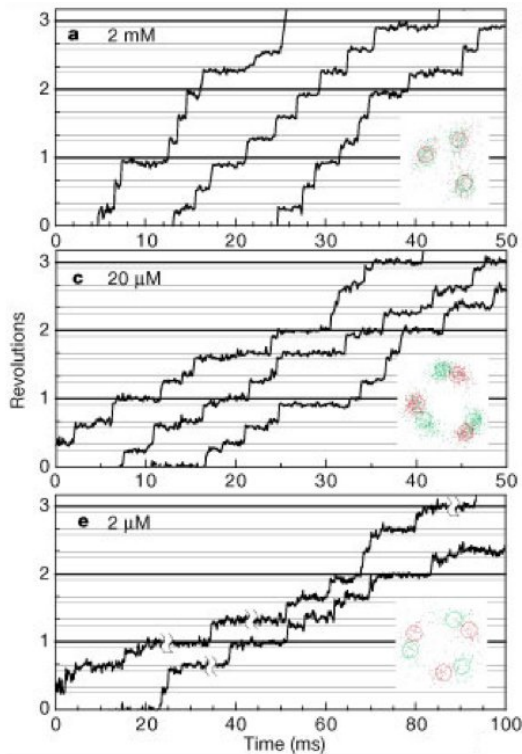
Figure 1.2: Graphs of revolution versus time for rotating 40nm beads at varying [ATP], as labeled. The traces are continuous recordings, but shifted to save space. The black horizontal lines are 120° apart, and the grey lines are 30° below the black lines. In the 2μM trace, some of the long dwells are cut short, as indicated. The insets show the positions of the bead, with red representing the 90° step and green the 30° step. Substeps of size 90° and 30° were later revised to 80° and 40° [66]. Figure adapted Yasuda et al, 2001 [46].

a 'double-exponential,' compatible with the requirement of two sequential processes[2] before a 40° substep can occur [46]. In a set of experiments that used a mutant that slowly hydrolyses ATP, it was demonstrated that one of the two reactions in the 40° substep is ATP cleavage [66]. Another set of experiments used fluorescently labeled ATP observed simultaneously with the rotation of a bead pair, to demonstrate that

---

[2]For the sake of clarity, for two sequential, independent Poisson processes with rate constants k_i, that is,

$$A \xrightarrow{k_1} B \xrightarrow{k_2} C, \tag{1.2}$$

the probability of observing a transition from A to C of time t is given by the 'double-exponential'

$$p(t) = \frac{k_1 k_2}{k_2 - k_1}(e^{-k_1 t} - e^{-k_2 t}). \tag{1.3}$$

11

the nucleotide stays bound to F_1 for two 120° steps. These experiments also confirmed that the motor takes an 80° subset immediately after binding ATP (± 1 video frame, 33ms) and that the orientation of the γ subunit dictates which β subunit will next bind ATP [67]. Another experiment using fluorescently labeled ATP and total internal reflection fluorescence (TIRF) microscopy demonstrated that ADP is released in the 80° substep after it has been bound for two 120° steps [68].

While the rotation of TF_1 is unidirectional, it is not continuous. In addition to the underlying stochastic stepping, TF_1 lapses into a long ($\sim$30s) paused state due to MgADP-inhibition [47], known as the ADP inhibited state. This state is induced by the stable entrapment of MgADP at a catalytic site, either from the immediate hydrolysis product becoming trapped to the enzyme [47] or being picked up by a free catalytic site from the bulk phase medium[3] [71]. MgADP-inhibition is a transient state, and the enzyme recovers to full activity. The angular location of the MgADP-inhibited pause coincides with one of the catalytic dwells [47]. When a magnetic bead and magnetic tweezers were used to exert torque in the ATP hydrolysis direction on MgADP-inhibited enzymes, it was found that TF_1 typically recovered more quickly from the inhibited state, suggesting that the external torque was twisting the γ subunit and lowering the binding affinity of the catalytic site to MgADP [72]. F_1 has also been observed to recover from the inhibited state when ATP binds to one of the noncatalytic nucleotide binding sites on the α subunit [73].

Single molecule experiments and crystal structures have combined to give us the current model for the mechanochemical coupling scheme of F_1, shown in Figure 1.3. The three β subunits operate cooperatively. During catalysis, the nucleotide-bound state of the three catalytic binding sites determines the conformation of the β subunits. Each β subunit adopts a different conformation, causing a particular interaction with the central γ subunit. The conformations of the β subunits then change sequen-

---

[3]The likelihood of rebinding MgADP and thus of pausing is greatly reduced by using an enzymatic coupled reaction that regenerates ATP from ADP and P_i in the activity buffers.

tially as the γ subunit rotates, such that each nucleotide binding affinity is adopted by each β subunit during one rotation. A different site completes its cycle every 120°, meaning that three ATP molecules are hydrolyzed or synthesized per rotation. The subunits are traditionally numbered in a CCW fashion, viewed from F_O, with β_1 as the subunit that is about to bind ATP, shown in green at 0° in Figure 1.3. ATP binds onto β_1, in concert with or possibly after the release of ADP from β_2 [68,69,74], initiating the 80° step to the catalytic dwell. Here, at least two processes occur. In TF$_1$, there is evidence for ATP hydrolysis on β_3 followed P$_i$ release on β_2 [66,68,70], initiating the 40° step to the binding dwell. From here the cycle repeats, with ATP binding to β_2 and ADP releasing from β_3. Overall, the ATP binding dwell is dependent on [ATP] [43], and once bound, an ATP molecule will remain intact until γ rotates through 200°, whereupon it will be hydrolyzed. The ADP product is released between 240° and 320°, more likely at 240°, with P$_i$ released at 320°. It has also been suggested that a third process may occur at the catalytic dwell, possibly a conformational isomerization such as Mg^{2+} ion translocation [75, 76].

1.2.3   Energetics

The free energy available from the hydrolysis of one ATP molecule is given by

$$\triangle G = \triangle G_0 + k_B T ln \frac{[ATP]}{[ADP] \cdot [P_i]} \tag{1.4}$$

where $\triangle G_0$ is the standard free energy and [ATP], [ADP], and [P$_i$] represent the molar concentrations of their respective chemical species. In the first rotation experiments of TF$_1$, the torque of the motor was estimated by multiplying the average speed of the motors at saturating [ATP] by the viscous drag coefficient of the filament. This calculation estimated the torque of TF$_1$ to be about 40pN nm rad^{-1} [43]. The torque of the motor was also calculated from the actin filament curvature, and this yielded
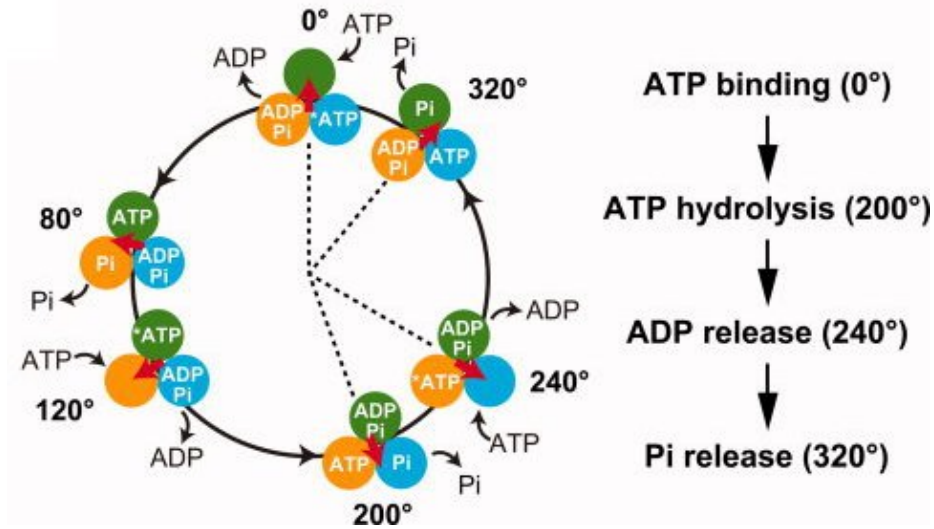
Figure 1.3: A proposed mechanochemical coupling scheme of F_1. Each circle represents the catalytic state of a β subunit. The subunit shown in green binds ATP at the 0° mark, then follows the processes listed on the side at the angles shown. The angular position of the γ subunit is represented by the central arrow. Once a catalytic site binds an ATP molecule, it remains bound for a 200° rotation of the γ subunit, whereupon it is hydrolyzed. ADP is released at 240° and P_i at 320° from the binding site. Each β subunit completes one hydrolysis of an ATP molecule per 360° degree rotation of the γ subunit, and the three β subunits are staggered in their catalytic state by 120°. This means that, defining 0° as the position of an ATP waiting dwell, at each ATP waiting dwell ADP will release from one subunit and ATP will bind to the previous subunit. Defining the catalytic dwell at 80° after an ATP waiting dwell, at each catalytic dwell the ATP bound to one subunit will hydrolyze and the P_i from the previous subunit will be released. Figure from Iino and Noji, 2013, [77]

a value of about 50pN nm rad^{-1} [78, 79]. The theoretical upper limit to the torque generated by F_1 is $\tau_{max} = (3 \cdot \triangle G)/2\pi$. Given that the energy released by one ATP molecule is about 80pN nm [80], this gives $\tau_{max} \approx 40$pN nm rad^{-1}. These results are thus consistent with the hypothesis that the motor operates near 100% efficiency at low speeds, high loads, and saturating [ATP] and that the chemical reactions are tightly-coupled to the mechanical events [65].

The use of small gold beads as probes instead of actin filaments [46] allowed for the investigation of the motor speed with respect to viscous load and [ATP]. With beads 100nm or less at saturating [ATP], speed was independent of both bead size

and [ATP]. This represents a regime where the rate limiting step in the enzyme's rotation is ATP hydrolysis and P_i release. With beads larger than 100nm at saturating [ATP], as the Stokes' drag of the bead increases, the motor speeds decrease, indicating that the mechanical rotation of the load is rate-limiting. For the smallest loads, the speed versus [ATP] relationship followed Michaelis-Menten kinetics with similar K_m as measured for ATP hydrolysis in bulk by unlabeled F_1, indicating that the attached load did not affect the kinetics of ATP hydrolysis [46]. Speed versus load and speed versus [ATP] graphs are shown in Figure 1.4. The load on F_1 is the Stokes' drag of the attached bead and is denoted viscous friction in Figure 1.4b. Stokes' Law is derived by solving the Stokes' flow limit for small Reynolds numbers of the Navier-Stokes equations, and Stokes' drag, denoted F_d is

$$F_d = 6\pi\mu R\nu, \tag{1.5}$$

where μ is the dynamic viscocity of the medium, R is the radius of the spherical bead, and ν is the particle's velocity.

It has been demonstrated that the F_1 catalytic cycle is driven by binding energy. Boyer and colleagues used ^{18}O isotopic exchange techniques to determine that the chemical reaction $ATP + H_2O \leftrightarrow ADP + Pi + H^+$ has a similar rate constant in both directions, and thus there is little free energy change associated with this step [81]. Instead, the free energy change that drives rotation comes from changes in affinity for the binding and release of substrates and products [36]. A theoretical model of how torque is generated in F_1 was put forth by Oster and colleagues [82, 83] and Kinosita and colleagues [84] which takes into account both the crystal structures and the single molecule experiments. To briefly summarize the model, as ATP enters the β subunit binding pocket, many weak bonds, mostly hydrogen bonds, are formed between the binding pocket and the ATP molecule. This 'zipping' around the ATP molecule causes
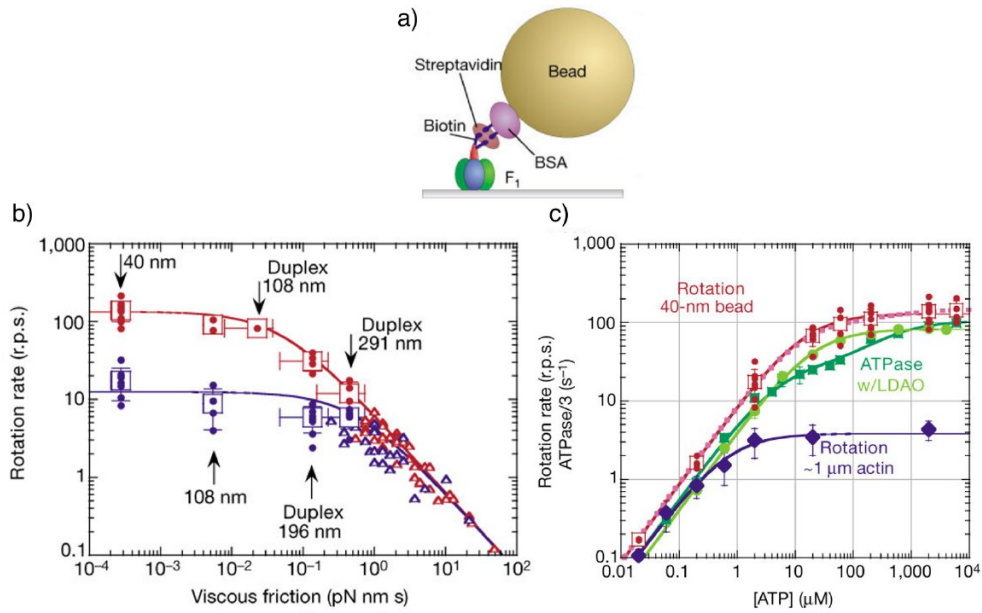
Figure 1.4: a) Side view of a gold bead labeled TF$_1$ molecule. TF$_1$ was immobilized to a coverslip via the α and β subunits. A 40nm bead was attached to the γ subunit via a biotin-streptavidin-biotin-BSA link. The bead was not large enough to impede rotation. b) A graph of rotation rate versus viscous friction. Circles indicate the average speed of a bead over at least 20 consecutive revolutions and squares indicate the average speed over multiple beads. Triangles are from actin filaments attached to the γ subunit. ATP concentration was 2mM and 2μM indicated by red and blue respectively. c) A graph of rotation rate versus ATP concentration. Red circles indicate time-averaged rotation rates for individual beads and red squares indicate rotation rate averaged over multiple beads. Dark green indicates a nucleotide-depleted TF$_1$ strain with an ATP hydrolysis rate of one-third the standard. Light green is the same strain but in the presence of LDAO, a suppressor of MgADP inhibition. Blue diamonds indicate the rotation of an actin filament attached to the γ subunit [43]. Figure adapted from Yasuda et al, 2001 [46].

a conformational change in the β subunit. Part of the free energy of binding initiates

a rotation and the primary power stroke in the γ subunit. The remainder of the free

energy of ATP binding becomes stored as elastic strain within the γ subunit. ATP

hydrolysis allows the release of the P$_i$ molecule, driving the second power stroke and

allowing the β subunit to return to the open conformation. Upon binding ATP, the

gradual formation of hydrogen bonds leads to the experimentally observed constant

torque of the motor, where the torque is defined as that on the external load [46, 84].

16

1.3 Bacterial Flagellar Motor

Many species of motile bacteria move through their environment by rotating one or more helical flagellar filaments via a rotary motor embedded in the cell envelope [85, 86]. Rotation of the bacterial flagellum was first demonstrated in the 1970's [85, 86], and bacteria are the only biological structures known to use rotation as a means of locomotion [87, 88]. With billions of years of optimization, the bacterial flagellar motor (BFM) is the fastest and one of the most sophisticated biomachines in existence. It is also one of the best characterized large biomolecular complexes and much is known about the structure, genetics, assembly, and function. However, it sill remains a mystery exactly how the BFM works.

The BFM is about 50nm in diameter and self assembles in the cell envelope of various species of motile bacteria. Powered by ions crossing the cell membrane, the BFM couples to and rotates an extracellular helical filament at around 100Hz, enabling a bacterium to swim towards favorable external conditions. Processes such as chemotaxis, phototaxis, magnetotaxis, and thermotaxis enable bacteria to regulate and switch the motor rotation and thus navigate their environment using a biased random walk [89–92]. While BFMs have been studied in several species and are broadly similar, those found in *Escherichia coli* and *Salmonella enterica Serovar typhimurium* are the most studied and most well understood. The following review of the BFM refers to these bacteria unless otherwise mentioned, and the experimental data of this thesis was obtained entirely from *Escherichia coli*.

1.3.1 Structure, assembly, and genetics

An *E. coli* cell is rod-shaped, about 1μm in diameter, and about 2μm long. Each cell contains around six BFMs [93], assembled at random points in the cell envelope, each driving a single helical flagellar filament. The flagella extend into the external

environment by many cell lengths. When all the left-handed filaments are rotated counter-clockwise (CCW, looking down the filament towards the cell body), they form a single bundle due to hydrodynamic interactions, pushing and propelling the cell parallel to its long axis. When one or more of the motors switches to a clockwise (CW) direction, that filament undergoes a torsionally induced polymorphic transformation to a right-handed state, splays from the bundle, and initiates a random reorientation of cell direction [94–97]. When all BFMs have resumed CCW rotation, the cell swims steadily again in a new direction. This 'run and tumble' movement executes a random walk. The frequency of motor switching from CCW to CW is suppressed as the external environment grows more favorable, thus biasing the random walk and allowing the cell to use chemotaxis to move towards more favorable environments [98–103]. Figure 1.5 shows a tumble of an *E. coli* cell in which most of the filaments undergo a polymorphic transformation.

The structure and architecture of the BFM has been elucidated using imaging techniques such as cryo-electron microscopy reconstructions and X-ray diffraction combined with genetic and biochemical data. The motor is constituted by rotor and stator components, with the rotor spanning the cell envelope. The BFM is composed of at least 45 different proteins, and the components of the motor are named after the genes that encode them. For example, genes for which mutant cells lack flagellar filaments are called *FliG*, *FliH*, *FliI*, or *FliJ*, and genes for which mutant cells produce paralyzed flagella are called *Mot* (for motility) [104].

The structure of the BFM is shown in Figure 1.6. Gram negative bacteria have a multilayered cell envelope consisting of an inner cytoplasmic membrane, the peptidogylcan layer, and the outer membrane. Spanning the cell envelope, the basal body of the motor, consisting of four rings and a rod, assembles first and is the core of the motor [105]. The rings of the motor are approximately 45nm in diameter [106]. The MS-ring (Membrane, Supermembranous) is assembled first and is made up of about
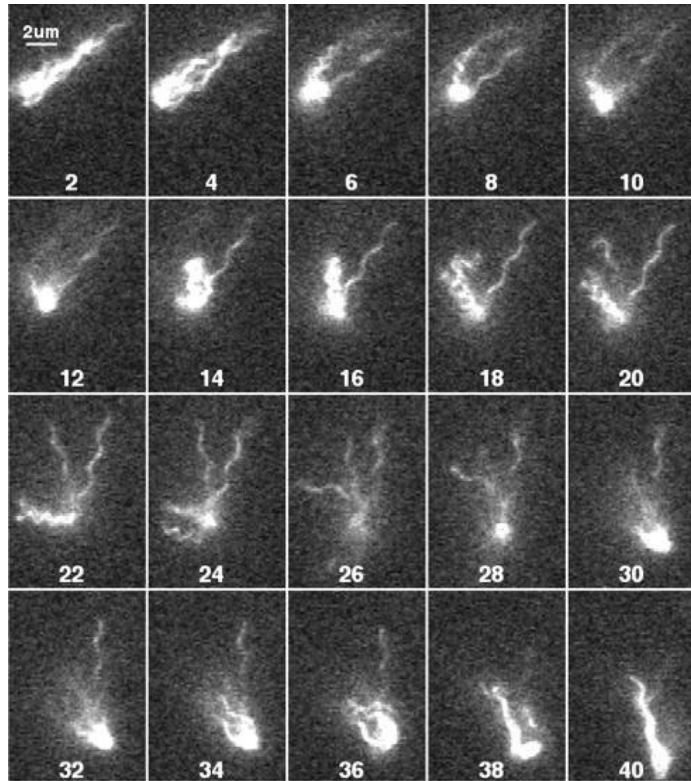
Figure 1.5: Successive images of a swimming *E. coli* cell where one filament maintains a constant orientation and waveform, while the others undergo a polymorphic transformation. This reorientates the bacterial cell. The body and filaments were labeled with Alexa Fluor 532 and illuminated by an argon-ion laser. The frame rate was 60Hz, and every other frame is shown. Image from Turner et al, 2000 [95].

26 FliF protein subunits [107–109]. The MS-ring serves as a platform for the remaining piece-wise assembly [110, 111]. Briefly, the C-ring attaches to the cytoplasmic face of the MS-ring [112], followed by the construction of the export apparatus [113–117]. Proteins are then exported to construct the rod and then the hook. Construction of the hook is paused while the P and L-rings assemble, then resumed [118]. After the hook finishes assembling, the flagellum assembles.

The C-ring (Cytoplasmic) is comprised of FliG, FliM, and FliN protein subunits, and this is the proposed site of torque generation [119–123]. There is evidence for 23-26 FliG subunits in the C-ring [124, 125], and a number of binding studies argue that FliF in the MS-ring and FliG in the C-ring are connected [126–130]. There are about 32-36 FliM subunits and about 100 FliN subunits [122, 131, 132]. Binding

studies argue that FliG, FliM, and FliN are bound to each other [127, 133, 134], and in vitro, one FliM can form a complex with four FliN molecules [135]. The mismatch in the number FliG and FliM subunits is curious. In one model, FliG is contained within the inner part of the C-ring with about 26 fold symmetry [122], and in another model, FliG spans both parts of the membrane, with the outer part having a number of defects equal to the mismatch in symmetry [136]. Two recent studies detailing the molecular structure of the FliG protein propose that exactly 34 FliG proteins are required to construct a ring that is consistent with current three dimensional electron microscopy structures, and that there may be no mismatch between FliG and FliM [137, 138]. However, there may not be a strict requirement for a particular FliG:FliM stoichiometry. C-rings of a range of sizes with periodicities of 31-38 are observed in *Salmonella* without a corresponding increase in MS-ring size [139]. In addition, a recent electron cryotomography (ECT) study of BFMs across many phylogenetically diverse bacteria has found that while the MS-ring is fairly conserved in size and shape, the C-ring diameters vary dramatically [140].

The P-ring, embedded in the peptidogylcan layer, and the outer L-ring, embedded in the lipopolysaccharide membrane, transmit rotation from the motor through the cell envelope. Composed of FlgI and FlgH proteins, it is not known whether they form part of the rotor, rotating within the cell membrane, or if they are fixed to the cell wall and the rod rotates within them. While it is possible that the MS-ring and the C-ring rotate relative to one another and at different speeds [131], it is generally assumed that they rotate as a unit, comprising the rotor of the BFM.

The ion-translocating stators of the proton-driven BFM are comprised of MotA and MotB [143], which span the cytoplasmic membrane, with a likely stoichiometry of four MotA to two MotB [144–146]. This stoichiometry was first suggested by reconstitution of the equivalent stator proteins in the sodium driven *Vibrio alginolyticus* BFM, PomA and PomB [147, 148]. MotA has four membrane-spanning α-helical seg-
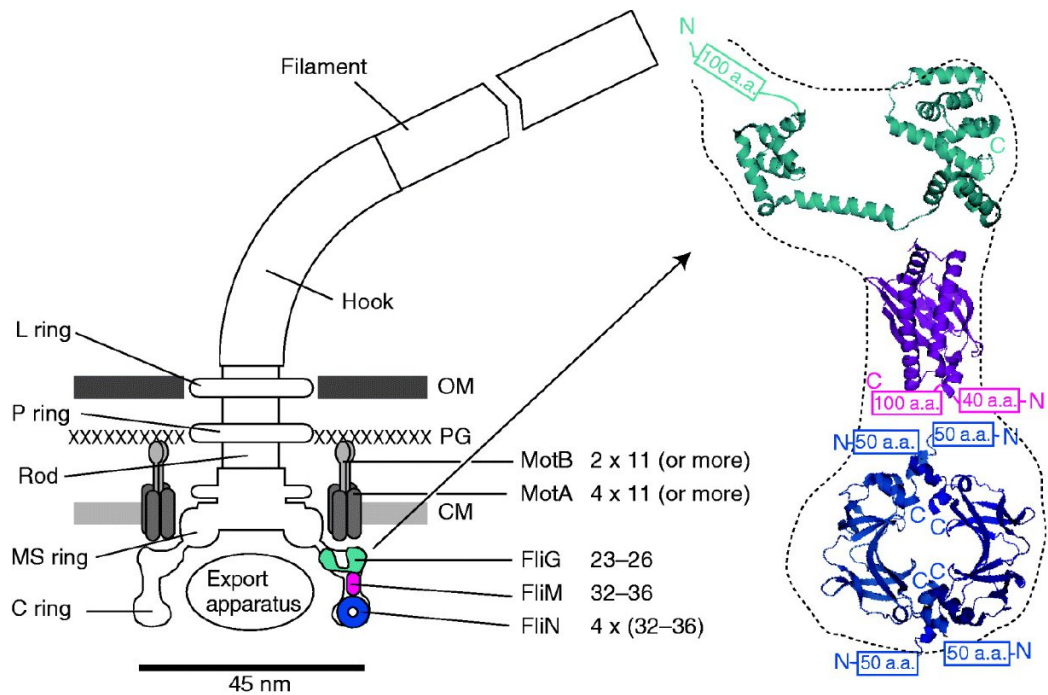
Figure 1.6: Left: A schematic side-view of the BFM spanning the three layers of the cell envelope: the outer membrane (OM), the peptidoglycan wall (PG), and the cytoplasmic membrane (CM). This schematic shows the four rings and rod of the motor, the stator complexes, formed by MotA and MotB proteins with stoichiometry A_4B_2, and the proposed location and copy number of the proteins involved in torque generation. Note that the number of FliG in the motor has recently shown evidence for 34 copies, instead of 23-26 [141]. Rotation of the motor is coupled to the flagellar filament via the hook. Right: X-ray crystal structures of three C-ring proteins, FliG (cyan), FliM (magenta), and FliN (blue) in their proposed docked position in the motor. The N- and C-termini and missing amino acids (aa) are indicated. Image from Sowa and Berry, 2008 [142].

ments [143, 149, 150] with two thirds of the molecule lying in the cytoplasm [143, 150], while MotB has one membrane-spanning α-helical segment [151, 152] with the rest of the molecule lying in the periplasm [152]. These subunits form the complex of the torque generating unit, each containing two proton channels [153–155]. Mutational studies have found Asp32 in MotB to be an essential proton-accepting residue in *E. coli* [156]. This residue is the only conserved charged residue in MotA or MotB, where charged residues are believed to be the sites of functionally important electrostatic interactions. Asp32 is surrounded by the four α-helices of MotA and is thought to

21

form part of one of the two ion channels [155]. Mutational studies have also found that Arg90 and Glu98 of MotA are critical for the positioning of stators around the motor and torque generation, respectively [123].

While no atomic level crystal structure exists for the stator complex, making it difficult to pinpoint the site of torque generation, biochemical crosslinking and site-specific mutagenesis studies have located the likely active regions. Stator topology is shown in Figure 1.7. Studies suggest that MotA and MotB interact with each other [134], and that MotA interacts with FliG to generate torque [157–161]. MotB contains a peptidoglycan-binding domain near its C-terminus [162], and it is believed that this anchors the stator unit to the cell wall [162]. The anchoring of the stator to the cell wall is necessary in order for the stators to be able to apply torque to the motor [163]. An interaction between two charged residues on the cytoplasmic domain of MotA and five charged residues on the C-terminal domain of FliG in the C-ring generates torque [156, 164, 165]. Introducing charge-reversing mutations in both proteins compensates, suggesting an electrostatic interaction between FliG and MotA [142]. A similar pattern is seen in PomA and FliG in the Na^+-driven BFM of *V. alginolyticus* [166]. Mutations in MotB-Asp32 in membrane-bound stator complexes alter the susceptibility of MotA to proteolysis [167]. It has been postulated that the protonation and deprotonation of Asp32 of MotB modulates the conformation of MotA, thereby changing the interaction of the charged regions of MotA with the complementary charged regions in FliG [167,168]. Crystal structures of MotA, MotB, and FliG are needed to understand how these seven residues interact during proton translocation to generate torque. Recent *in situ* ECT studies have improved the 3D map of the BFM and confirmed that the MotAB stators are positioned on the outside of the MS-ring, in contact with the outer periphery of the C-ring [169–172].

Each BFM is driven by an ensemble of several stators which dynamically bind and unbind from the motor in a process of continual turnover. Such turnover is suggested
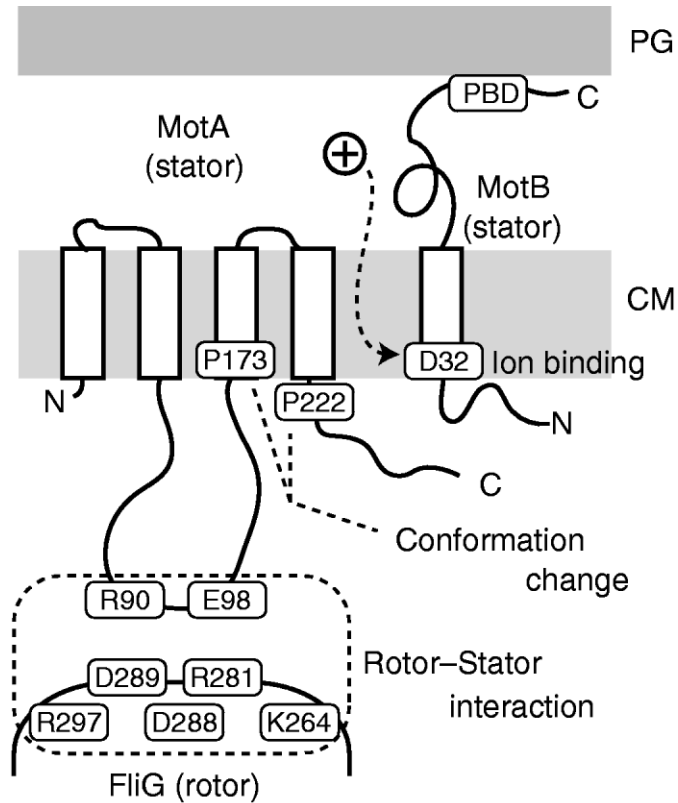
Figure 1.7: A schematic showing the stator topology and the interaction between the rotor and stator in *E. coli*. MotA and MotB have four and one α-helices which span the cytoplasmic membrane (CM), respectively. MotB contains peptidoglycan binding domains (PBD) near its C-terminus, anchoring the stator to the peptidoglycan (PG) cell wall. Charged residues in the cytoplasmic domain of MotA interact with charged residues of FliG to generate torque. Figure from Sowa and Berry, 2008 [142].

by the observation of transient speed changes [173] and confirmed using Total Internal Reflection Fluorescence (TIRF) microscopy to observe green-fluorescent protein (GFP) labeled MotB in live cells [174]. In these experiments, the average time a stator remained attached to a motor was about 30 seconds. The reason for such turnover is unknown, though postulated to be the replacement of damaged stator subunits. It should be noted that GFP-MotB is less functional than wildtype Mot-B, and it is unknown how their stabilities in the motor compare [174,175]. A freely diffusing pool of GFP labeled MotB molecules has been observed in the cell membrane, and stators exchange between the this pool and the motor [174].

In a technique called 'resurrection', the controlled expression of stator protein within a cell leads to an increase in the number of stators engaged with a motor, each stator causing a step-wise increase in motor speed. Such experiments demonstrate that each BFM contains several torque-generating units [176,177] and that the stators operate individually, contributing equally to motor output in a high-load regime [173]. Early resurrection experiments demonstrated that motors could contain up to eight stators [177], while more recent experiments have shown that motors can rotate with at least 11 stators [173,174]. Figure 1.8 shows a resurrection of motors in an *E. coli* BFM.
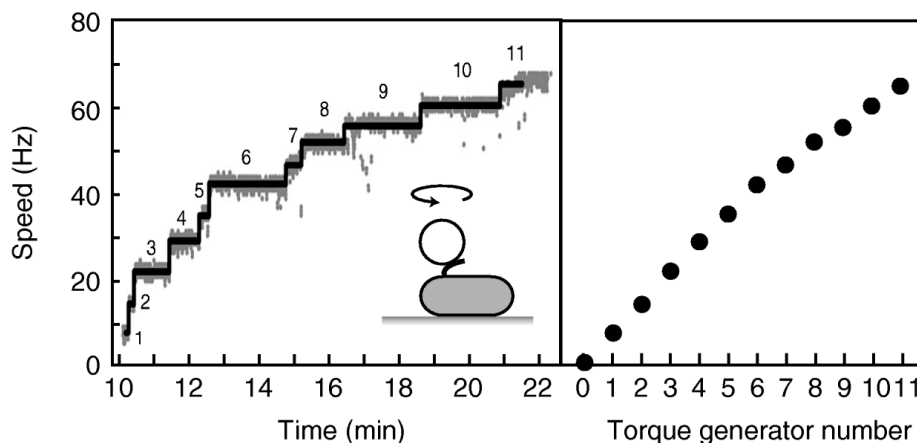
Figure 1.8: A 'resurrection' of a BFM with defective stator protein by induced expression of functional stator protein in *E. coli*. The graph on the left shows speed versus time during the resurrection, and the graph on the right shows speed versus stator number. The BFM was labeled with a 1μm bead and shows up to 11 or 12 stators. This experiment demonstrates that the stators function as independent torque-generating units. Figure adapted from Sowa and Berry, 2008 [142] with data from Reid et al, 2006 [173].

Stators are not the only component of the BFM that is in continual turnover. While it was long assumed that the structure of the motor was static, recent fluorescent recovery after photobleaching (FRAP) experiments using TIRF microscopy have demonstrated that GFP labeled FliM and FliN proteins are dynamically exchanged in the motor [174]. The experiments showed that FliN is exchanged in tens of minutes

and FliM is exchanged at a slightly slower rate, even in rotating motors. GFP labeled FliG showed no evidence of exchange. It is yet to be seen if other proteins of the BFM are similarly dynamic. The exchange of motor subunits may be an important property in sustaining the function of the machine.

The rod connects the MS-ring to the hook, a tubular polymer filament flexible enough to allow the filaments of multiple motors to bundle [178]. The hook is thus a universal joint, 55±6nm in length [179], and composed of about 120 copies of a single protein, FlgE. The FlgE proteins are arranged into 11 parallel protofilaments which continually switch from compressed on the cell side to extended on the opposite side during rotation [104, 111]. This is possible due to the ability of FlgE subunits to slide alongside and rotate relative to one another. Experiments using a genetically modified hook that can be stiffened by binding streptavidin to biotinylated monomers has shown that stiffened hooks impede the action of the universal joint and result in atypical swimming behavior [180]. Thus, the universal joint property of the hook is necessary for filament bundle formation.

The hook is connected to the filament via junction proteins FlgK and FlgL [111]. The filament is also a tubular polymer made of 11 parallel chains of a single protein, FliC. A fully formed filament is typically 5-10μm, containing up to 20,000 copies of FliC. Unlike the hook, the filament is fairly rigid and the protofilaments remain fixed. The protofilaments can be of two distinct conformations: L-type where the subunits form long protofilaments and R-type, where the subunits are closer together [181]. The protofilaments are twisted slightly relative to the cylinder axis, and R and L refer to the direction of twist. If the filament is composed entirely of L-type protofilaments, it is straight with left-handed symmetry, whereas if composed of all R-type protofilaments, it is straight with right-handed symmetry [182]. If composed of a mixture, the filament has curvature and twist and is helical [183], where the pitch and radius of the helix depends on the number of R-type protofilaments [184]. When

a motor switches from CCW to CW, the filament subunit structure changes, causing the filament to splay from the bundle. The structures of the hook and filament are shown in Figure 1.9.
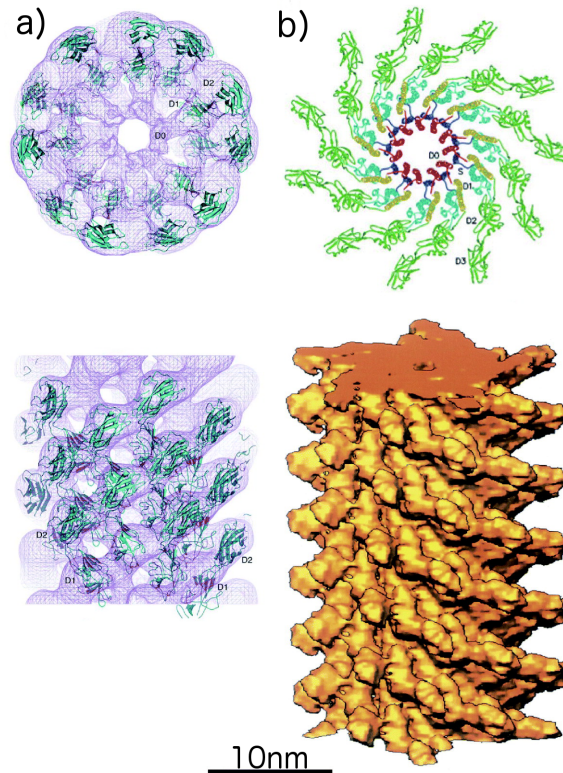
Figure 1.9: An end on and side view of the hook and filament. a) Model of the hook obtained via X-ray crystallography. Purple shows the crystal structure and cyan is a refined model using electron cryomicroscopy data. b) A ribbon diagram of an R-type filament obtained via electron cryomicroscopy: on top, an end-on image of the distal end of a filament, showing 11 subunits, and on bottom, a side view of a filament. The scale bar is 10nm. Figure adapted from Sowa and Berry, 2008 [142] and comes originally from Yonekura et al, 2003 [181] and Samatey et al, 2004 [178].

The proteins that constitute the rod, hook, and filament are exported by a type III export apparatus [111,185,186]. Composed of six membrane-embedded proteins [111], the export apparatus is found in the C-ring of the motor and is potentially gated by a domain of FliF [187]. It is related to the injectisome found in many gram-negative pathogens. After being exported, the constituent proteins travel through the hollow interiors of these structures and self-incorporate onto the distal end.

26

For recent reviews providing more details on the structure of the BFM, refer to [142, 186, 188, 189].

1.3.2 Motility and energetics

Bacteria are small and they live in very different hydrodynamic world than we are accustomed to, one of low Reynolds number. The Reynolds number is a dimensionless parameter quantifying the relative importance of inertial forces compared to viscous forces. Mathematically, it is defined as

$$Re = \frac{av\rho}{\eta} \tag{1.6}$$

where a is the characteristic length of the particle, v is the velocity of the particle moving through the fluid, ρ is the specific gravity of the fluid, and η is the fluid viscosity [190].

A large Reynolds number means that inertial forces dominate, whereas a small Reynolds number means that viscous forces dominate. Using equation 1.6, the Reynolds number of a human swimming in water is on the order of 10^5, and the Reynolds number of a bacterium swimming in water is on the order of 10^{-5}. The human feels inertia, while the bacterium does not. When the bacterium stops propelling itself, it coasts to a stop over a distance of only 0.1Å (though due to Brownian motion, the bacterium never really stops) [191, 192].

At low Reynolds number, a particle's motion is determined by what the particle is doing at that moment, and is unaffected by the past [191]. Therefore, in a time invariant low Reynolds number environment, reciprocal motion doesn't get you anywhere. At the length scales of bacteria, in order for propulsion to occur, the movement must be distinguishable in the forwards and backwards directions. Oscillating propellers, such as cilia on cells and the tails of sperm, accomplish non-reciprocal motion by

using a 'flexible oar,' capable of a power stroke and recovery stoke. In the case of flagellated bacteria, the rotation of one or more helical filaments generates thrust. While the axial symmetry of the helix causes components to cancel in the lateral axes of the cell, there is a net propulsion along the helix and cell's longitudinal axis. When the cell is swimming, this thrust is balanced by viscous drag on the cell body. The torque generated by rotation of the filaments is balanced by a counter rotation of the cell body.

Unlike F_1ATPase, the free energy source for the bacterial flagellar motor is ions moving down an electrochemical gradient as they cross the cytoplasmic membrane. The amount of work per unit charge an ion can do in crossing the cytoplasmic membrane is called the ion motive force, IMF. Different species of bacteria are powered by different ions, either protons or sodium, in which case this force is called the proton motive force (PMF) or sodium motive force (SMF), respectively. In general, the IMF consists of an enthalpic term and an entropic term, and mathematically it is defined as:

$$IMF = V_m + \frac{k_B T}{q} ln \frac{C_{in}}{C_{out}} \tag{1.7}$$

where V_m is the electrical potential across the membrane, k_B is the Boltzmann constant, T is the temperature, q is the ionic charge, C_{in} and C_{out} are the ionic concentrations inside and outside the cell, and the IMF is measured in volts. The enthalpic term, V_m, arises from the transmembrane electrical potential difference, and the entropic term, $\frac{k_B T}{q} ln \frac{C_{in}}{C_{out}}$, arises from the transmembrane chemical potential difference or pH difference. By convention, both terms are the internal potential less the external potential.

The first direct evidence that the BFM is ion-driven came from experiments with starved *Streptococcus* and *Bacillus subtilis* cells. Flagellar rotation was observed when these starved cells were provided with either an artificial membrane potential or a pH gradient in the absence of ATP [193,194]. In later experiments, filamentous cells were

drawn partially into micropipettes, the cytoplasmic membrane was made permeable, and the external part of the membrane was energized by voltage clamping the pipette. A high load was applied to the motors via markers to monitor motor rotation, and it was found that speed was proportional to V_m over the physiological range (up to -150mV) [195]. Later experiments investigated the dependence of IMF on speed with lower loads on the motor. Using an ionophore to gradually collapse the IMF, it was found that the speeds of motors with low loads was proportional to the speeds of motors with high loads. Given that at high load motor speed is proportional to IMF, it was shown that the same is true for the BFM at low loads, though the relative contributions of the membrane potential and pH gradient were not known [196].

The wild-type motor of *E. coli* and many other bacteria are powered by protons [142]. Yet some bacteria, specifically marine bacteria such as *Vibrio alginoliticus* and others that live at high pH, are powered by sodium ions [197, 198]. Protons and sodium ions are the only sources of energy for the BFM, with other anions and cations ruled out [199–201][4]. In *V. alginolyticus*, some motor components are homologous to those in *E. coli*. For example, the stator proteins PomA and PomB are structurally similar to MotA and MotB. Other motility proteins, such as MotX and MotY, are not homologous [202]. Rotation speeds of the BFM in sodium motors are much higher than in proton motors; the sodium motor of *V. alginolyticus* can reach speeds up to 1700Hz at low load [203, 204], whereas proton motors are limited to about 300Hz.

The similarity between MotA/MotB and PomA/PomB has inspired the construction of many functional chimeras. A chimeric fusion protein called PotB was made between the periplasmic C-terminal domain of *E. coli* MotB and the membrane-spanning N-terminal domain of PomB in *V. alginolyticus*. This chimeric PotB, in combination with PomA, creates a sodium-driven motor in *E. coli* [205]. Such a chimera is useful because it allows one to control the two components of the IMF

---

[4]However, Dr. Alex Rowe performed unpublished experiments where chimeric *E. coli* was observed to rotate near normal speeds using Li^+ as an energy source.

individually without affecting cell function. In sodium-driven motors, the ion concentration can be controlled independently of the pH, which affects the membrane voltage, allowing independent control of the two components of the IMF [206, 207].

A chimeric sodium-driven strain of *E. coli* was used to measure the effects of both components of the IMF at both low and high load [205–208]. The membrane voltage was controlled by changing the external pH and the sodium gradient was controlled by changing the external sodium concentration. The membrane voltage and intracellular sodium concentration were measured using two fluorescent dyes. It was found that at high load, motor speed was proportional to SMF with equivalent contributions from each component of the SMF, agreeing with previous work. At low load, the two components of SMF were not equivalent [206]. For a constant sodium gradient and varying membrane voltage, speed was proportional to SMF. However, the proportionality constant was larger for higher sodium gradients. This result agreed with a previous experiment on *V. alginolyticus* [209], and this suggested that in the low-load regime, ion binding is the rate limiting step of the BFM. A more recent set of experiments measured torque speed curves of single stator chimeric motors for 25 different SMF values, varying both the external pH and the external sodium concentration, confirming the relationships mentioned above [210]. They found that below the knee of the torque-speed curve, chimeric BFM speed is more sensitive to pH than to membrane voltage. A systematic investigation of the curves led to the conclusion that ion transit or ion release is the rate limiting step at low load, except at the lowest sodium conditions, where ion binding becomes rate limiting. Using the measured torques in the plateau region of the torque-speed curves, these experiments estimate that 37 ± 2 sodium ions are needed to energize the motor per revolution, and this result is independent of SMF.

It is also known that the presence of an IMF is crucial for stator unit assembly [211]. Under typical biological conditions, a single ion transit provides approximately

$6k_BT_0$ [142]. Ion transit is hypothesized to coordinate conformational changes in MotA via Asp32 of MotB [167]. In an experiment to measure the ion flux through the BFM of *Streprococcus* cells, an antifilament antibody was used to crosslink the filaments, causing the motors to stop rotating. The shift in the rate of pH change of a weakly buffered suspension of cells estimated the ion flux to be 1240±240 protons per revolution of the motor over a speed range of 20-60Hz [212].

1.3.3 Torque and speed

The aim of much of the research on the BFM is to understand the mechanism of torque generation in the motor and how ion flow is coupled to rotation. Historically, one of the best ways to quantify the mechanochemical cycle of the motor has been to investigate the relationship between the motor's torque and speed. Using a variety of methods, the torque of the BFM has been measured over a large range of speeds, including speeds in which the motor is forcibly driven backwards, in order to characterize motor output. The methods are covered more thoroughly in Chapter 2 and will only be alluded to here.

As the viscous load on the motor is equal to the motor torque during steady state rotation, varying the load on the motor and measuring the speed of motor rotation yields a torque speed curve. The torque exerted on the motor due to a load is equal to the rotational drag coefficient of the load multiplied by the velocity, as shown in Equation 1.5. This assumes a Newtonian medium, such as a dilute aqueous medium without long unbranched molecules [213]. The load on the BFM can take the form of the cell itself, as in tethered cell experiments, or a particle attached to the filament or hook, as in bead assay experiments [214–216, 216, 217]. Larger particles impose a large viscous load due to a larger drag coefficient. The load can be further varied by changing the viscocity of the surrounding medium [218] or by applying an external torque to the motor via electrorotation [219, 220]. Torque-speed curves of both wild

type (proton driven) and chimeric (sodium driven) *E. coli* motors obtained from a combination of these methods are shown in Figure 1.10.
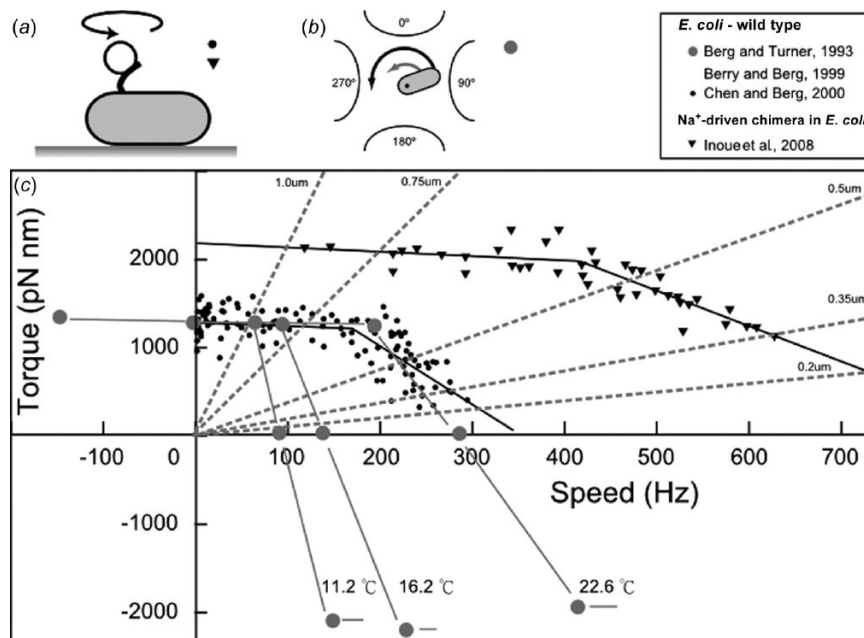
Figure 1.10: Torque-speed relationships for flagellar motors of proton-driven wild-type and Na^+-driven chimeric *E. coli* at high induction (maximum number of stator units). Method A) shows a bead assay where the torque is controlled by the size of the bead attached to the truncated flagellar filament at high load, or to the hook at low load. Data using this method is indicated by black circles [218] or black triangles [217]. Load lines for six different sized beads are shown on the plot as dashed grey lines. Method B) shows an electrorotation assay where microelectrodes create a MHz rotating electric field at the cell that applies an external torque that adds to the motor torque. Data using this method is indicated by grey circles [219]. Except where indicated, all measurements were made at room temperature. For further details, see the references indicated in the legend. Figure adapted from Baker and Berry 2009 [221] using data from Sowa and Berry [142] and Yuan and Berg [216].

The torque-speed curve appears to be a piece-wise linear function characterized by two regimes, high load and low load. The high load regime is characterized by a plateau of nearly constant (slowing decreasing) torque, where the motor is limited by the mechanical relaxation of the load. At high load, motor torque is independent of temperature [219, 222], solvent isotope substitution[5] [218], and the composition of the IMF [223]. The low load regime is characterized by a steeper region that decreases

---

[5]In this case, protons replaced by deuterons.

linearly to zero torque. In this regime, motor torque is dependent on temperature, solvent isotope substitution, and the composition of the IMF [218, 219, 222, 224]. This is what one would expect if in the low load regime the motor is limited by mechanical and chemical transitions, for example, the binding, transit, or unbinding of ions or conformational changes. The intersection of the high and low load regimes is called the 'knee' of the torque-speed curve. As Figure 1.10 shows, the position of the knee is temperature dependent, with lower temperatures causing the BFM to transition between the two regimes at higher loads. However, at low speeds, the torque of the motor is independent of temperature. This is consistent with the assumption that, at low speeds, the BFM operates near thermodynamic equilibrium and at high efficiency. In both regimes, the motor speed varies linearly with IMF [196].

The torque-speed curves also show the maximum torque of the motor, arising at zero speed or the stall of the motor, and the maximum speed of the motor, arising at zero external torque. The maximum torque generated by the wild-type *E. coli* motor was measured to be 1260±190pN nm rad^{-1} (at 23°C, pH 7.0) [173], but this value is slightly higher in the chimeric motor. The maximum speeds of the proton-driven wild type motor and sodium-driven chimera of *E. coli* at zero torque is around 300Hz and 900Hz, respectively [216, 217]. Electrorotation experiments in which a non-switching strain of the BFM was forced to rotate backwards (CW) show a continuity in torque on both sides of the motor stall. This demonstrates that there is no irreversible step in the mechanochemical cycle. If such a step did exist, there would be a step-wise change in motor torque as the motor was forced to switch directions [215]. When large amounts of CheY are expressed in cells, the BFMs rotate exclusively CW. The torque speed curve of of the BFM when rotating CW is different to when rotating CCW. The torque in the CW rotating BFM has been shown to simply decrease linearly with speed [225].

While Figure 1.10 shows torque-speed curves of motors with native expression of stator protein, torque-speed curves have also been measured for different number of stators driving the BFM, and this is shown in Figure 1.11. As shown, at high load, torque is proportional to the number of stators. Similar experiments were performed at low load using a small gold bead attached directly to the hook [216]. These experiments measured the speed of the motor for different levels of stator induction, concluding that, near zero load, motor speed is independent of the number of stators. These results suggest that the motor operates on a high duty cycle, meaning that the stator units spend most of the time engaged with the motor. Conservation of energy sets a lower limit to the number of ions that must flow in the motor per revolution, N_{min}:

$$N_{min} = \frac{2\pi T_m}{q \cdot IMF} \tag{1.8}$$

where T_m is the motor torque and q is the ion charge. For a single-stator chimeric motor at high SMF driving a 1μm bead, $N_{min} = 37\pm2$ per stator [210].

Referring again to Figure 1.10, it was assumed for a long time that each torque speed curve had the same number of stators driving the motor. This assumption is necessary in order to extrapolate these torque speed curves to low torque and suggest that the limiting speed of the motor is independent of the number of stators. However, recent experiments have demonstrated for the first time that stators are dynamic mechanosensors, and the number of stators in a motor is dependent on the external load. In these experiments, TIRF microscopy was used to image yellow fluorescent protein (YFP) tagged MotB proteins while the BFM experienced a sudden increase in viscous drag. This was achieved by either using an optical trap to attach a 1μm latex bead to a rotating filament stub or by allowing a rotating filament stub to tether to the surface of a coverslip. The speed of the motor was measured from the instant of increase in load, as was the fluorescence of the motor. Simultaneous step-wise decreases in motor speed and increases in motor fluorescence were observed after the
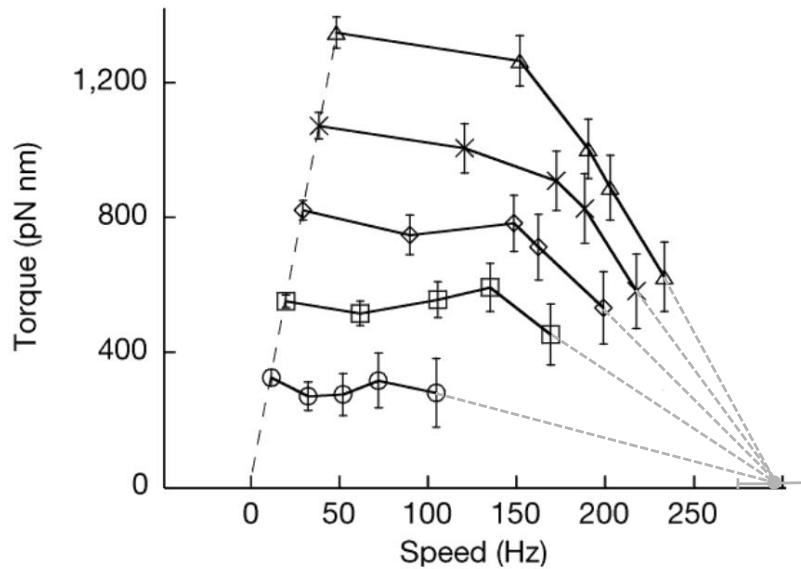
Figure 1.11: Torque-speed curves with 1-5 stators; the bottom curve shows 1 stator and increasing upward with the top curve showing 5 stators. The measurements were made with a strain where MotA proteins were induced. The measurements in black were made by Ryu et al [226]. Examining an extrapolation of the curves to low torque, they predicted that the limiting speed of the motor near zero load is independent of the number of stators, implying that each stator has a high duty ratio. The single data point in grey is from Yuan and Berg who measured the speed of motors near zero load and concluded that speed is indeed independent of the number of stator units [216]. The dashed lines in grey connect Ryu et al's data to Yuan and Berg's. Figure adapted from Ryu et al, 2000 [226] including data from Yuan and Berg 2008 [216].

increase in load. Motors at low loads were driven by 1 and at most 2 stator units, and motors at high loads were driven by 6-11 stator units, as measured once the motors reached maximum speed [227]. Similar results were achieved by an independent set of experiments which observed GFP-MotB while simultaneously recording motor speed for many cells with different loads. The load was varied by probe size and medium viscosity, and motors were stalled by attaching a paramagnetic bead to the filament and using an external magnetic field. The data for both sets of experiments, confirming that the number of stators bound to a motor is dependent upon the external load, are shown in Figure 1.12. This suggests that zero-load speeds of the BFM may not be independent of stator number. To date, all torque speed curves

have been created by pooling measurement of motors with varying loads without controlling for the number of stator units.
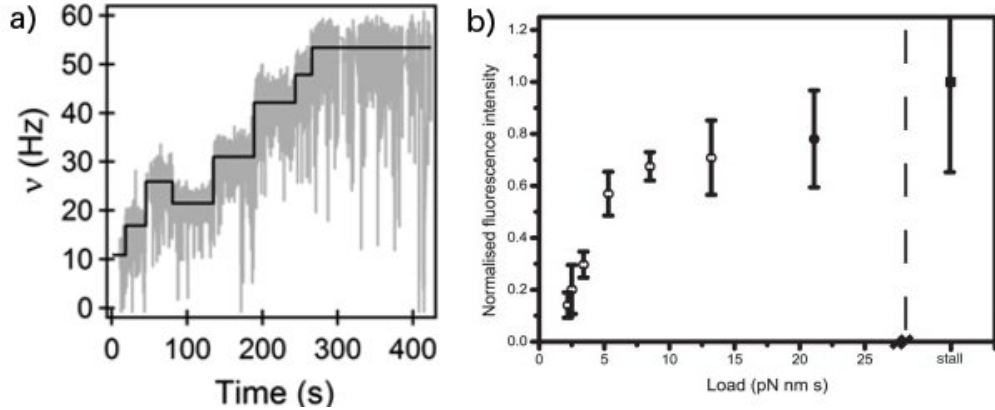
Figure 1.12: a) A graph of velocity versus time, starting immediately after the attachment of a 1μm polystyrene bead in a CCW-locked rotating motor, showing a step-wise increase in rotational velocity attributed to additional stators joining the motor. b) Fluorescence intensity versus load for CCW-locked motors. The fluorescence is from GFP-MotB, and the load was varied using different sized beads, different medium viscosity and stalling via external magnets. Each point represents the mean of 15 motors except at stall, where 5 motors were measured. Figure adapted from Lele et al 2013 (a) [227] and Tipping et al 2013 (b) [228].

1.3.4 Switching

The BFM's ability to actively control the direction of motor rotation is a crucial element in responding to stimuli in the environment. The C-ring is composed of FligG, FliM, and FliN proteins. Along with being the proposed site of torque generation and the housing of the export apparatus, these proteins are referred to as the 'switch complex', because mutations lead to defects in motor switching [229, 230]. The switch complex is considered to be a ring of 34 identical protomers, consisting of $\sim$1 FliG, 1 FliM, and a tetramer of FliN subunits. FliN is thought to provide a scaffold for the switch [231].

Under typical conditions, the *E. coli* BFM switches directions on the order of once every second due to a chemotactic signaling system. The likelihood of changing

direction is enhanced by the presence of CheY, a small response regulator protein. Chemotactic switching is induced when the phosphorylated form of CheY, called CheY-P, binds to FliM [133, 232, 233] at the N-terminus [234]. Strains which lack CheY or the kinase required for its phosphorylation, CheA, rotate exclusively CCW. The CheY-P concentration in the cell is controlled by a well-studied chemotactic signaling system (see recent reviews, [92, 101, 102, 104, 235]). After CheY-P binds FliM, it is believed that conformational changes in FliM cause conformational changes in FliG, interfering with the torque generating units to change the direction of motor rotation [208, 231, 236–240].

Early experiments suggested that switching was an all-or-none Poisson process because the motor appeared to run at full speed either CW or CCW, and the distribution of switch intervals was exponential [241–244]. Later studies found that the CW bias (ie the percent of time a motor spent spinning CW) had sigmoidal dependence on the CheY concentration. It was thus proposed that switching is a thermal isomerization process with two potential wells, jumping from one to another with exponentially distributed waiting times. Further experiments showed that the bias of the motor is strongly dependent upon the concentration of CheY-P in the cell, with a Hill coefficient of around 10 [245, 246]. This suggested that the switch mechanism of the motor can not be explained by cooperative binding, and this has been further confirmed using fluorescence resonant energy transfer (FRET) to quantify the binding between CheY and FliM and finding a Hill coefficient less than 2 [247–249]. Figure 1.13 shows a graph of the CW bias of the BFM versus the CheY-P concentration.

The current best candidate to explain the switch mechanism of the motor is a conformational spread model which allows for a multistate switch [250]. A change from one state to another is accompanied by a change in free energy. Conformational spread describes the stochastic growth and shrinkage of domains of neighboring sub-units sharing a particular conformation state, assuming that conformation-dependent
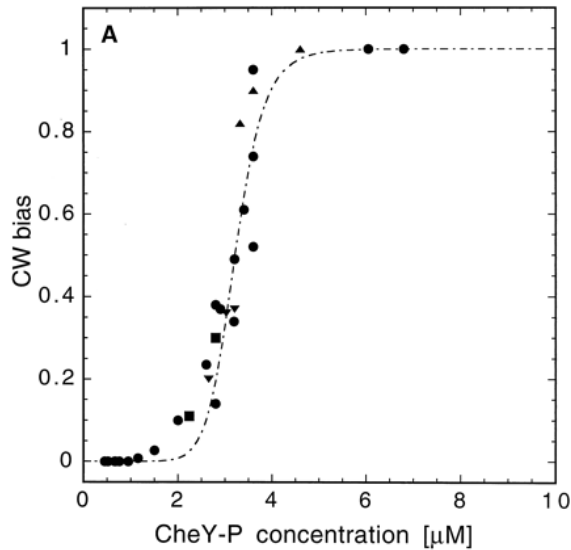
Figure 1.13: Sigmoidal response of BFMs in response to CheY-P concentration where each data point represents an individual bacterium. The concentration of intracelllar GFP tagged CheY-P was measured with fluorescence correlation spectroscopy. The dashed line shows the best fit of a Hill function, with a Hill coefficient of 10.3 ± 1.1. Figure from Cluzel et al, 2000 [245].

cooperative interactions between adjacent FliMs favor like conformations. If one FliM undergoes a conformational change, the change may spread to the rest of the FliM proteins present in the ring. If all FliMs change conformation, the motor switch occurs, and if not, the FliMs that underwent conformational change will return to their original state. The latter event may describe some of the fluctuations in speed and pauses that are observed in the motor [251]. In 2010, high resolution measurements of the switching of single motors provided strong evidence for the model of conformational spread, and Figure 1.14 shows a diagram of this model. For more details, see Bai et al, 2010 [103].

1.3.5 Stepping

Attempts to detect steps in the rotation of the BFM began soon after the confirmation of motor rotation [252]. As the BFM operates on a periodic track consuming a discrete number of fuel molecules per rotation, one would assume that there are
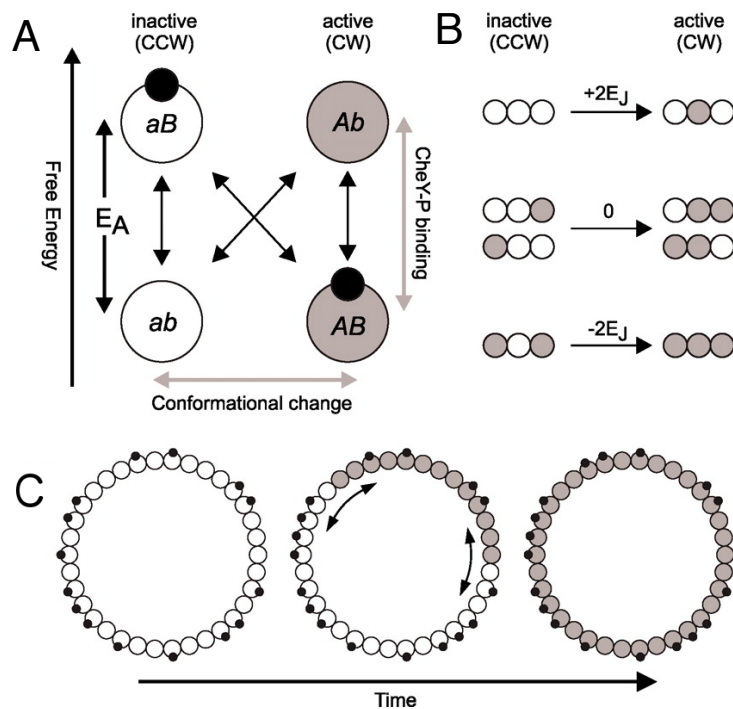
Figure 1.14: The conformational spread model of the bacterial flagellar switch. The switch complex consists of ~34 identical protomers, each composed of ~1 FliM, 1 FliG, and a tetramer of FliN subunits. A) a free energy diagram of the four potential states of a protomer where the CW bias (fraction of time spent rotating in the CW direction) is 0.5. The black circle marks bound CheY-P. B) The interactions between adjacent protomers, assuming that the free energy is lower by E_J for a like pair compared with an unlike pair. C) Above a critical value of E_J, the switch complex ring spends a majority of time in a coherent state. Stochastic switches to the opposite configuration are usually due to nucleation of a single domain followed by conformational spread. This entails a biased random walk until the entire switch complex has either switched state or collapsed back to its previous state. Figure adapted from Bai et al, 2010 [103].

discrete mechanical steps in the motor's rotation where force generation occurs. The observation of such steps can be used to obtain a more detailed picture of the motor mechanism. Discrete steps had been observed in kinesin by 1993 [253], the first observation of discretized molecular motion in a molecular motor. Steps were observed in F_1-ATPase in 1997 [9], and in 2001, these steps were further resolved into substeps [46]. Steps in myosin and dynein were observed in 1999 and 2000 respectively [254, 255].

The first indirect evidence for a stepping mechanism in the BFM came from comparing the mean and variance of motor rotation speeds of tethered cells. This analysis yielded a quadratic relationship, the predicted result for any mechanism involving a Poisson stepper with exponentially distributed dwell times [256]. A further analysis of this data predicted 50 steps per revolution per stator in the BFM [257]. The predicted increase in steps as the number of stators increases suggests that each stator is connected to the rotor most of time, that is, the stators operate with a high duty ratio. Broken motors showed free rotational diffusion [256, 257]. These early experiments suggested that the direct observation of steps in the BFM would present a technical challenge. It should, however, be noted that the predicted steps from this experiment need not correspond to physical movement of the rotor or observable steps. This analysis, based upon Poissonian statistics, estimates independent sequential stochastic events, which may or may not be observed in rotation. Figure 1.15 shows the results of this analysis, a graph of the estimated number of steps versus the number of torque generating units [257].
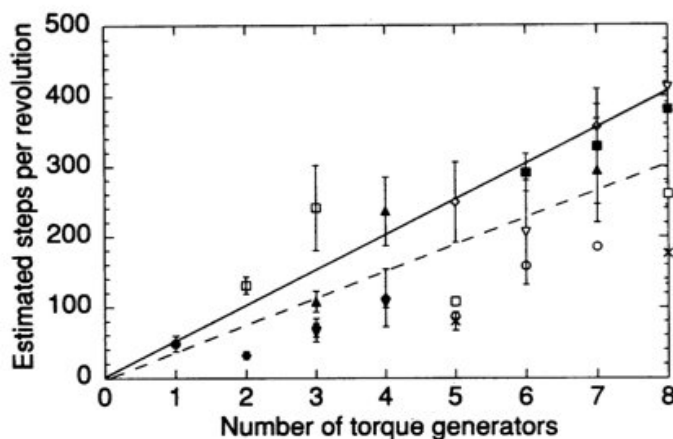
Figure 1.15: A graph showing the estimated number of steps versus the number of torque generating units for tethered cells. The solid line was drawn by hand and the dotted line is a linear regression. The estimated number of steps was calculated from the variance in rotation period: a model of a Poisson stepper predicts that the variance in the rotation period for a fixed angular displacement is inversely proportional to the square of the mean rotation rate. Figure from Samuel and Berg, 1996 [257].

The high speed of the BFM under standard biological conditions combined with a high number of steps per revolution necessitated high spatial and time resolution. In addition, the hook acts as a filter, smoothing out steps in the rotation of a bead attached to a filament. The stiffness of the hook was measured to be between 100pN nm rad^{-1} [258] and 1000pN nm rad^{-1} [180] using optical tweezers to apply a torque to a tethered cell and measuring its relaxation time . A single stator exerting a torque of 150pN nm [173] twists the hook by about 20°. In order to resolve steps, the time between motor steps must be longer than the relaxation time of the bead, which is the viscous drag coefficient of the bead divided by the spring constant of the elastic hook. While a smaller bead reduces the drag coefficient and thus the relaxation time, it also reduces the load on the motor, leading to a faster motor speed and thus less time between steps.

A solution to these technical challenges was found in 2005 by Sowa et al, leading to the first direct observation of steps in the BFM [208]. In these experiments, 500nm polystyrene and 200nm fluorescent polystyrene beads were attached to the truncated filaments of a sodium-driven chimeric strain of *E. coli* [205]. According to the necessary criterion that the relaxation time of the bead is shorter than the dwell time between steps of the motor, for beads of this size, the BFM needed to be slowed down to about 12Hz. This was partially accomplished by keeping the BFMs at low stator number by controlling the amount of stator protein in the cells. The SMF was also reduced by either limiting the amount of sodium in the medium or by exposing the cell to high intensity light, thus photodamaging the cell and decreasing the membrane voltage. The relationship between SMF and sodium concentration was not known at the time, nor was the specific mechanism of photodamage. But, by controlling both the number of stators and the SMF, the motors spun at 10Hz or less [208].

Both methods allowed for the first direct observation of discrete steps in the BFM, demonstrating that the BFM takes 26 steps per revolution. This corresponds to a step size of 13.8°, and the number of steps per revolution corresponds nicely to the proposed number of FliG proteins in the rotor, the site of proposed torque generation [109, 122]. Figure 1.16 shows data from these experiments [142, 208]. The SMF was neither able to be measured nor well controlled, and there was variation in motor speed from cell to cell. The step size, however, was the same for all speeds, and in a recording of a single motor, the dwell angles remained the same in successive revolutions. Interestingly, occasional back steps that occurred during the recordings demonstrated a slightly smaller average step size of 10.9°. The number of stators was unknown, but it is likely that all the measurements in this experiment were single-stator.

If steps of 13.8° are the smallest unit of movement in the BFM, it should be possible to calculate the number of ion transits that correspond to a single step via energy conservation. The stall torque for the chimeric motor sets an upper bound to the step size enabled by a single ion transit. The maximum step size is just the free energy per ion divided by the torque exerted by a single stator. Under biological conditions, the chimeric BFM dragging a 1μm bead would need 36±6 sodium ions to energize one revolution of the motor [206]. This corresponds to a 35-fold symmetry of the C-ring, but it suggests that, at high load, if the motor is tightly coupled, a single step requires more than one ion transit but less than two. Calculations of the chimeric motor driving a 350nm bead at low SMF ([Na$^+$] = 1mM, pH = 5) suggest that a minimum of 20±9 ions are needed per revolution [206]. The observation of 26 steps per revolution of the chimeric motor at low load and low SMF suggests that either the number of ions required for one step of the motor under physiological conditions is greater than one (but less than two) or that the number of steps at high load is higher than 26.
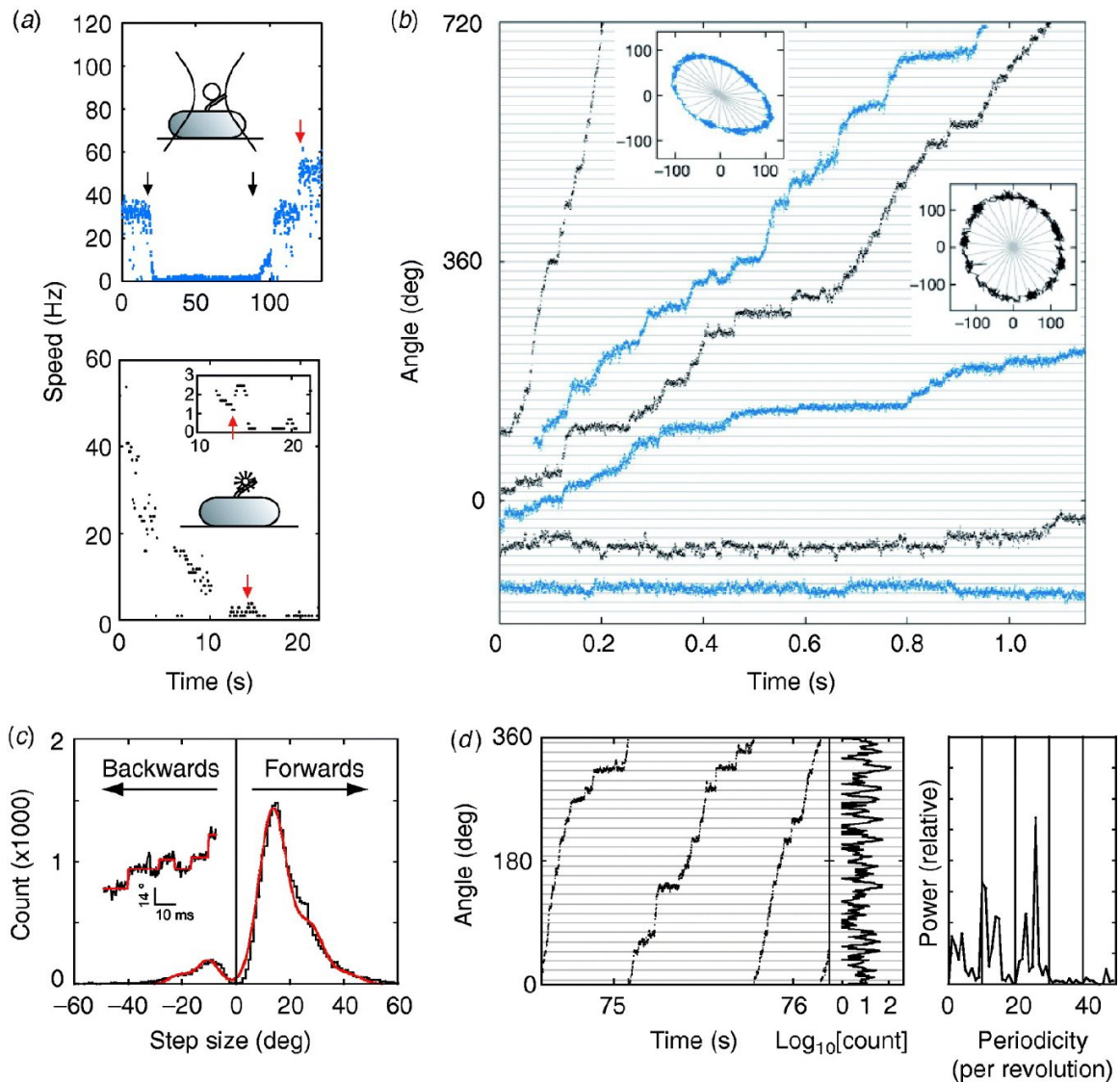
Figure 1.16: Steps in deenergized BFM's. a) The two methods used for reducing the SMF in these experiments. The top graph shows reducing the sodium concentration from 5 to 0.1mM (black arrows), and the bottom graph shows photodamage. Red arrows indicated speed doublings, presumably when the motor went from one stator to two. Traces in blue were taken using optical interferometry and reduced sodium in the medium. Traces in black were taken using fluorescence microscopy and photodamage. b) Stepping rotation for multiple BFM traces at varying speeds. Radial lines show 1/26th of a revolution, and insets show the position of the bead stuck to the flagellar filament. c) A histogram of step size distribution (black) and a multiple Gaussian fit (red). The peak in step size when rotating CCW (forward) is 13.7°, while the peak when rotating CW (backwards) is slightly smaller. The inset shows an example of steps found with the step-finding algorithm. d) A plot of angle versus time for three revolutions and a histogram of the dwell angles. A power spectrum of the histogram shows a peak at 26 steps per revolution. Figure from Sowa and Berry, 2008 [142], adapted from Sowa et al, 2005 [208].

The only other experiment to directly resolve steps in the BFM was performed with the proton-driven *Salmonella* motor in a strain where the number of functional stators was reduced [259]. Potassium benzoate was used to lower the external pH in order to further slow the motor rotation. As the experiments were performed with a fluorescent bead under high illumination, it is possible that the motors were further slowed from photodamage. The strain used was one that rotates both CCW and CW, so steps were measured in both directions. Using a 100nm fluorescent bead stuck to a filament stub, it was found that the BFM of *Salmonella* takes around 14° steps when rotating either CCW or CW, suggesting a symmetric mechanism of torque generation. Backwards steps of smaller size were also observed, though this was hypothesized to be an artifact due to the elastic response of the hook and filament. Interestingly, they also observed an occasional shift in the angular step positions, and this was hypothesized to be due to the exchange of an active stator with a new one anchored at a different location. However, this result was based upon analysis from less than a single revolution, and is thus very tenuous.

A set of experiments performed with *Rhodobacter sphaeroides* provides evidence for 27-28 steps per revolution in chemotactically stopped motors [260]. Unlike many bacteria which swim with a bidirectional motor, *R. sphaeroides* employs a single unidirectional motor which uses a stop start mechanism to induce cell reorientation. An investigation of beads attached to the flagella of chemotactically stopped motors with a full complement of stators showed that some motors exhibit slow stepping rotation during the stops, stopping at 27-28 discrete angles around the motor. The similarity in periodicity of steps observed in the chemotactially stopped *R. sphaeroides* with a full complement of stators and *E. coli* [208] or *Salmonella* [259] with one or few stators seems to suggest that either the step size is governed solely by the periodicity of the rotor ring, or the stators are separated by an integer multiple of the rotor periodicity [261].

The problem of dividing 36 ions into 26 steps raises interesting questions in the roles of different rings of the motor in torque generation and how ion transit corresponds to mechanical stepping of the motor. It may be the case that the measured stall torque of the motor is incorrect or that the motor is not tightly coupled to ion translocation for some or all loads (involving a slipping of the motor). It is also possible that the mechanochemical cycle and the observed steps are not the same thing. This would require an elastic linkage between the site of torque generation and another site of 26 fold potential. It is likely that steps will be the best biophysical probe to explore the motor's mechanochemical cycle in the future. Thus, there is a current need for large quantities of stepping data under known SMF conditions and, ideally, in fully energized and undamaged cells.

1.3.6 Models for rotation

Many models have been proposed to explain the mechanism of torque generation and elucidate the energy profile of the BMF (for recent reviews, see [87, 219, 262]). A successful model must be able to predict motor behavior, particularly the torque-speed curve and stepping signatures, and must also be consistent with structural data. Due to operating in a low Reynolds number environment, motor mechanisms such as flywheels and tuning forks are out of the question, as the motor can not coast. The most well-developed models fall within three categories: ion turnstiles, ion turbines, and binding with conformational change.

In an ion turnstile model, ions move from outside the cell to inside the cell through two sequential stator channels. Ions move from the outside medium to the rotor through one channel in a stator unit and can only complete the transit after they are carried by diffusion of the rotor to a second type of channel on the stator unit, which connects with the cell interior [263, 264]. This model is a type of 'thermal ratchet' because the transit of ions supplies free energy to 'save' thermal fluctuations in a

particular direction as opposed to directly creating a torque-generating state [262]. This type of mechanism is shown in part (a) of Figure 1.17. While this type of model may well describe F_O-ATPase [82, 265], the lack of an essential conserved residue for ions halfway across the membrane argues against this type of model for the BFM. These models predict a barrier to backwards rotation, which is not observed when BFMs have been forced to rotate backwards using electrorotation [215]. Additionally, these models predict that the motor torque should fall steadily towards the zero-torque speed, and thus fail to produce the characteristic shape of the torque-speed curve.

In an ion turbine model, the path of ions across the membrane is formed by a channel consisting of elements of the stator and elements of the rotor, tilted with respect to each other. One example of this is a model where the elements of the ion channel are half-binding sites on the rotor and stator that need to be aligned in order to fully bind an ion [266]. Another example incorporates ion channels in the stator that interact with tilted lines of charge on the rotor via long-range electrostatic interactions [267–269]. This model is supported by site-directed mutagenesis studies that have shown that various charged residues are important for motor function, and that removal or replacement of individual charges impairs but does not destroy motor function [161, 164, 165]. The turbine model is a 'powerstroke' mechanism because the transit of ions supplies free energy that is directly coupled to the creation of a torque-generating state. This type of mechanism is shown in (b) of Figure 1.17. The key difference between the turnstile and turbine models lies in the path the ions take through the motor. In the turnstile model, the transmembrane ion transit and motor rotation occur in separate steps, while in the turbine model they occur simultaneously.

In a conformational change model, ion transit is coupled to a cyclical conformational change of the stator, and this change exerts torque on the rotor. This torque can be due to either long-range electrostatic interactions or short-range steric interactions [270]. This type of mechanism is the best model of F_1-ATPase. In the BFM,

46

conformational changes in MotA linked to the proposed ion binding site of MotB support this model [167]. There are few models to date that successfully reproduce the knee in the torque-speed curve, and they fall within this category. One is a model from Xing and colleagues [261, 271] based on the model of Blair and colleagues [167] and the other is a model from Wingreen and colleagues [272].
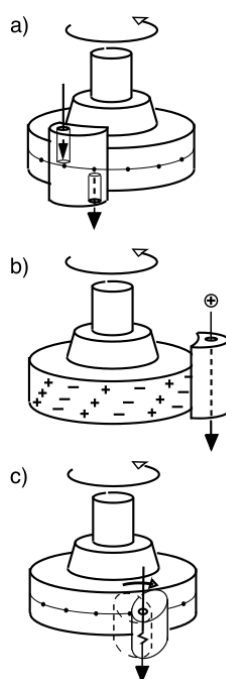
Figure 1.17: Three models for rotary motors. a) Ion turnstile model. Ions move from the outside of the cell and are deposited on the rotor by one channel. They are removed from the rotor by a second channel, which extends into the cytoplasm. In order to make the full transit, ions must be carried from one channel to the other by thermal rotation of the rotor. b) Ion turbine model. Ions flowing through the stator attract/repel ions of opposite/same charges on the rotor arranged in tilted lines. Electrostatic forces along these tilted lines lead to rotation. c) Conformational change model. The stator binds the rotor, then undergoes a conformational change which generates torque. The stator then unbinds and returns to its original conformation. These events are coupled to the transit of one or more ions. Figure adapted from Berry, 2000 [262].

Xing et al propose a reaction-diffusion model that is grounded in four assumptions. First, the rotation of the motor is observed through a soft elastic linkage between the motor and the load, allowing the motor and the load to move on different time scales.

A consequence of this is that the BFM torque is constant in the low speed high load regime. Secondly, motor rotation and ion translocation are tightly coupled. Thirdly, the powerstroke is driven by a conformational change in the stator that is driven by ions hopping on and off the stator. The second and third assumptions ensure the linear dependence of speed on IMF in the low load and high load regimes. Fourthly, the ion channel through the stator is gated by the motion of the rotor. This assumption allows the ion conductance to vary with motor speed. Xing et al use the model of Kojima et al [167] as their starting point.

The mechanistic details and stator energy profile of the original Xing et al model are shown in (a) and (b) of Figure 1.18. The power stroke is driven by the free energy of two ions binding the Asp32 sites on MotB, causing a transition between state 1 (solid lines) and state 2 (dashed lines). These transitions are possible only at the angles corresponding to the upper shaded area. The release of the ions into the cell, completing ion transit, can only occur at the angles indicated by the middle shaded area. The start of the next mechanochemical cycle is indicated by the lower shaded area. The complete cycle involves two half strokes, where the two MotA loops alternate contact with successive FliG proteins. The linear sections of the energy profile produce constant torque in the high load slow speed regime, while the peaks are necessary to prevent slipping. Two ions are coupled at once to allow sufficient free energy for the rotor to move $\frac{1}{26}$th of a revolution and generate the torques measured at low speeds. Otherwise, the two state kinetic cycle and potentials were chosen to be as simple as possible, with the hope for refinements as more structural and kinetic data becomes available.

The model of Xing et al uses the Langevin equation [273] to compute the angle of the rotor relative to a single stator. The dynamics of a single stator motor pulling

a viscous load via an elastic linkage can be written as:

$$\zeta_R \frac{d\theta_R}{dt} = -\frac{\partial}{\partial \theta_R} V_R(\theta_R, s) - \kappa(\theta_R - \theta_L) + [2k_B T \xi_R]^{1/2} f_R(t) \tag{1.9}$$

where ξ_R is the drag coefficient of the rotor, θ_R is the angle of the rotor, V_R is the energy potential of mean force along the minimum energy path, s is a binary variable describing the state of the stator, κ is the spring constant of the link to the load, θ_L is the angle of the load, and $f_R(t)$ is the uncorrelated white noise. The left hand side of the equation gives the viscous drag torque on the rotor, and the right hand side gives the rotor stator potential of mean force, the elastic coupling force between the rotor and load, and the stochastic Brownian torque on the stator. For motors with multiple stators, V_R can be replaced by the sum of potentials from all stators. A similar Langevin equation describes the motion of the bead, obviously lacking the V_R term [271].

Simulations and numerical analysis of this model confirm that, at high load, the elastic linkage of the hook allows the motor to work against an approximately constant torque. This guarantees that chemical transitions occur before the motor leaves the allowed transition zone, thus producing the plateau region of the torque-speed curve. For small loads, the bead relaxes faster, and it is likely the rotor will reach the minimum of an energy profile before a chemical transition takes the system to the next state. At the minimum of the energy profile the torque is zero, producing steeply decreasing motor torque as the load is decreased. Therefore this model succeeds in reproducing the knee and overall shape of the torque speed curve.

In 2009, Xing and colleagues revisited this model [261]. The original model required synchronous transitions from all the stators in order for the rotor to rotate. A consequence of this was the prediction that the zero-load speed would decrease with increasing number of stators as stators impede the interaction of other stators

with the motor. However, in 2008, experiments performed by Yuan and Berg suggested a lack of dependence of zero-load speed on stator number. In order to explain these results, compliant springs linking the stators to the cell wall were added to the original model. Instead of coordinated stepping, stator springs allow each stator to step independently, storing the energy in its own spring. This model reproduces the torque-speed curve in its entirety and also the stepping data of the BFM. It makes experimentally testable predictions for the dwell time distributions between steps. A schematic of the stator spring model is shown in (c) of Figure 1.18 When stator springs were added into the model, the Langevin equation changes only slightly:

$$\zeta_R \frac{d\theta_R}{dt} = -\frac{\partial}{\partial \theta_R} V_{RS}(\theta_R - \theta_S, s) - \kappa(\theta_R - \theta_L) + [2k_B T \xi_R]^{1/2} f_R(t) \qquad (1.10)$$

with the right hand side reflecting the difference in angle between the rotor and the stator.

Recent experiments may render the 2009 modification in the model of Xing and colleagues unnecessary. The model was modified in order to account for experiments that suggested a lack of dependence of zero-load speed on stator number [261]. However, recent experiments by Berg and colleagues have demonstrated that the number of stators engaged with a motor is dependent upon load [227]. Therefore, the dependence of zero-load speed on the number of stators in a motor is not known. For example, it is possible that in the 2008 experiments at zero load, Berg and colleagues only observed motors with a single stator. The compliant springs linking the stators to the cell wall that were added to the original model by Xing et al [271] may not be necessary to accurately reproduce the behavior of the BFM at low load.

The model of Wingreen and colleagues [272] incorporates three underlying assumptions. First, each stator contributes independently and additively to the total torque. Secondly, the torque from each stator is applied to the rotor via a sta-
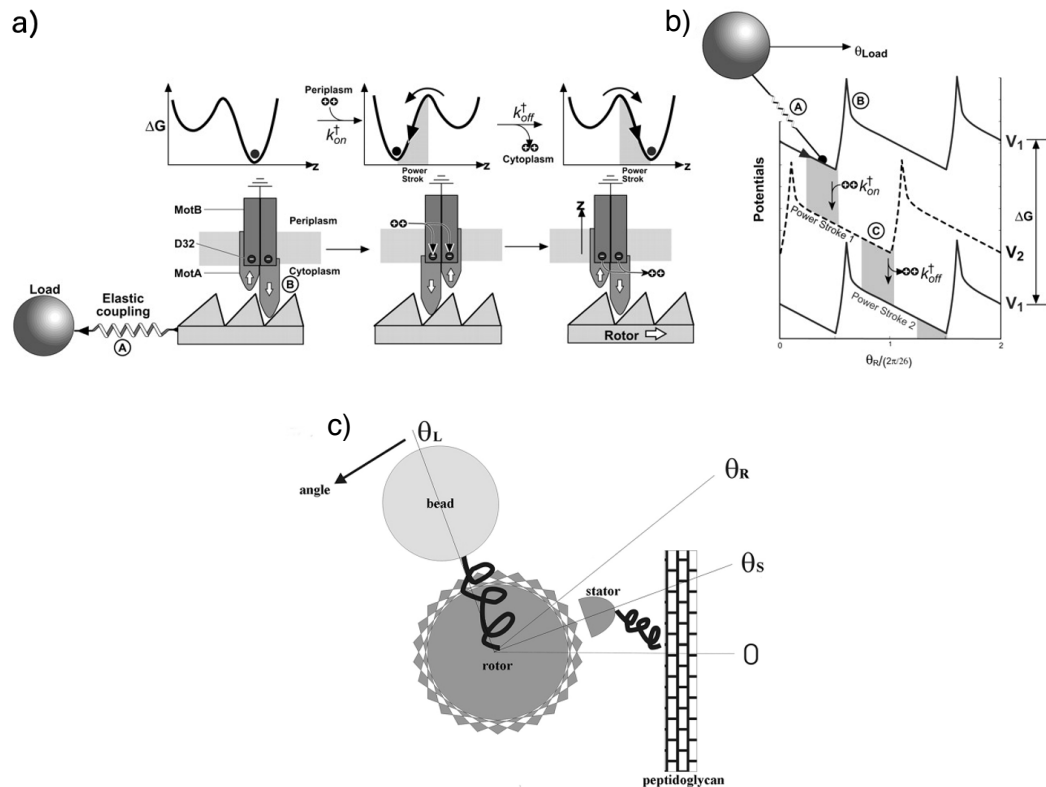
Figure 1.18: Schematics of the model proposed by Blair et al, with calculations from Xing et al, and revisited by Bai et al. a) A schematic of one motor cycle. The graph on the left shows a stable conformation with an unprotonated D32 residue. One MotA (the right one) is engaged with the rotor. Two protons bind, allowing a thermal transition to the other conformational equilibrium position with the other MotA loop engaging the rotor. This transition is characterized by the rate constant k_{on}^+, which is a combination of the ion binding rate and the rate of thermal transition. At the end of the first powerstroke, the two ions are released into the cell, triggering another conformational change and the right MotA loop engages again. This transition is characterized by the rate constant k_{off}^+. At the end of the second powerstroke, the rotor has advanced one step to the right. The rotor is almost always engaged, so the duty cycle is close to 1. The MotA loops interact sterically with the FliG proteins, and asymmetry in the steric interactions determines direction of rotation. b) The free energies of the stator in (a) were approximated with piecewise linear functions offset by half a step. The elastic coupling between the motor and load is indicated by the spring A. The sharp peaks in potential labeled B ensure tight coupling between rotation and ion flux and may be due to steric interactions between the FliGs and MotA. The shaded regions specify the positions where the transitions between potentials can occur. Each transition between the two potentials initiates a power stroke, and in each motor cycle, two ions cross the membrane, and the motor advances $\frac{2\pi}{26}$. c) A schematic of the compliant springs linking the stators to the cell walls. These springs are a necessary component of the model if it is to reproduce the result that the zero-load speed does not vary with the number of stators engaged with the motor. Figure adapted from Xing et al 2006 (parts a and b) [271] and Bai et al, 2009 (part c) [261].

51

tor spring, and ion translocation stretches a stator spring to its next attachment site. This assumption ensures tight coupling between ion translocation and rotation. Thirdly, ion transolcation occurs in three reversible steps: first, n protons load into an external gate, then they all cross an energy barrier to an internal gate, then all n are released into the cell. While the barrier-crossing is the rate limiting step, the external and internal gates ensure the nonlinear dependence of the torque-speed curve on ion concentration. In this model, ion translocation is limited by the loading and unloading of the external and internal gates, and this limit reproduces the knee of the torque-speed curve. The model predicts that diffusion of the motor at low load should depend strongly on ion cooperativity, though this prediction has yet to be experimentally tested [272]. Part (c) of Figure 1.19 shows a graphical representation of this prediction.

Wingreen and colleagues [274] also propose a simple model to explain the observed steps in the BFM. The model proposes that the stator supplies a nearly constant torque to the rotor, but the contact forces on the rotor produce a potential and thus an additional torque with an approximate periodicity of the 26 fold FliG proteins. The model describes flagellar rotation as a circular random walk on a bumpy potential biased by stator torque. Their model accounts for the different sized steps between forwards and back steps. As well as the 26 fold FilG proteins, there may be other potentials as well, such as the 11 fold filament and hook, the 6 fold FlgB, FlgC, and FlgF between the L and P-rings, or the 9 fold FliE at the rod MS-ring junction. In this model, the rotor angle was modeled by the following Langevin equation:

$$\frac{d\theta}{dt} = -\frac{1}{v}\frac{\partial U}{\partial \theta} + \xi(t) \tag{1.11}$$

where $\xi(t)$ is Gaussian white noise and accounts for thermal fluctuations, and

$$U(\theta) = V(\theta) - \tau\theta \tag{1.12}$$

where $V(\theta)$ is contact potential and τ is the total torque. Since the relaxation time of the marker is fast, the model assumes the linkage between the rotor and load is instantaneous. Figure 1.19 (a) shows a schematic of the motor, stator springs, and contact forces, and (b) shows the motor steps lining up with the physical potentials of the rotor.
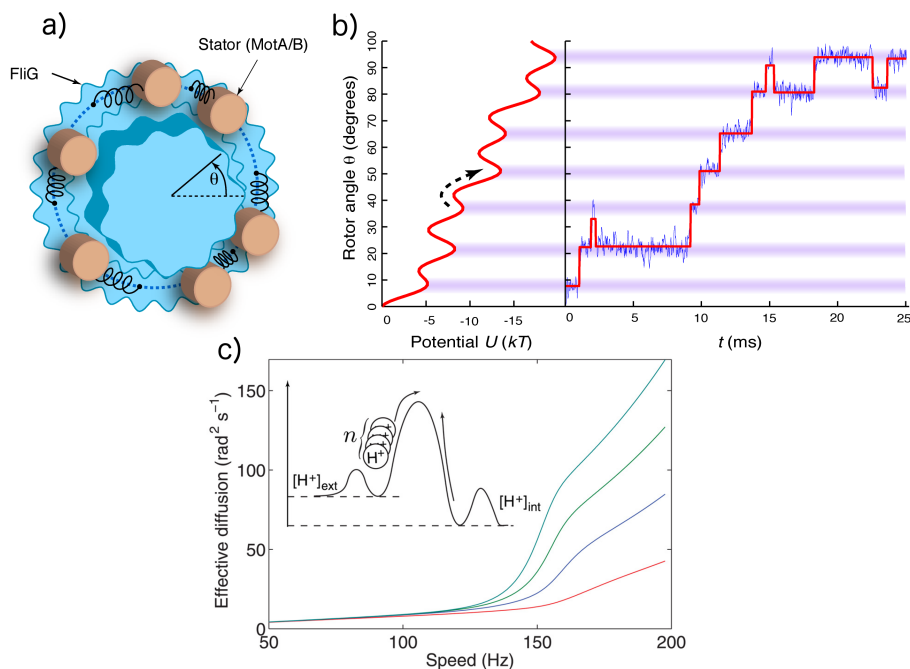
Figure 1.19: a) A model of the top view of the motor showing the protein 'springs' which link the peptidoglycan stator complexes to the rotor. As ions cross the inner membrane, these springs stretch, applying torque on the motor. Contact forces between the stator and rotor produce a periodic contact potential. θ represents the absolute angular position of the rotor. b) Rotation of the rotor corresponds to a viscously damped random walk in a tilted corrugated potential, $U(\theta)$. The graph on the right shows a model-generated trace. C) The effective diffusion versus rotation speed for a motor with a single stator. The lines show different ion translation cooperativities (n = 1-4 from bottom to top). The inset shows a schematic of the cooperative ion translocation. Figure adapted from Mora et al 2009 [272, 274].

Meacci and Tu proposed another model that shares the idea of the Wingreen model where torque is applied to the motor via a spring [275]. This model succeeds in reproducing the key results from BFM experiments, including the presumed independence of zero-load speed on stator number. The Langevin equation used to

describe the dynamics of the motor is the same as Equation 1.10. The defining characteristic of this model is that the stepping rate of the stator depends upon the force between the stator and the rotor. From this general assumption, they find that the zero-load speed of the motor is determined by the maximum stepping rate. Each stator has two force generating springs which interact with the FliGs of the rotor and move in a hand-over-hand fashion. This model also predicts that the step size varies inversely with the number of stators in a motor. Figure 1.20 shows a schematic of the hand-over-hand interaction of the stators and rotor. In 2011 Meacci et al added two additional details to their model [276]. The first addition was a finite probability for stator back stepping, and the second was a spring linking the stator to its anchor point on the peptidoglycan wall.
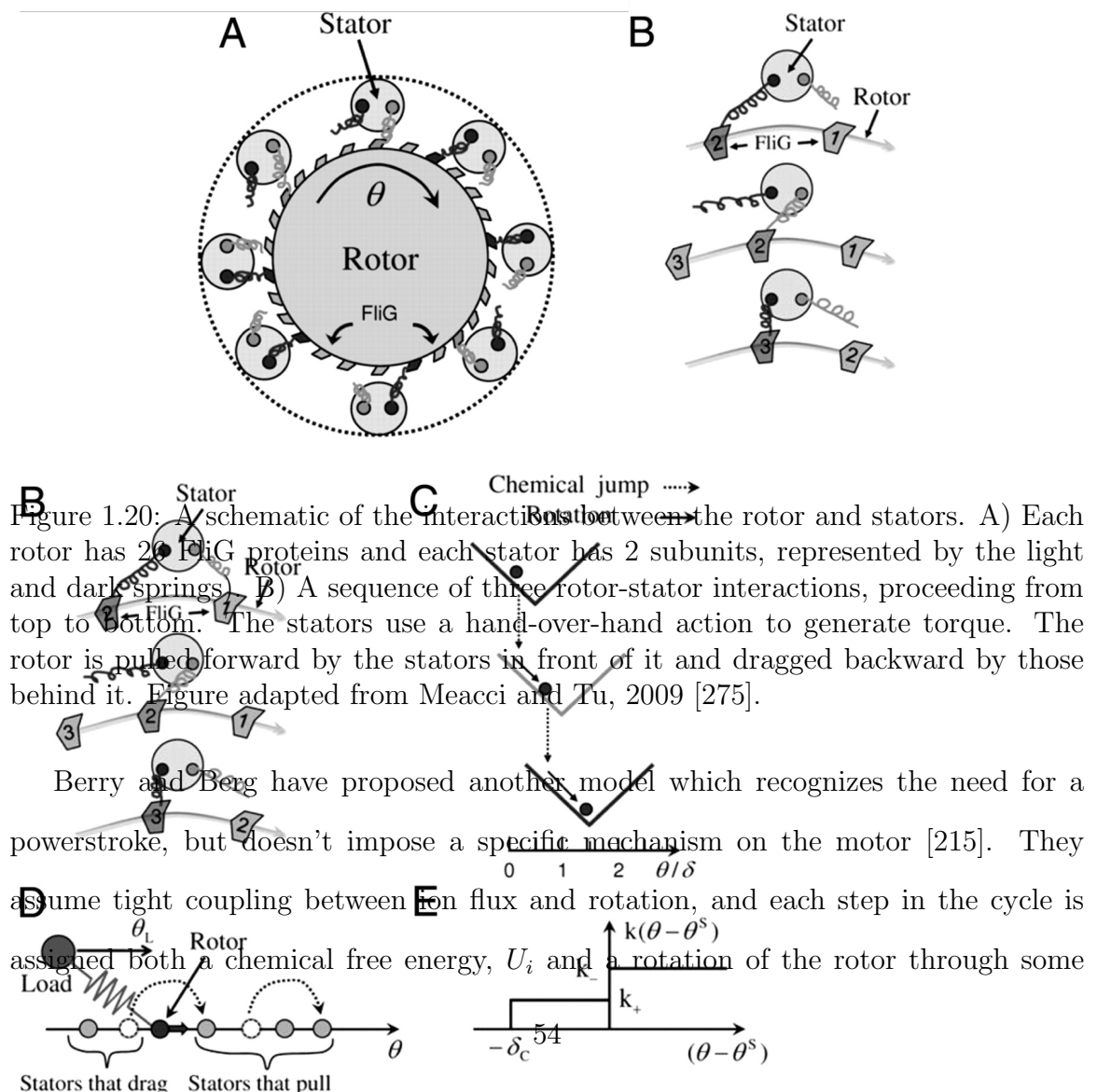
Figure 1.20: A schematic of the interactions between the rotor and stators. A) Each rotor has 26 FliG proteins and each stator has 2 subunits, represented by the light and dark springs. B) A sequence of three rotor-stator interactions, proceeding from top to bottom. The stators use a hand-over-hand action to generate torque. The rotor is pulled forward by the stators in front of it and dragged backward by those behind it. Figure adapted from Meacci and Tu, 2009 [275].

Berry and Berg have proposed another model which recognizes the need for a powerstroke, but doesn't impose a specific mechanism on the motor [215]. They assume tight coupling between ion flux and rotation, and each step in the cycle is assigned both a chemical free energy, U_i and a rotation of the rotor through some

angle, w_i. If ϕ is the amount moved in one cycle, B_i is the fraction moved in step i, and Γ is the motor torque, then in step i, the motor does work, $W_i = B_i \phi \Gamma$. The sum of all U_i must equal $nq \cdot IMF$ where n is the number of ions crossing the membrane and q is the charge of an ion. Defining the absolute rate of each step to be k_i, the rates for the forward and backwards steps are given by:

$$k_{fi} = k_i e^{\frac{U_i - W_i}{2k_B T}}$$

(1.13)

$$k_{bi} = k_i e^{\frac{-(U_i - W_i)}{2k_B T}}$$

(1.14)

assuming that U_i and W_i affect the forwards and reverse rates symmetrically. With torque and IMF specified, the coupled ordinary differential equations can be solved to give the occupancy probability of each kinetic state. Assuming steady state, this yields the number of ions used during each mechanochemical cycle and the speed of the motor.

An exploration of the parameter space of this model is shown in Figure 1.21. The assumptions that went into this model were that there are 8 stators per motor, each stator completes 120 mechanochemical cycles per revolution, and each cycle takes either 1 or 2 protons per stator. While we now know that motors can have up to 11 stators [173], and that they likely do 26 cycles per revolution [208], changing these values does not change the model's prediction of the shape of the torque speed curve. Therefore, the strength of kinetic models such as these is that they allow rapid searching of the parameter space in order to match experimental observations, giving us constraints on potential models of the motor mechanism.

Recently, Berry and colleagues have returned to this model with the addition of 25 torque speed curves for chimeric motors in *E. coli* [210]. This data set is an order of magnitude larger than what was available previously, is simplified because it examines only single stator motors, and is characterized by different energetic combinations of
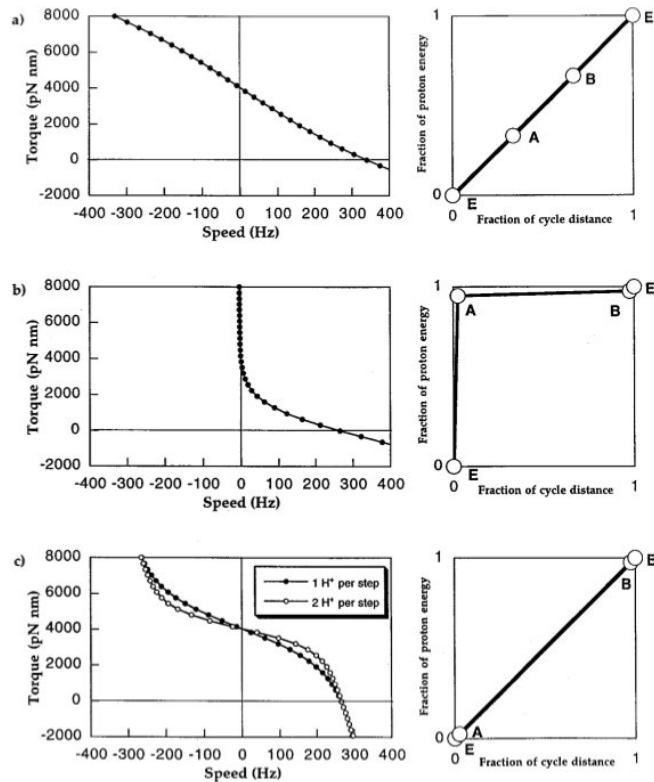
Figure 1.21: The left column shows the relationship between torque and speed, as predicted by the model of Berry and Berg, 1999. The right column shows a graphic representation of the degree to which each step in the mechanochemical cycle dissipates the free energy from ion translocation versus the rotation of the motor. a) All three steps are equivalent, and the predicted torque speed curve is approximately linear. b) The dissipation of the ion energy and the rotation of the motor are in separate steps. This creates a barrier to backwards rotation. c) A single step couples ion free energy to rotation. The predicted curve shows a plateau region at low speeds and a steeper torque dependence at high speeds. This model reproduces the experimentally observed torque speed curve. Figure from Berry and Berg 1999 [215].

SMF. This data set allowed a systematic survey of the space of kinetic models. The survey found an 11 parameter, three state model, similar to the model described previously [215], within a 25 parameter, four state model, thus defining a subset of important parameters. For both models, a powerstroke mechanism was found to be necessary, either in ion binding from the cytoplasm, ion transit, or both.

1.4 Summary

The work described in this thesis aimed to elucidate the stepping dynamics of the two rotary molecular motors introduced above. While much of the knowledge of the mechanochemical cycle of F_1 has come from studies of F_1 from the thermophilic *Bacilus* PS3 (TF$_1$), only mitochondrial F_1 has been well characterized by high-resolution crystal structures. Single molecule studies of mesophilic F_1 are needed to bridge the gap between our knowledge of F_1 structure and function. Currently, steps in the BFM have only been resolved in severely deenergized motors, likely driven by a single stator. A detailed statistical examination of high time resolution measurements of fully energized BFMs with varying numbers of stator units is needed in order to elucidate the origin and details of the stepping mechanism.

The first aim of the work that follows was to construct a microscope capable of resolving substeps in full speed mesophilic F_1 and steps in fully energized BFMs, both at low load. The second aim was to develop methods to analyze the acquired data. The results presented in subsequent chapters detail the results of this work and analysis.

Chapter 2

Experimental Methods and Materials

2.1   Single Molecule Microscopy Techniques

In order to understand the mechanism of rotary motors, we need to measure their motion. While these motors are too small to image with traditional optical microscopy, there are numerous single molecule microscopy techniques that have allowed measurements of their angle and force. Such measurements have allowed preliminary reconstructions of energy profiles and state transitions. Some of the commonly used techniques, tools, and assays in studying $F_1$1-ATPase and the BFM are reviewed below.

2.1.1 F_1 assays

The earliest demonstration of the rotation of F_1 was a 1997 experiment, where a genetically engineered F_1 was attached to the coverslip surface via His-tags on the β subunits. A cystein mutation on the α subunit allowed a fluorescently labeled actin filament to be attached through a biotin-streptavidin-BSA link [9]. ATP dependent rotation of the filament was observed with an epifluorescent microscope. A later experiment, done in a similar fashion, attached the fluorescent actin filament to the ϵ subunit demonstrating that the ϵ subunit, as well as γ, forms the F_1 rotor [277]. Replacement of the actin filaments by large (>300nm) bead duplexes provides similar viscous drag but allows the rotation to be recorded in a conventional bright field microscope.

Single or duplex beads smaller than this allow the observation of fast behavior if sampled at a sufficiently high frame rate. This can be accomplished with a commercial high-speed camera with either bright or dark field microscopy, depending on the size of the bead [46, 49]. The position of the bead can then be computed by calculating the centroid of the bead or by fitting an empirical function (often a 2-D Gaussian) to the image of the bead. As it is a single bead being tracked, the Rayleigh criterion is not relevant in this case, and the precision with which the bead can be located is dependent only on the image contrast and number of photons collected.

FRET microscopy has been used to study the conformation of the ATP binding dwell and stepwise rotation of the γ subunit by placing a donor fluorophore on the β subunit and an acceptor fluorophore on the γ subunit [54–56] or ϵ subunit [57]. At very low load, the polarization of single fluorophores attached to the γ subunit has been used to observe 120° steps in TF_1 rotation [53]. The polarization of gold nanorods has also been used to measure F_1 rotation with very high temporal resolution [14, 58, 59, 278]. Polarization methods offer the advantage of measuring rotation angle via intensities, rather than inferring it from the position of a marker. While this

method is promising, there exist technical difficulties with the use of gold nanorods in unambiguously determining angle.

2.1.2 BFM assays

The earliest demonstration that the BFM rotates was achieved using brightfield microscopy to observe cells rotating around fixed tethers [85, 86]. Cells with genetically deleted filaments and long polyhooks were attached to a glass coverslip using polyhook antibodies. The cells were observed to rotate around their tethers instead of oscillate, confirming that the BFM is a rotary motor. In such experiments, the micron-sized probe attached to the rotor is the bacterium cell itself.

A more modern version of the tethered cell assay is performed by fixing the cell body to the microscope coverslip and attaching a polystyrene bead to a filament that has been previously truncated via mechanical shearing. The size of the bead can be controlled, and each size has a defined viscous drag, providing control over the load on the motor. Beads have most commonly been tracked by back-focal-plane interferometry [206–209, 217, 218, 222, 226, 279], but fluorescent beads have also been tracked using fluorescence microscopy [208]. While the angular resolution of the measurement is better than $1°$, time resolution is limited to milliseconds or worse by the relaxation time of the flexible hook [208, 258].

In 2008, the time resolution was drastically increased by attaching 60nm gold beads directly to the hook of the BFM in a strain that lacked flagellar filaments. The rotation of the bead was observed with a laser darkfield microscope where the forward scattered light was focused onto a pinhole in front of a photo multiplying tube. The speed of rotation of the bead was calculated using the power spectrum. The viscous drag coefficient of the gold bead was two orders of magnitude less than previous BFM bead assays, and the relaxation time of the hook was approximately 6μs [216]. In

these experiments, the angular resolution was too low to reveal steps within a single revolution.

2.1.3 Imaging techniques

In order to reconstruct the underlying mechanisms of rotary motors, we need to understand attributes such as structure, speed, and kinetic transitions. Single molecule imaging techniques play a crucial role in measuring the motion of motors.

Electron microscopy and x-ray crystallography Electron microscopy and x-ray crystallography are the prime techniques for imaging objects of nanometer scales. These methods typically require dead samples and are not able to give a dynamic picture of rotary motors, but provide the structural information that has been key in discovering the functions of individual proteins.

X-ray crystallography is a means by which to solve 3D protein structures to atomic detail, analyze their functions, and potentially characterize binding interactions. It involves purifying a soluble protein, allowing the protein solution to supersaturate, then, under the right conditions, protein crystals will nucleate and grow. The difficulties often lie in purifying the protein and finding conditions under which the protein will form a regular crystal. Membrane proteins are particularly difficult to crystallize. Once the crystal is made, diffraction patterns must be collected and the phase problem must be solved to transform the data and allow for creation of a molecular model.

Numerous atomic structures of the cytoplasmic part of F_1-ATPase have been obtained by X-ray crystallography. They have been from many species, but mostly from bovine heart mitochondria. The first of these was obtained in 1994 by Walker, Leslie, and colleagues with a resolution of 2.8Å [8]. Several crystal structures have been obtained subsequently [280–282]. These structures differ from the 1994 structure in the

61

γ-subunit orientation or the number and location of nucleotides. Atomic structures exist for the filament and hook of the BFM, as well as for isolated protein fragments from the rotor, including FliG [141, 238], FliM [240], FliN [135], the stator protein MotB [283, 284], and the activated response regulator CheY [285]. Motor rings are too large to crystallize.

Cryo-electron microscopy is a type of transmission electron microscopy done at cryogenic temperatures. Compared to X-ray crystallography, cryo-electron microscopy does not require specimens to be crystallized, but produces images at much lower resolution, typically suitable for resolving the shape of proteins but not the atomic arrangement. The overall structure of F_1F_O-ATP synthase was first obtained with cryo-electron microscopy [18, 20]. The overall structures of the rotor [109], the flagellar filament [181, 286–288], and the sodium-driven stator units [289] of the BFM were also determined in this manner.

Cryo-electron tomography   Cryo-electron tomography (CET) is the combination of electron microscopy with cryo-techniques. CET produces a three dimensional image from samples which have been rapidly frozen in a fully hydrated native state, preserving molecular structures without harmful alterations from chemical fixation or staining procedures. This allows thin regions ($<1\mu$m) of bacterial or eukaryotic cells to be imaged with up to 3nm resolution, though the signal to noise ratio is typically low [290]. The three dimensional image is reconstructed from a set of electron micrographs acquired at various angular orientations to the sample.

CET has been used to image the BFM of *Borrelia spirochetes* at 4.6nm resolution [170], *Borrelia burgdorferi* at 3.5nm resolution [171], and *Vibrio alginolyticus* [291]. These images have provided details of the stator and rotor structures, including the connections between the stator and the peptidoglycan, and the T-ring of the basal

body. CET has also provided details of the sequential assembly of the BFM in *Borrelia burgdorferi* [292].

Brightfield and darkfield microscopy As rotary motors are too small to be seen with visible light, a larger particle or fluorophore must be attached to a part of the motor in order to garner information about the behavior of the motor. In both brightfield and darkfield microscopy, images can be formed from either the transmitted or the reflected light. In brightfield, illumination light, diffracted by the sample, is collected by the objective and produces a diffraction pattern in the back focal plane and a focused image in the image plane. The incident light that does not interact with the sample is transmitted undeviated, and the interference of these 0th order rays and higher order diffracted rays in the image plane creates a contrast image, seen as a dark object against a bright background. While light from at least two orders of diffraction must be collected by the objective in order to form an image, resolution increases the more diffraction orders that are collected. The cone of light collected by an objective is dependent upon the numerical aperture (NA) of the objective. Raleigh's criterion dictates that the spatial resolution of a microscope is dependent upon the wavelength of light and the NA. The diffraction pattern in the back focal plane of the objective is the Fourier transform of the image. In darkfield, the non-diffracted rays are excluded, such that only the diffracted rays interfere to form the image. This causes the specimen to appear bright against a dark background. Brightfield is ideal for transparent specimens with medium optical density, while darkfield is ideal for specimens which scatter light well.

Any probe used to observe the rotation of a rotary motor places a load on the motor due to viscous friction. In order to resolve stepping dynamics, smaller probes are ideal, yet smaller probes decrease image contrast. The solution has been to replace $\sim 1 \mu$m sized polystyrene probes, best imaged in brightfield, with $\sim$100nm
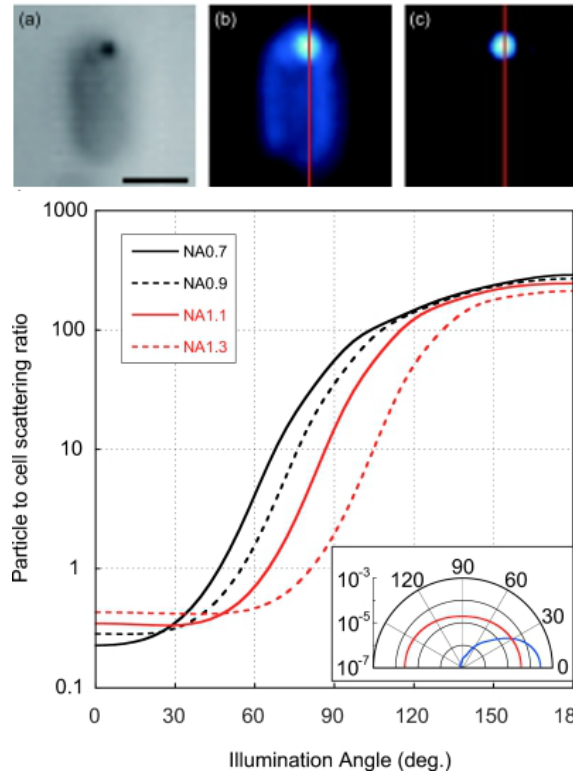
Figure 2.1: A comparison between conventional forwards scattering darkfield and back scattering darkfield microscopy. Images (a)-(c) show a 100nm gold nanoparticle stuck to the BFM of an *E. coli* cell in brightfield (with an NA 1.2 dark field condenser), forward scattering dark field, and back scattering darkfield, respectively. d) The calculated ratio of scattering from a 100nm gold bead to a bacterial cell over different illumination angles and objective NAs. Forward scattering is 0° and backscattering is 180°. The inset shows a polar diagram of the scattering cross section to scattering angle of a 100nm gold bead and cell body, red and blue respectively. The signal to noise ratio is nearly three orders of magnitude better for back scattering over forward scattering. The calculations were performed in SCATLAB; refer to the publication for further details. Figure adapted from Sowa et al 2010 [293].

sized gold probes, best imaged in a laser darkfield microscope. Gold nanoparticles demonstrate localized surface plasmon resonance (LSPR), a collective oscillation of the nanoparticle conductive electrons, which produces strong scattering spectra [294]. Gold nanoparticles have been shown to have optical cross-sections a few orders of magnitude higher than conventional fluorescent dyes [295]. In addition, a laser darkfield microscope allows for increased illumination levels, thereby increasing the contrast and the spatial resolution [46, 296–299]. In the case of F_1 assays, the ratio of scat-

tered light from the gold bead to scattered light from the enzyme is very high. In the case of BFM assays, this ratio is smaller because bacterial cells scatter optical wavelengths well. In 2010, Sowa et al demonstrated the advantage of using backscattering dark field microscopy over forward scattering to image a 100nm gold bead on a BFM [293]. Due to their relative sizes, a bacterial cell scatters visible wavelengths more efficiently in the forward direction, while a 100nm gold bead scatters fairly evenly in all directions. As Figure 2.1 shows, the signal to noise ratio makes backscattering an advantageous setup for the assay of a gold bead on a BFM.

Fluorescence microscopy Modern biology relies heavily on fluorescence microscopy due to its high contrast and the ability to specifically target cellular components. A fluorescent molecule (fluorophore) is characterized by a long-lived excited state from which radiative recombination can occur. Most molecules at room temperature exist in the ground electronic state. When a fluorophore absorbs a photon, one of its electrons passes to an excited singlet state. The electron quickly undergoes radiative decay back to the ground state, emitting a photon. The absorbance and emission spectra of a fluorophore are often mirror images of each other with the emission spectrum shifted to lower energies and longer wavelengths by an amount known as the Stokes shift [300]. This shift occurs because electrons typically decay to the lowest energy level of the excited state prior to radiative emission. This is also the reason that the emission spectrum is almost independent of the excitation wavelength [301].

Fluorophores can go through many cycles of excitation and emission over a short period of time, with the exact number depending on the fluorophore and the environment. This is followed by permanent bleaching of the fluorophore, caused by photon induced chemical damage, and it renders the molecule unable to fluoresce. In microscopy, photobleaching may be delayed by using short time exposures and minimal excitation light. Fluorescence recovery after photobleaching (FRAP) experiments

take advantage of the photobleaching of fluorophores in order to measure turnover or diffusion. In these experiments a particular area of the sample is deliberately photobleached. The subsequent measured fluorescence is of fluorophores that have diffused into the originally bleached area.

Fluorescence Resonance Energy Transfer Microscopy (FRET) uses the principle of dipole-dipole energy transfer between fluorophores to determine distances between structures. A typical dipole-dipole interaction falls off as $1/r^6$. For FRET to occur, the emission spectrum of the donor must overlap with the excitation spectrum of the acceptor fluorophore. FRET was used to measure rotation of the β subunit with respect to the γ or ϵ subunit in EF_1F_O [55–57] and in TF_1 [54].

Epifluorescence is the most common type of fluorescent microscopy. The specimen is illuminated with a wavelength falling within its excitation spectra, the fluorescence emission returns towards the excitation source and is separated from reflected excitation light, and the emission is detected with a high sensitivity device. Epifluorescence has been used to measure the response of membrane voltage to temperature by imaging a voltage sensitive dye [302]. Many of the fluorescent bead rotation assays of both F_1 and the BFM have used epifluorescence.

In total internal reflection fluorescence (TIRF) microscopy, the illumination light strikes the specimen at an angle that is larger than the critical angle for total reflection. This produces an exponentially decaying evanescent wave with a depth of only a few hundred nanometers. While fluorophores near the surface are excited, fluorophores throughout the rest of the sample are not. This both reduces the background fluorescence and allows for a very thin optical section. FRAP combined with TIRF has been used to demonstrate the turnover of stator units in the BFM through detection of green fluorescent protein (GFP) labeled MotB [174]. These experiments were able to count the stator units in a motor, measure the diffusion of freely diffusing stator units in the membrane, and measure the average time a stator unit remains

engaged with a motor. TIRF was also used to observe the binding of a fluorescent ATP analog in TF_1 and the subsequent release of ADP 240° from the where the ATP molecule bound [68].

2.1.4 Force measurement and manipulation techniques

In order to understand the mechanism of rotary motors, we need not only to measure their structure and motion but also the forces they exert. Tools capable of measuring force, applying force, and measuring small motions with piconewton and nanometer precision have been extensively employed in the experimental investigation of rotary motors.

Optical tweezers Optical tweezers use laser light with a Gaussian intensity profile to exert force on an object with higher refractive index than its surroundings. Optical tweezers are able to both exert and measure piconewton forces, and weak optical tweezers can be used to measure displacements on the nanometer scale. A change in position of a bead can be measured as an associated intensity shift of the laser light in the back focal plane by a position sensitive detector such as a quadrant photodiode (QPD).

Optical tweezers have been used to exert force on a tethered cell body or onto a polystyrene bead attached to an immobilized cell [50, 214]. In an experiment where torque was exerted on non-switching (ΔCheY) tethered cells with optical tweezers, it was found that motor torque is very similar when the cell was rotated slowly in either direction [214]. This confirmed the result from electrorotation that there is no barrier to backwards rotation in the BFM [215, 303]. Optical tweezers have also been used to apply torque via a pair of 0.5μm polystyrene beads to both the BFM and F_1-ATPase [50], with the bead pair used to provide a lever arm to convert the force into a torque.

Magnetic tweezers A magnetic field may also be used to exert torque on a bead attached to a rotary motor. Magnetic tweezers have predominantly been used to investigate biological processes of nucleic acids, especially coiling of DNA [304, 305]. Traditionally, a magnet or electromagnet is placed directly above the specimen, and a paramagnetic bead experiences a force proportional to the gradient of the field. Using a rotating field with near-zero gradient, tweezers will exert a torque on the bead. Magnetic tweezers are able to exert much smaller forces than optical tweezers, and there is no worry of localized heating or photodamage [306]. Magnetic tweezers have been used to apply external torque to magnetic beads attached to the γ-subunit of F_1-ATPase [61, 62, 72, 307]. They may soon become an important tool in measuring torque and angle of the BFM. However, they currently do not enable the spatial or temporal resolution of optical tweezers, and the torque exerted by current magnetic tweezers setups is too small to be useful for the BFM.

Electrorotation Electrorotation uses microelectrodes arranged in a cross to generate a rotating electric field in order to apply torque onto a dielectric object, such as a cell. It was first used in the field of rotary motors to measure BFM torque [219, 220, 308], and has subsequently been used to demonstrate that there is no barrier to backwards rotation [215, 303]. Electrorotation is a difficult setup, requires a very low ion concentration in the medium, and does not achieve the spatial or temporal resolution of optical tweezers.

2.2 F_1 Experiments

2.2.1 Sample preparation and image acquisition

The F_1 data analyzed in this thesis were collected by Dr. Bradley Steel. For these experiments, F_1 was immobilized to a glass coverslip within a tunnel slide. The

tunnel slides were constructed by placing two strips of double-sided tape onto a slide about 0.5cm apart, then placing a coverslip on top. The coverslip was pressed firmly to the tape and the excess tape was removed from the slide. This forms a tunnel between the coverslip, slide, and tape that is about 100μm high and about 10μL in volume. A schematic of a tunnel slide is shown in Figure 2.2. F_1 was immobilized either directly to a coverslip cleaned with a potassium hydroxide and ethanol solution (EF_1 data) or to an Ni-NTA coated coverslip via His_{10} tags on the α and β subunits, as described previously (YF_1 data) [61,65]. A streptavidin coated gold nanoparticle was attached to a biotinylated cysteine on the γ subunit [61]. This assay is shown in Figure 2.3. A laser backscattering darkfield microscope and a high speed camera (Photron Fastcam 1024PCI) were used to record the rotation of gold beads at up to 30kHz. The microscope used for these experiments was either that described in Section 2.3 (EF_1 data), or a precurser built by Dr. Bradley Steel and Dr. Yoshi Sowa (YF_1 data). Table 2.1 shows the strains of F_1 used in these experiments and the relevant sections of this thesis where the results of the analysis are discussed.

Species	Parent	Plasmid(s)	Relevant section
E. coli	pBUR17-108C [49]	pBUR17AH10GC2	Section 3.1
S. cerevisiae	W303-1A [309]	pRS304, pRS305, pRS306	Section 3.2

Table 2.1: The experimental data analyzed in this thesis came from the above F_1 strains.

2.2.2 Data analysis

F_1 selection and position measurement   The bead positions were determined using a custom MATLAB program written by Dr. Bradley Steel. First, a high and low pass filter were applied to the mean of the first ten frames of the recording, and then the gold beads were identified by searching for local maxima within the filtered
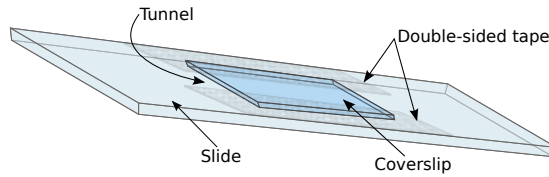
Figure 2.2: A schematic of the tunnel slides used in this thesis for imaging F_1 and *E. coli* cells. The tunnel slide consists of a 76x26x1mm slide, two strips of double-sided tape or plastic film about 0.1mm thick and 5mm apart, and a 22x22x0.15mm coverslip pressed on top. The tunnel is formed by the slide, coverslip, and two pieces of tape or film. Solution is flowed in from one end of the tunnel and wicked away at the opposite end. The tunnel is sealed with nail varnish.
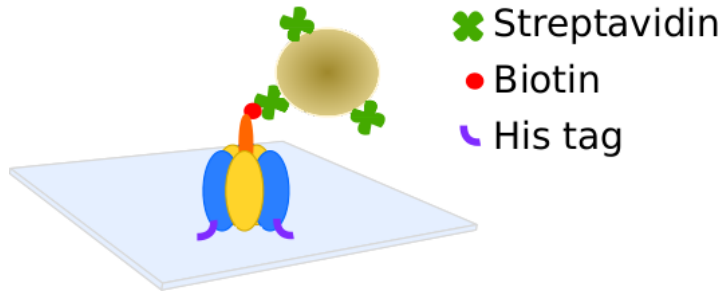
Figure 2.3: A schematic of the F_1 assay. The $\alpha_3\beta_3\gamma$ complex is stuck to the coverslide via His-tags. The γ subunit is biotinylated, and a streptavidinated gold bead is attached. This coverslip forms one surface of the tunnel slide shown in Figure 2.2.

mean image. Once identified, the beads were localized using a Gaussian Mask fitting algorithm, suitably seeded. The Gaussian Mask fitting algorithm was derived from a simplified least-squares analysis, equivalent to a least-squares fit of a Gaussian distribution with specified width [310].

Spinning beads were identified using the power spectrum of the position signal, which is the square of the discrete Fourier transform of the signal. For a bead following a circular trajectory with angular speed w_0, the position in x and y can be written

as:

$$P_x(t) = A\cos(w_0)t$$
$$P_y(t) = A\sin(w_0)t \qquad (2.1)$$

and the complex signal can be written:

$$P(t) = P_x(t) + iP_y(t) \qquad (2.2)$$

The complex power spectrum of $P(t)$ yields the power of the signal for each frequency w in between the negative and positive values of the Nyquist frequency. A windowed Fourier transform, F, and a power spectrum, $\Phi(w)$, were calculated as follows:

$$F(w) = \frac{1}{\sqrt{2\pi}} \sum_{-\infty}^{\infty} P(t)e^{-iwt} \qquad (2.3)$$

$$\Phi(w) = \left| \frac{1}{\sqrt{2\pi}} \sum_{-\infty}^{\infty} P(t)e^{-iwt} \right|^2 = \frac{F(w)F(w)^*}{2\pi} \qquad (2.4)$$

The dominant peak in the power spectrum relates to the angular speed of the bead, w_0. The sign of the peak signifies the direction of bead rotation.

Individual traces were characterized by their power spectral bias in order to allow rapid and systematic detection of rotating molecules in a recording. The power spectral bias was defined as the difference in the magnitude of the power spectrum at positive and negative frequencies, normalized by the sum of the two. That is,

$$Bias = \frac{P_{CCW} - P_{CW}}{P_{CCW} + P_{CW}} = \frac{\int_{\frac{-f_s}{2}}^{-L} PSD(w)dw - \int_{L}^{\frac{f_s}{2}} PSD(w)dw}{\int_{\frac{-f_s}{2}}^{-L} PSD(w)dw + \int_{L}^{\frac{f_s}{2}} PSD(w)dw} \qquad (2.5)$$

where P is the magnitude of the power spectrum in the CW or CCW direction, $PSD(w)$ is the power spectral density at a given frequency, f_s is the sampling frequency, and L is a low frequency cutoff used to remove noise due to microscope drift.

71

Beads with high values of bias were saved for further evaluation, and beads with low values of bias were discarded.

F_1 Kinetic analysis Ellipses were fit to the x,y coordinates of the bead using an algebraic least squares fitting algorithm [311]. Angular position was derived from the ellipse fits. A histogram of dwell angles was created for each molecule. For those molecules at high and low [ATP] clearly showing three dwell positions, three Gaussians were fit to the histogram of dwell angles. The peaks of the Gaussian fits were used to define the locations of each state. Where the Gaussian fits overlapped, the divisions between the three states were demarcated by the minimum in the overlapping Gaussians. Where the Gaussians were narrow enough that there was no overlap, the midpoint between two points, each three standard deviations from their respective Gaussian peaks, was used to define the edge between states.

For molecules at intermediate ATP concentrations which showed six dwell states per cycle, there was more potential overlap of data from neighboring dwell states. To minimize this contamination, the angular position data was padded at the beginning and end, then smoothed using an L1-PWC filter with a gamma value of 10 radians [312]. The L1-PWC filter is a step-preserving smoothing algorithm, and gamma is set with knowledge of the noise in the trace, allowing the preservation of steps that are just large enough to be detected above the noise. A dwell angle histogram was created from the filtered data, and this was used to create a kernel density plot using a Gaussian kernel with a bandwidth of 0.07-0.12 radians. The kernel density plot was fit using the six peak Gaussian function:

$$n(\theta) = \sum_{i=1}^{6} A_i e^{\frac{(\theta - \theta_i)^2}{2w_i^2}} \tag{2.6}$$

The positions θ_i defined the location of each state and the minima were used to define the edges of each state. The angular separation between states gave the angular separation between the catalytic and ATP binding dwells.

To determine the time each F_1 molecule spent within each state, each camera frame was assigned a dwell state based upon the angular position or the filtered angular position. Dwell times were calculated by summing the number of frames within each dwell state and multiplying by the temporal length of a frame. Pauses and their adjacent dwells were removed from the angular position versus time traces, where an Mg:ADP-inhibited pause was defined as any dwell that was longer than seven times the mean dwell time. A histogram of the dwell times was constructed for each enzyme. Six models were considered as potential fits to the histogram of dwell times. The models were comprised of one, two, or three kinetic parameters, both with and without a time offset parameter, and are described further in Table 2.2. The dwell time histograms were fit to each model and rate constants were derived with a maximum likelihood estimation (MLE) algorithm. The likelihood of these six models were compared using the Bayesian information criterion (BIC). These methods are described below.

Maximum likelihood estimation is an analytic estimation procedure which begins by defining a likelihood function of the sample data, which is the probability of obtaining that particular set of data, given the chosen probability distribution model. The MLE algorithm selects the set of values for the model parameters that maximizes the likelihood function [313]. Algorithmically, this was performed by minimizing the negative log likelihood function. The negative log likelihood function, L_{k_1}, is written as:

$$L(k_1) = -\sum_i ln(p(t_i)) \tag{2.7}$$

where t_i is the set of dwell times generated by any of the exponential probability functions in Table 2.2.

Kinetic states	Time offset	Probability function	Model represented
1	-	$P(t) \propto e^{-kt}$	$S^1 \xrightarrow{k} S^{1'} \to S^2$
1	✓	$P(t) \propto e^{-k(t+\delta)}$	$S^1 \xrightarrow{k} S^{1'} \xrightarrow{\delta} S^2$
2	-	$P(t) \propto e^{-k_1 t} - e^{-k_2 t}$	$S^1 \xrightarrow{k_1} S^{1'} \xrightarrow{k_2} S^{1''} \to S^2$
2	✓	$P(t) \propto e^{-k_1(t+\delta)} - e^{-k_2(t+\delta)}$	$S^1 \xrightarrow{k_1} S^{1'} \xrightarrow{k_2} S^{1''} \xrightarrow{\delta} S^2$
3	-	$P(t) \propto e^{-k_1 t} - e^{-k_2 t} - e^{-k_3 t}$	$S^1 \xrightarrow{k_1} S^{1'} \xrightarrow{k_2} S^{1''} \xrightarrow{k_3} S^{1'''} \to S^2$
3	✓	$P(t) \propto e^{-k_1(t+\delta)} - e^{-k_2(t+\delta)} - e^{-k_3(t+\delta)}$	$S^1 \xrightarrow{k_1} S^{1'} \xrightarrow{k_2} S^{1''} \xrightarrow{k_3} S^{1'''} \xrightarrow{\delta} S^2$

Table 2.2: The six models which were considered as potential fits to the dwell time histograms of F_1. Each model is comprised of one, two, or three kinetic parameters, and may or may not contain a time offset parameter. In the last column, S^1 and S^2 represent two subsequent ATP binding angles, separated by 120°. The prime notation indicates a chemical change but no physical rotation, occurring with the rates indicated over the arrows. If the time taken to rotate between states is able to be resolved, it is marked as δ.

The Bayesian information criterion, sometimes called the Schwarz information criterion, is a criterion for model selection where overfitting is addressed by introducing a penalty term for each additional parameter. It can be applied to any set of MLE based models, penalizing the complexity of a model [314]. It is calculated as:

$$BIC = -2ln(L) + kln(n) \tag{2.8}$$

where -ln(L) is the negative log likelihood from the MLE fit, k is the number of fitting parameters, and n is the number of data points, in this case, the number of observed dwells. For large sample sets, the fitted model favored by BIC ideally corresponds to the model which is *a posteriori* most probable, that is, the one rendered most probable by the available data.

2.3 Dark Field Microscope

In 2010, Sowa et al demonstrated the advantage of using backscattering dark field microscopy instead of forward scattering to image a 100nm gold bead on a BFM [293]. The *S. cerevisiae* F_1 experiments which are analyzed in this thesis were performed on this microscope. The noise of this microscope was sub-nanometer per axis in a 55kHz bandwidth. However, in order to achieve measurements of this quality, experiments needed to be performed in the middle of the night and after waiting a few minutes for the piezo to relax; the noise of the microscope during the day increased to 2-5nm, presumably due to the presence of more electrical and acoustical noise in the building. It was hypothesized that most of this noise was picked up by the stage and the piezoelectric actuators. In addition, the optical setup was such that 92% of the backscattered light collected by the objective was passed to the imaging pathway, while 8% was obscured by the optics. There was a desire to minimize the noise and optimize photon collection in order to achieve the spatial resolution necessary to detect steps in the BFM at high speeds. This motivated the construction of a laser backscattering dark field microscope similar to the existing one but with improved stability and backscattered light collection.

In an attempt to improve the stability of this microscope, it was constructed in the basement of the building on a laminar flow, actively damped, optical air table (Newport S2000). The microscope was designed to incorporate four illumination sources in three illumination pathways. The four sources include a 633nm HeNe laser (Melles Griot LHX1, 10mW), a 532nm diode-pumped crystal laser (Roithner LaserTechnik, 100mW), a supercontinuum laser emitting from 400nm to 2400nm (NKT Photonics SuperK Extreme EXW), and a high power LED (Thorlabs 617L2). The three illumination pathways include one for condenser brightfield (Nikon 1.4NA

condenser) and two for laser darkfield, one providing a large ($\sim15\mu$m) focused spot at the image plane and the other providing a small focused spot ($\sim1\mu$m)[1].

There are numerous individuals who assisted in the construction of this microscope; wherein this is the case, their contributions are duly noted below.

2.3.1 Stage

Principal Contributor: Dr. Richard Branch

A custom stage with high mechanical stiffness was designed and constructed by Dr. Richard Branch and Dr. Bradley Steel, based upon a previous design by Dr. Richard Berry. The performance of multiple models and makes of piezoelectric actuators was tested by Ashley Nord and Dr. Bradley Steel. This was accomplished by monitoring the motion of gold nanoparticles stuck to the surface of glass slides while the piezoelectric actuator was attached to the stage. The presence of each actuator magnified the noise picked up by the stage and the motion of the bead by a factor of 3 or more. As the advantages of a piezoelectric actuator on the stage were not worth the additional noise, the actuator was not included in the current microscope. The stage is instead controlled by three differential micrometers. The micrometer which moves the stage in a vertical direction is part of a kinematic mount.

2.3.2 Monochromatic sources

Principal Contributors: Ashley Nord, Dr. Bradley Steel

The 532nm and 633nm conventional continuous wave lasers are coupled into two shared laser illumination pathways via single mode optical fibers. In order to maximize coupling efficiency of each source, the beams were characterized by imaging the laser with a CMOS camera at various distances from the laser and fitting a 2D Gaus-

---

[1]These numbers represent the waist halfwidths in the image plane and correspond to the halfwidth at $\frac{1}{e^2}$ intensity and the fullwidth at $\frac{1}{\sqrt{e}}$.

sian to the beam profile at each distance. The wavefront radius of the $\frac{1}{e^2}$ irradiance contour versus distance from the front of the laser was plotted and fit using Gaussian beam optics, and the location of the beam waist was determined. Both lasers were coupled into two shared fibers, and the breadboard was designed such that each fiber was mounted at the location where the waists of both laser beams matched the mode field diameter of the fiber. Half-wave plates combined with a polarizing beamsplitter cube allow independent control of the laser intensity in both pathways, and custom-designed shutters allow the lasers to be easily blocked. A schematic and photograph of this breadboard is shown in Figure 2.4.
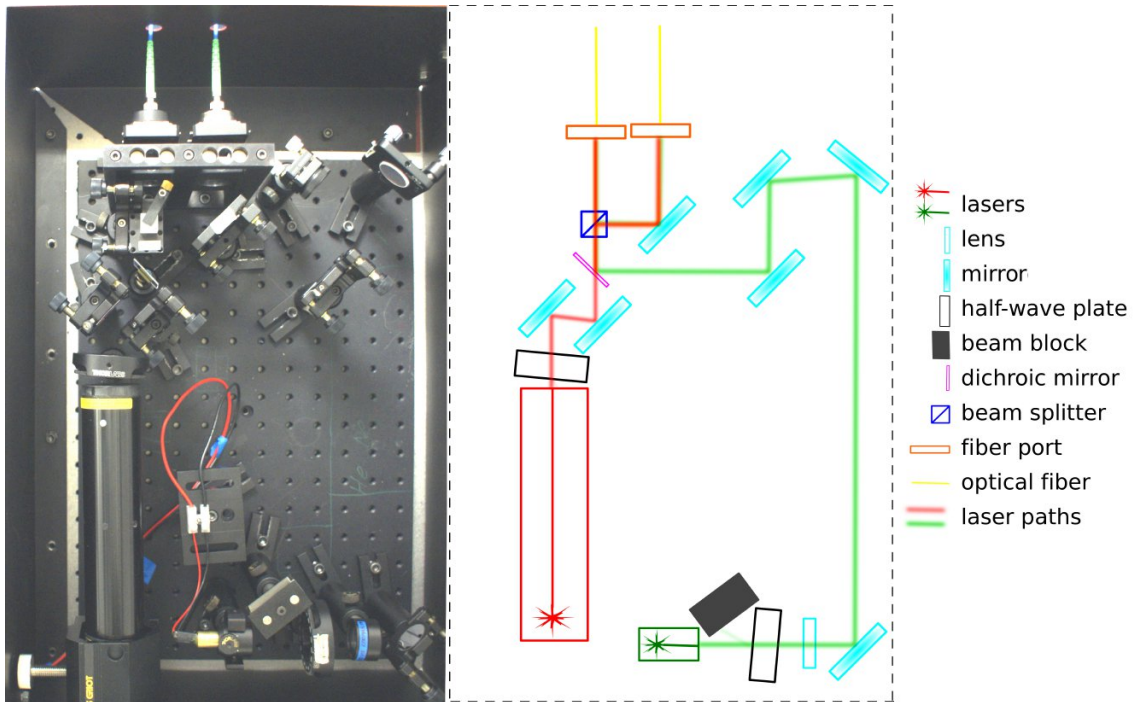
Figure 2.4: A photograph and schematic of a view looking down onto the breadboard coupling the 633nm HeNe laser and the 532nm diode-pumped crystal laser. The paths of the 633nm and 532nm laser light are shown as red and green respectively in the schematic. Other components used include: zero-order half wave plates, broadband dielectric mirrors, a 605nm dichroic mirror, a 450-680nm polarizing beamsplitter cube, a 600nm focal length lens, 5-axis adjustable fiberports, and 488nm single mode fibers (all from Thorlabs). The shutters (not shown) allow the user to quickly block light going to either illumination pathway, and the half-wave plates allow the user to easily control the intensity of light going to either pathway.

2.3.3 Supercontinuum source

Principal Contributors: Dr. Richard Berry, Ashley Nord, Aidan Russell

The supercontinuum laser was installed to provide bright non-monochromatic illumination, which eliminates high-order interference fringes. It also allows for rapid custom selection of the wavelength and bandwidth of laser light illuminating the sample. This laser emits wavelengths from 400nm to 2400nm, but as a safety precaution, the infrared light is dumped into a beam block near the head of the laser. The light then travels through a prism where it is dispersed into its constituent spectral colors. The dispersion of light is then filtered using a custom wavelength selector which is able to control both wavelength and bandwidth. The selected wavelengths are recombined using the same prism and coupled into an optical fiber. The method for spatially filtering the supercontinuum laser light and the mechanism of the wavelength selector were designed by Dr. Richard Berry and Dr. Bradley Steel. The wavelength selector was built by Aidan Russell. The design of the breadboard, the implementation of the filter, and the laser coupling was performed by Ashley Nord. Figure 2.5 shows a schematic and photograph of this setup.

2.3.4 Microscope illumination optics

Principal Contributors: Ashley Nord, Dr. Bradley Steel

The main body of the microscope combines inputs from the two fibers delivered into lower and upper paths, and delivers this light to the sample via a high NA objective. The backscattered light from the sample is collected and imaged. In order to reduce the effects of dust, a cage system (Thorlabs) was used to enclose the optics. The cage design and the optics within are shown in Figure 2.6. The upper path produces a larger illumination spot at the specimen ($\sim 15\mu$m), while the lower path produces a smaller spot ($\sim 1\mu$m). The lenses in both paths were placed a focal length from the back focal plane of the objective. The optical fibers were connected
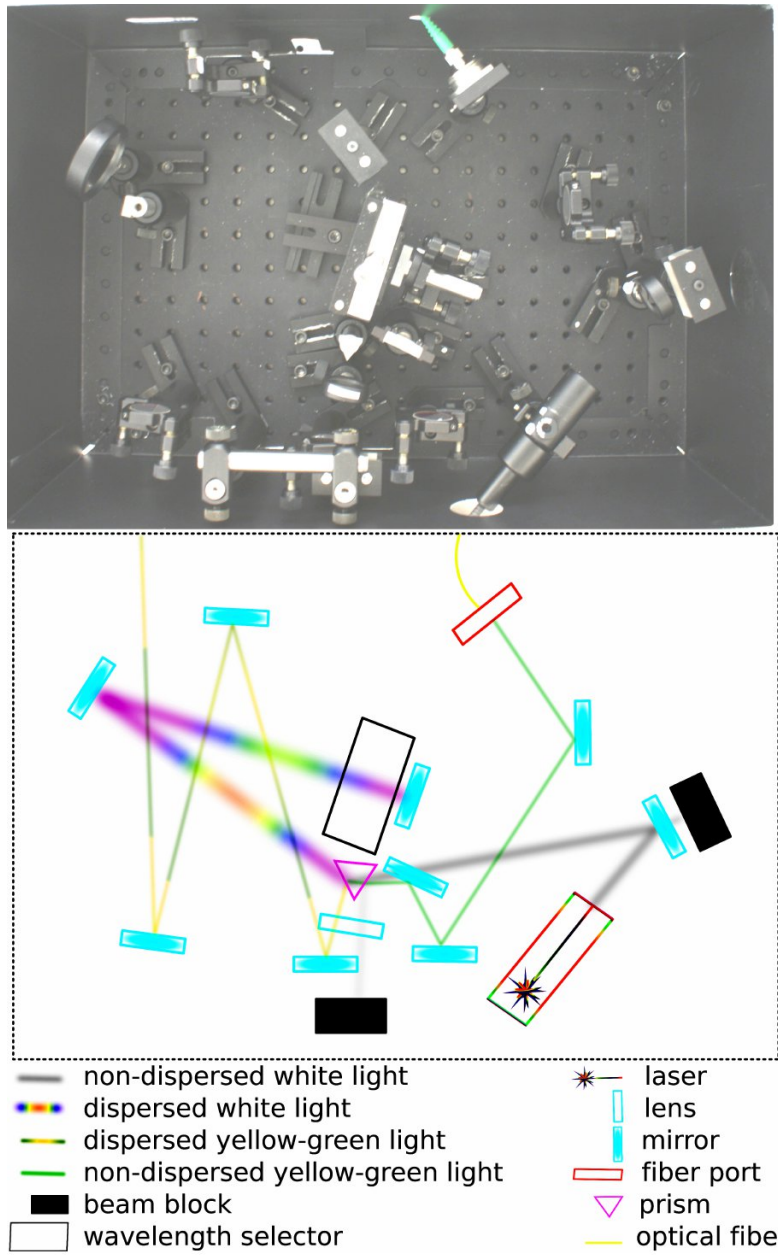
Figure 2.5: A photograph and schematic of a view looking down onto the breadboard coupling the supercontinuum laser. Most of the infrared light is filtered from the beam with a heat absorbing filter (UQG Optics, TKG1253) and sent to a beam block. The beam is dispersed by a prism, spatially filtered, reflected back through the prism and recombined, then coupled to a fiber. The spatial filter is easily adjusted to control the wavelength and bandwidth. Some of the spatially filtered dispersed beam is reflected from the face of the prism. Mirrors and a lens were placed to image this light onto the wall of the laser box. This allows the user to quickly see the visible wavelengths being coupled into the fiber.

to fiberports attached to micrometer translation mounts (Thorlabs). These mounts, combined with the controls on the fiberports, provide four degrees of freedom for the incoming laser light, corresponding to x, y, θ_x, and θ_y in regular nomenclature. The upper path includes a 90° corner, using a silver, cube-mounted 45° mirror, to allow the fiberport to be inserted without blocking the lower path. The lower path uses a dielectric cube-mounted 45° mirror to create a vertical beam, a 420-680nm polarizing beamsplitter is used to recombine the two optical paths, and a quarter-wave plate creates circularly polarized illumination for isotropic imaging. A photograph of the laser illumination pathways is shown in Figure 2.6, and the entire laser backscattering dark field microscope is shown in Figure 2.7.

The illumination laser light travels vertically through a hole in a mirror that is mounted at 45° with respect to the optical path. The mirror was made by securing a Thorlabs broadband dielectric mirror to a 45 degree mount, and using a Dremell rotary tool to carefully drill a hole through the mirror. The mirror was then glued to a 45 degree mount below the objective. The laser light passes through the hole in the mirror and is focused at the back focal plane of the objective (Nikon Plain Flour 100x oil), illuminating the sample. The sample is clamped at two points to a custom sample holder, which is screwed to the stage. The backscattered light is collected by the objective and reflected to the imaging pathway by the 45° mirror. The hole in the mirror is about 1mm in diameter, compared to a back focal plane diameter of 5.2-5.6 mm (NA 1.3-1.4), so very little backscattered light is lost. Figure 2.8 shows a photograph looking down on the objective and the 45° mirror, and Figure 2.9 shows a photograph of the sample.
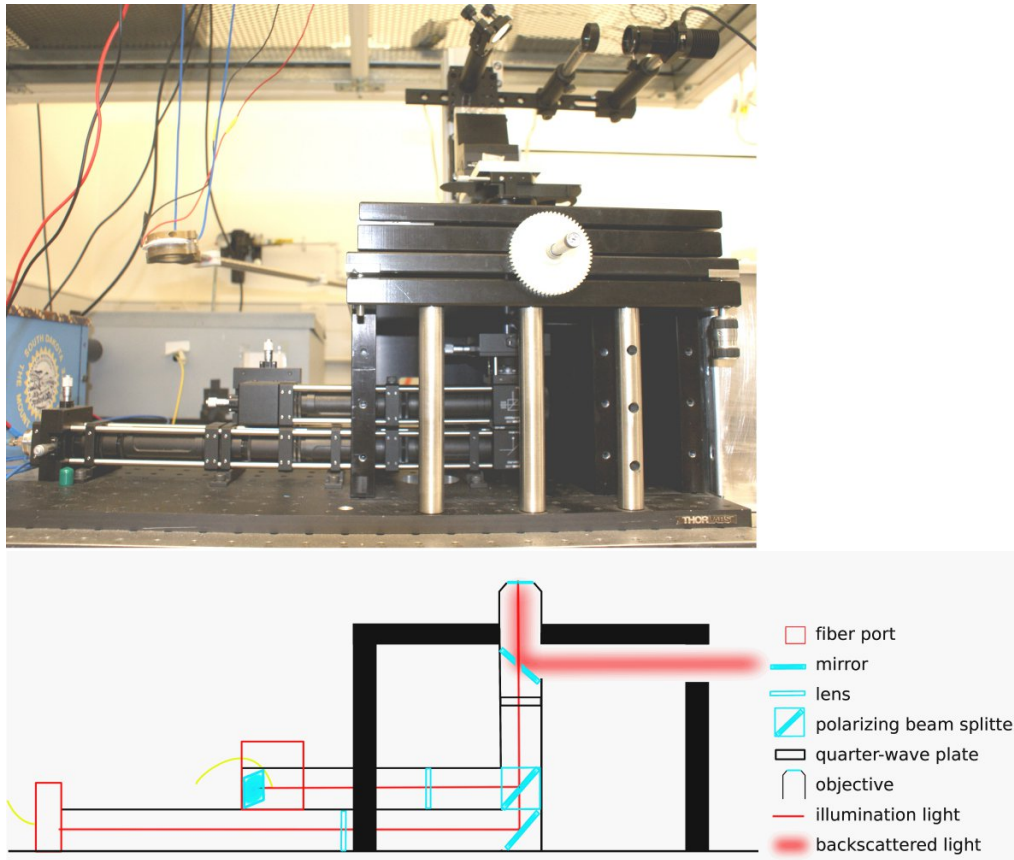
Figure 2.6: A photograph and schematic of the optical setup of the two laser illumination paths. The upper path was designed to provide a large area of illumination at the image plane, while the lower path was designed to provide a small area of illumination. The light from both pathways passes through a hole in a 45° mounted mirror before entering the objective. This mirror reflects the backscattered light towards the imaging pathway.

2.3.5 Microscope imaging optics

Principal Contributors: Ashley Nord, Dr. Bradley Steel

A flip mirror was used to direct the outgoing light down one of two paths: one path is split between a CMOS camera (Prosilica GC1280) and a segmented quadrant photodiode (QPD, SPOT 4DMI), and the other path goes to a high speed camera (Photron Fastcam 1024PCI). The high speed camera is capable of recording at 109,500 frames per second at a resolution of 16x128 pixels for 16 seconds. The four photodiodes of the QPD share a common grounded cathode and have separate anodes. The output
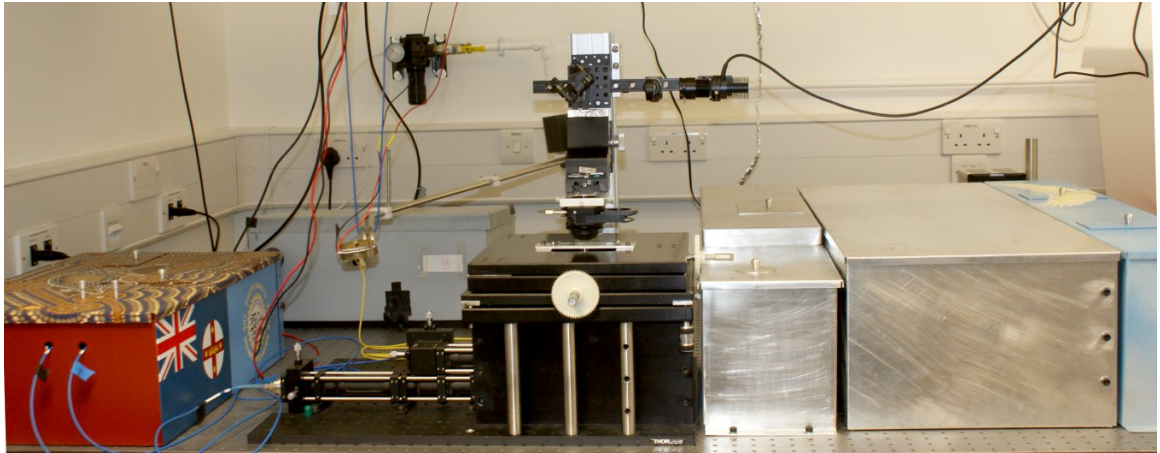
Figure 2.7: A photograph of the entire laser darkfield microscope. The box to the left of the microscope contains the 633nm and 532 nm lasers, and the box behind and to the left of the microscope contains the supercontinuum laser. The three boxes to the right contain the imaging optics, including pathways to the QPD, CMOS camera, and high-speed camera.
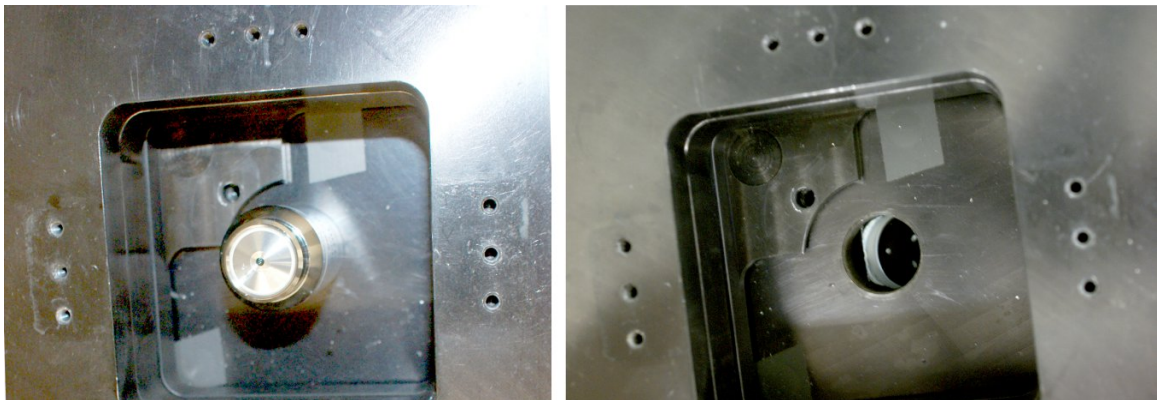
Figure 2.8: Two photographs looking down onto the stage. The image on the left shows the objective in place, and the image on the right shows the objective removed, with the 45° mirror visible. Illumination light passes through the 1mm hole in the mirror, which is visible. A second hole is also visible; the hole lies outside the area illuminated by backscattered light, and thus does not affect the mirror's performance.

current from each photodiode is converted to a voltage by a transresistance amplifier, which gives a linear relationship between the light intensity and the output voltage. A labview program was written to read the four voltage signals via a data acquisition board (National Instruments CompactDAQ), convert voltages to bead position, use a windowed Fourier transform to calculate and display the power spectrum, and record
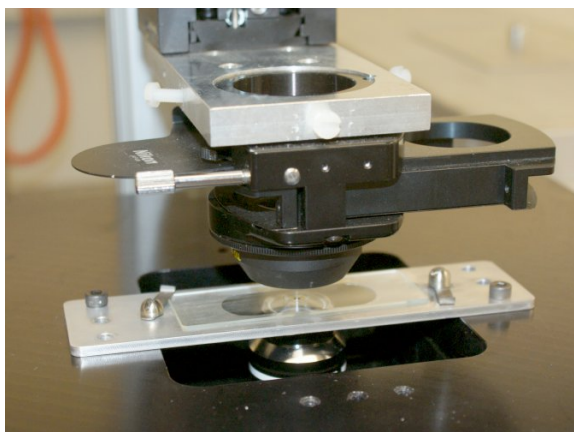
Figure 2.9: A photograph of the sample holder. The condenser above is used for brightfield illumination.

the signals from the QPD when triggered by a button. Two piezo electric actuators were temporarily mounted to the stage in order to test the linearity of the QPD. A 200nm bead stuck to the coverslip in a tunnel slide was centered onto the QPD. A labview program was written to move the slide by small increments in a grid pattern and record the voltages from the QPD for every position on the grid. The bead was illuminated by the small focused laser spot and the diffraction limited image of the bead was magnified by a factor of 250. Under these conditions, the voltage response of the QPD was linear for bead positions within a 350nm radius from the center.

When the flip mirror is oriented such that the backscattered light is imaged by the high speed camera, another mirror can be inserted to send the light through three beamsplitters and one prism. These optics were arranged by Dr. Bradley Steel and are positioned very close to one another to allow for all four resulting rays to be reflected off a single mirror and imaged onto the high-speed camera. The four paths contain light polarized at 0°, 45°, 90°, and 135° from the vertical, and from the intensity of the four polarizations, the angle of a rod rotating on a BFM can be calculated. An alternative path to the CMOS camera exists which incorporates a single polarizing beam splitter. Two paths of 0° and 90° polarization are imaged onto two halves of the CMOS detector. A Labview program was written to align the images on each half of

the detector and calculate the correlation between corresponding pixels. The program highlights areas in the image where the intensity of corresponding pixels from the 0° and 90° polarized beams are varying in an anticorrelated manner, allowing rapid detection of spinning rods within a large field of view. The imaging pathways are shown in Figure 2.10, and the beamsplitters and prism are shown in Figure 2.11. Details on how the angle of a rod can be determined from the intensities of these four paths is included in Section 2.4.2.
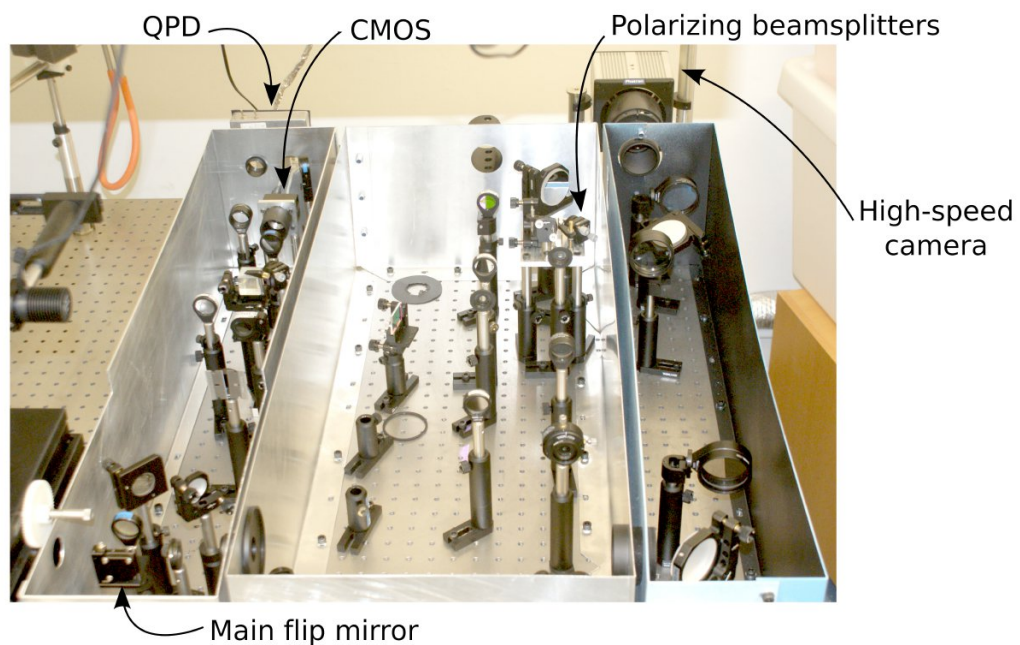
Figure 2.10: A photograph from above of the imaging pathways. The main flip mirror can direct the backscattered light to be split between the QPD and CMOS camera, housed in the left box, or it may be flipped out of the way to allow the light to go to the high-speed camera, housed in the right box. The middle box contains optics for separating the beam into four polarizations prior to sending it to the high-speed camera. The middle box also contains optics for a fluorescent imaging pathway which will be finished in the future.
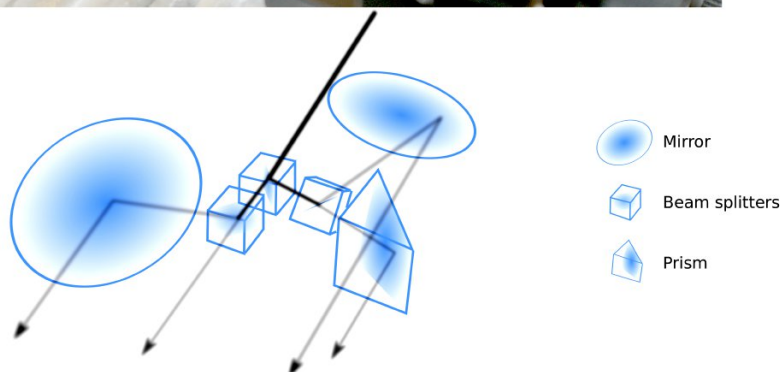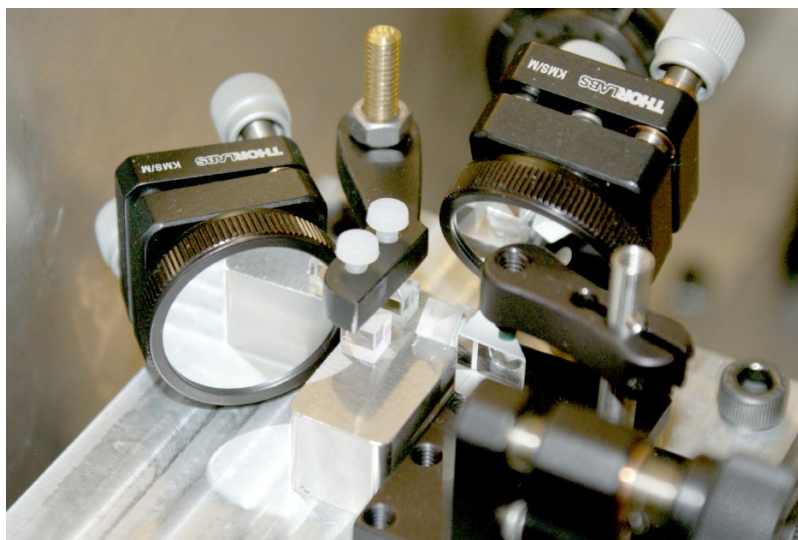
Figure 2.11: A photograph and schematic of three beamsplitters and a prism used to separate the backscatered light into four beams of polarization 0°, 45°, 90°, and 135°. The first beamsplitter is non-polarized, while the second two are polarized. These beams are spatially separated and imaged simultaneously onto the high-speed camera. The intensity of the four beams changes with the orientation angle of a gold nanorod. When the nanorod is attached to the hook of a BFM, this method allows for direct recovery of rod angle and thus motor angle.

2.3.6 Performance

This microscope was designed to image individual gold particles, so the resolution of the microscope is defined by the precision with which it localizes a particle. Although the particles of interest are diffraction limited, the location of the center of a single particle can be determined arbitrarily precisely given a sufficient number of photons in the point spread function [315]. As the goal is to image the gold particle over time, in the shot noise limited case, the constraint in spatial resolution is the stability of the

microscope. In order to measure this, a tunnel slide was constructed using a coverslip cleaned in a potassium hydroxide solution. Gold beads of 100nm diameter were introduced into the tunnel slide and incubated for 15 minutes. The unstuck beads were washed out and the tunnel slide was sealed with nail varnish. The position of a bead was recorded with the high speed camera for 1.9 seconds at 109,500 frames per second. The MATLAB program described in Section 2.2.2 was used to determine the bead position with a Gaussian Mask algorithm [310]. The power spectrum was calculated to show the noise contributions at various frequencies, integrated to give a cumulative power spectrum, and this is shown in Figure 2.12. As shown, the newly constructed darkfield microscope is characterized by less than $1nm^2$ noise. In addition, most of the noise picked up by the new darkfield microscope is contained within a 100Hz component, most likely from electrical noise. This noise can potentially be removed from recordings with a digital notch filter, if additional stability is required.

The newly constructed laser dark field microscope is thus capable of sub-nm spatial resolution and a temporal resolution of about $20\mu s$ (at 109500 frames per second). At low load and fully energized, the wild type BFM spins at about 300Hz. At high load and low speeds, the chimeric BFM has previously been observed to take 26 steps per revolution. If this stepping behavior remains unchanged at low load, the high speed camera in this setup will record an average of 14 frames at each individual step for each revolution, and these steps will be separated by about 12nm. Therefore, both the temporal and spatial resolution of this setup are more than sufficient to resolve steps in fully energized BFMs for the first time.
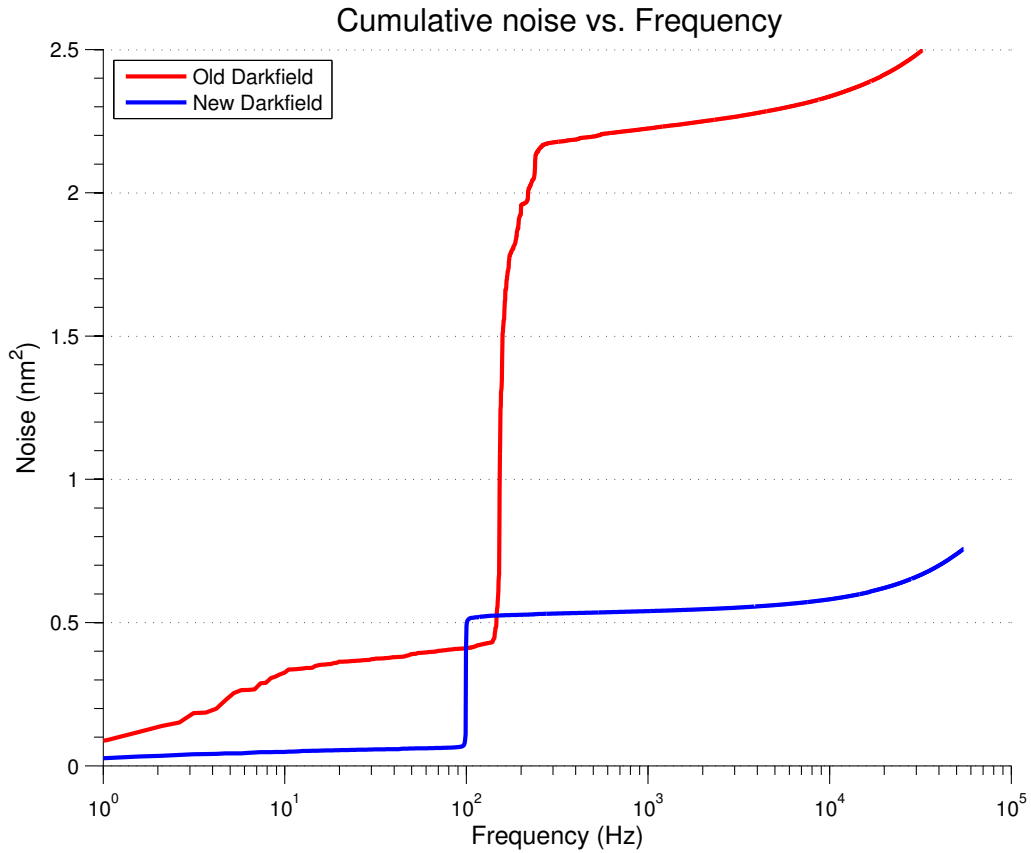
Figure 2.12: The integrated mean power spectrum of a 100nm gold bead stuck to a coverslip. The old laser darkfield microscope is shown in red, with the new design in blue. The cumulative power spectrum gives an estimate for the amount of noise inherent in each microscope, which, for the new design, is less than 1nm per axis. This represents about a 3 fold improvement in stability from the previous dark field microscope.

2.4 BFM Experiments

2.4.1 Sample preparation and image analysis

Bacterial strains Table 2.3 shows the strains of bacteria used in this thesis, including the parent strains and genetics. These experiments are described in Chapter 4. *E. coli* was used for all experiments on the BFM. The chimeric strain was originally created by Asai and colleagues in order to investigate ion selectivity [316]. The parent for all the strains used in this thesis is YS34, prepared at Nagoya University by Dr. Yoshi Sowa and brought to the Berry Lab in 2003. YS34 was derived from

RP4979 and has the following genotype: $\triangle cheY$, $\triangle pilA$, $\triangle motAB$, $fliC$::TN10 [208]. $\triangle cheY$ indicates that CheY has been deleted, and the motor therefore does not switch [244]. $\triangle pilA$ indicates that the pili, short, hair-like structures on the surface of the cell, have been deleted in order to prevent rotational markers from adhering to the pili. $\triangle motAB$ indicates that the stator units have been deleted [317], and $fliC$::TN10 indicates that a transposon called TN10 has been inserted into $fliC$, rendering filament expression inactive [226, 318]. Avi-tag $flgE$, referred to in Table 2.3, indicates that FlgE, the protein of the hook, has been replaced with an Avidity tagged peptide fused FlgE for conjugation of biotin [180]. YS34 was also transformed by up to two plasmids. Plasmid pYS11 ($fliC$ sticky filaments, ampicillin resistance, pBR322 derivative) expresses a 'sticky filament' which promotes hydrophobic interactions [244, 318]. This allows particles such as polystyrene beads to stick to the filaments without the need for antibody coating. Plasmid pYS13 ($pomApotB$, isopropyl-β-D-thiogalactoside (IPTG) inducible, chloramphenicol resistance) expresses chimeric sodium-driven PomAPotB stator proteins which are induced depending on the IPTG concentration during growth [205]. Some strains instead contained plasmid pDFB27 ($motAmotB$, arabinose inducible, ampicillin resistance) which expresses wild type stator proteins induced by arabinose [177]. Plasmid pMTAN01 ($motAmotB$, arabinose inducible, ampicilin resistance) expresses wild type stator proteins with a mutation of the acidic residue at position 32 on MotB. Previous studies using this mutation in *E. coli* have shown a swimming rate of less than 10% that of wild type and half the wild type motor torque, as measured with a tethered cell assay [156].

Cell growth and slide preparation Cells were grown aerobically for 5.5 hours at 33°C with shaking from frozen stocks (stored at -80°C). The growth medium included 5mL of tryptone broth (TB, 1% tryptone, 85mM sodium chloride) containing the appropriate antibiotics and inducers. The amount of cell inoculant used was con-

Strain	Parent	Genome	Plasmid	Stators
YS34	RP4979	$\triangle cheY$ $\triangle pilA$ $\triangle motAB$ $fliC$::TN10	pYS11 pYS13	chimeric
YS1243	YS34	$\triangle cheY$ $\triangle pilA$ $\triangle motAB$ $fliC$::TN10	pYS13	chimeric
MTB24	YS34	$\triangle cheY$ $\triangle pilA$ $\triangle motAB$ $fliC$::TN10 Avi-tag FlgE	pYS13	chimeric
RB3	YS34	$\triangle cheY$ $\triangle pilA$ $\triangle motAB$ $fliC$::TN10	pDFB27	wild type
MTB22	YS34	$\triangle cheY$ $\triangle pilA$ $\triangle motAB$ $fliC$::TN10 Avi-tag FlgE	pDFB27	wild type
ALN01	YS34	$\triangle cheY$ $\triangle pilA$ $\triangle motAB$ $fliC$::TN10 Avi-tag $flgE$	pDFB27 pMBAN01	wild type + MotB D32E

Table 2.3: Bacteria strains used and referred to in this thesis. The host for all strains is *E. coli*. $\triangle cheY$ indicates a CheY deletion and a non-switching motor [244]. $\triangle pilA$ indicates a pili deletion [317]. $\triangle motAB$ indicates stator protein deletion [317]. $fliC$::TN10 indicates that filament expression is inactive [226, 318]. Plasmid pYS11 expresses a sticky filament [244, 318]. Plasmid pYS13 expresses inducible pomApotB stators [205]. pDFB27 expresses inducible motAmotB stators [177]. pMBAN01 expresses inducible motAmotB stators with a mutation in MotB where residue Asp 32 is replaced by Glutamate.

trolled such that the growth conditions yielded an optical density OD_{600} of 0.5-0.7, ensuring that the bacterial cells were in mid-log growth phase. Optical density was measured with a spectrophotometer (UV-mini 1240, Shimadzu). Cells were immediately washed three times by centrifugation at 3000g for 2 minutes and resuspended by gentle pipetting into motility buffer (MB, 10mM potassium phosphate, 0.1mM $EDTA^2$, 10mM lactate, 70mM NaCL, pH 7.0) with a final resuspension of $400\mu L$. All of the MB chemicals were ordered from Sigma-Aldrich.

Gold beads of 100nm diameter were attached to the hook of the BFM via two different methods. In the first, gold beads were conjugated with anti-rabbit IgG (Sigma-Aldrich R5506) in the following manner [216, 319]: IgG was activated with LC-SPDP[3] (Pierce, 21651) according to the manufacturer's instructions; $2.5\mu L$ of this solution was added to $500\mu L$ of the gold beads (British Biocell International) and left to incubate for 2 hours at room temperature; $10\mu L$ of mPEG-SH 5000[4] (Sigma-Aldrich, 81323) was added and incubated at room temperature overnight. A rabbit anti-FlgE antibody (gift from Howard Berg, University of Harvard) was purified using an IgG purification kit (Dojin-Do, kit A). Using the Bradford Method[5] [320], the purified antibody was measured to be 0.1mg/mL. Then, $2.5\mu L$ of purified rabbit anti-FlgE antibody was added to $100\mu L$ of washed cells and allowed to incubate for 25 minutes on a tabletop spinner. The antibody-treated cells were washed twice with $300\mu L$ of MB and resuspended in $40\mu L$ of MB. An eppendorf of $100\mu L$ of the IgG-gold was centrifuged at 1000g for 3 minutes and resuspended with the $40\mu L$ of antibody treated cells. This mixture was incubated for 25 minutes at room temperature on a tabletop spinner. Finally, this solution was centrifuged at 1800g, decanted, and

---

[2]ethylene diamine tetraacetic acid

[3]succinimidyl 6-[3-(2-pyridyldithio)-propionamido]hexanoate

[4]O-[2-(3-mercaptopropionylami-no)ethyl]-O'-methylpolyethylene glycol

[5]The Bradford method is a spectroscopic analysis used to measure the concentration of a protein in solution. It is based on an absorbance shift of the Coomasssie dye when bound to the hydrophobic amino acid residues of the protein. The increase in absorbance at 595nm is proportional to the amount of bound dye and thus the amount of protein.

resuspended in 300μL of MB. This procedure was slightly modified from that of Yuan and Berg, 2008 [216].

The second method of attaching 100nm gold beads to the hook of the BFM used strain MTB22 which replaces FlgE with an Avi-tag FlgE [180]. BirA is an enzyme in *E. coli* that catalyzes the site-specific covalent bond of biotin to an Avi-tag (a lysine side-chain within a 15-amino acid acceptor peptide). Both BirA and biotin are produced naturally within the cell, and this allows for FlgE to be biotinylated *in vivo*. This strain was grown and washed with the normal protocols. Then, 2μL of 100μM streptavidin (NBS 497) was added to 50μL of washed cells and incubated at room temperature on a tabletop spinner for 5 minutes. An eppendorf of 60μL of thirty-fold dilution 100nm biotin conjugated gold beads (British Biocell International) was washed and resuspended at the same concentration in MB. The streptavidin labeled cells were washed and resuspended by the solution of biotin conjugated gold beads and left to incubate at room temperature on a tabletop spinner for 5 minutes. Finally, 300μL of MB was added to this solution. The two methods for conjugating beads to the hooks of BFM are shown schematically in Figure 2.13.
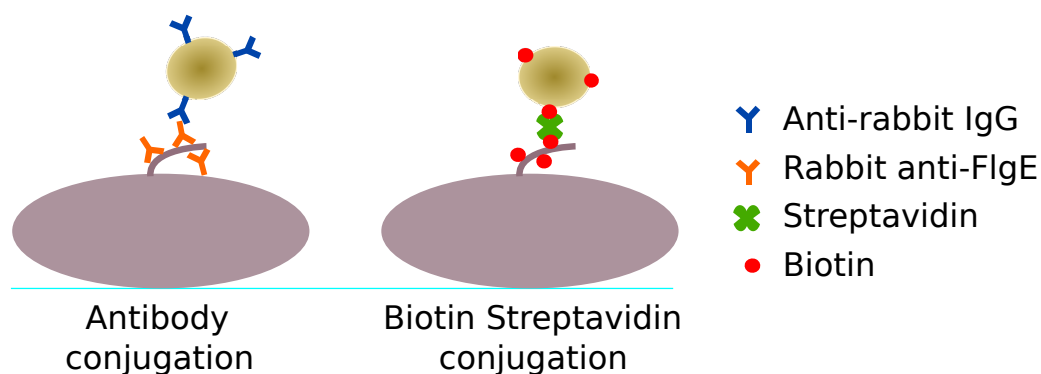
Figure 2.13: 100nm gold beads were attached to the hook of the BFM using two separate methods. Antibody conjugation used anti-rabbit IgG conjugated gold beads and rabbit anti-FlgE stuck to the hook. Biotin streptavidin conjugation used genetically modified biotinylated hooks, free streptavidin, and biotinylated gold beads.

With both protocols, the cells were imaged within a tunnel slide, constructed as shown in Figure 2.2, using coverslips straight from the box (ie uncleaned). These coverslips were compared with coverslips cleaned with a saturated potassium hydroxide and ethanol solution and those cleaned baked at 80°C for 4 hours. Polystyrene beads of 1μm diameter were attached to truncated flagellas, and the cells were immobilized on the coverslips with poly-L-lysine. When the three coverslips were compared, both the percentage of motile cells and the speed of the motors were indistinguishable, and it was thus concluded that cleaning the coverslips had no effect on the experiments.

Fluid was delivered to the tunnel slide by placing the tip of the pipette at one end of the tunnel and an absorbent towel at the other end of the tunnel to wick fluid through. Care was taken to avoid introducing air bubbles into the tunnel. Cells were adhered to the surface of the coverslip using poly-L-lysine (0.01% solution in water, 70-150kDa, Sigma-Aldrich P4707). Undiluted poly-L-lysine was added to a tunnel slide and left to incubate for 1 minute with the coverslip downwards. The poly-L-lysine was then washed out twice with 100μL of MB. The bacteria cells were wicked in and left to incubate for seven minutes with the coverslip downwards. This incubation took place in a humidity chamber to prevent evaporation from the ends of the tunnel. The cells were then washed out twice with 100μL of solution containing 90% MB and 10% TB. The ends of the tunnel slide were sealed with nail varnish. The cells were then imaged for up to 90 minutes before the slide was discarded.

Gold nanorods 100nm by 53nm in size (Nanopartz) were attached to BFM hooks in a similar manner to gold nanospheres, except that the incubation was performed in the tunnel slide. In this assay, washed MTB22 cells were flowed into a tunnel slide and allowed to adhere to the coverslip. After unattached cells were washed out, 4μM streptavidin in MB was flowed into the tunnel and allowed to incubate for 5 minutes before being washed out with MB. Biotin conjugated rods were sonicated in the commercial buffer, then diluted with MB immediately before being flowed into

the tunnel slide. The rods were left to incubate for 7 minutes, then washed out with MB and the slide was sealed with nail varnish. The gold nanorods aggregated within tens of minutes in MB, so they were stored in their commercial solution until use.

The commercial nanorods are sold as"biologically friendly". In order to ensure that commercial solution was not affecting the BFM, an experiment was performed where 1μm biotin beads were attached to the biotinylated hooks of MTB22 after adding streptavidin in solution. The mean speed of motor rotation was measured before and after adding a concentrated amount of nanorods in solution. The mean speed of 15 motors 45 minutes after adding the nanorods solution was the same as before adding the solution.

Full recipes and protocols are included in Appendix A.

Image acquisition Brightfield microscopy imaged onto the CMOS camera was used to locate bacterial cells on the coverslip. Cells with a 100nm gold bead stuck to the hook showed a small dark spot somewhere on the cell. Once located, the image of the gold bead illuminated by the HeNe laser was centered on the QPD. If the hook was rotating, the power spectrum of the QPD signal showed a peak at the speed of rotation. Once rotating hooks were located, their rotation was recorded in one of two ways. In some experiments, longer recordings were acquired with the QPD, and in other experiments, the acquisition mirror was flipped in order to image the gold bead on the high speed camera, where short recordings were acquired. In both cases, this process was continued until 90 minutes had elapsed and the slide was discarded or until the memory of the camera became full. Figure 2.14 shows a brightfield image of a few cells within a tunnel slide, one of which has a 100nm gold bead stuck to the hook of a BFM, and the corresponding dark field image of the same field of view.

Table 2.4 shows the number of QPD and high speed camera recordings of spinning gold beads acquired for each strain. The QPD recordings were acquired at 20kHz and
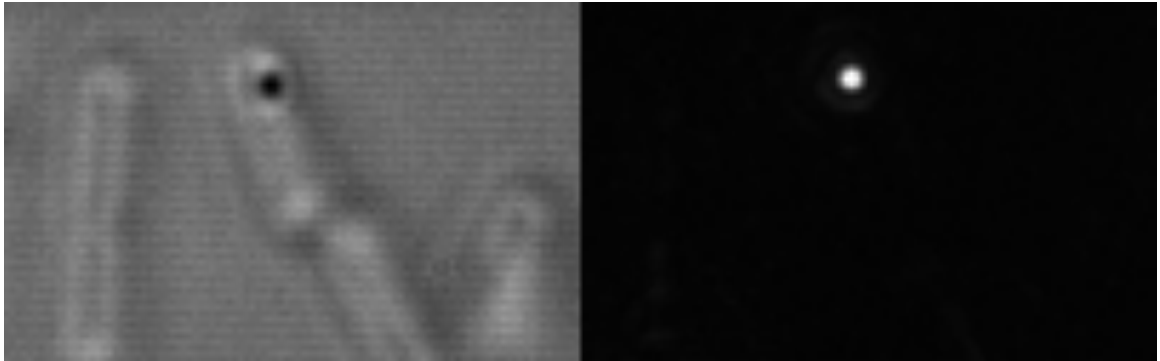
Figure 2.14: Two images of the same field of view acquired with the high speed camera. The left image uses brightfield illumination and the right image uses backscattered darkfield illumination. There are a few cells stuck to a poly-L-lysine coated coverslip within a tunnel slide. On one cell, a 100nm gold bead is stuck to the hook of a BFM. While this bead is visible in brightfield, the signal to noise ratio is greatly improved with backscattering darkfield.

are 15-200 seconds in length, and the high speed camera recordings were acquired at 109.5kHz and are 0.9-2 seconds in length.

Strain	Attachement	Mobility phenotype	QPD	High speed camera
YS1243	Antibody	Chimera	38	224
MTB24	Biotin	Chimera	14	-
RB3	Antibody	Wild type	336	4
MTB22	Biotin	Wild type	32	89
ALN01	Biotin	Wild type + D32E	62	65

Table 2.4: Number of recordings of spinning 100nm gold beads acquired for each strain of *E. coli* with the quadrant photodiode and the high speed camera. For the YS1243 strain, 61 of the high speed traces were recorded by Dr. Yoshi Sowa.

Gold nanorods were imaged in a similar manner. In order to optimally illuminate the rod, the supercontinuum laser was used with a selected wavelength to match the excitation peak of the longitudinal axis of the rod and a selected bandwidth to approach camera saturation. The lateral movement of a rod on the BFM was not sufficient to detect rotation on the QPD, as expected. Instead, an image showing the calculated degree of anticorrelation in intensity between orthogonal polarized images

94

on the CMOS camera was used as a test for motor rotation. About 50 recordings of 1 second duration at 109.5kHz were recorded of gold rods on BFM hooks.

2.4.2 Data analysis

Position and speed measurement For the QPD recordings, the signals from the four quadrants were used to determine the x and y coordinates of the bead position. Referring to Figure 2.15 of the QPD, the bead position was calculated as:

$$x = \frac{(b+c) - (a+d)}{a+b+c+d}$$
$$y = \frac{(a+b) - (c+d)}{a+b+c+d} \quad (2.9)$$

where x and y correspond to the coordinate system defined in the figure. The speed of the motor was measured over 1s windows spaced 0.05s apart and was determined by finding the maximum of the unfiltered power spectrum of the position signal, performed with a fast Fourier transform. Histograms of BFM speeds over tens of seconds long traces were created, and the number of distinct speed populations was judged by eye. A non-linear optimization algorithm was used to decompose the overlapping-peak signal into its component parts. Multiple trial fits with varying starting values were performed, and those with the lowest mean fit error were used to represent the distinct speed populations within the histograms. As is normally done with high load data, each distinct speed population was presumed to represent a different number of stators in the motor. Where appropriate, an ellipse were fit to the x,y data using the same algorithm as for the F_1 data [311]. For periods where the motor speed was near zero, the mean squared displacement of the bead was calculated for non-overlapping (independent) segments of the period.

For the high speed camera recordings, gold beads were identified and localized using the software described in Section 2.2.2. Depending on the location of the BFM
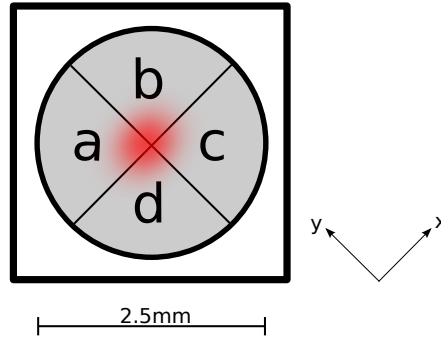
Figure 2.15: A schematic of the quadrant photodiode. The position of the gold bead determines the intensity of light that falls on each quadrant. The signals from the four quadrants are used to calculate the position of the gold bead as given in Equation 2.9.

on the cell body, the two dimensional paths traced by the gold beads were either circular or elliptical. Ellipses were fit to the x,y coordinates of the bead using the same algorithm as for the F_1 data [311]. From the ellipse fit, the angular position of the bead was derived.

A subset of recordings were chosen for preliminary speed and stepping investigations, along with an evaluation of analysis algorithms. The results of this analysis appear in Chapter 4. The subset of recordings includes a wild type strain that has previously been investigated at low load [216], and one chimeric strain for comparison. Recordings where the bead was on the side of the cell, characterized by a negligible minor axis of the ellipse, were ignored. For high speed camera data, distributions of rotational speed were created by calculating the speed of the gold bead per revolution, where an arbitrary angle was chosen to mark the beginning of each successive revolution. From histograms of rotational speeds, the number of distinct speed populations was judged by eye. Gaussian distributions were fit to the distinct speed populations in the same manner as for the QPD speed distributions.

The Gaussian peaks were used to define the characteristic speed for a given number of stators. The transition point from one distinct speed population to another, characterized by the gain or loss of a stator, was marked by the half way point between

the Gaussian peaks. The variance in the rotational period of the BFM was calculated for each stably spinning period within each trace, defined by a period lasting at least seven revolutions within one speed population.

Stepping and kinetic analysis In order to resolve steps and calculate stepping kinetics, the angular position signal was first padded and smoothed with a L1-PWC filter [312], using a gamma value of 0.1 radians. A dwell angle histogram was created, and the probability density function of the angular position was estimated with a kernel density function using a Gaussian kernel and a bandwidth of 0.03 radians. The similarity of multiple kernel density estimations (KDEs) was determined using a cross correlation analysis where the lag between the KDEs was applied circularly over a 2π range, in small increments of $\frac{2\pi}{1000}$.

The dwell states of a motor were defined by the local maxima of the KDE, and the boundaries between individual dwells were defined by the local minima of the KDE. Dwell times were calculated using the same methods as for the F_1 analysis in Section 2.2.2. For each step of the BFM, dwell time histograms were fit using the models described in Table 2.2. The likelihood of each model was determined using the BIC value, and the rate constants were calculated using an MLE algorithm.

Angle measurement with nanorods The shape-induced anisotropic optical properties of gold nanorods allow for the determination of particle orientation. Resonantly scattered light from gold nanorods is strongly polarized along the long and short axes [321]. When excitation light is tuned to the absorption peak of the long axis, the scattered intensity has sinusoidal dependence on the in-plane angle of the rod; the scattered light is maximal and minimal when the long axis of the rod is parallel and orthogonal to the plane of polarization, respectively, [59, 322]. Using a square mask around the point spread function of the rod, the intensity of the rod was calculated for each polarization channel for each frame. The angle of the rod, θ, was defined by

the following two equations:

$$sin(\theta) = \frac{p_1 - p_3}{p_1 + p_3}$$
$$cos(\theta) = \frac{p_2 - p_4}{p_2 + p_4}$$

(2.10)

where p_1 and p_3 are the intensities from two orthogonal polarized channels and p_2 and p_4 are the intensities from the other two orthogonal polarized channels. The rod angle θ spans from 0 to π. For rotating motors, this angle was unwrapped to span from 0 to 2π.

2.5 Summary

In order to resolve steps in BFMs at high speed, there was a need for both higher spatial and temporal resolution. The new laser dark field microscope setup constructed for this purpose and described in this chapter meets these needs. Analysis algorithms were written to assign rotational angles to an x,y position signal, fit the position of F_1 dwells, calculate dwell times, and determine the model which best fit the distribution of dwell times. These algorithms were initially applied to F_1 data, part of which was acquired on the newly built microscope. A data set of unprecedented quality and size was then acquired for the wild type and chimeric BFM. Using the algorithms originally designed for F_1 analysis, a subset of this data, characterized by an elliptical bead trajectory, was chosen to investigate the stator and stepping dynamics of fully energized, low load BFMs.

Chapter 3

Single-Molecule Studies of Mesophilic F_1

F$_1$-ATPase is one of the best-studied molecular machines, and single-molecule studies over the last two decades have elucidated its full mechanochemical cycle. While most of this work has been done on F$_1$ from the thermophilic *Bacilus* PS3 (TF$_1$), only mitochondrial F$_1$ (MF$_1$) has been well characterized by high-resolution crystal structures, and single-molecule studies of mesophilic F$_1$ are lacking. As an effort to bridge this gap, new analysis tools were applied to data from high resolution single molecule experiments of F$_1$ from *E. coli* and yeast. Section 3.1 presents evidence that mesophilic F$_1$-ATPase from *E. coli* (EF$_1$) is governed by the same mechanism as TF$_1$ under laboratory conditions. Section 3.2 presents evidence that wild type yeast F$_1$ (YF$_1$) from *Saccharomyces cerevisiae* is also governed by the same mechanism as TF$_1$ under laboratory conditions. This analysis also investigated seven mutant forms of F$_1$ from *S. cerevisiae*, resolving a previously unobserved kinetic step within three of the mutants.

3.1 *E. coli* F_1-ATPase

While mesophilic EF_1 shares considerable homology with TF_1, the two enzymes function at very different natural temperatures. The mechanism of TF_1 has been well characterized at room temperature, far outside its natural conditions. Until recently, it was unknown whether EF_1 shared this mechanism. At room temperature, EF_1 rotates almost four times as quickly as TF_1 [48, 49, 52], making single-molecule measurements difficult. The analysis in this chapter forms part of a larger collection of conclusive evidence that mesophilic EF_1 shares the same mechanism as thermophilic TF_1 when investigated under the same conditions. The experiments at intermediate [ATP] described in this section were performed by Dr. Bradley Steel and analyzed by Ashley Nord. The results were compared to experiments and analysis performed at low and high [ATP] by Dr. Tom Bilyard.

3.1.1 Michaelis-Menten kinetics

Single molecule experiments have shown the Michaelis-Menten dependence of TF_1 rotation on [ATP]. Recent experiments have shown a Michaelis-Menten dependence in EF_1 over six orders of magnitude of [ATP] and four orders of magnitude of marker size, shown in (b) of Figure 3.1 [41].

In Michaelis-Menten kinetics, the reaction rate, v, is related to the concentration of a substrate S by the following equation:

$$v = \frac{V_{max}[S]}{K_m + [S]} \tag{3.1}$$

where V_{max} is the maximum rate of a system at saturating substrate concentration, K_m, called the Michaelis constant, is the substrate concentration at which the reaction rate is half of V_{max}, and [S] is the concentration of substrate S. A simple phenomenological model proposes that the time F_1 takes to do one revolution is just the sum of
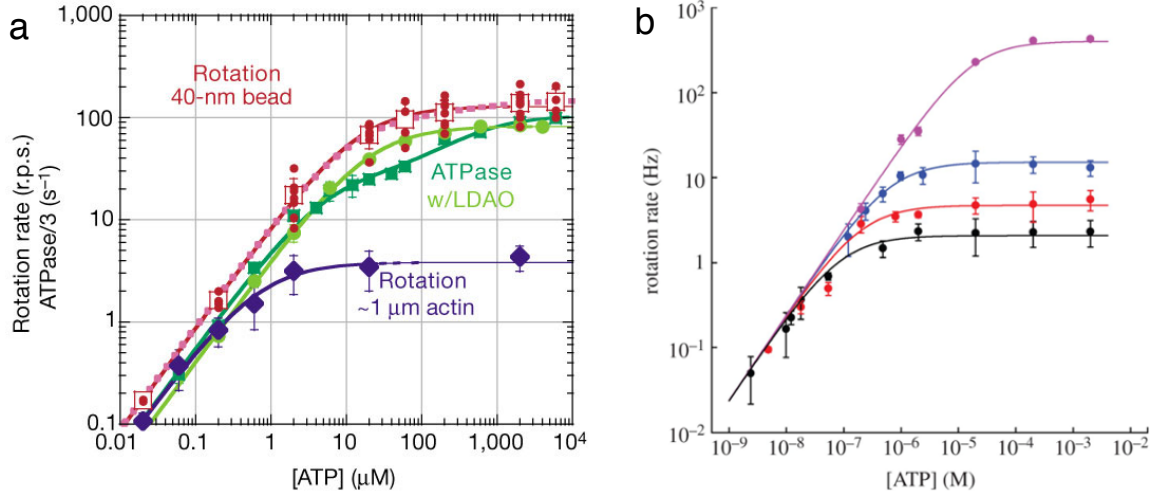
Figure 3.1: Graphs showing the Michaelis-Menten dependence of (a) TF_1 and (b) EF_1 on [ATP]. In (a), red shows the rotation of 40nm beads and blue shows the rotation of $\sim 1\mu$m long actin filaments on TF_1. In (b), pink and blue show the rotation of 60nm and 220nm beads respectively, and red and black show 340nm and 495nm bead duplexes respectively on EF_1. All curves show the best fit of Michaelis-Menten kinetics, using Equation 3.3 and a shared value for a between the curves. Images from a) Yasuda et al 2001 [46] and b) Bilyard et al 2013 [41].

the time taken for ATP binding, t_{ATP}, the time taken for internal catalytic processes, t_i, and the time taken to rotate the marker through the viscous medium, t_r. That is,

$$\frac{1}{v} = t_{ATP} + t_i + t_r \tag{3.2}$$

If ATP binding is first order with [ATP], then $t_{ATP} = 3/k_{on}[ATP]$, and Equation 3.2 rearranges to ,

$$v = \frac{\frac{1}{3}k_{on}[ATP]}{1 + \frac{1}{3}k_{on}(t_i + t_r)[ATP]} = \frac{a[ATP]}{1 + b[ATP]} \tag{3.3}$$

where $a = V_{max}/K_m = k_{on}/3$ and $b = 1/K_m = k_{on}/3(t_i + t_r)$ [41]. In Equation 3.3, a is independent and b is dependent on marker size.

At saturating ATP, $t_{ATP} \to 0$. In this regime, at high load, marker rotation time is rate-limiting $(t_r \gg (t_{ATP} + t_i))$, and rotation speed is inversely proportional to the viscous drag coefficient of the marker. At low load (60nm gold beads or smaller), speed

is independent of marker size, and the internal catalytic processes are rate limiting $(t_i \gg (t_{ATP} + t_r))$. Single molecule experiments in this regime observe F_1 molecules rotating in 120° steps, with dwells to allow catalytic processes to occur. At low [ATP] ([ATP]<K_m), ATP binding is rate limiting $(t_{ATP} \gg (t_i + t_r))$ and the rotation rates for all marker sizes converge. Single molecule experiments in this regime observe F_1 molecules rotating in 120° steps, with dwells to allow ATP to bind.

For both TF_1 and EF_1, the Michaelis-Menten model is a good fit to the experimental data, as shown in Figure 3.1. This confirms that the enzymes bind ATP with first order kinetics, generate constant torque while moving the marker through a viscous fluid, and that the internal catalytic processes are independent of both load and [ATP]. Figure 3.1 also demonstrates that EF_1 rotates at speeds 3-4 times greater that TF_1 at room temperature. As the native temperature for TF_1 is much higher than those for EF_1, this is unsurprising. Under physiological temperatures, TF_1 rotates faster than EF_1 [74].

3.1.2 EF_1 at intermediate [ATP]

In the experiments on EF_1 shown in Figure 3.1, single gold beads in the range of 60-220nm (British BioCell) were attached to the γ subunit of surface-immobilized EF_1 as depicted in Figure 2.3. The beads rotated counter-clockwise in the presence of ATP, and an ATP-regenerating system was used in all experiments, consisting of 1 mM phosphoenolpyruvate (Roche) and 50μg/ml pyruvate kinase (Roche). Similar experiments were performed by Dr. Bradley Steel at intermediate [ATP] (20μM-50μM), and the recordings from these experiments were analyzed for this thesis. At intermediate [ATP] concentrations, the rotation of the gold bead was recorded at 22.5kHz and the position and angle were derived by Dr. Bradley Steel as described in Section 2.2. These traces are of interest because, at intermediate [ATP] and low load, the ATP-binding and catalytic dwells can both be resolved in a single trace. In

TF$_1$, the binding of ATP causes an 80° substep, and the molecule dwells here until two catalytic processes occur, upon which a 40° substep occurs [46,66]. The following analysis is the first to characterize both dwells in single traces in EF$_1$.

Traces were initially automatically filtered to select rotating beads, characterized by the power spectral bias of the bead position. Traces were further automatically filtered to choose those that formed an ellipse of a sensible size, eliminating rotating beads where the angle of attachment yielded poor angular resolution, and bead pairs, characterized by large ellipses and high brightness. Pauses were removed from the traces, and finally, traces were filtered by eye for those that showed six distinct dwells in the kernel density plot of the dwell angles. This left 7 traces at intermediate [ATP] which showed six distinct dwells. Figure 3.2 shows two of these traces.

The locations and dwell times of the ATP-binding state and catalytic state were determined as described in Section 2.2. At the ATP concentrations used, dwells at the ATP-binding state and the catalytic state take approximately the same amount of time. The mean angular distance between the two states was 35.3°, with a standard deviation on the mean of 12° and a standard error of the mean of 2.7° (n = 21). ATP binding occurred about twice as fast in EF$_1$ than in TF$_1$, and the catalytic step occurred about four times as fast.

Histograms of the dwell times of the ATP-binding and catalytic dwells were constructed for each trace as described in Section 2.2.2. Six potential models were fit to each state containing up to three exponential components and one time offset, and these fits were judged by their BIC value, as described in Section 2.2. As Figure 3.3 shows, there was no one model that was the best fit for each of the seven traces analyzed. This may be partially due to overlapping Gaussians in the histograms of dwell angles causing some observations to be mis-assigned to neighboring dwells. This affects the dwell time histograms, introducing error into the fits. Nonetheless, the fits are compatible with single exponential and double exponential models.
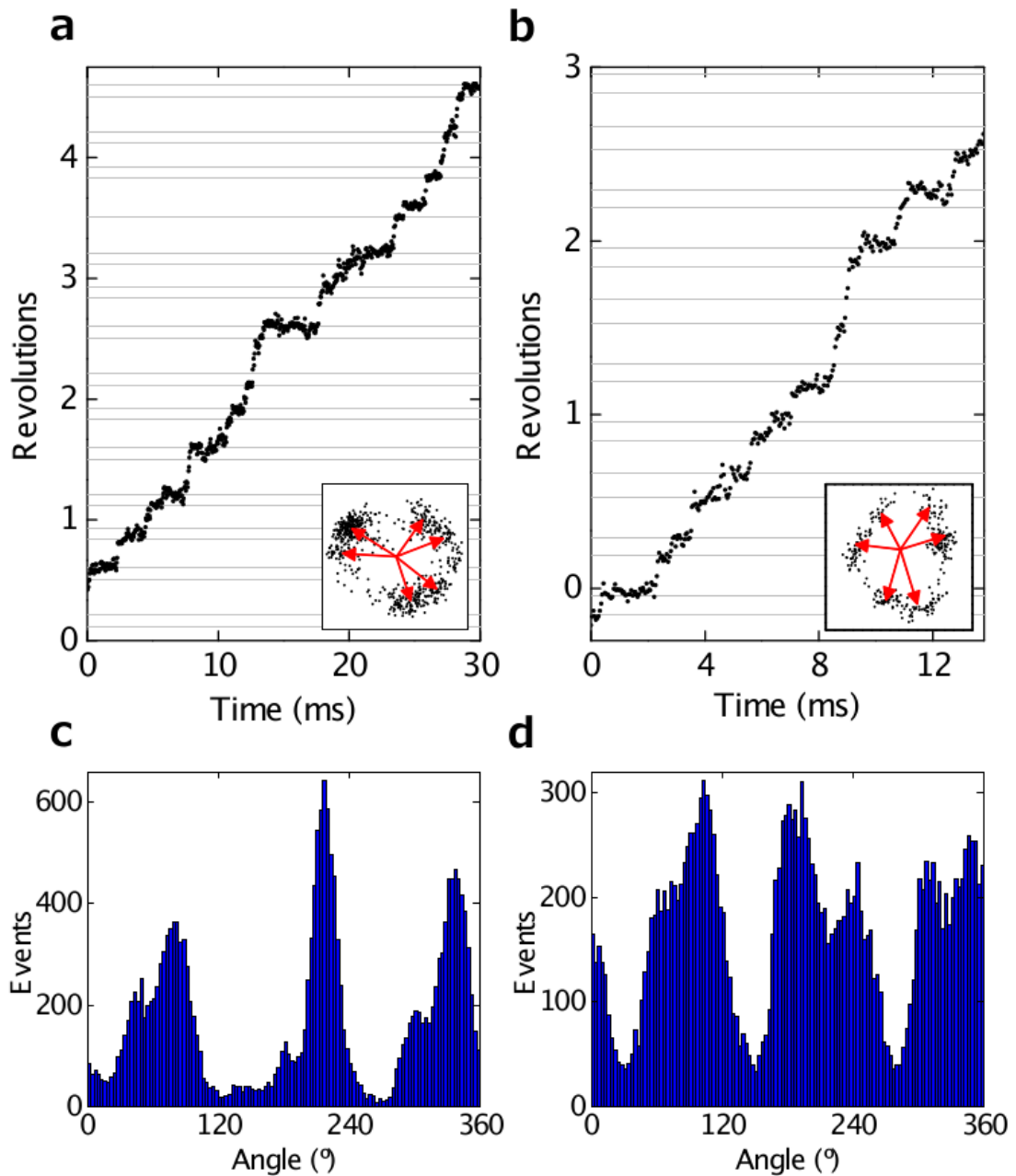
Figure 3.2: a,b) Two examples of traces of a 60nm gold bead stuck to the γ subunit of a surface immobilized EF_1 molecule at intermediate [ATP]. These graphs show the revolutions of the bead versus time, with horizontal lines drawn at the dwell locations, as assessed from the full recording. These traces are two of seven analyzed that showed distinct substeps. Trace (a) was recorded in $20\mu M$ ATP and trace (b) in $50\mu M$ ATP. The insets to these graphs show the x,y position of the gold bead for the time shown, with red arrows pointing to the dwell locations. c,d) The corresponding histograms of angles constructed with $3°$ bins. The average separation between the catalytic and ATP-binding state was a) $33°$ and b) $42°$, compared to the average separation of $35°$. Image adapted from Bilyard et al 2013 [41].
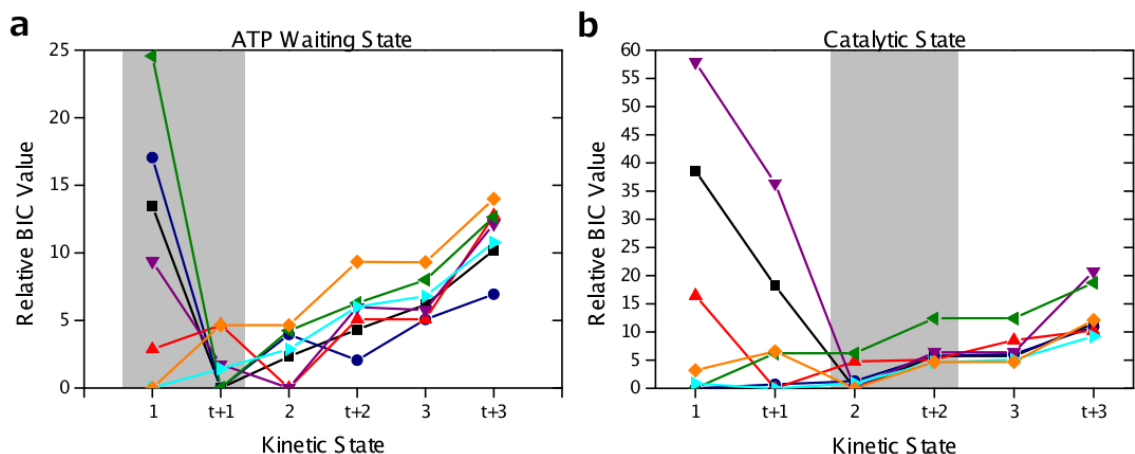
Figure 3.3: Graphs of relative BIC values for the six kinetic models tested for molecules at intermediate [ATP] showing six distinct dwell angles. Fits for the ATP-waiting dwell are shown in (a) and for the catalytic dwell in (b). A lower BIC value indicates a better fit, where the best model for each state has a value of 0. The seven traces are shown by the different colored lines. For each model, one to three kinetic parameters were fit with or without a time offset parameter that would correspond to the time a bead spent rotating between dwells. No model is the best fit for all of the 7 traces, though there are definite trends: the ATP-waiting dwell was typically well fit by one kinetic parameter and a time offset or two kinetic parameters, and the catalytic dwell was typically well fit by two kinetic parameters. The grey shaded areas correspond to the models which best match molecules at (a) low [ATP] and (b) high [ATP] (analysis of low and high [ATP] data was performed by Dr. Tom Bilyard, and is not included in this thesis) [41]. Image adapted from Bilyard et al 2013 [41].

An analysis of EF_1 data showed that molecules at low [ATP], where the ATP binding is rate-limiting, were best fit by models with one kinetic parameter or one kinetic parameter with a time offset, and molecules at high [ATP], where the catalytic processes are rate-limiting, were best fit by models with two kinetic parameters or two kinetic parameters with a time offset[1] [41]. Figure 3.3 demonstrates that both dwells can be resolved in a single trace at intermediate [ATP], and the models which fit the data well for each dwell are consistent with those that best fit the data at both low and high [ATP]. However, the overlap between adjacent dwells in the case of intermediate [ATP] makes this analysis a worse estimate for the kinetics of the two

---

[1]The analysis at low and high [ATP] was performed by Dr. Tom Bilyard. The analysis at intermediate [ATP] was performed by Ashley Nord.

dwells than the low and high [ATP] data where the contribution of one of the dwells is negligible.

The above analysis, combined with further analysis by Bilyard et al [41] suggests the following mechanism for EF_1: the binding of an ATP molecule at the $0°$ position initiates an $85°$ rotation of the γ subunit to the catalytic dwell. Experiments by Panke et. al. [78] suggest that the torque during this rotation is constant at approximately 50pN nm. During the catalytic dwell, at least two processes occur, each lasting 0.2-0.4ms. It is assumed that these two processes are ATP hydrolysis and phosphate release, as in TF_1 [46]. The γ subunit then rotates the remaining $35°$ to dwell at the $120°$ position, where it awaits another ATP molecule. This process is qualitatively similar to TF_1 at room temperature, but the rates of rotation, ATP binding, and the combination of ATP hydrolysis and phosphate release are faster in the case of EF_1. Previous studies have recorded a third unknown process in TF_1 occurring during the rotation from the catalytic dwell to the ATP waiting dwell [52, 323], but this process has not been observed in EF_1.

3.2   Yeast F_1-ATPase

High resolution crystal structures have thus far only been achieved in mitochondrial F_1: structures exist for a number of different states of bovine F_1 [8,25,26,282,324–328] and for yeast F_1 in both the presence and absence of bound nucleotides [25, 26]. Insights into the behavior of F_1 from yeast suggest to what extent the extensive knowledge of TF_1 can be applied to mitochondrial F_1. YF_1 also allows a direct comparison between single-molecule rotation studies and high resolution crystal structures. The physiological temperature of *S. cerevisiae* is similar to that of *E. coli*, and much lower than that of thermophilic *Bacilius*, and YF_1 rotates at a maximum speed similar to EF_1, about five times faster than TF_1 [41, 46, 49].

A class of mutations called mitochondrial genome integrity (mgi) mutations, allow cells to survive losing their mitochondrial DNA [329–332] and have been shown to uncouple the flow of protons through the mitochondrial membrane from the synthesis of ATP [309]. These mutations do not simply inhibit the phosphorylation of ADP to ATP, but reduce the efficiency of ATP synthesis. These mutations have been mapped to the α, β, and γ subunits of ATP synthase, but the relationship between the effect of the mutations and the resulting phenotypes is unclear. Many mutant forms of yeast F_1 from *S. cerevisae* with mgi mutations have been created [309, 333], and crystal structures exist for four of these mutations [333]. These structures suggest two mechanisms by which mutations uncouple the yeast ATP synthase and identify crucial regions involved in the coupling process.

In this section, the behavior of wildtype mitochondrial F_1 from *S. cerevisiae* at varying [ATP] was investigated and the lifetimes of the ATP binding and catalytic states were quantified. Similar analysis was performed for seven forms of F_1 containing a single point mutation relative to the wildtype; for four of these mutations, the results are compared to high-resolution crystal structures. This analysis demonstrates the first observation of the kinetics of mitochondrial F_1, and it is one part of a larger collection of conclusive evidence that mitochondrial F_1 shares the same mechanism as mesophilic EF_1 and thermophilic TF_1 when investigated under the same conditions [41] [2]. This finally provides a platform to compare single-molecule data directly to high resolution structural data in F_1, both in wild type and mutants. The results are applicable to eukaryotic mitochondrial F_1, and hence to human medicine.

3.2.1   Michaelis-Menten kinetics

Gold beads of 60nm diameter (BBInternational) were functionalized with either neutravidin or streptavidin and attached to the γ subunit of surface-immobilized F_1 as

---

[2]Manuscript in preparation; Steel BC, Nord AL, Wang Y, Pagadala V, Mueller DM, Berry RM

depicted in Figure 2.3. Using the darkfield microscope in Section 2.3, multiple enzymes, each with a gold bead attached, were imaged onto the high speed camera simultaneously at frame rates of up to 30kHz. These experiments were performed by Dr. Bradley Steel. The position of each gold bead in each frame was determined using the Gaussian Mask algorithm described in Section 2.2, and an ellipse was fit to each trace. The data was automatically filtered as with the EF_1 analysis, described in Section 3.1, in order to choose traces where the bead was rotating and the trace was well characterized by an ellipse. Pauses in rotation were removed prior to analysis. For traces which showed three separate dwells, an MLE algorithm was used to fit kinetic models, and the quality of the fits was judged using BIC. These fitting methods, described in Section 2.2, were similar to those used for the EF_1 traces. The ability to record large fields of view containing many molecules and to automatically detect rotating molecules via their power spectral bias allowed for the collection of thousands of traces.

Seven forms of yeast F_1 containing a single point mutation with respect to the wildtype were investigated. One of the mutants, γG278D, contains a change at the C terminus of the gamma subunit, and is the yeast analog of the change found in human liver F_1 relative to that present in the heart. The other six mutants contain *mgi* mutations, converting *petite* negative yeast to *petite* positive, allowing yeast to survive the loss or deletion of mitochondrial DNA.

Figure 3.4 shows the speeds of wildtype F_1 along with the seven mutant forms for various [ATP]. All fit well to Michaelis-Menten kinetics, with the exception of βR401I, which shows a peak in rotation rate at intermediate [ATP] and a decrease in rotation rate at saturating [ATP]. The γG278D mutant is, within error bars, indistinguishable from the wildtype enzyme. The six *mgi* mutants are characterized by a significant reduction in the maximum rotation speed, on the order of 2 to 7 times slower than wildtype. At low [ATP], the rotation rate is only slightly affected.
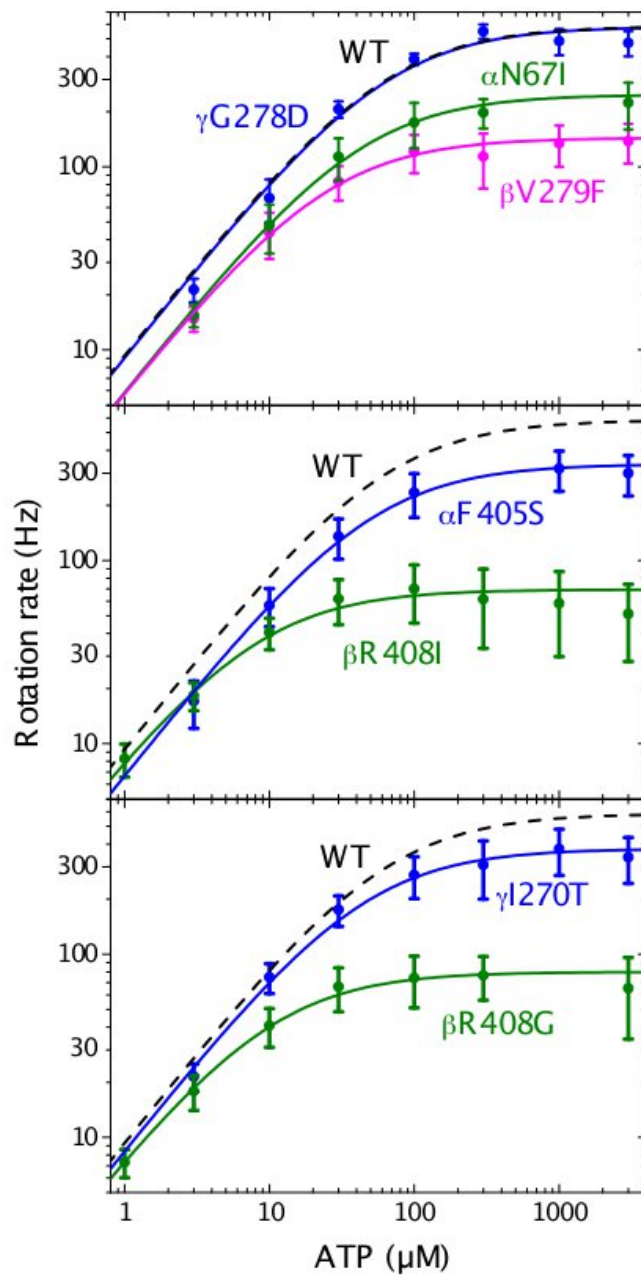
Figure 3.4: Rotation speed of wildtype yeast F_1 and seven mutant forms of yeast F_1 as a function of ATP concentration. Error bars mark the standard deviation of observed speeds, and Michaelis-Mentin fits are shown as a solid line. The bottom two graphs show the wildtype curve as a dashed line for reference. While γG278D is indistinguishable from the wildtype enzyme, the other mutants show reduced maximum rotation speed. All the mutants are well fit by a Michaelis-Mentin kinetics model with the exception of βR401I, which shows a decrease in rotation rate at maximum [ATP].

3.2.2 YF$_1$ kinetic analysis

The kinetics of the dwell states were investigated at low, intermediate, and high [ATP] for the wildtype enzyme and each of the mutants. Figure 3.5 shows a single wildtype molecule exhibiting typical behavior at low, medium, and high [ATP]. This recording was made in a tunnel slide where the buffer was easily exchanged using tubes into and out of the tunnel, called a flow slide. Flow slides were used in order to vary the ATP concentration over time. Consistent with the model of TF$_1$ rotation, at low ATP, most wildtype molecules showed three discrete dwells corresponding to the ATP waiting dwell. At high ATP, most molecules showed three discrete dwells corresponding to the catalytic dwells. At intermediate ATP, many molecules showed six dwells, where both the ATP binding and the catalytic dwells were able to be resolved.

For TF$_1$, the ATP binding and catalytic dwells dwells are about 40° apart [46,66], with little measured variation in this separation (39.1 ± 1.7°, n = 15 dwells) [66]. In contrast, yeast F$_1$ demonstrated significant variation in the measured angles between these two dwells. Some molecules showed three broad peaks, likely signifying that the two dwells were too close to individually resolve, and others showed six discrete peaks where the distance between the two dwells was larger than 40°. In order to quantify the distance between the ATP binding and catalytic dwell, the three dwells of individual molecules were measured at both low [ATP] and high [ATP] within a flow slide. This experiment is equivalent to measuring the position of six peaks at intermediate [ATP], but eliminates any bias that would come from overlapping or unresolved peaks. An analysis of 18 molecules (54 dwells) yielded a separation of 33° ± 19°. The reason for the increased variation seen in YF$_1$ is unknown.

The histograms of dwell times for wildtype YF$_1$ showed that, at saturating [ATP], the molecules were well fit by a short time offset (0.13 ± 0.06ms) and a double kinetic rate (2.5 ± 1.2ms^{-1} and 4.3 ± 2.3ms^{-1}). At low [ATP] (3-10μM), molecules were well
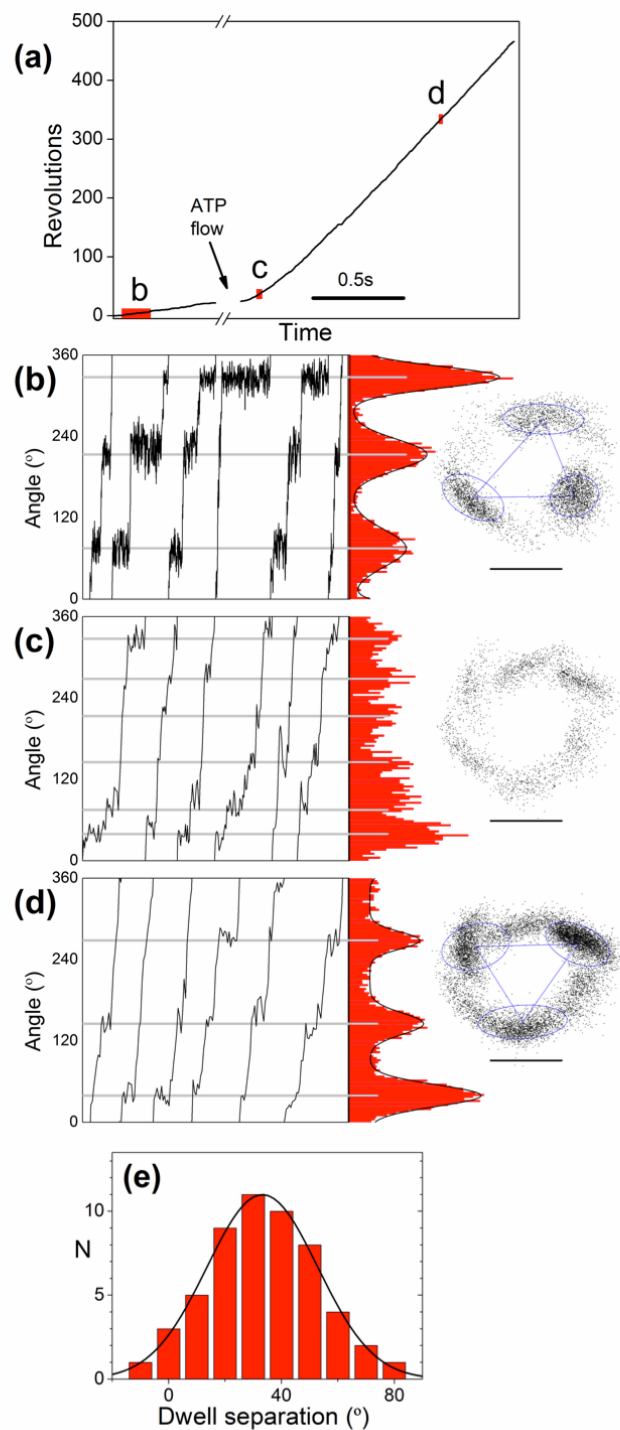
Figure 3.5: One wildtype yeast F_1 molecule observed at low, intermediate, and saturating ATP concentrations. a) The time course of the molecule, where the time frames shown in (b-d) are highlighted in red. While the ATP concentration as a function of time is not shown, b) shows low [ATP], c) intermediate [ATP] and d) saturating [ATP], after the rotational speed has stabilized. The scale bar marks 40nm. e) A histogram of 48 dwell angle separations, observed from 16 molecules, and a least squares Gaussian fit to the histogram.

111

fit by a double kinetic rate model with one ATP dependent rate ($18 \pm 6\mu\text{M}^{-1}\text{ms}^{-1}$) and one ATP independent fast rate ($1.8 \pm 1.2\text{ms}^{-1}$). This fast rate is consistent with being due to the combination of processes occurring at saturating ATP, and is likely combined into one kinetic rate because of less data due to the dominance of the ATP dwell. Dwell distributions of a composite of 15 molecules at both low and saturating [ATP] are shown in Figure 3.6. These results suggest that the fundamental kinetics of yeast F_1 are similar to that of TF_1 and EF_1: there is one ATP dependent process which occurs at the ATP binding angle and two ATP independent processes which occur at the catalytic dwell angle, separated by an angle of 30°-40°. Given the similarity of behavior to TF_1, the processes which occur at the catalytic dwell angle can likely be ascribed to ATP hydrolysis and phosphate release. In yeast, a short time offset, likely due to bead rotation, was also observed. This offset was observed for EF_1 [41], but not for TF_1, though it's likely that in the later case, less drag (due to a 40nm rather than 60nm bead) and a slower framerate meant that the experiments lacked the time resolution to observe a potential time offset due to bead rotation [26, 46].

A similar kinetic analysis was performed on the dwell time histograms for each of the mutants, and the results are shown in Table 3.1. The γG278D mutant is, within error bars, indistinguishable from the wildtype enzyme for both the Michaelis-Menten fits and the dwell analysis. The observed ATP binding rate was fastest in wildtype, though the reduction of the ATP binding rate was only significant (95% confidence interval) with three of the mutants. These forms were βV279F, αN67I, and αF405S, and the ATP binding rate was about 2/3 that of wildtype. For the *mgi* mutants, while one of the processes occurring in the hydrolysis well remained relatively unchanged from wildtype, the other was slowed by 2 to 5 fold. Thus, *mgi* mutations seem to have a strong effect on either the rate of ATP hydrolysis or phosphate release, but little effect on the rate of ATP binding.
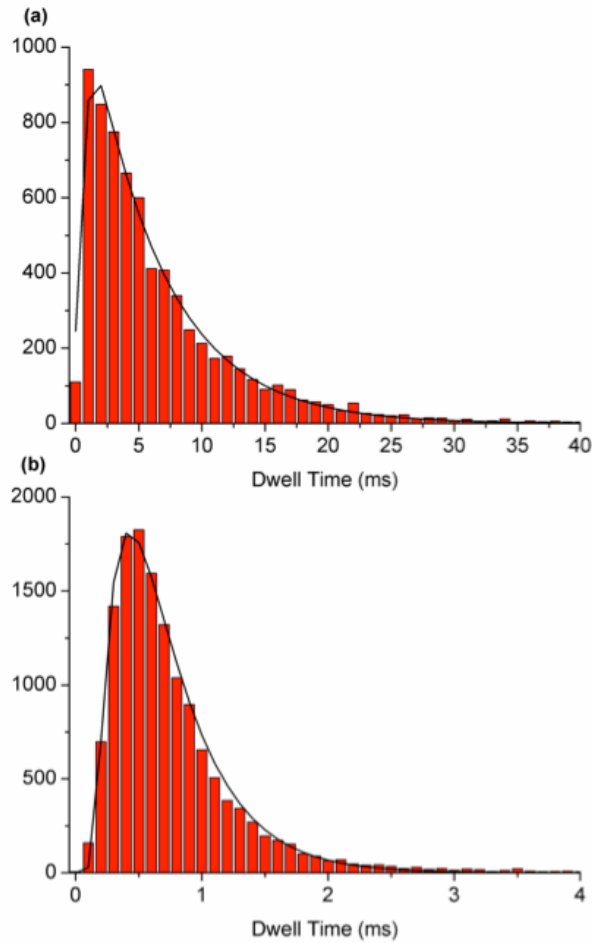
Figure 3.6: Dwell distributions for a composite of 15 wildtype molecules each at a) low (10μM) ATP and b) saturating 3mM ATP. The composite of 15 low [ATP] traces is well fit by a double kinetic rate, and the composite of 15 saturating [ATP] molecules is well fit by a double kinetic rate with a time offset.

Data collected from the βR408I mutant showed a clear difference at saturating ATP from wildtype. At 3mM [ATP], the rate of ATP binding is approximately 80ms^{-1}, which is unresolvable given the frame rates used. One would thus expect to see three discrete dwells at the hydrolysis angles. Instead, six dwells are observed in the majority of high quality traces in both intermediate and saturating [ATP]. Examples of such traces are shown in Figure 3.7. Although these dwells are not typically present at high [ATP] for the other forms of F$_1$ investigated, more subtle

113

Form	*mgi* Class	Michaelis-Menten fits				Dwell Analysis			
		v_{max} (revs s^{-1})	k_M (μM)	k_{ATP} ((ms)$^{-1}$ μM^{-1})	n	k_{ATP} ((ms)$^{-1}$ μM^{-1})	k_2 ((ms)$^{-1}$)	k_3 ((ms)$^{-1}$)	n
Wildtype	–	586±24	62±9	28.3±3.6	2177	18±6	2.5±1.2	4.3±2.3	18, 36
γG278D	–	7582±137	63±33	27.6±10.2	89	26±2	2.8±2.1	3.4±1.3	2, 5
βV279F	I*	144±13	24±5	17.9±2.8	537	16±1	0.33±0.10	3.4±2.6	3, 9
αN67I	I*	248±47	41±12	18.0±2.6	432	15±2	0.34±0.10	3.2±7.3	6, 3
βR408G	II	80±11	10.0±2.6	24.1±4.0	439	19±5	0.20±0.05	1.7±2.1	15, 16
αF405S	II*	336±40	49±11	24±3.2	1044	15.9±6.1	0.66±0.52	2.5±2.1	58, 55
γI270T	I*	377±92	44±15	25.7±4.4	2190	21.9±5.2	0.77±0.48	2.5±2.0	103, 31
βR408I	II	69±13	7.9±2.5	26.4±4.7	6519	22±7	0.20±0.07	4.9±20	361, 57
Bacillus PS3	–	129±22	15±5	25.8					
E. coli	–	449±39	21.1±1.0	43±4					

Table 3.1: The results of the analysis from the Michaelis-Menten fits (performed by Dr. Bradley Steel) and the dwell time histogram analysis (performed by Ashley Nord) for wildtype and the seven mutants screened in these experiments. All values are quoted with 95% confidence intervals, with the exception of *Bacillus PS3* and *E.coli*, where the values were drawn from [46] and quote standard deviations. The number of traces used is denoted by n. For the dwell analysis, the first value of n corresponds to the number of traces used to calculate k_{ATP} and the second value for the number of traces used to calculate k_2 and k_3. High resolution structures exists for the *mgi* mutants with an asterisk after their class [333].

signatures occasionally appear in wildtype, βR408G, αF405S, and γI270T. Examples of such traces are also shown in Figure 3.7. Due to its short duration and variability in prominence, this state is difficult to characterize. It is clear that some process which occurs during the ATP binding dwell is significantly slowed in βR408I, and it may be the case that there is a fast but ATP independent process which occurs here in yeast F_1.
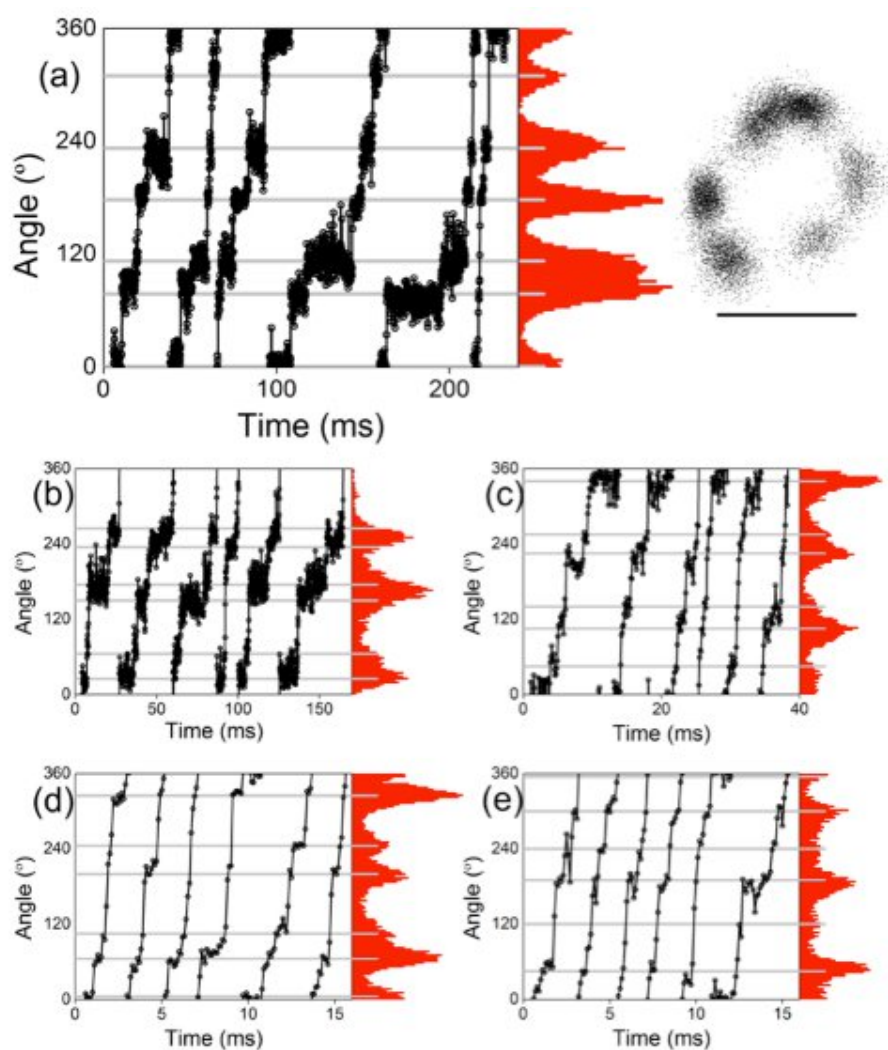
Figure 3.7: a) A typical trace of βR408I at saturating ATP showing six discrete dwells. b-e) Atypical traces of substeps at saturating ATP for b) βR408I (3mM ATP), c) α4505S (1mM ATP), d) wildtype (3mM ATP), and e) γI270T (3mM ATP).

The *mgi* mutants investigated for which crystal structures exist are αN67I (I), βV279F (I), γI270T (I), and αF405S (II), where the number in parentheses corresponds to the proposed mechanism of uncoupling. βR408G and βR408I have also been categorized as group II forms [309], though crystal structures are lacking. The single molecule data shows significant quantitative differences between these mutants and wild type. One notable feature is the contrast of the effect of the mutation at low and high [ATP]. While the ATP binding rate at low [ATP] is 70–100% that of wildtype, the rotation rates at high [ATP] are 15–50% that of wildtype. This suggests that the mutations may have a strong effect on the rate of ATP hydrolysis or phosphate release, but little to no effect on the rate of ATP binding.

It is hypothesized that the mutations present in the group I forms alter the empty catalytic binding site, where phosphate binding or release occurs, with little or no change to other nuclueotide binding sites. It is proposed that, during ATP synthesis, γ rotates without phosphate bound to the site, diminishing ATP synthesis and reducing efficiency [333]. The single molecule data shows a speed reduction of 1.5–4 fold at the hydrolysis dwell angle for the group I forms, with respect to wild type. Given the crystallographic data, this change may be due to the disruption of phosphate release from the enzyme. While these forms also demonstrate up to a 20% reduction in the ATP binding rate, this may be explained by the mutation disrupting the coordination between α/β and γ, which has been shown to reduce the ATP binding rate [334]. It is also possible that the structural changes needed to reduce the ATP binding rate by this amount are simply to small too be observed.

The mutations of the group II forms are hypothesized to reduce the steric hindrance of a region called the Catch 2 region of the β subunit, allowing rotation of the γ subunit with less impedance. This allows γ to slip past a catalytic site either before phosphate is bound to the empty catalytic site or before ADP is converted to ATP in the ADP bound catalytic site, resulting in lower efficiency of ATP synthesis [333]. In

the single molecule data, the group II forms demonstrate about a 2-5 fold increase in the dwell time at the hydrolysis angle, with a large change in one of the rate limiting process and a small change in the other. Given the crystallographic data, a potential candidate for this behavior is a disruption to communication between the β and γ subunits, causing a reduced ATP hydrolysis rate and a nearly unaffected phosphate release rate.

The above analysis, combined with further analysis by Steel et al[3], suggests that the rotation of yeast F_1 is governed by one ATP-dependent process located at the ATP binding dwell and two ATP-independent processes which occur at the catalytic dwell, located about 33° from the ATP binding dwell. Thus, the fundamental mechanism of YF_1 is similar to that of EF_1 and TF_1. This suggests that the extensive knowledge acquired characterizing the mechanochemical cycle of thermophilic F_1 is generally relevant to F_1 from eukaryotic sources. Of the six *mgi* mutants investigated, the qualitative behavior was similar in five of the forms. Kinetic analysis revealed that for these five mutants, one of the processes occurring at the catalytic dwell was slowed, while the other remained relatively unchanged. The sixth mutant showed this behavior in addition to a longer dwell at the ATP binding angle which was not ATP dependent. Further single molecule investigations are needed in order to conclusively demonstrate some of the preliminary hypotheses given above linking the single molecule studies with the structural data of the four mutants presented.

---

[3]Manuscript in preparation; Steel BC, Nord AL, Wang Y, Pagadala V, Mueller DM, Berry RM

Chapter 4

Speeds and Steps of the BFM

The rotational BFM data collected for this thesis includes over 10,000 seconds of recordings from over 800 BFMs at unprecedented spatial and temporal resolution. A small subset of this data will be discussed in this chapter, drawing preliminary yet novel inferences about the behavior of the BFM. Mining the entirety of this data set will be a very large task. Further analysis and additional experiments will be necessary to confirm the results presented below and will comprise a project separate from this thesis.

4.1 Speed and Stators

4.1.1 Only one stator at zero load

In 2008, Berg and colleagues investigated the speeds of 60nm gold beads stuck to the hooks of BFMs lacking flagellar filaments using a resurrection assay. Forward scattered light from the gold beads was collected and focused onto a pinhole in front of a photomultiplier tube, where it was sampled at 3kHz. Power spectra were computed

for consecutive 1s blocks of the data in order to calculate the rotational speed of the gold bead. Upon the induction of wild type MotA, non-rotating BFMs were observed to immediately begin rotating at about 300Hz. Unlike resurrection assays performed at high loads, the speeds of the motors did not continue to increase in a step-wise fashion, attributed to the addition of stators. Instead, the BFMs were reported to continue to rotate at 300Hz, with occasional toggles between 0Hz and 300Hz, which were attributed to transient attachment of stators to the motor. From these experiments, it was concluded that the maximum speed of the BFM at low load was independent of the number of active stators [216]. This important conclusion instigated a revamp of multiple models of the BFM which had previously predicted the speed of the motor to increase [272] or decrease [271] with additional stators at low load. Figure 4.1 shows the results of these low load resurrection experiments.
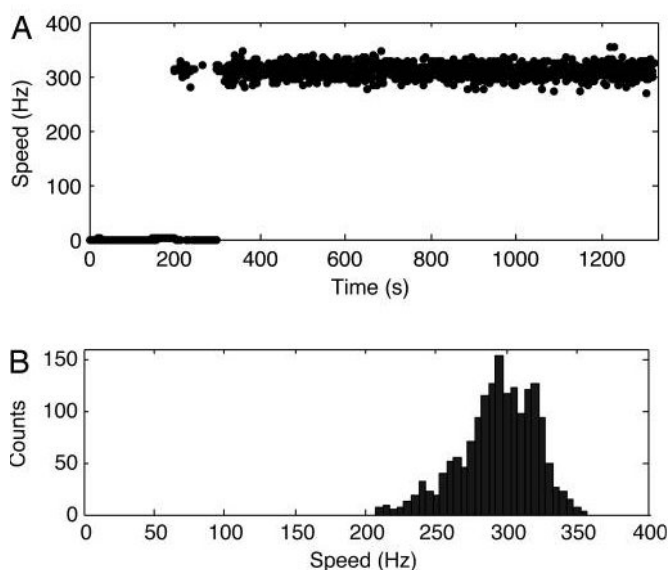
Figure 4.1: A) Speed as a function of time of a 60nm bead attached to a hook of a BFM lacking a flagellar filament after induction of MotA. The speed of the BFM goes from 0Hz to 300Hz immediately, sometimes transiently toggling between 0 and 300Hz. The speed of the BFM does not increase beyond 300Hz, even at high induction. B) A histogram of the speeds of 40 separate 60nm gold spheres attached to BFMs at high induction. In these experiments, forward scattered light was imaged onto a pinhole in front of a photomultiplier tube, where it was sampled at 3kHz. Power spectra were computed for 1 second blocks, and the resulting speed versus time plot was median filtered with rank 4. Image adapted from Yuan and Berg, 2008 [216].

119

In 2013, Berg and colleagues performed a set of experiments where the viscous load on a BFM was changed by a large factor while monitoring the motor speed both before and after the load increase. From the initial speed after the load change, it was inferred that motors with very low loads are driven by one or at most two stators. The conclusion of these experiments was that stators appear to act as dynamic mechanosensors [227]. This result appears to negate the conclusion from the 2008 experiments; thus, how motor speed at low load varies with the number of stator units is yet unknown.

4.1.2 Multiple stators at zero load

The two sets of experiments mentioned above were performed on BFMs with wild type motors. Similar experiments were performed on both chimeric and wild type motors for this thesis. The experiments differed from those of Berg and colleagues in four ways:

1. 100nm gold beads, instead of 60nm beads, were attached to the hooks of BFMs.

2. The scattered light from the gold beads was imaged onto a high speed camera or QPD instead of onto a pinhole in front of a photomultiplier tube.

3. The rotation of the bead was sampled at either 109kHz or 20kHz, as opposed to 3kHz.

4. For wild type cells, the gold bead was attached to the hook using a biotin streptavidin link instead of antibodies.

With the exceptions listed above, great care was taken to reproduce the protocols of Berg and colleagues, facilitated by personal communication with members of the lab. Every step of the protocols was carried out in the manner of Berg and

colleagues; the chemicals were purchased from the same suppliers, as were the glass slides, coverslips, and double sided tape used to construct the tunnel slides.

Nonetheless, in the experiments performed for this thesis, the speeds of the BFM deviated from those previously observed by Berg and colleagues. Figure 4.2 shows two histograms of speeds from wild type BFMs. Figure 4.2a) is composed of recordings acquired at 109kHz on the high speed camera where the speed is averaged over an entire revolution. This averaging was chosen in order to eliminate potential artifacts within a single revolution, such as the gold bead interacting with the cell surface lipopolysaccharides at a particular angle. Figure 4.2b) is composed of recordings at 20kHz on the QPD where speeds were calculated from the powerspectrum and averaged over 1 second blocks at 0.05s intervals. Averaging over 1s was chosen to match the analysis previously performed on wild type at low load [216]. As these histograms show, multiple speeds were observed in the BFM at low load, possibly due to varying numbers of stators in the motors. Within errors, the speeds are the same between the high speed camera and QPD recordings, as expected. Despite much effort over two years to ensure the protocols of Berg and colleagues were exactly duplicated, these results differ both in the number of speeds observed and in the maximum speed.

The traces shown in Figure 4.2b were sampled at 20kHz and averaged over 1 second blocks spaced 0.05s apart. In order to determine if the discrepancy between this data and that of Berg and colleagues was due to different sampling rates, this data was downsampled to match the resolution of Berg and colleagues. That is, 20kHz was downsampled to 3.3kHz by retaining every 6th sample, the speed was computed from a power spectrum of consecutive 1 second blocks, and the speed versus time traces were rank 4 median filtered. The results of this analysis are shown in (a) of Figure 4.3. This distribution is still distinctly different from that presented by Berg and colleagues, suggesting that the difference in observed distributions is not due to sampling rate. When the traces in Figure 4.2b are selected by eye for those
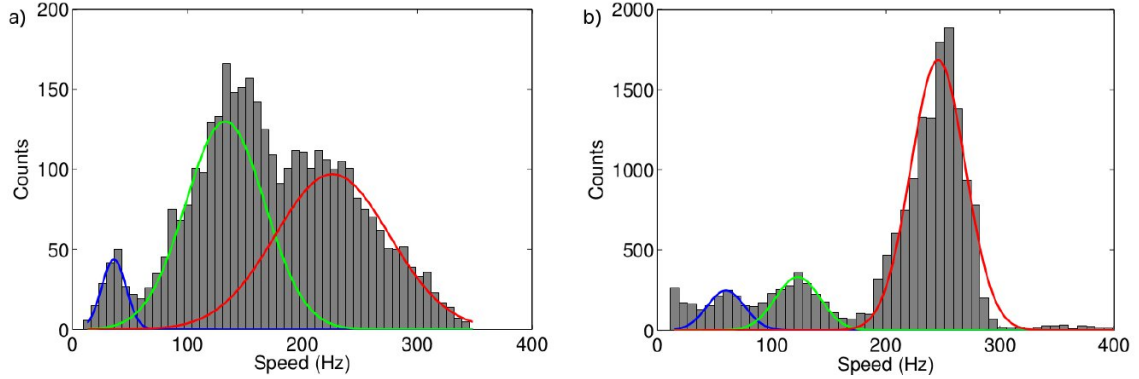
Figure 4.2: Two histograms showing the speeds of wild type *E. coli* BFMs. a) A histogram of the speeds of 100nm gold beads attached to BFM hooks, sampled at 109.5kHz onto a high speed camera. The speeds were calculated over entire revolutions of the bead. As three distinct speeds are observed in the histogram, three Gaussians were fit to the distribution, centered on 36Hz (blue), 133Hz (green), and 226Hz (red). There are 17 traces included in this histogram, where the selection criterion was an elliptical bead trajectory. b) A histogram of the speeds of 100nm gold beads attached to BFM hooks, sampled at 20kHz onto a QPD. The speeds were calculated from the power spectra of 1 second blocks spaced 0.05s apart. Three Gaussians were fit to the distribution, centered on 56Hz (blue), 123Hz (green), and 246Hz (red). There are 21 traces included in this histogram, where the selection criterion was motors that were spinning for at least 20% of the recording. To within error, these speeds match those of the high speed camera recordings.

that demonstrate stable spinning at maximum speed, incorporating approximately one third of the traces, the resulting histogram is shown in Figure 4.3b. While the maximum speed is still about 50Hz less than that observed by Berg and colleagues, this distribution is otherwise similar.

Figures 4.4 and 4.5 show histograms of speeds from chimeric *E. coli* BFMs, recorded by the high speed camera and the QPD, respectively. For the high speed camera data, speeds were measured in six different SMF conditions by controlling both the sodium concentration and the pH of the motility medium. This data shows two distinct speed populations in four of the six SMF conditions, presumably due to motors with one and two stators. Three of these SMF conditions (1mM, 10mM and 30mM[Na$^+$], pH 7.0) can be compared to previously published values for low load
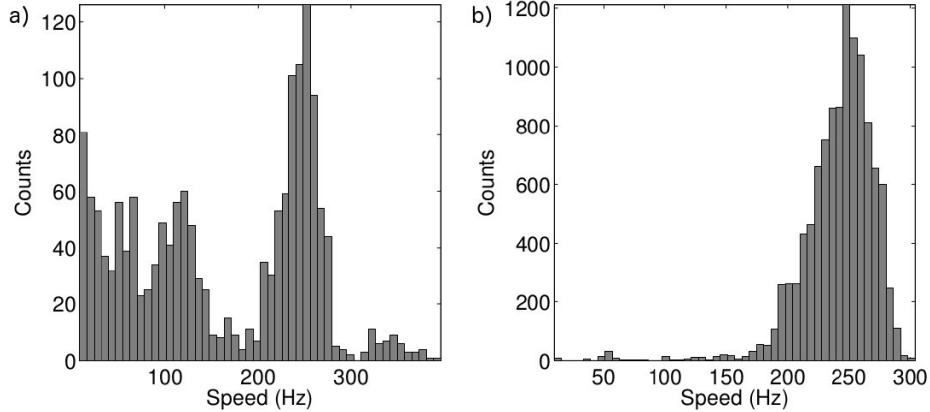
Figure 4.3: Two histograms showing the speeds of wild type *E. coli* BFMs. a) The same 21 traces from Figure 4.2b are represented here. The 20kHz traces were downsampled to 3.3kHz traces, the speeds were calculated over 1s consecutive blocks, and the speeds were then rank 4 median filtered. While this analysis matches that performed by Berg and colleagues [216], the distribution is distinctly different from that shown in Figure 4.1. b) Of the 21 traces shown in Figure 4.2b, 6 demonstrating relatively stable speed at maximum speed were chosen for this histogram. This distribution resembles that acquired by Berg and colleagues. This distribution does not change significantly if the 6 traces are each downsampled (not shown).

single stator speeds, and they are consistent [210]. The QPD traces were acquired for a single SMF condition (20mM, pH 7.0), and while it shows the same speeds, within errors, as the high speed camera data acquired for the same SMF, the QPD data also shows a third distinct population.

Figure 4.6 plots distinct speeds observed in the chimeric motor against each other for each SMF condition. It has been assumed that these distinct states correspond to one and two stator motors (with the speed of a motor with two stators higher than that with one stator). As with all previous resurrection experiments, the number of stators is an assumption based upon the observation of discrete changes in speed. The best fit line to the points in Figure 4.6, denoted by a red line, is 2.79 ± 0.04. The blue line, which shows the best fit line passing through the origin, has a slope of 2.49 ± 0.06. This result is distinct from the behavior of the BFM at high load, where the speed of the motor with two stators is twice that with one [173, 226]. This result also
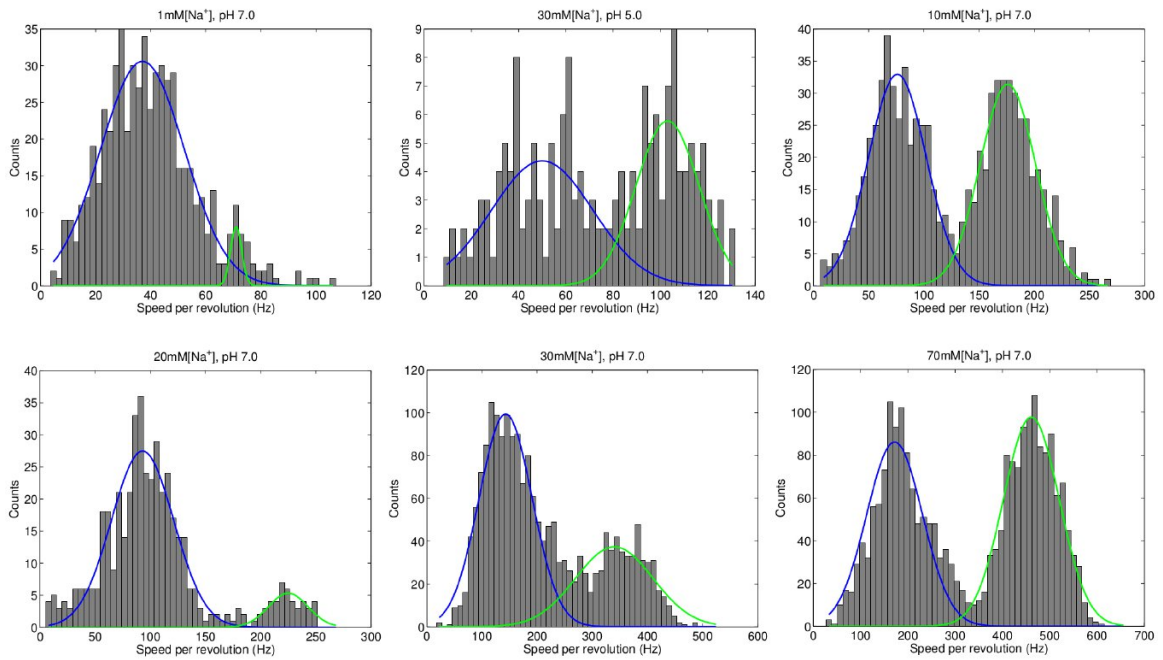
Figure 4.4: Histograms showing a total of 82 high quality 109.5kHz traces of 100nm gold beads attached to chimeric *E. coli* BFMs. Six different SMF conditions were used, and each histogram is labeled by the sodium concentration and pH of the motility medium. The speeds were calculated over entire revolutions of the bead. As two clearly distinct speeds are observed in four of the six histograms, two Gaussians were fit to each of the six distributions, assuming continuity. The distinct speeds potentially represent motors with one and two stators. The speeds for each histogram are as follows: 1 mM [Na$^+$] pH 7.0, 37Hz and 71Hz ; 30 mM [Na$^+$] pH 5.0, 50Hz and 103Hz; 10 mM [Na$^+$] pH 7.0, 76Hz and 176Hz; 85 mM [Na$^+$] pH 5.0, 93Hz and 225Hz; 30 mM [Na$^+$] pH 7.0, 143Hz and 340Hz; 85 mM [Na$^+$] pH 7.0, 172Hz and 461Hz.

fails to match the predictions of sublinear torque at low load made by Wingreen and colleagues [274]. However, this analysis is based upon only a few short recordings at each SMF, and longer QPD traces at each SMF are necessary.
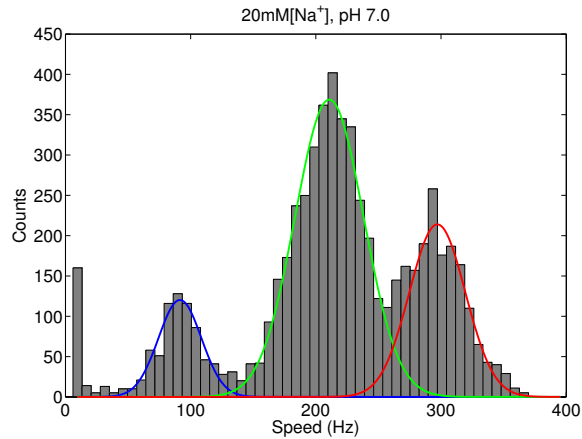
Figure 4.5: A histogram of the speeds of 100nm gold beads attached to chimeric *E. coli* BFMs at pH 7.0 and 20mM[Na$^+$]. The histogram is composed of 7 traces lasting approximately 2 minutes each, sampled at 20kHz, with speeds calculated from the power spectrum of 1s consecutive windows spaced 0.05s apart. The first and second Gaussians show the same speeds, within errors, as the Gaussians for the same SMF condition in Figure 4.4. In this case, a third distinct speed population is present. There were no differences in the experimental conditions, only in the length of time the BFM's were recorded. The Gaussians are centered at 91Hz (blue), 210Hz (green), and 297Hz (red) respectively
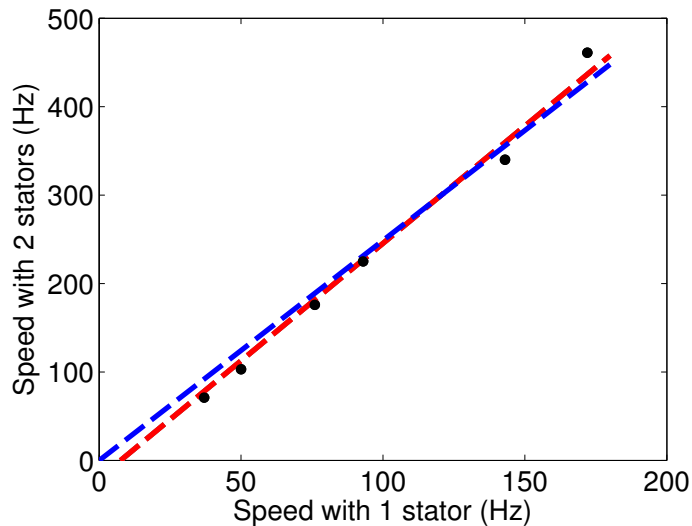
Figure 4.6: A graph of the speeds of the chimeric motors from each SMF represented in Figure 4.4. The vertical axis represents the two stator motor speeds, and the horizontal axis the one stator speed for the same SMF. The points are well fit with a line of slope 2.79 $\pm$ 0.04, shown in red. Forcing a line through the origin, the points are fit by a line of slope 2.49 $\pm$0.06, shown in blue. This differs from BFM behavior at high load, where stators contribute equally to motor speed.

4.1.3 Types of speed changes

The QPD allowed for long traces of motor rotation to be recorded at 20kHz. Often, motors appear to rotate continuously at a stable speed for hundreds of seconds. However, Figure 4.7 and Figure 4.8 show two typical traces each of wild type and chimera motors, respectively, where the motor demonstrates multiple discrete changes of speed during the recording. A histogram of the speeds within each trace is shown on the side. Speed populations were divided by eye, and horizontal lines were drawn on the trace marking the average speeds of each population. Such traces argue for two novel ideas which will be expanded upon below. Firstly, if we assume that such speed transitions are attributable to changes in stator number, it appears the speed of the motor increases with increasing stator number, as in high load experiments. Secondly, transient 'toggling' between zero and non-zero speeds is not always due to a loss of a stator unit, as proposed by Berg and colleagues.

Figures 4.7 and 4.8 show multiple speed transitions. Theses transitions are presumed to be due to the loss or gain of a stator units, as in resurrection studies[1]. Apart from similarity to behavior at high load, there is no obvious reason to argue that an increase in speed is due to the gain of a stator rather than the loss of a stator. In fact, the original model of Xing and colleagues proposed that at low load, additional stators interfere with one another and impede motion of the rotor. Figure 4.9 shows multiple angle versus time traces during the presumed loss or gain of a stator. These traces are sections of the top trace shown in Figure 4.8, and the times can be used to locate the corresponding velocity change in the trace. As shown in the x,y traces of Figure 4.9, the trajectory of the bead is not an ellipse; there is a cusp on one side of unknown origin. It may be the case that the hook undergoes a transition at this angle, possibly driven by the bead hitting the surface of the cell. Such trajectories

---

[1]However, there is no proof that such transitions are due to stators, and it remains possible that such transitions have nothing to do with stators. For want of a better hypothesis, this chapter assumes that transitions between discrete speeds occur when a stator is lost or gained.
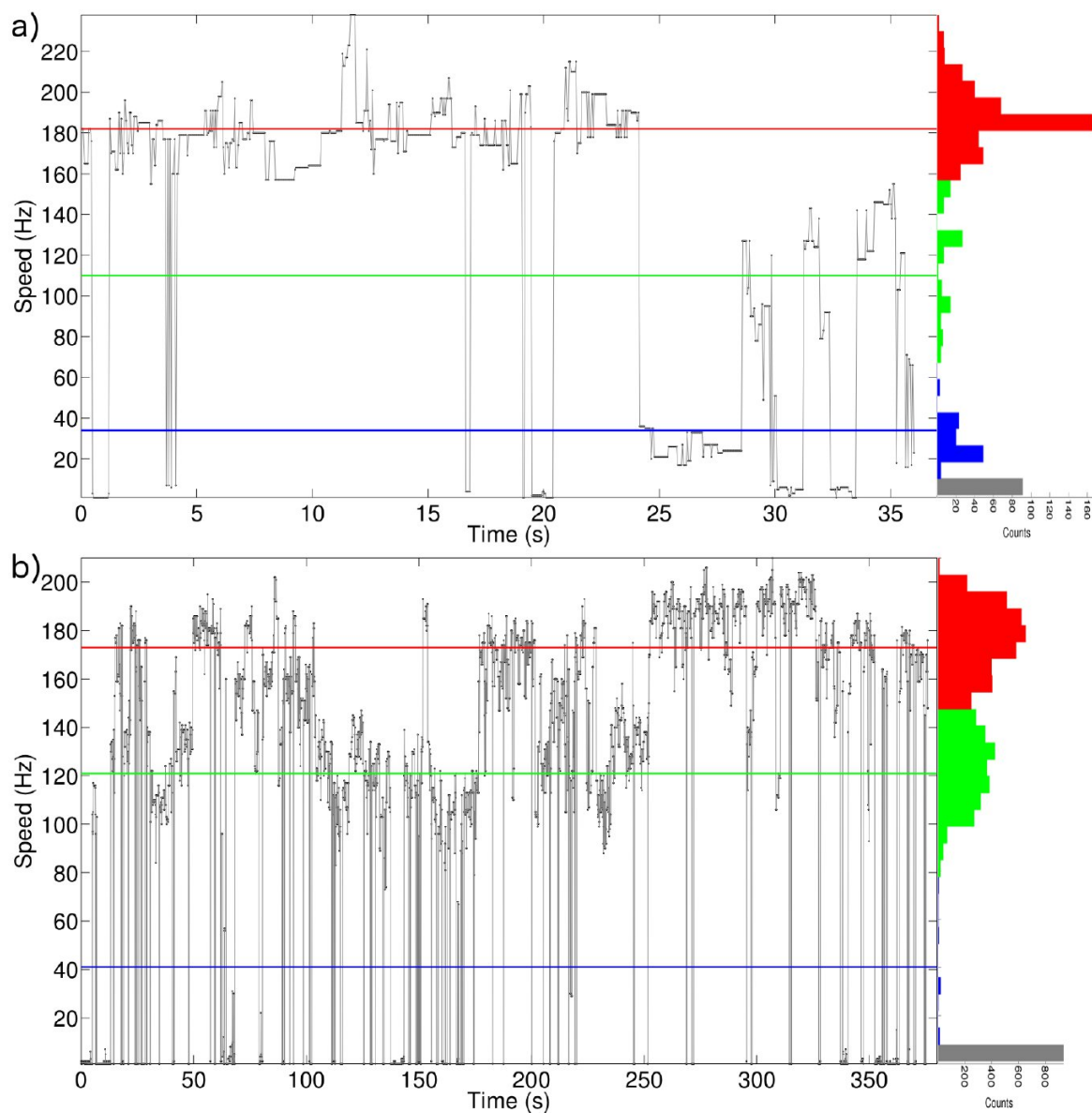
Figure 4.7: Two velocity versus time graphs of a gold bead stuck to the hook of a wild type motor, with the corresponding speed histograms to the right. These traces were chosen because they show multiple discrete changes of speed, presumed to be the gain and loss of stators. The blue, green, and red horizontal lines represent discrete speed levels, and are simply the average of populations separated by eye. These speed levels potentially correspond to one (blue), two (green), and three (red) stators driving the motor. These traces were sampled at 20kHz, and the speeds were determined from power spectra of 1s blocks spaced 0.05s apart.
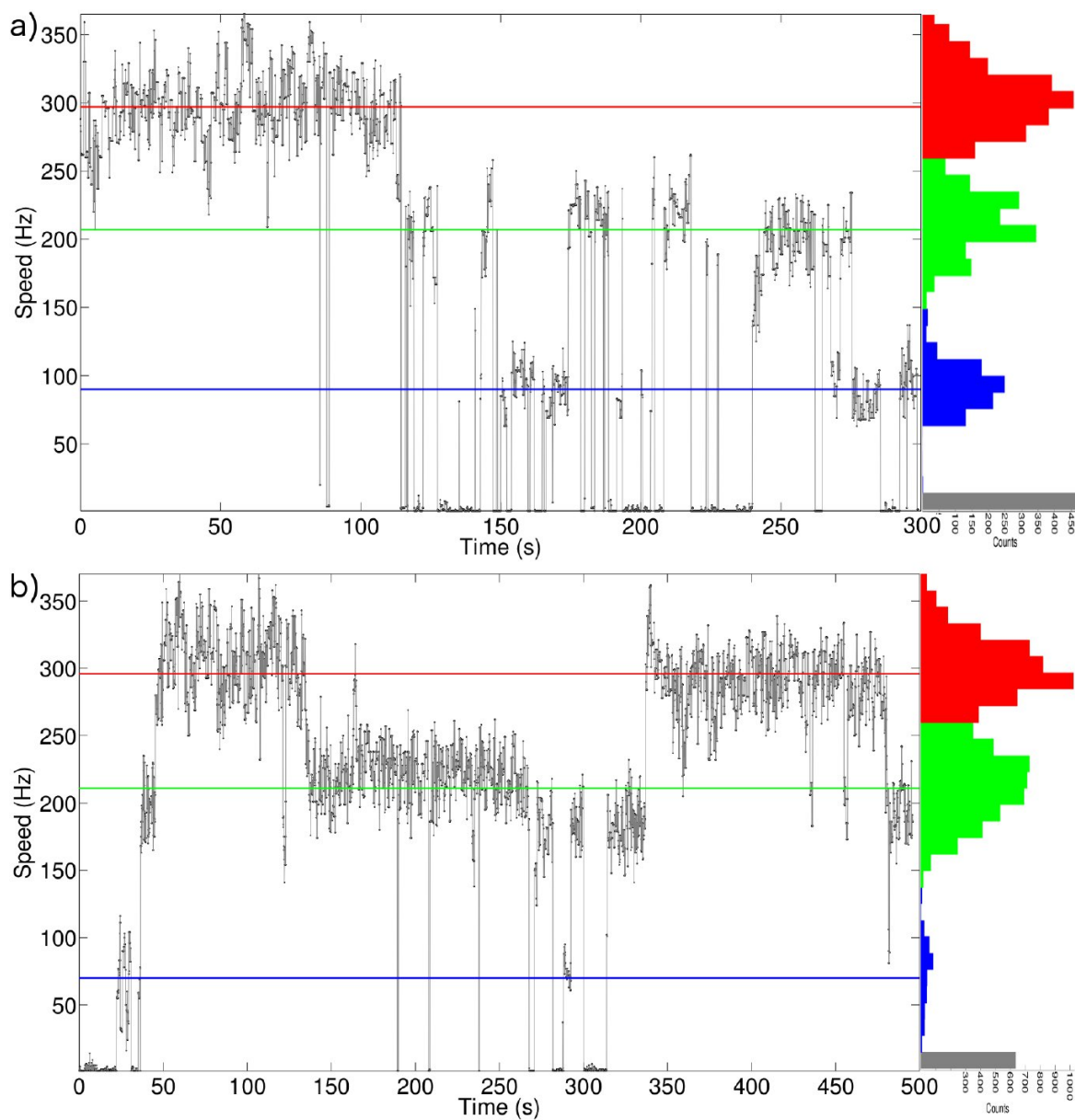
Figure 4.8: Two velocity versus time graphs of a gold bead on the hook of a chimeric motor at pH 7.0, 20mM [Na$^+$], with the corresponding speed histograms to the right. These traces were chosen because they show multiple discrete changes of speed, presumed to be the gain and loss of stators. The blue, green, and red horizontal lines represent discrete speed levels, and are simply the average of populations separated by eye. These speed levels potentially correspond to one (blue), two (green), and three (red) stators driving the motor. These traces were sampled at 20kHz, and the speeds were determined from power spectra of 1s blocks spaced 0.05s apart. Figures 4.9–4.10 below correspond to subsections of the top trace here.

are not uncommon. The cusp causes a wiggle in the angle versus time traces, and the analysis below avoids analyzing data from angles near this wiggle. Nonetheless, Figure 4.9 shows that, with the exception of speeding up or slowing down, the presumed change in stator number leaves no mark in either the angles versus time traces or the x versus y traces.

When all stators leave a motor, a motor is expected to be free to do unrestrained Brownian motion. If, as Berg and colleagues propose, the transient 'toggles' in speed from zero to max speed are due to transient stator attachment, the periods of zero velocity should demonstrate free Brownian motion. Some examples of such 'toggles' in the motor speed are shown in Figure 4.10. These traces are again drawn from the corresponding time periods in the top trace of Figure 4.8. Using the diffusion coefficient for a 100nm bead calculated from Fick's laws, a bead doing free Brownian motion should complete a revolution in about 0.01s. The 'toggle' periods of zero velocity shown in Figure 4.10, while they vary in appearance and duration, are not characteristic of free Brownian motion. Therefore, instead of transient detachment of the stator(s), these events seem to represent the motor in a transiently 'jammed' or restricted state.

Twenty five periods of zero velocity, similar to those shown in Figure 4.10, were selected for analysis from the top trace of Figure 4.8. Non-overlapping segments were used to plot the mean squared displacement of the bead versus time. Of the 25 periods analyzed, 17 were qualitatively similar to the trace shown in Figure 4.11a), and 7 were qualitatively similar to Figure 4.11b). Trace (a) seems to represent a bead initially diffusing, then trapped within a potential well. Trace (b) seems to represent a bead initially diffusing, then continuing to diffuse at a slower rate. The initial diffusion rates from those in group (a) are indistinguishable from those in group (b); this initial diffusion coefficient is $103 \pm 61 \frac{rad^2}{s}$, which is about 15 fold slower than that of free Brownian motion of the bead. This may suggest significant interaction
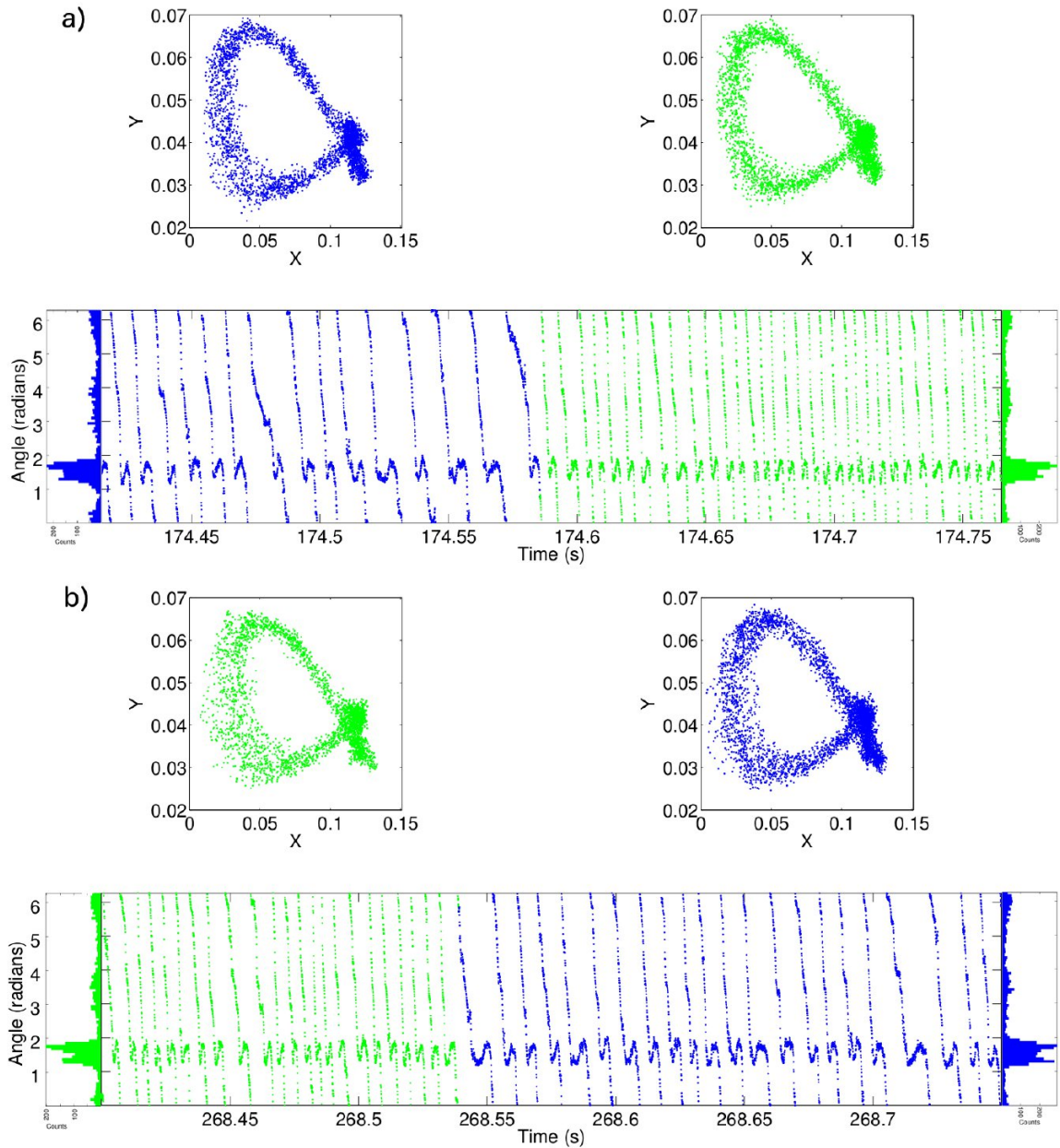
Figure 4.9: Two separate angle versus time graphs for portions of the top trace in Figure 4.8. a) An increase in speed, attributed to a stator gained. b) a decrease in speed, attributed to a stator lost. Blue portions represent a lower speed, presumably one stator, while green portions represent a high speed, presumably two stators engaged with the motor. Histograms on each side show the distribution of motor angle for respective sections. The x versus y traces show the position of the bead for each portion. These traces show that events involving a distinct change in speed, attributed to the gain or loss of a stator, show no other sign of disruption. The wiggle in the angle versus time traces is due to the cusp seen in the x versus y traces. The cause of this feature is unknown, but may be due to interaction between the bead and the cell surface.

130
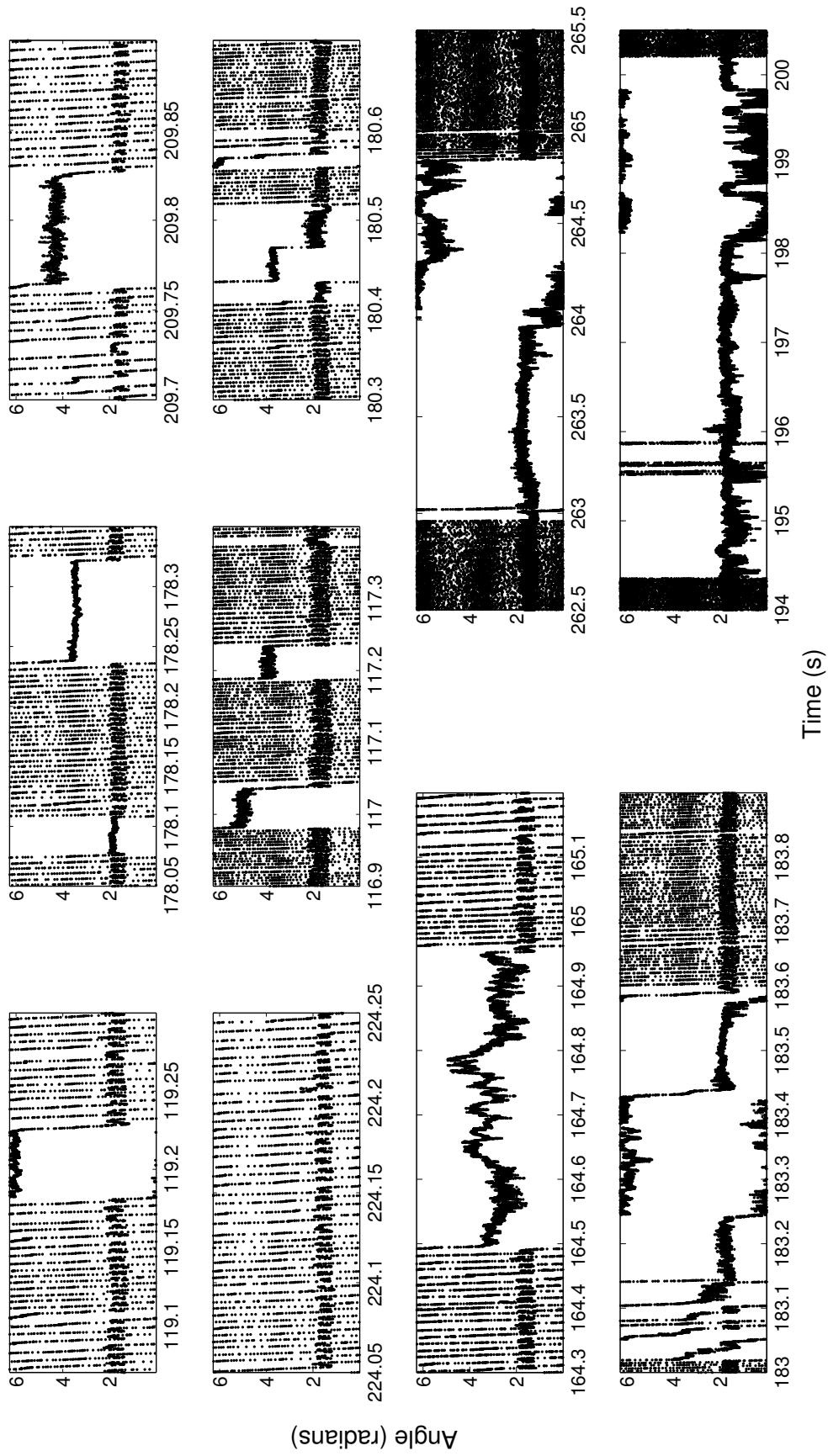
Figure 4.10: Graphs of angle versus time from various sections of the top trace in Figure 4.8 where the motor displays 'jammed' or restricted behavior as the speed goes to zero. In the episodes shown here, the motor dwells at certain angles longer than normal, but continues to rotate in between such sticking points. These traces were sampled at 20kHz with no filtering.

between the gold bead and the cell surface lipopolysaccharides. For those in group (a), the average size of the potential well is 0.2 ± 0.1rad. The periods within group (b) were all in the lowest distinct speed immediately prior to the 'toggle', while those of group (a) came from any of the three distinct speeds immediately prior to the 'toggle'. While these results and characterizations are very preliminary, one hypothesis is that periods similar to group (a) represent a motor becoming 'jammed' for an unknown reason, potentially due to a stator which stops working and becomes a spoke in the motor. Group (b) could potentially represent periods where the one stator that was previously driving the motor has fallen out. However, if this is the case, it would be necessary to explain a resulting diffusion coefficient that is much slower than predicted for a bead attached to a free motor.

Examining Figures 4.7 and 4.8 again, speed change events fall within a few categories. There are discrete increases or decreases in non-zero speed, where the speed of the motor only increases or decreases to the closest distinct speed level. There are sudden 'toggles' from spinning to zero speed, which are characterized by 'jams', where the motor is confined to a potential well. These events are always followed by one of two scenarios: either the motor returns to the same speed as before, or the motor returns to one distinct speed lower. One interpretation of this may be that when a motor returns from a 'jammed' state, it is either the case that it has retained all the stator units during the jam, or one stator has left the motor during the jammed period. Sometimes, motors in the lowest distinct speed suddenly 'toggle' to zero speed, and the motor continues to diffuse slowly, rather than remaining trapped within a potential well. Motors in higher speed states are not observed unless either, 1) the motor first passed through lower speed states, or 2) the motor was already in the higher spinning state immediately before a 'jam'. This seems to provide an argument for additional stators causing increases in speed rather than decreasing motor speed.
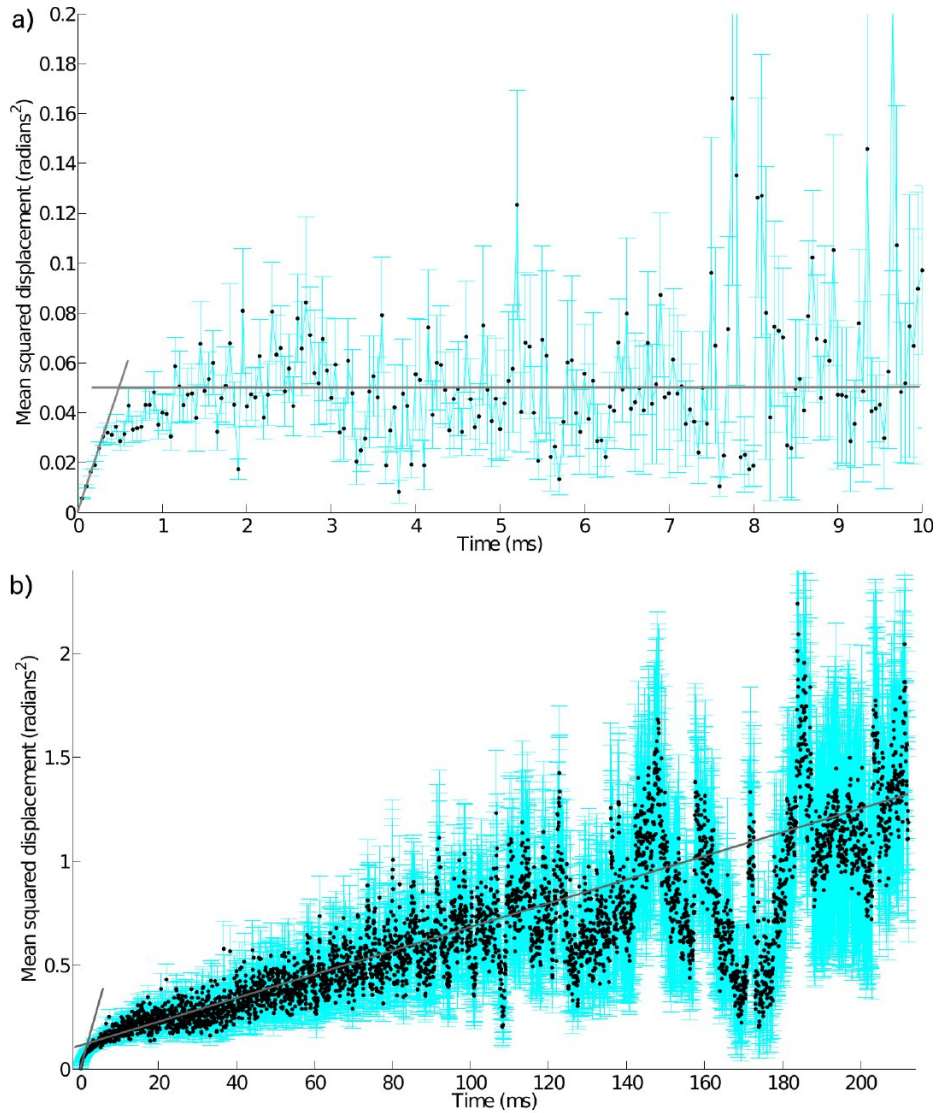
Figure 4.11: Mean squared displacement versus time of a 100nm gold bead attached to the hook of a BFM during two separate 'toggle' periods of zero velocity. The mean squared displacement values, denoted by black points, were calculated over non-overlapping windows of an angles versus time recording sampled at 20kHz by the QPD. The cyan error bars represent the standard error in each mean. Of 25 'toggle' periods extracted from the top trace of Figure 4.8, 17 were qualitatively similar to the trace shown in (a), and 7 were qualitatively similar to the trace shown in (b). The grey lines are best fit lines to two segments of the traces, separated by eye. The initial diffusion rates, represented by the first grey line in each trace, were similar for traces in both groups. This initial diffusion coefficient, calculated over all 25 periods, was $103\pm 61\frac{rad^2}{s}$, about 15 fold slower than theoretical free Brownian motion of a 100nm bead. After the initial diffusion, (a) seems to be trapped within a potential well, and (b) continues to diffuse, albeit at a slower rate.

133

Figures 4.12 and 4.13 illustrate these categories of speed changes by comparing the speed of one 1s block to the very next block for both wild type and chimeric BFMs. In Figure 4.12, the grey lines separating the graphs into a grid indicate the transition between stators. The values for these lines were drawn from one half the lowest distinct speed, then half way between each of the next two distinct speeds. The grey points, comprising most of the points in the graph, represent no change in the number of stator units in the motor. Blue and green points represent the loss or gain of a stator, respectively. In order to define a change in the number of stator units, the speeds of adjacent blocks had to fall within separate portions of the grid, and their difference had to be greater than one half the difference in speeds of their respective speed populations. Jams of the motor were defined as any speed less than 10Hz, and jams where the motor previously had only one stator were marked as potentially being either jams or the loss of a stator. These points could potentially be differentiated by examining mean squared diffusion data. There are a few points in Figure 4.12a) which represent what has thus far been assumed to be a forbidden transition, either from one stator to three or from three to one. The nature of these points is unknown, but could be an artifact of discrete sampling. They are not observed in the chimeric data, Figure 4.12b. Figure 4.13 shows the same data in a bar graph for comparison among the transitions.

4.1.4 Summary

The data within this section has demonstrated multiple speeds in both the wild type and chimeric BFMs at low load for the first time. As shown in Figure 4.3, data acquisition rate can not explain the difference in our observations of wild type BFM at low load (Figure 4.2) and those of Berg and colleagues (Figure 4.1). The difference may be due to a selection criterion for stable spinners, and Figure 4.14 shows a typical trace from this data set which meets this criterion. It may also be the case
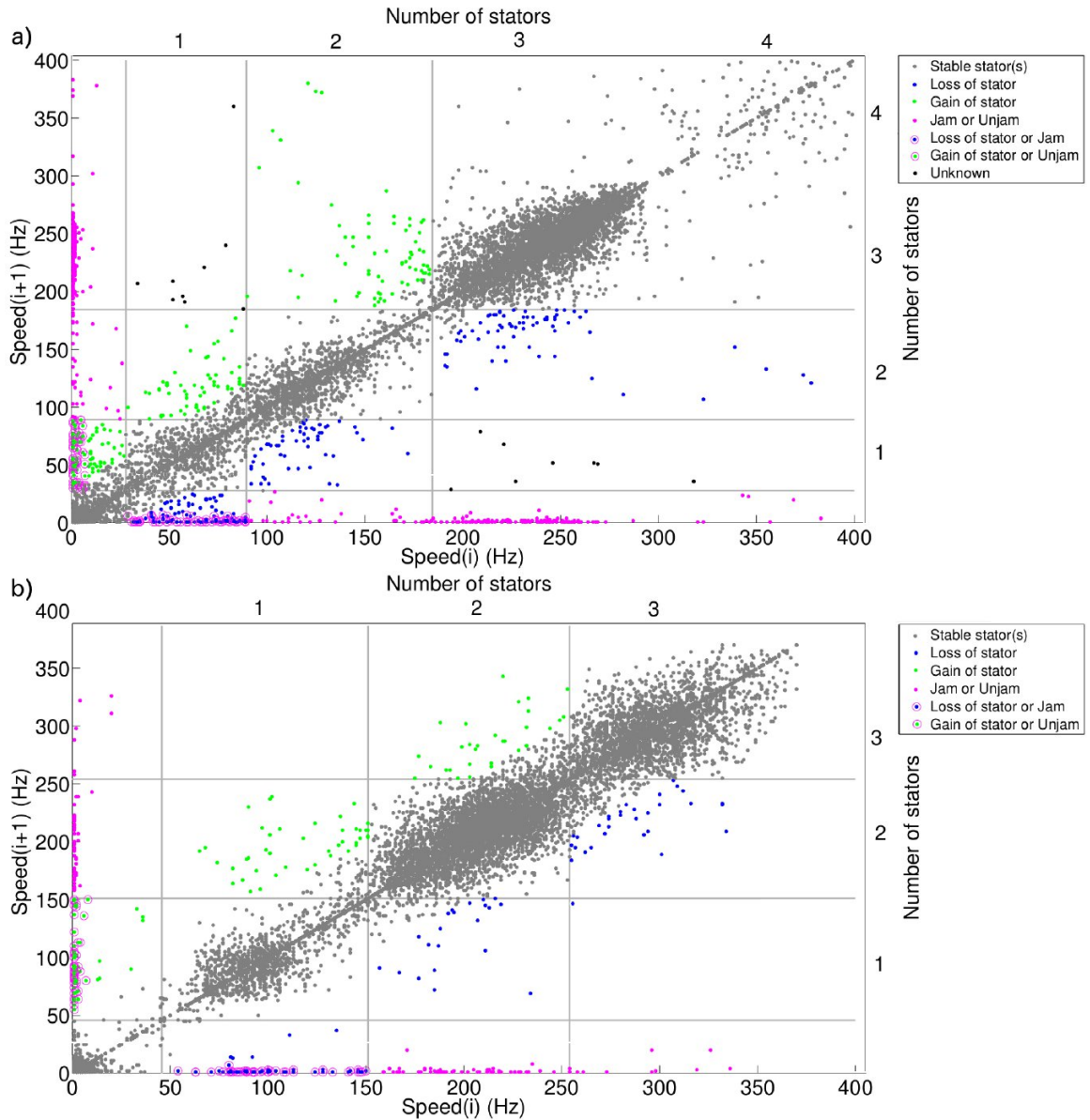
Figure 4.12: Rotational speed, comparing one 1s block (denoted i) to the next (i+1), from a) wild type BFMs (the same data as in Figure 4.2b), and b) chimeric BFMs (the same data as in Figure 4.5). For both (a) and (b), the traces were recorded with a QPD at 20kHz, and speeds were determined over 1s windows. The grey points show stability in speed at what is presumed to be one, two, or three stators (with a few points representing a potential 4th stator in wild type). The blue and green points show the loss or gain of a stator, respectively. The magenta points show a 'jam', where the motor suddenly toggles to zero or near zero speed. The magenta points with blue or green circles represent where it is unknown whether a stator was gained or lost, or whether the motor jammed, though this information may be extractable from mean squared diffusion plots. The black points in (a) are events not explained by the proposals put forth within this chapter. The grey lines are one half the lowest speed, then equidistant from the Gaussian peaks for each distinct speed.
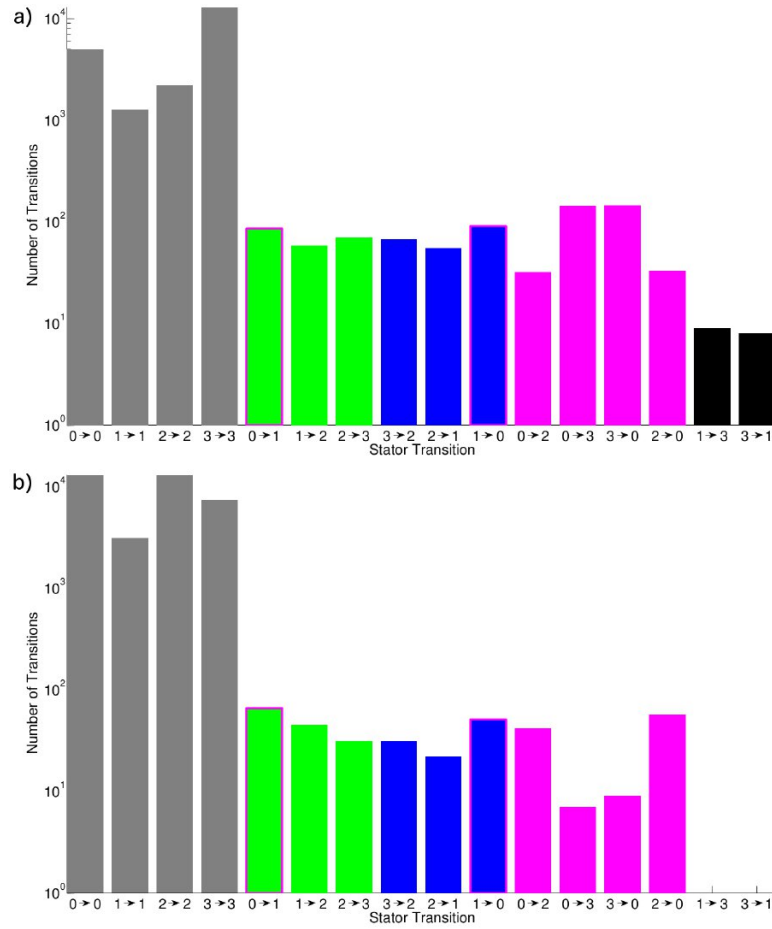
Figure 4.13: An alternative visualization of the data in Figure 4.12. The bars represent the number of transitions between particular stator numbers for a) wild type and b) chimera. The color scheme is the same as in Figure 4.12; grey represents no change in stator number, green represents a gain in stator, blue represents a loss in stator, magenta represents a 'jam', and green or blue with magenta outline represents transitions that could be attributed to either a jam or a gain or loss of stator, respectively. Black represents transitions which are unexplained under the current proposal of speed transitions. The transitions represented in these graphs are from QPD traces, and is the same data as represented in a) Figure 4.2b) and b) Figure 4.5).

that the samples of Berg and colleagues contained more motors with higher numbers of stators, and the only plausible explanation for this could be that our samples were photodamaged by the highly focused beam of the dark field microscope, reducing the IMF. This explanation seems unlikely, as increasing laser power did not cause a change of speed or behavior in these experiments, and motors were often observed to rotate stably for minutes. It also remains unknown why the maximum speed measured in

the wild type data presented above is around 250Hz as opposed to 300Hz measured by Berg and colleagues. This difference could also be attributed to photodamage, or potentially to the difference in load between a 100nm and 60nm bead. The later seems unlikely, as the torque required to spin a 100nm bead at 300Hz is about 4pN nm, less than 3% of the single stator torque output at speeds below 100Hz [210]. However, it is possible that a 100nm bead interacts with the cell surface lipopolysaccharides differently than that of a 60nm bead. It is also possible, and most likely, that this difference is simply due to a different strain of wild type *E. coli*.
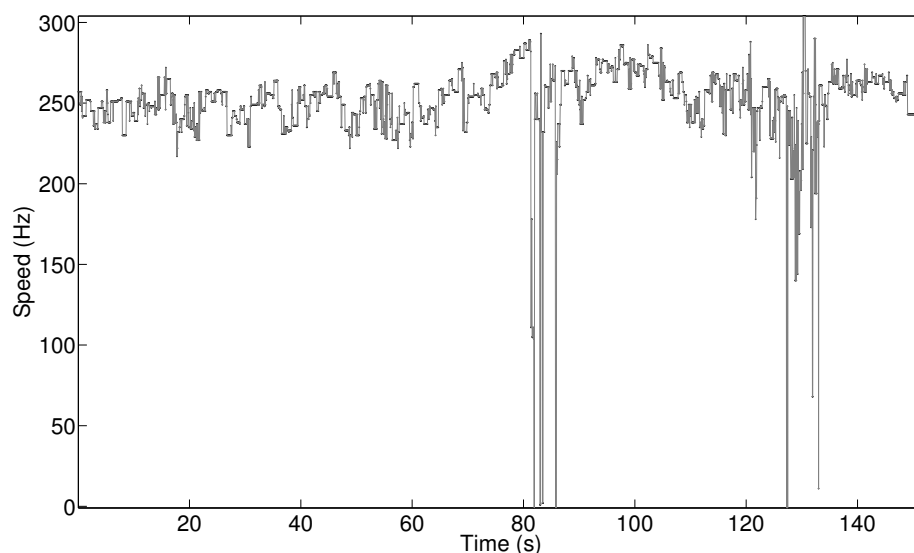
Figure 4.14: A representative speed versus time trace of a wild type BFM, demonstrating stable rotation over more than two minutes with few speed changes. This trace was sampled at 20kHz, and the speed was calculated from power spectra over 1s blocks spaced 0.05s apart.

Figures 4.7 and 4.8 were chosen for their prevalence of discrete speed changes, and are typical traces which wouldn't meet a stability criterion. Assuming the distinct speeds observed can be attributed to stator number, long QPD traces will allow for a future analysis of stator dynamics at low load. Distinct from changes in stator number, the 'toggles' noted by Berg and colleagues, are not obviously due to transient attachment of the stator units, as previously presumed. These events fall within two distinct categories. In some cases the motor 'jams' and, based upon mean squared

137

displacement analysis of the bead, seems to remain bound within a potential well. In other cases, the motor pauses and diffuses slowly for a period of time before beginning to rotate again.

4.2 A Poisson Stepper?

4.2.1 High load

For a constant number of active stator units, fluctuations in the speed of the BFM come from at least two separate sources: Brownian noise and the intrinsic probabilistic stepping dynamics of the stators. In 1995, Samuel and Berg investigated the variance of the rotation rate of the BFM in tethered cells. Upon finding the variance in rotation rate to be proportional to the mean rotation rate, they proposed that the BFM is a Poisson stepper, with the proportionality constant equal to the number of steps per revolution of the BFM [256].

The proposal that the BFM may be a Poisson stepper is based on the following derivation of the expected number of elementary steps of a Poisson stepper as a function of mean rotational speed and variance. For a Poisson process, the probability of observing n events in a given time interval is

$$P(n; \mu) = \frac{\mu^n}{n!} e^{-\mu}, \tag{4.1}$$

where μ is the product of the probability per unit time of the occurrence of an event and the length of the time interval [192]. Samuel and Berg decided to measure the variance over a fixed angular displacement instead of over a fixed time due to concerns over asymmetric tethering causing surface effects, thereby potentially causing motors to slow down at particular angles. The probability that a time t elapses between two

138

events in a Poisson process is

$$P(t; \lambda) = \lambda e^{-\lambda t}, \tag{4.2}$$

where λ is the probability per unit time of the occurrence of an event. The mean waiting time between events is

$$\langle t \rangle = \int_0^\infty \lambda e^{-\lambda t} dt = \frac{1}{\lambda}. \tag{4.3}$$

The number of elementary steps is strictly proportional to the distance traveled, and the time required for a cell to make n steps is equal to the sum of the time intervals between steps:

$$T = \sum_{i=1}^n t_i. \tag{4.4}$$

If each elementary steps is assumed to be a Poisson process, the mean time and the mean-square time are given by the following equations:

$$\langle T \rangle = \left\langle \sum_{i=1}^n t_i \right\rangle = \sum_{i=1}^n \langle t_i \rangle = \frac{n}{\lambda}, \tag{4.5}$$

$$\langle T^2 \rangle = \left\langle \left(\sum_{i=1}^n t_i \right)^2 \right\rangle = \sum_{i=1}^n \langle t_i^2 \rangle + \sum_{i \neq j} \langle t_i t_j \rangle = n \langle t^2 \rangle + n(n-1) \langle t \rangle^2, \tag{4.6}$$

$$\langle T^2 \rangle = \frac{2n}{\lambda^2} + \frac{n(n-1)}{\lambda^2} = \frac{n(n+1)}{\lambda^2}, \tag{4.7}$$

and the variance is thus

$$\langle T^2 \rangle - \langle T \rangle^2 = \frac{n}{\lambda^2}. \tag{4.8}$$

Combining Equations 4.8 and 4.5, the number of elementary steps is simply the ratio of the squared mean of the rotational period over the variance:

$$n = \frac{\langle T \rangle^2}{\langle T^2 \rangle - \langle T \rangle^2} \tag{4.9}$$

Equation 4.9 is based on the assumption that a single step of the motor's biochemical cycle is rate-limiting, and thus each elementary step is an event in a Poisson process. If several biochemical steps are rate-limiting and have comparable kinetics in each elementary step, the prior assumption leads to an overestimate in the number of steps per revolution. This derivation also assumes that the bead tracks the motor state, neglecting variation due to smoothing applied by the tether, Brownian motion of the bead, and measurement error.

Using Equation 4.9, Samuel and Berg found that the fluctuation behavior of tethered cells at full speed matches that of a Poisson stepping mechanism characterized by about 400 elementary steps [256]. At the time of these experiments, the maximum number of stator units within a motor was believed to be 8 [176, 177], so Samuel and Berg proposed that, if the elementary steps corresponded to steps of the independent stator units, each stator stepped 50 times per revolution of the motor. By measuring the rotational period during resurrection experiments where the number of stators was inferred from discrete increments in average motor speed, Samuel and Berg demonstrated that the average number of elementary steps per revolution of the BFM was dependent on the number of torque generating units, and concluded that each stator steps independently [257]. However, Samuel and Berg noted that these Poisson events could potentially instead correspond to a non-observable process, such as ion translocations.

From Equation 4.9, the size of each step, ϕ, is

$$\phi = \frac{\theta}{n} = \theta \frac{\langle T^2 \rangle - \langle T \rangle^2}{\langle T \rangle^2}, \tag{4.10}$$

where θ is the fixed angular distance over which the rotational period is measured. Substituting

$$\left\langle \frac{d\theta}{dt} \right\rangle = \frac{\theta}{\langle T \rangle} \tag{4.11}$$

into Equation 4.10 yields an inverse quadratic dependence between the variance in rotational period and the square of the rotation rate, for a fixed number of steps:

$$\langle T^2 \rangle - \langle T \rangle^2 = \left. \frac{\phi \theta}{\left\langle \frac{d\theta}{dt} \right\rangle^2} \right|_n . \tag{4.12}$$

Figure 4.15 shows the results of these variance studies on tethered cells. The graphs in (a) and (b) show the linear dependence of the estimated number of steps upon the motor speed or number of stators. It should be noted that Samuel and Berg defined only 8 distinct speeds in tethered cell rotation, whereas more recent evidence suggests that, at high load, each BFM may contain at least 11 stators [173] and should thus be characterized by at least 11 distinct speeds. This suggests that the calculation of 50 steps per stator per revolution of the BFM is an overestimate. The graph in (c) shows the inverse quadratic dependence between the variance in rotational period and the square of the rotation rate predicted by Equation 4.12. As a comparison, Samuel and Berg performed a similar analysis on broken motors capable of freely rotating when torque was applied via electrorotation. The results of this analysis are shown in graph (d).
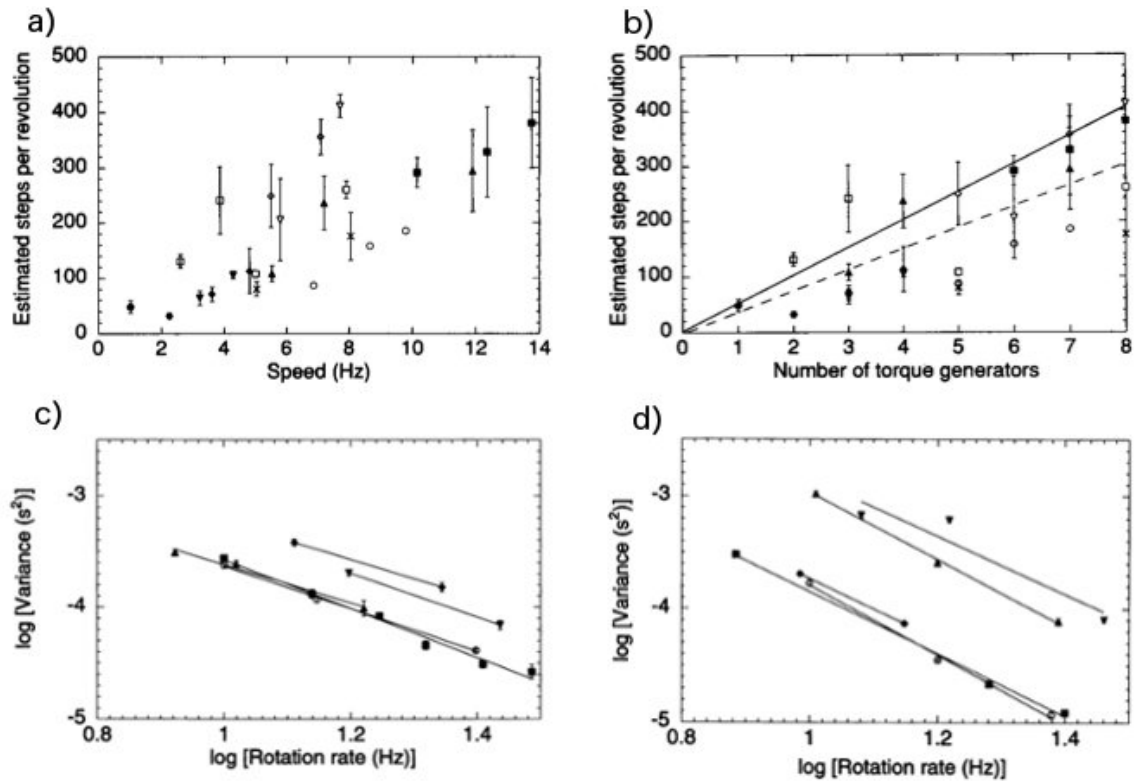
Figure 4.15: Four figures from the measured rotation rate of tethered *E. coli* cells. a) The estimated steps per revolution, calculated from Equation 4.9, as a function of the mean rotation rate. b) The segments used for the generation of a) were assigned a number of stator units based upon their speed, and the plot shows estimated steps per revolution as a function of the number of active stator units in the motor. c) Equation 4.12 predicts that, for a Poisson motor with a constant number of steps, the variance in the rotation period over a fixed angular distance should be inversely proportional to the square of the rotation rate. This is a log-log plot of the variance in rotation rate over 10 revolutions as a function of the rotation rate for tethered cells with the open circles representing simulated data. The slopes of the lines fitted to the experimental data are -1.9 ± 0.2, matching the slope of -2 predicted by Equation 4.12. d) The same graph as in c), but for motors which were broken by driving tethered cells backwards with electrorotation. The motors were then driven forward with a constant torque applied via electrorotation, and the variance in the rotation rate was measured over 10 revolutions. The slopes of the lines fitted to the experimental data are -2.8 ± 0.2. The open circles in this graph show simulated data of freely diffusing motors with constant drift rates. Refer to [256] for more details. Figures a,b from Samuel and Berg et al 1996 and c,d from Samuel and Berg et al 1995.

4.2.2 Low load

A very similar analysis (see Section 2.4.2 for details) was done for chimeric and wild type *E. coli* cells rotating a 100nm gold bead on a hook. As surface effects are still a concern (in this case, the gold bead on the cell surface), and as the model of Wingreen and colleagues suggests an uneven potential in the motor could cause the motor speed to vary within a single revolution, motor speeds were measured over an entire revolution for this analysis. The characteristic speed for a given number of stators was defined by the Gaussian peaks in Figures 4.2a) and 4.4. The transition point from one distinct speed population to another, was marked by the half way point between the Gaussian peaks. The variance in the rotational period of the BFM was calculated for each stably spinning period within each trace, defined by a period lasting at least seven revolutions within one speed population. Figures 4.16 and 4.17 show the results of this analysis for the chimeric and wild type *E. coli* data acquired at 109.5kHz.

As shown in Figure 4.16, the spread in the estimated number of steps per revolution is large. For a single stator, the estimated steps per revolution is 63 ± 96 in the chimeric BFM and 31 ± 21 in the wild type BFM. For two stators, the estimated steps per revolution is 79 ± 87 in the chimeric BFM, and 62 ± 37 in the wild type BFM. A third speed was clearly identified in the wild type BFM, and for three stators the estimated steps per revolution is 135 ± 96. The spread in this data is much larger across BFMs than it is within a single BFM (not shown), suggesting a large heterogeneity among motors. While these numbers agree, within their large errors, with the number of estimated steps published by Samuel and Berg, and while it seems true that the estimated number of steps scales with the number of stators, the large spread in the data prevents more firm conclusions on the number of steps per revolution of the BFM. It may be the case that the behavior of the motor is different at low loads than at high.
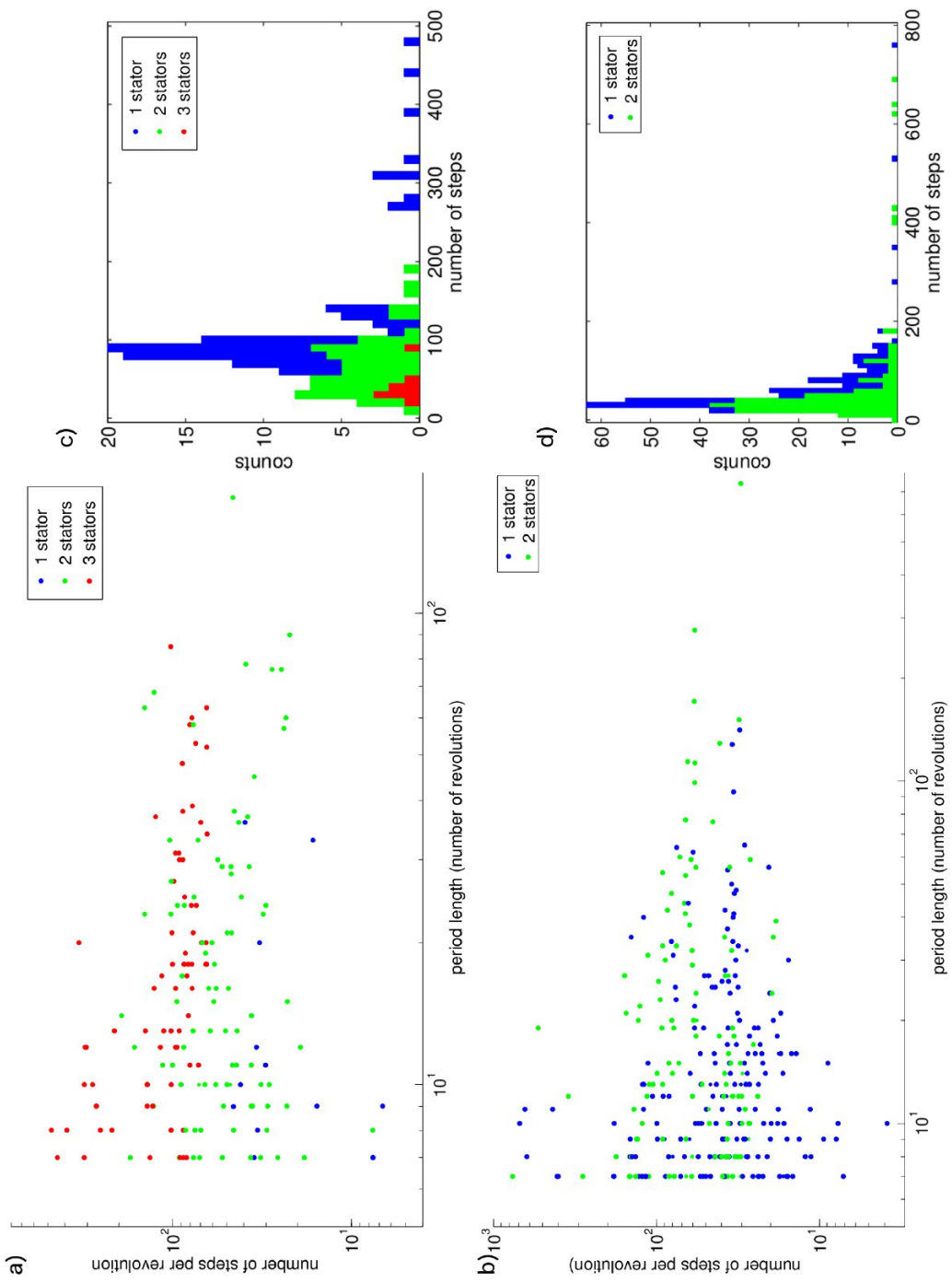
Figure 4.16: The estimated number of steps, calculated as in Equation 4.9, against the length of the segment over which the variance was measured, for a) wild type and b) chimeric BFMs. Histograms of the estimated step number are shown in (c) wild type, and (d) chimeric BFMs. The estimated number of steps was calculated for each segment of every trace where the speed remained within one distinct speed population for at least seven revolutions. The spread in the estimated number of steps for a given stator number is much larger across BFMs than it is within a single BFM, and as shown, the number of estimated steps is not a function of the length of the segment. For a single stator, the estimated steps per revolution is 31 ± 21 in the wild type BFM (calculated from 12 segments taken from 7 cells) and 63 ± 96 in the chimeric BFM (calculated from 185 segments taken from 55 cells). For two stators, the estimated steps per revolution is 62 ± 37 in the wild type BFM (calculated from 54 segments taken from 14 cells) and 79 ± 87 in the chimeric BFM (calculated from 130 segments taken from 26 cells). A third speed was clearly identified in the wild type BFM, and for three stators the estimated steps per revolution is 135 ± 96 (calculated from 68 segments taken from 10 cells).

144

Figure 4.17 shows a log-log plot of the variance as a function of the rotation rate for both the chimeric and wild type data, using the same stable periods as in Figure 4.16. Equation 4.12 predicts that, for a fixed number of stators, the variance in the rotational period should be inversely proportional to the square of the rotation rate. Therefore, each stator number represented in the log-log plot of Figure 4.17 should have a slope of -2. For wild type, the slopes of 1, 2, and 3 stators are -1.8 ± 0.5, -5.1 ± 0.6, and -1.0 ± 0.1, respectively. For the chimera, the slopes for 1 and 2 stators are -2.3 ± 0.2 and -2.0 ± 0.2, respectively. Therefore, data for the two stators of chimera and for the first stator of wild type reproduce the behavior of the motor at high load, while the second and third stators of the wild type motor do not. From Equation 4.12, if motor speed is proportional to the stator number[2], then the variance in the rotational period should be inversely proportional to the cube of the rotation rate over all stator numbers. A best fit line of this relation is shown as a black dashed line in Figure 4.17. With slopes of -3.6 ± 0.1 and -2.4 ± 0.1 for wild type and chimeric BFMs respectively, these lines lie on opposite sides of the expected slope of -3. More data is needed in order to better determine if the variance in the motor speed is consistent with the hypothesis that the BFM is a Poisson stepper. Long recordings with the QPD will be optimal for such an analysis. It may also be necessary to consider other sources of fluctuations at low load, such as rate limiting ion translocations, or an increase in the relative effect of contact forces between the stators and rotor predicted by the model of Wingreen and colleagues. The transient motor 'jams' shown in the previous section must also be considered.

---

[2]This is true at high load [173]. The speed histograms shown in this chapter (with the exception of the high speed data from wild type) suggest this is approximately the case at low load.
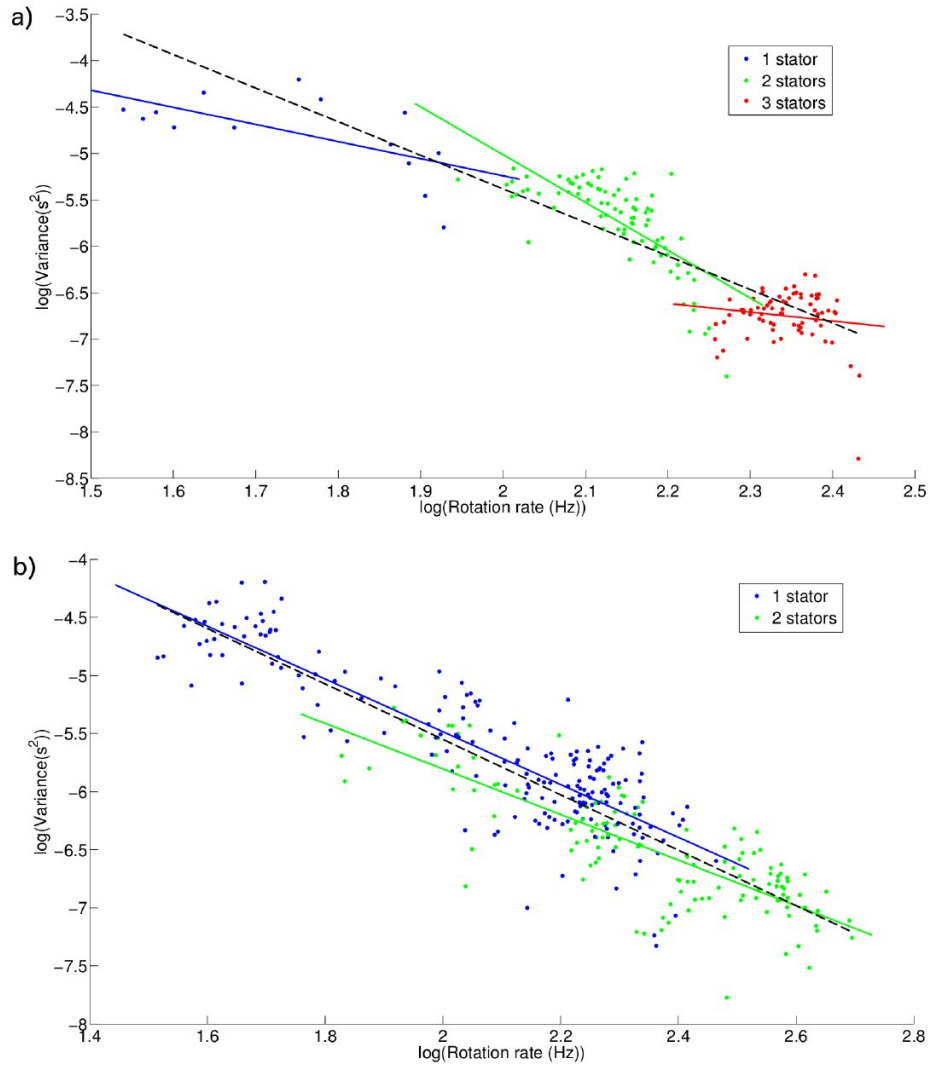
Figure 4.17: Equation 4.12 predicts that, for a Poisson motor with a fixed number of steps, the variance in the rotation period over a fixed angular distance should be inversely proportional to the square of the rotation rate. Graph (c) of Figure 4.15 agrees with this prediction for BFMs at high load. These plots show the log of the variance versus the log of the squared rotation rate for a) wild type, and b) chimeric cells at low load. The data represented here is the same as is represented in Figure 4.16. Drawing best fit lines for each stator number yields the following slopes: a) one stator (blue) = -1.8 ± 0.5; two stators (green) = -5.1 ± 0.6; three stators (red) = -1.0 ± 0.1. b) one stator (blue) = -2.3 ± 0.2; two stators (green) = -2.0 ± 0.2. Drawing best fit lines over all stators yields the following slopes: a) -3.6 ± 0.1 b) -2.4 ± 0.1.

4.3 Resolving Steps

4.3.1 26 steps per revolution

Discrete steps have previously been observed in the BFM in deenergized and photodamaged *E. coli* [208] and *Salmonella* [259] cells rotating 10Hz or less with an unknown number of active stators. Until now, restrictions in spatial and temporal resolution have prevented the study of fully energized and undamaged motors, and it was unknown whether this 26 fold periodicity in the motor was an artifact of damaged motors or if this periodicity depended on either speed or the number of active stator units. Furthermore, the simulations performed by Xing and colleagues predict that lateral fluctuations of the stators, due to soft springs linking MotB to the peptidoglycan, will smear the steps in a motor trajectory. They thus predict that stepping behavior will only be observed in BFMs rotating less than 10Hz [261].

Figure 4.18 shows a chimeric BFM rotating at about 215Hz for nearly 1 second. This trace was analyzed following the methods described in Section 2.4.2. The kernel density plot of the angular position of the motor shows 26 clear peaks, and the autocorrelation of the dwell angles show a clear 26 fold periodicity. This suggests that the 26 steps in the BFM observed previously were not an artifact of damaged motors, and motors take the same number of steps at low energization as they do at physiological energization. Of the 224 traces of chimeric BFMs, this trace is one of very high quality, and there are about a dozen showing a clear 26 fold periodicity in the kernel density plot. These traces are all characterized by nearly circular trajectories of the gold bead, whereas most traces are elliptical, due to the motor position on the cell. Figure 4.19 shows an angle versus time plot for sections of this same trace.
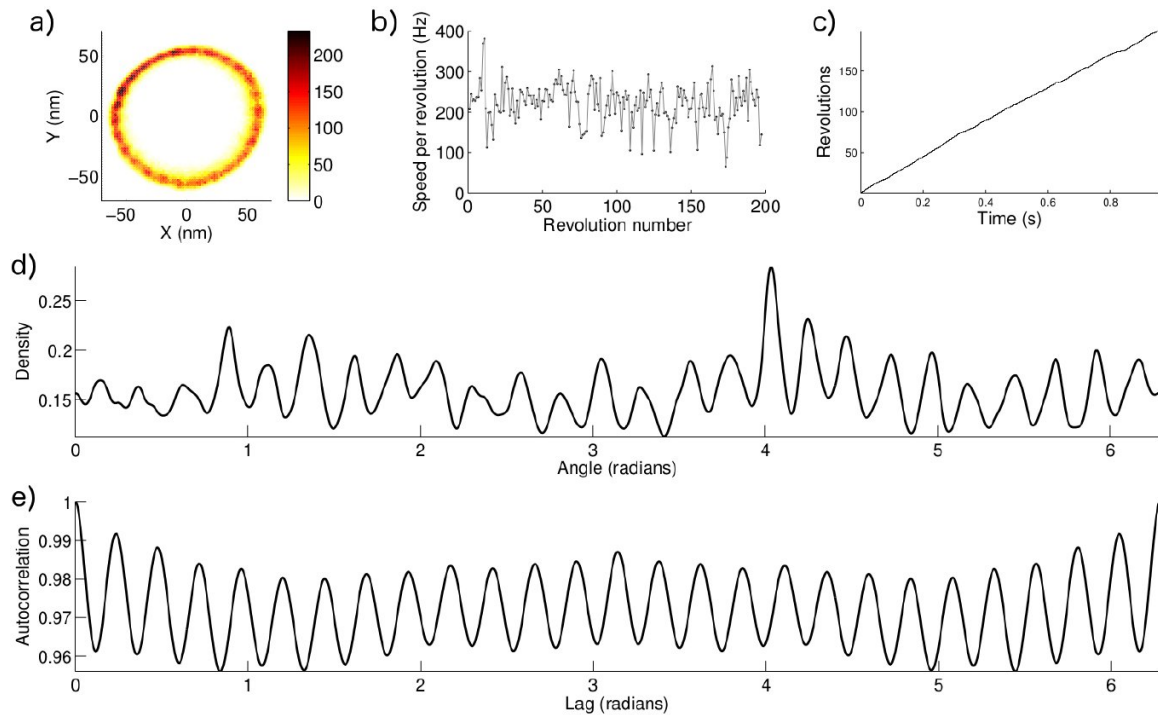
Figure 4.18: These plots are from a 1s long recording of a 100nm gold bead on a chimeric BFM, sampled at 109.5kHz. a) A 2D histogram of bead position, where the bin size is 2nm by 2nm. b) Speed per revolution as a function of revolution number. c) Cumulative revolutions versus time. d) Kernel density plot of the dwell angles of the gold bead showing 26 clear dwells. e) Circular autocorrelation of the kernel density signal, showing 26 clear peaks.

4.3.2 Stator effects

Wingreen and colleagues propose that this observed stepping behavior arises solely from steric hindrance within the motor. Their model interprets BFM rotation as a viscously damped random walk in a tilted and corrugated potential. The heterogeneous potential is a product of contact forces between the rotor and the stator, potentially between the MotA/B stator units and FliG proteins, but possibly also by contact with FliF (MS-ring), FlgH or FlgI proteins (distal rod, L, and P rings, respectively). In this model, the observed steps of the BFM correspond to jumps between adjacent wells of the tilted potential, with crossings of energy barriers possible due to thermal fluctuations. This model predicts a 2π periodicity of the potential, where the absolute angular position of the rotor with respect to either the stator or

148
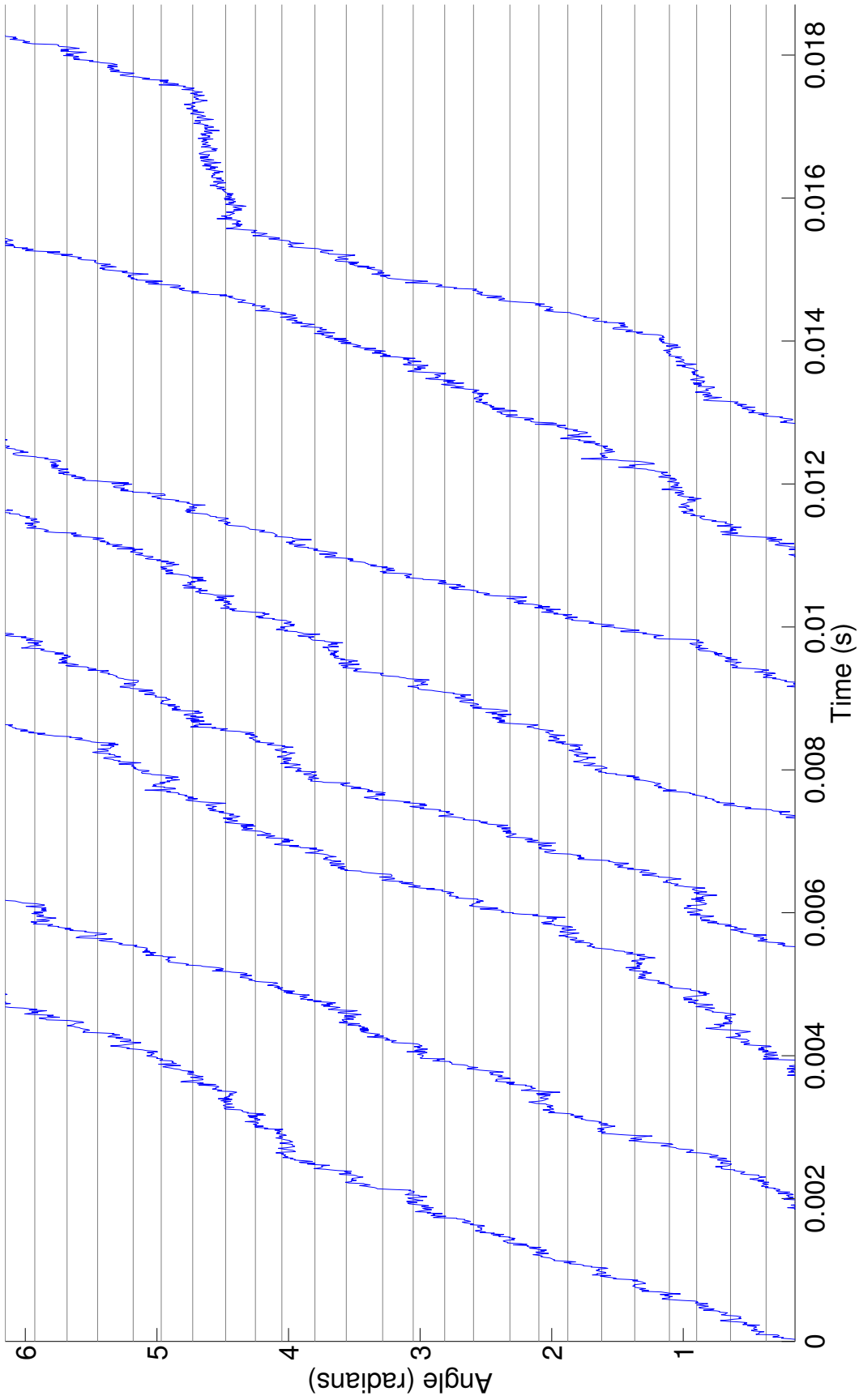
Figure 4.19: Angle versus time plots for eight randomly chosen revolutions of the trace shown in Figure 4.18. The revolutions are non-consecutive, but plotted adjacent to one another with a small time offset for ease of viewing. The grey horizontal lines show the dwell angles of the motor, as determined by the peaks of the of the kernel density function of the entire trace, shown in d) of Figure 4.18.

the outer rings determines the step statistics. This model predicts that, the potential, as discerned from the dwell angles of a gold bead attached to the hook of the motor, should remain the same regardless of the number of stators and where the stators are docked around the rotor. Conversely, Xing and colleagues propose that, depending on the positioning of the stators around the motor, the number and positions of the steps may change [261].

Figure 4.20 shows a gold bead trace with an event, shown in green, that would be characterized as the transient loss of a stator by Berg and colleagues. The dwell angles of the motor remain the same to within less than one twentieth of a step prior to and after the event. While this fits the model of Wingreen and colleagues, this would be a surprising result for the model of Xing and colleagues, unless the new stator happened to dock in the same position as the previous stator. However, for the reasons given in Section 4.1, we believe that such an event is unlikely to be the loss of a stator. Instead, we believe this to be a 'jam' in the motor, which, as shown in (c) of Figure 4.20, occurs at a single dwell angle. If this is the case, the fact that the motor potential is the same before and after the event could be explained by either the Wingreen or Xing models.

The model of Wingreen and colleagues predicts that the number of observed steps in the motor should remain constant as a function of the number of stators. If the BFM is a Poisson stepper, as proposed by Berg and colleagues, and if the Poisson steps correspond to individual steps of the stators, the number of steps should scale linearly to the number of active stators. The analysis in Section 4.2 supports the hypothesis that the number of elementary steps generally increases with the number of stators. The model proposed by Meacci and Tu also predicts such a relationship, due to a duty ratio near unity and independent stepping of the stators [275]. The model proposed by Xing and colleagues proposes that, if a second stator joins a BFM an integer distance over the rotor periodicity from the first, the step size and
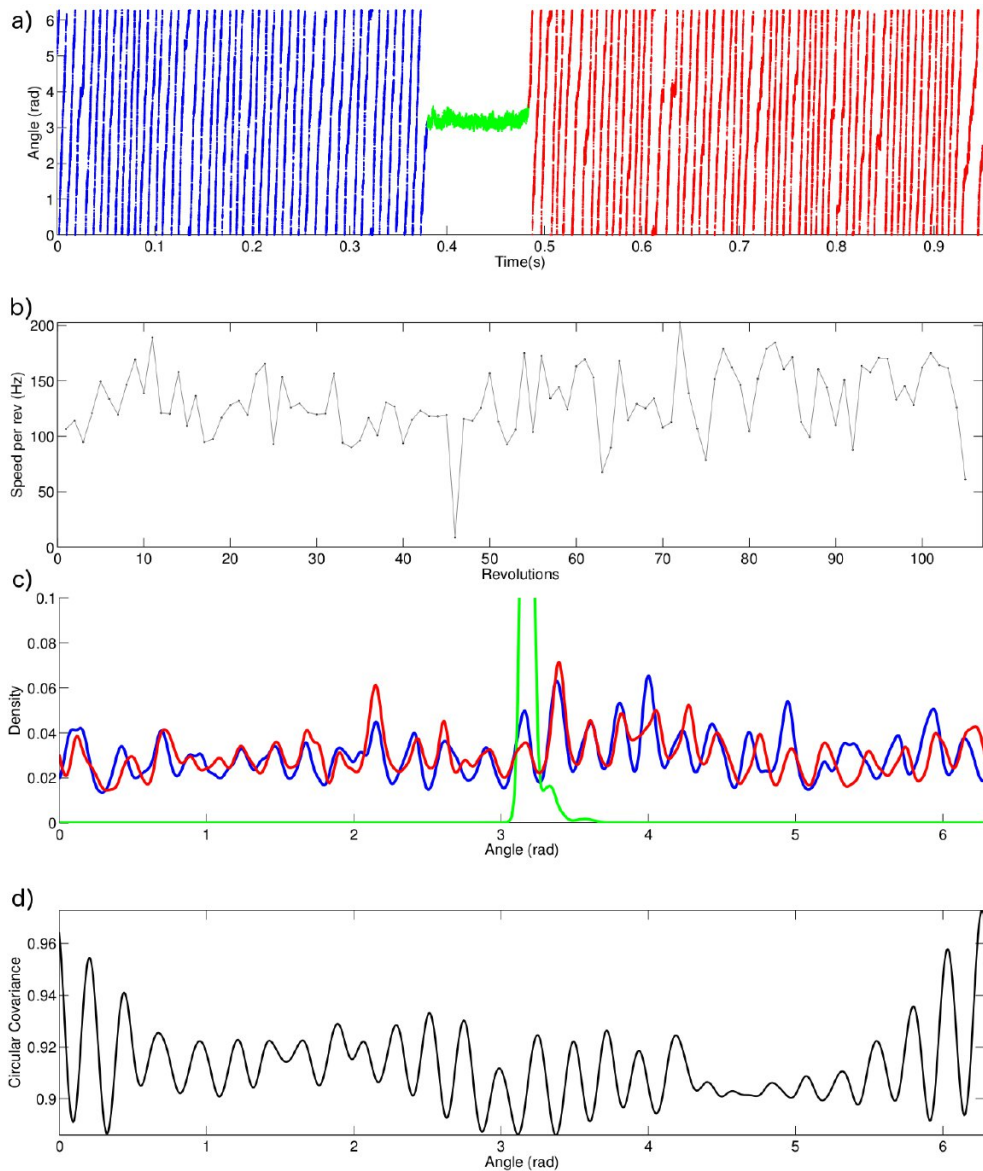
Figure 4.20: A trace of a gold bead on a chimeric BFM hook showing a 'jam' of the motor part way through the trace. a) A plot of angle versus time. The trace has been broken up into three separate segments, showing the 'jam' of the motor in green. b) A plot of speed per revolution versus revolution number. c) A kernel density plot showing 26 clear dwell angles for both the blue and red segments of the trace. The green line shows that the 'jam' of the motor occurs mostly in a single dwell angle. d) A plot of the circular cross correlation between the blue and red segments of the trace versus a wrapped around lag of one of the segments. A value of 1 would signify perfect correlation, while a value of -1 would signify perfect anticorrelation. This plot shows the highest cross correlation at a value of 6.27 radians. This means that the blue segment lags behind the red segment by 0.01 radians, a small fraction of a single step, which is ∼0.24 radians. This seems to imply that the potential has remained the same before and after the 'jam' of the motor.

thus the number of steps will not change. If the second stator joins an non-integer distance from the first, the number of steps will double. However, for sufficiently soft stator springs, they note that the number of steps per revolution may remain the same regardless of the stator separation [261]. Figures 4.21 and 4.22 suggest that the potential of the motor does not change with the addition of new stator units and that the number of steps per revolution also remains the same. While the preliminary data shown in this section suggests that the potential of the motor may be static and independent of stators, additional analysis and additional high quality traces are needed in order to fully explore the the potential of the motor during both the gain and loss of stators, and also before and after the loss of all stator units from a motor.
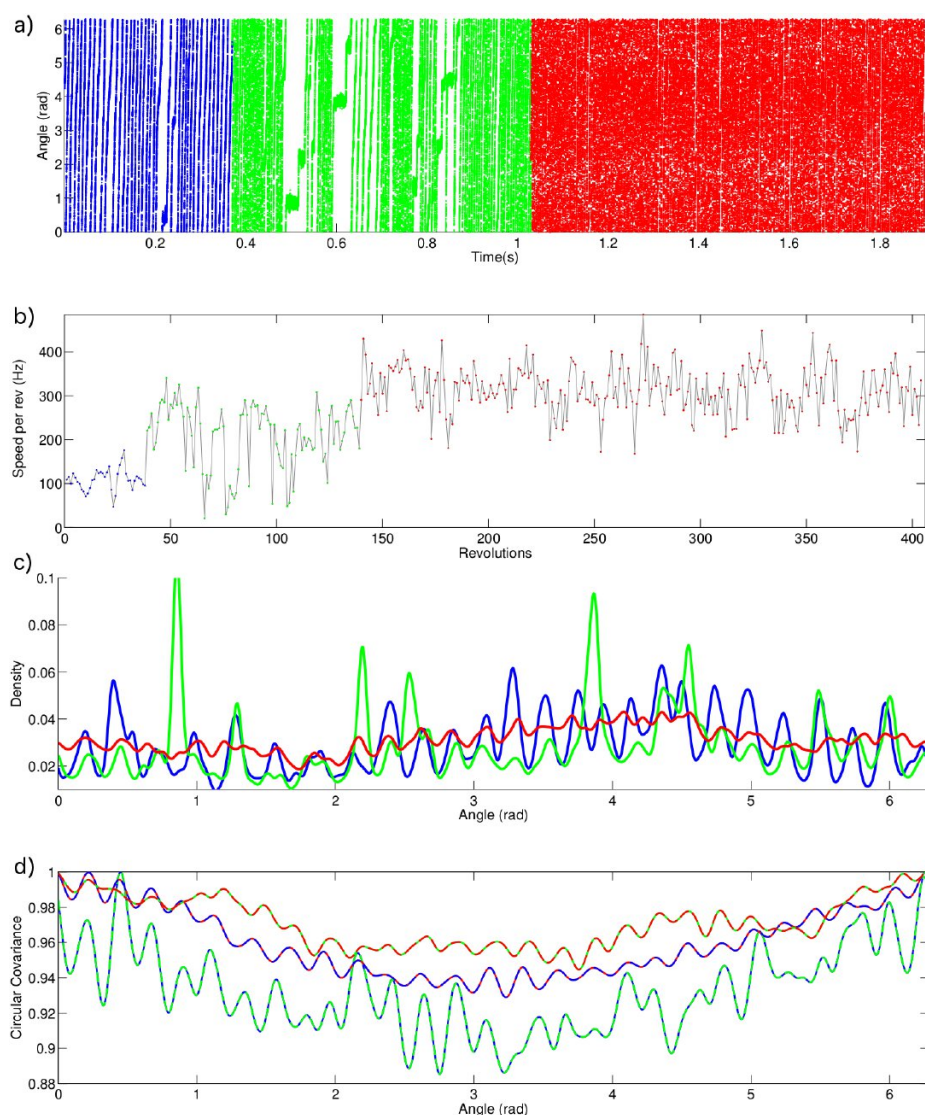
Figure 4.21: A trace of a gold bead on a chimeric BFM hook showing three discrete speeds. a) A plot of angle versus time. The trace has been broken up into three separate segments. b) A plot of speed per revolution versus revolution number, with colors corresponding to the segments in (a). c) A kernel density plot showing dwell angles for the three segments of the trace. The blue segment most obviously demonstrates 26 dwells. d) A plot of the circular cross correlations between the segments versus a wrapped around lag of one of the segments. The dual color of each line indicates a crosscorrelation of the correspondingly colored segments. The crosscorrelations have been normalized for ease of viewing. The maximum crosscorrelation values indicate that green lags behind blue by 0.46 radians ($\sim$2 steps), green lags behind red by only 0.01 radians, and red lags behind blue by only 0.01 radians. This seems to imply that the potential has stayed the same between blue and red and between green and red. Though blue and green seem to be separated by about two steps, the crosscorrelation value at zero lag is nearly equal to that at 0.46 radians. Overall, this seems to suggest that the potential of the motor has not changed, despite discrete changes in speed, likely due to the addition of stators. However, it is interesting to note that the pauses within the green section seem to lie in anti-phase to the 26 fold potential.

153
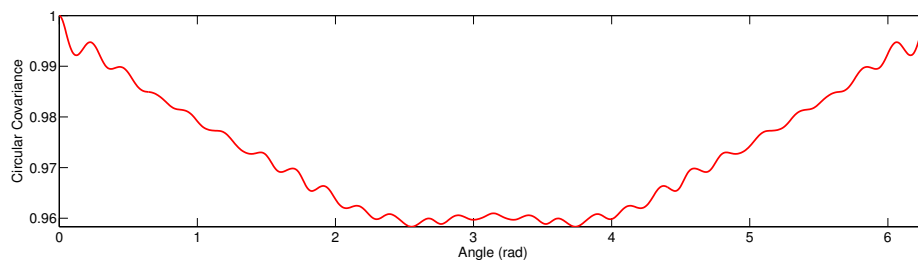
Figure 4.22: The circular autocorrelation of the red segment from Figure 4.21. The autocorrelation shows 26 distinct peaks for a motor that is likely driven by more than one stator. This seems to suggest that the number of steps per revolution does not change with the incorporation of new stators.

4.3.3 Chimera versus wild type

All of the stepping data shown above has come from the chimeric BFM. None of the high speed traces from the wild type motors show clear steps in the kernel density traces. As noted previously, in order to resolve steps in this manner, the trajectory of the gold bead must be nearly circular. Given that such traces make up a small percentage of the data from chimeric motors, the fact that similar quality traces do not exist for wild type motors may simply be explained by statistics and the need for more data.

In ninety percent of the wild type traces, the 100nm biotin gold bead was attached to a biotinylated hook via a streptavidin linker. It was predicted that this manner of attachment would crosslink the hook, making it stiffer, and provide better angular resolution of steps. Preliminary studies of the motion of beads stuck to the hooks of unenergized cells suggests that the biotin hooks are not significantly stiffer. The lack of quality stepping data for wild type may suggest that this method of attachment is inferior to antibodies. Further direct comparisons of the two methods would be necessary to verify this.

It may also be the case that differences between the wild type and chimeric motors are to blame for the lack of quality stepping data in wild type. Xing and colleagues

154

predict that the stator springs, 7-8nm long α helices which link the stators to the peptidoglycan, allow lateral fluctuations of the stators around an equilibrium position [261]. If these springs are too soft, steps of the motor will be smoothed [335]. Xing and colleagues use simulations to show that soft stator springs cause a noisier trajectory of an attached nanoparticle. The slopes of the lines in Figure 4.17 suggest that there may be an intrinsic difference in the behavior of wild type and chimeric motors at low load, and this may be related to the lack of wild type traces showing clear steps.

4.4   Stepping Kinetics

In theoretical models of stepping motors, each step is the result of a cycle consisting of multiple sequential processes. The time the BFM spends between each step of the motor is the duration of this cycle, and for a set the stochastic processes, this dwell time is also stochastic. The probability distribution of this dwell time is a convolution of the probability distributions for each constitutive reaction [336]. If the motor's cycle is dominated by a single rate-limiting process, the dwell time distribution will be exponential, as in a Poisson stepper. Samuel and Berg, proposing the BFM to be a Poisson stepper, predicted exponentially distributed dwell times [257]. The model of Wingreen and colleagues predicts that the distribution of waiting times to cross each barrier is exponential, and that due to the heterogeneity of barriers, the overall waiting-time distribution is a 'stretched' exponential [274]. In the model of Xing and colleagues, each motor cycle has two half-steps. The first predicted half step is the binding of ion(s) from the periplasm and is rate-limiting, and the second half step corresponds to ion(s) release into the cytoplasm and is predicted to occur too rapidly to be resolved. Thus, this model similarly predicts an exponential distribution of dwell times for each dwell.

The spatial and time resolution of the high speed recordings acquired for this thesis are sufficiently high to begin to test these predictions. The relaxation time of a bead stuck to the elastic hook of the motor is the viscous drag coefficient of the bead divided by the torsional spring constant of the hook. Using a spring constant of 400pN nm rad^{-2} [258, 337], the expected relaxation time of a 100nm gold bead is about 6μs. With a frame rate of 109.5kHz, the relaxation time of the bead is not expected to be resolved. One might thus expect the dwell time distributions to be best fit by a single exponential without the need for a time offset.

In order to measure dwell time statistics, the traces must be sufficiently clean to resolve individual dwells. As with the measurements of Section 4.3, this requires traces where the gold bead follows a nearly perfect circle, which make up a small portion of the entire data set. As a preliminary examination, a dwell time analysis was performed on the three traces shown in Figures 4.18, 4.20, and 4.21, each showing 26 clear steps. The dwell time distributions were fit to the six models represented in Table 2.2 with the methods described in Section 2.4.2. The results of this analysis are shown in Figure 4.23.

In each of the three traces analyzed, the model which best fit the largest number of the 26 dwells was two exponentials and a time offset. The time offsets were between 12.9 $\pm$ 0.3μs and 33.0 $\pm$ 0.4μs, which are larger but of the order of the predicted relaxation time of a gold bead on a hook. This could indicate that the viscous drag coefficient on the gold bead is larger than expected, possibly due to dragging on the cell surface, or that the stiffness of the hook is smaller than previously measured. This time offset is also of the order predicted to restretch the protein strings in the model of Wingreen and colleagues. The bar graphs of Figure 4.23 argue that the dwell time distributions are not well fit by a single exponential, as predicted by all of the models, and are also generally not well fit by a single exponential with a time offset, with the exception of the distribution in b). Thus, it's possible that there are two sequential

processes occurring in each dwell, both of which are resolvable in many cases. These processes, one faster than the other, could potentially correspond to the binding of ion(s) from the periplasm and the subsequent release of ion(s) into the periplasm.

However, the analysis performed for Figure 4.23 is subject to a large flaw in the case of this BFM data. By dividing the kernel density distribution into 26 dwells and counting the number of frames the gold bead spent in each dwell, the dwell time distribution becomes skewed when the noise of the signal is on the order of the dwell sizes. When this occurs, short dwell times present in the data are shifted to longer dwell times by bleed over from adjacent dwells. This may be sufficient to explain the lack of short dwell times in the three distributions shown, and suggests that the stepping kinetics of the BFM are yet unknown. In order to gain an accurate picture of the kinetics, there is a need for high quality traces with less angular noise, or a probabilistic recovery of bead angle, potentially with a Hidden Markov Model. In addition to higher quality traces, further data spanning different IMF conditions will allow insight into the dependence of the time constant(s) on components of the IMF.
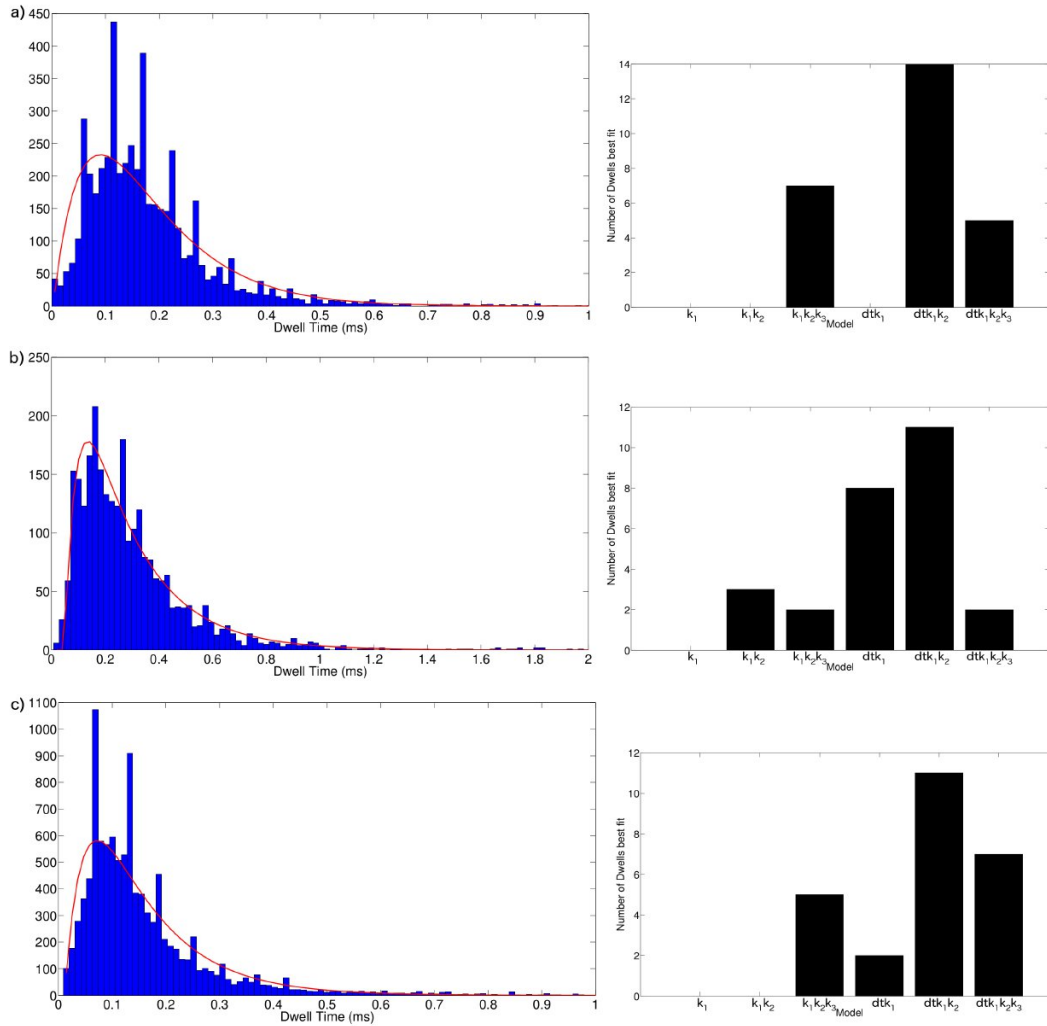
Figure 4.23: The dwell time kinetic analysis for the three traces shown in Section 4.3. The left column shows a histogram of the overall dwell times for all of the 26 dwells for each trace. The right column shows the number of dwells which were individually best fit by each model. In all three cases, the best model for fitting individual traces was two parameters and a time offset. The red fit line shown in the histograms uses this model to fit the overall distribution. The calculated parameters are as follows: a) dt= $13.7 \pm 0.2\mu$s; k_1= 11.46 ± 0.03ms^{-1} k_2= 12.95 ± 0.03ms^{-1}. These dwell times correspond to the trace shown in Figure 4.18. b) dt= $33.0 \pm 0.4\mu$s; k_1= 5.07 ± 0.02ms^{-1} k_2= 14.49 ± 0.06ms^{-1}. These dwell times correspond to the trace shown in Figure 4.20. c) dt = $12.9 \pm 0.3\mu$s; k_1= 9.31 ± 0.05ms^{-1} k_2= 24.8 ± 0.2ms^{-1}. These dwell times correspond to the trace shown in Figure 4.21. In each of (a), (b), and (c), while the cumulative distribution of all 26 dwells was best fit by three parameters and a time offset, the fit shown is that which best fit the most individual dwells, two parameters with a time offset. All errors quoted are 95% confidence intervals.

158

4.5 Angle Measurements with Nanorods

The use of nanorods instead of nanospheres to observe the rotation of the rod is appealing because rods allow for direct recovery of the hook angle, whereas assymetrically attached spheres allow for localization, which is then converted to angular data through ellipse fitting. We thus predicted that nanorods would provide cleaner traces of BFM rotation. Preliminary experiments provided a lower yield of nanorods stuck to hooks as opposed to nanospheres, and more work is needed to optimize this assay. However, Figure 4.24 demonstrates the potential improvement using rods over spheres. Trace (b) of Figure 4.24 shows a rod attached to a BFM hook which is oriented perpendicular to the illumination. The motor is not energized, so the rod diffuses freely. Preliminary experiments have shown that, as in the case of nanospheres, traces where the rod is oriented perpendicular to the illumination are rare, and it is more common that the angle of the rod to the illumination is not constant. While this complicates the analysis, three dimensional orientation tracking of anisotropic metallic nanorods has previously been demonstrated [322, 338]. Therefore, rods may not only allow for better angular resolution of the hook, but also allow angular resolution from hooks situated anywhere on the cell body, as opposed to only those directly on top.
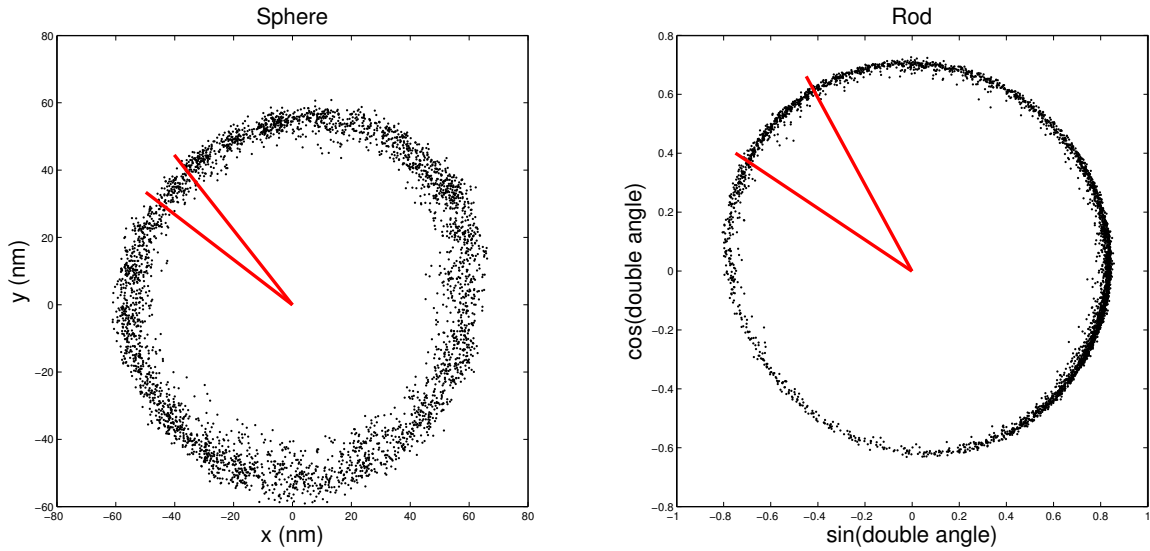
Figure 4.24: A comparison of a 100nm gold bead on a hook, and a 110nm by 53nm gold rod on a hook, showing the potential for increased angular resolution with nanorods. a) The x and y positions of a gold bead on a spinning BFM hook, from a high quality trace. The bead was localized using the methods described in Section 2.4.2. The two red lines are spaced $\frac{1}{26th}$ of a revolution apart. b) A trace of a gold nanorod on a BFM hook where stators have not been induced, so the rod is doing Brownian motion. Here, the x and y axes represent the sine and cosine of the 'double' in-plane angle of the rod, as calculated from the intensities of the four polarization channels. Details of this method are given in Section 2.4.2. As evident from Equation 2.10, the rod angle spans from zero to π, and must be unwrapped. That is, the rod traverses the circle shown twice per revolution. Consequently, the two red lines are spaced $\frac{1}{13th}$ of a revolution apart. The two red lines in (a) and (b) show the relative size of one step, allowing a comparison of the noise within one step. It is apparent that directly measuring the angle of the hook using a nanorod yields a cleaner trace compared to localizing the position of a bead asymmetrically attached to the hook. The frame rate for both (a) and (b) was 4500Hz.

Chapter 5

Conclusions and Outlook

The aim of the work presented in this thesis was to elucidate the stepping dynamics of F_1-ATPase and the bacterial flagellar motor in order to further understand the stepping mechanism, the mechanism of rotation, and the mechanochemical cycle. This chapter summarizes the major results of these efforts and discusses prospects for further investigations.

5.1   Backscattering Dark Field Microscope

After deenergized and photodamaged BFMs were observed to take 26 steps per revolution [208], it was clear that, in order to resolve steps under physiological conditions, a microscope capable of nanometer spatial resolution, at least 60μs temporal resolution, and providing sufficient contrast between the cell body and rotational marker would be required. With these design requirements in mind, the backscattering laser dark field microscope described in Chapter 2 was designed and constructed. Using a 100nm bead as a rotational marker and imaging with the high speed camera, this microscope is capable of sub-nm and 20μs resolution. In conjunction with Dr. Bradley

Steel, algorithms and programs were written to identify and track gold beads, extract angular positions, determine the speed of rotation, and calculate the stepping kinetics. These programs were developed for the analysis of F_1 data, then applied to the analysis of BFM data.

Most of the data collected and analyzed for this thesis used gold beads illuminated by a 633nm HeNe laser. However, as Section 4.5 demonstrates, gold nanorods present a potentially significant improvement over beads for angular measurements. The supercontinuum laser with a custom built filter allows for illumination of adjustable wavelength and bandwidth, which may be tuned to nanorods of any chosen dimension. The four polarization imaging pathway described in Section 2.3 allows for the recovery of the three dimensional orientation of an illuminated nanorod. It is expected that this method may quickly supersede the use of gold beads as rotational markers for both F_1 and the BFM, and initial experiments are in progress.

There are two additional modifications to this microscope under way which will greatly extend its capabilities. The first modification involves recording time. Due to memory limitations of the high speed camera, at the highest frame rate of 109kHz, only 16s worth of data may be recorded per sample. While the download time of this amount of data has recently improved from a few hours to about 25 minutes, this represents the most significant limitation to acquiring large amounts of high speed data. A custom built array of 25 avalanche photo diodes (APDs) is currently being constructed to replace the high speed camera. This array will have similar sensitivity to the high speed camera and will be able to acquire data at up to 250kHz. The APD arrary will reduce the amount of stored data by eliminating unnecessary pixels recorded by the camera, and most importantly, it will allow for continuous recording. Once in operation, this array will be able to double the amount of high speed data that has been acquired for this thesis in only three days of experiments.

The second modification planned for the dark field microscope is the ability to simultaneously image gold nanoparticles via backscattering dark field along with fluorescent molecules. Fluorescence illumination and imaging pathways are currently under construction. With the suppercontinuum laser capable of producing illumination from 400–2400nm, and with multiple dimensions (and thus excititations) of nanorods commercially available, this will allow the use of almost any fluorescent molecule in concert with gold nanorods.

5.2 F_1-ATPase

Chapter 3 presented evidence that both mesophilic EF_1 and wild type YF_1 from *S. cerevisiae* behave in a manner similar to TF_1 under laboratory conditions. The mechanochemical cycles of both EF_1 and YF_1 were determined to be qualitatively similar to TF_1, that is, the binding of an ATP molecule at the $0°$ position initiates an $85°$ rotation of the gamma subunit, whereupon ATP hydrolysis and phosphate release occur, and gamma rotates another $35°$ and awaits another ATP molecule. In the case of EF_1 and YF_1, the rate of rotation, ATP binding, and the combination of ATP hydrolysis and phosphate release are all faster than TF_1, measured at room temperature. The qualitatively similar behavior suggests that the knowledge gleaned of the mechanochemical cycle of TF_1 is relevant to F_1 from eukaryotic sources and can be compared to high resolution structures available for yeast and bovine F_1.

Chapter 3 also demonstrated that forms of F_1 which contained a single point mutation relative to wild type spent more time at the catalytic dwell. Kinetic analysis revealed that one of the two catalytic dwell processes was slowed, while the other remained relatively unchanged. From preliminary comparisons with the crystallographic data, it is hypothesized that group I *mgi* mutants are characterized by disrupted phosphate release, and group II *mgi* mutants are characterized by disrupted

ATP hydrolysis. While further investigations are needed to confirm these hypotheses, these experiments have demonstrated a direct comparison between single molecule investigations and high resolution crystal structures, and they have demonstrated that YF_1 can be used to investigate mutant forms of F_1. While crystallography provides insight into the exact effects of a mutation, crystal structures only capture one transient state of the enzyme's cycle. Single molecule data complements this with insight into the entire F_1 cycle. Future studies incorporating fluorescent ATP into the assay will help further determine the mechanism of theses mutations. There are also many molecules that inhibit the rotation of F_1, and crystal structures exist of the bovine enzyme inhibited by many such molecules [41, 47, 70, 75, 76, 324, 326, 339]. Future single molecule studies will hopefully provide insight into the mechanical pathway of this inhibition. Due to the highly shared homology between the bovine and yeast enzymes, YF_1 presents an ideal platform for these studies.

It is hoped that the use of nanorods will significantly improve the angular resolution of F_1 rotation. Some experiments in TF_1 have recorded an unknown third process occurring between the catalytic dwell and the waiting dwell [52,323]. A few of the YF_1 mutants investigated for this thesis hinted of a potential third process occurring during the catalysis dwell, also suggesting that there may still be an unidentified process in the mechanochemical cycle of F_1.

5.3 Bacterial Flagellar Motor

Contrary to earlier published results, the experiments performed on the BFM at low load for this thesis showed multiple distinct motor speeds, proposed to correspond to multiple stators in both the wild type and chimera motors. It appears that, as in the high load regime, the speed of the motor increases with the number of stator units engaged. As current models of the BFM have assumed that the speed

of the motor is independent of the number of stator units at low load, the results of these experiments change an underlying assumption of the BFM models. More long recordings of BFMs are necessary to properly characterize these speeds, both in wild type and at multiple SMFs in chimera. Curiously, the relationship between 1 and 2 stator speeds at different SMFs in the chimera is a linear one with a slope greater than two. This differs from the behavior at high load, is not predicted by any current model of the BFM, and is yet unexplained.

In addition to speed changes that occur with what has been presumed to be the addition or subtraction of one stator unit from the motor, at low load the motor also demonstrates transient 'toggles' to zero speed. This state can occur when any number of stators are engaged with the motor, and after the 'toggle', the motor either immediately returns to the previous speed, or immediately returns to a speed representative of one fewer stators in the motor. A potential explanation for this behavior is that a single stator jams the motor, and after some time, that stator either becomes unjammed, or falls out of the motor. The fact that the speed attributed to a stator falling out of a motor is lower than the speed prior to the jam would indicate that speed increases with stator number.

During the 'jammed' state, the mean squared displacement of the bead suggests bound Brownian motion of the motor within a potential well. The size of this well is about $\frac{1}{26th}$ of a revolution. This suggests that the 26 fold potential that creates the observed steps in the motor is still present during the 'jam'. Occasionally, motors driven by a single stator will experience a 'toggle' where the motor speed drops to zero and the mean squared displacement of the bead suggests that the motor is not trapped in a potential well and is free to diffuse, but at a rate much slower than free Brownian. These events could potentially represent the last stator falling out of the motor. Or, it may represent a situation similar to the 'jam' except the motor is able to hop over the 26 fold potential, leading to a discrete random walk which appears

to be Brownian motion with a small diffusion constant. However, these results are preliminary and the explanations are only conjectures at this point; the cause of these 'jammed' states of the motor is unknown.

At both high load and low load, the variance in the rotation rate of the BFM decreases linearly with speed, and if we believe the motor to be a Poisson stepper, the number of elementary steps increases with stator number. For a particular stator number, the relation between the variance in motor speed and speed is consistent with the expected behavior of a Poisson stepper for the chimera, but not necessarily for wild type. However, these results are based upon a small number of data points; more data is needed to evaluate the hypothesis that the BFM behaves as a Poisson stepper at low load.

Of all the high speed data acquired for this thesis, very few traces show distinct steps in the motor. Those that do are characterized by a nearly circular trajectory of the bead with small radial noise. However, these few traces begin to suggest answers to questions about the nature of the BFM's steps. These traces show the very first evidence that the 26 fold periodicity, observed initially in deenergized and potentially damaged chimeric cells, is still observed in fully energized and healthy chimeric cells. A few traces show that this 26 fold periodicity does not depend on stator number and that the phase of the periodicity is constant with the addition of stators. While QPD data showed 'jams' of the motor where the mean squared displacement of the bead suggests the motor is trapped in a potential well, high speed camera data shows that the position of the motor during such jams aligns with one of the stepping dwells of the motor. More high quality traces are currently being acquired to determine if these characteristics of the motor potential are true in all cases. If the number of steps of the motor is constant with stator number, this implies that the predicted step numbers measured in Chapter 3 using variance of motor speed correspond to

elementary steps of the motor as opposed to observed rotational steps. One candidate for the elementary steps is ion translocations.

Chapter 4 presented a preliminary kinetic analysis of the steps in the BFM, performed similarly to F_1 kinetic analyses. The dwell time histograms for most of the 26 dwells over three motors were best fit by two kinetic processes and a time offset. The angular noise in these traces was large enough such that there was significant cross contamination between dwells, which biases longer dwell times. In order to do a proper kinetic analysis for the BFM, there is a need for either cleaner traces with less angular noise, or potentially a probabilistic recovery of the bead angle. Initial data from nanorods attached to the hook of the BFM show significantly less angular noise, and it is hoped that rods will enable a full kinetic analysis of the BFM in the near future.

The set of BFM data acquired for this thesis is large and contains much information that has not been explored in this thesis. Further speed analyses are currently being performed on the additional wild type and chimera strains. The longer QPD traces will prove especially useful to construct speed histograms and to measure the rate at which stators join and leave a motor and the rate at which motors becomes 'jammed'. It is evident that additional traces with low angular noise and high time resolution are required for analyses of the number of steps the motor takes, the phase of the motor periodicity, and the kinetics of each step. With the use of nanorods instead of nanospheres and the use of the new APD arrary, we predict that large amounts of high quality data will be collected in a short amount of time. The protocols necessary for these experiments have been optimized, and the analysis algorithms are in place.

The original model by Xing and colleagues predicted a decrease in low load motor speed with increasing stator number. Their second model incorporated stator springs, producing a new prediction that motor speed at low load is independent of stator

number. Wingreen and colleagues and Meacci and Tu also predict a low load speed independent of stator number. However, the current models were created after Berg and colleagues concluded that motor speed was independent of stator number at low load. Therefore, the results of Chapter 4 showing multiple discrete speeds at low load require an alteration in each of these models. A kinetic model proposed by Ryu, Berry, and Berg [226] is able to reproduce increasing speed with increasing stator number at low load if the duty ratio of the stators is low. While a high duty ratio was originally assumed, the consequences of this parameter modification are worth exploration.

Berg and colleagues predict an increase in motor steps per revolution with increasing stator number, while Meacci and Tu predict a decrease. Xing and colleagues predict the number of steps will increase or stay the same, depending upon the position of the stator units and the flexibility of the stator springs, and Wingreen and colleagues predict that motor steps will be independent of the number of stators. Preliminary evidence suggests only the later two models correctly predict stepping behavior, and further experiments should determine whether the number of steps is always or sometimes constant. Finally, all of the models predict that the dwell time distribution will be well fit by a single exponential. Preliminary analysis suggests that a single exponential may be a poor fit to the distribution, but further experiments are necessary. It is expected that future experiments will continue to illuminate new motor characteristics, demanding a reconsideration of each of the current BFM models.

There are a few additional investigations that may prove fruitful for these experiments. As it is predicted that much of the angular noise stems from the flexible hook attachment, a method for stiffening the hook may provide cleaner traces. While it was hoped that crosslinking a biotinylated hook with steptavidin might achieve this, these experiments were unsuccessful. It may also be the case that the springs attach-

ing the stators to the peptidoglycan wall contribute to angular noise, and a manner of stiffening these springs might prove useful. Finally, these experiments beg to be combined with fluorescent microscopy in order to simultaneously observe the rotation of the motor and GFP labeled stators surrounding the motor. Such experiments will provide clarity to the analyses in Chapter 4 where the number of stators engaged with a motor and the addition and subtraction of stators was presumed via the speed recordings.

References

[1] *Pilizota T, Sowa Y, and Berry RM* (2009). *Handbook of Single Molecule Biophysics*, chapter Single Molecule Studies of Rotary Proteins. Springer.

[2] *Imada K, Minamino T, Tahara A, and Namba K* (01). *Proceedings of the National Academy of Sciences*, volume 104, chapter Structural similarity between the flagellar type III ATPase FliI and F_1-ATPase subunits, pages 485–490. National Academy of Sciences.

[3] *Kanazawa H, Mabuchi K, Kayano T, Noumi T, Sekiya T, and Futai M* (1981). Nucleotide sequence of the genes for F_O components of the proton-translocating ATPase from *Escherichia coli*: prediction of the primary structure of F_O subunits. *Biochemical and Biophysical Research Communications*, 103(2):613–620.

[4] *Walker JE, Fearnley IM, Gay NJ, Gibson BW, Northrop FD, Powell SJ, Runswick MJ, Saraste M, and Tybulewicz VL* (1985). Primary structure and subunit stoichiometry of F_1-ATPase from bovine mitochondria. *Journal of molecular biology*, 184(4):677–701.

[5] *Hudson GS, Mason JG, Holton TA, Koller B, Cox GB, Whitfeld PR, and Bottomley W* (1987). A gene cluster in the spinach and pea chloroplast genomes encoding one CF_1 and three CF_O subunits of the H^+-ATP synthase complex and the ribosomal protein S2. *Journal of molecular biology*, 196(2):283–298.

[6] *Boyer PD* (1993). The binding change mechanism for ATP synthase–some probabilities and possibilities. *Biochimica et biophysica acta*, 1140(3):215–250.

[7] *Boyer PD and Kohlbrenner WE* (1981). *Energy Coupling in Photosynthesis*, chapter Present status of the binding-change mechanism and its relation to ATP formation by chloroplasts, pages 231–241. North Holland Elsevier, B edition.

[8] *Abrahams JP, Leslie AG, Lutter R, and Walker JE* (1994). Structure at 2.8 Å resolution of F_1-ATPase from bovine heart mitochondria. *Nature*, 370(6491):621–8.

[9] *Noji H, Yasuda R, Yoshida M, and Kinosita KJ* (1997). Direct observation of the rotation of F_1-ATPase. *Nature*, 386(6622):299–302.

[10] *Engelbrecht S and Junge W* (1997). ATP synthase: a tentative structural model. *FEBS Letters*, 414(3):485–491.

[11] *Junge W, Lill H, and Engelbrecht S* (1997). ATP synthase: an electrochemical transducer with rotatory mechanics. *Trends in Biochemical Sciences*, 22(11):420–423.

[12] *Ueno H, Suzuki T, Kinosita K, and Yoshida M* (2005). ATP-driven stepwise rotation of F_OF_1-ATP synthase. *Proceedings of the National Academy of Sciences of the United States of America*, 102(5):1333–1338.

[13] *Tsunoda SP, Aggeler R, Yoshida M, and Capaldi RA* (2001). Rotation of the c subunit oligomer in fully functional F_1F_O ATP synthase. *Proceedings of the National Academy of Sciences of the United States of America*, 98(3):898–902.

[14] *Ishmukhametov R, Hornung T, Spetzler D, and Frasch WD* (2010). Direct observation of stepped proteolipid ring rotation in *E. coli* F_1-ATP synthase. *The EMBO Journal*, 29(23):3911–23.

[15] *Diez M, Zimmermann B, Börsch M, König M, Schweinberger E, Steigmiller S, Reuter R, Felekyan S, Kudryavtsev V, Seidel CAM, and Gräber P* (2004). Proton-powered subunit rotation in single membrane-bound F_OF_1-ATP synthase. *Nature structural & molecular biology*, 11(2):135–141.

[16] *Duser MG, Zarrabi N, Cipriano DJ, Ernst S, Glick GD, Dunn SD, and Borsch M* (2009). 36 degrees step size of proton-driven C-ring rotation in F_OF_1-ATP synthase. *The EMBO Journal*, 28(18):2689–96.

[17] *Watanabe R, Tabata KV, Iino R, Ueno H, Iwamoto M, Oiki S, and Noji H* (2013). Biased brownian stepping rotation of F_OF_1-ATP synthase driven by proton motive force. *Nature Communications*, 4:1631.

[18] *Stock D, Leslie AG, and Walker JE* (1999). Molecular architecture of the rotary motor in ATP synthase. *Science*, 286(5445):1700–5.

[19] *Baker LA, Watt IN, Runswick MJ, Walker JE, and Rubinstein JL* (2012). Arrangement of subunits in intact mammalian mitochondrial ATP synthase determined by cryo-em. *Proceedings of the National Academy of Sciences of the United States of America*, 109(29):11675–11680.

[20] *Wilkens S, Zhou J, Nakayama R, Dunn SD, and Capaldi RA* (2000). Localization of the delta subunit in the *Escherichia coli* F_1F_O-ATPsynthase by immuno electron microscopy: the delta subunit binds on top of the F_1. *Journal of molecular biology*, 295(3):387–391.

[21] *Stewart AG, Lee LK, Donohoe M, Chaston JJ, and Stock D* (2012). The dynamic stator stalk of rotary ATPases. *Nature Communications*, 3:687.

[22] *Rubinstein JL, Walker JE, and Henderson R* (2003). Structure of the mitochondrial ATP synthase by electron cryomicroscopy. *The EMBO Journal*, 22(23):6182–6192.

[23] *Schwem BE and Fillingame RH* (2006). Cross-linking between helices within subunit A of *Escherichia coli* ATP synthase defines the transmembrane packing of a four-helix bundle. *The Journal of Biological Chemistry*, 281(49):37861–37867.

[24] *Fillingame RH* (1996). Molecular rotary motors. *Science*, 286(5445):1687–1688.

[25] *Kabaleeswaran V, Puri N, Walker JE, Leslie AGW, and Mueller DM* (2006). Novel features of the rotary catalytic mechanism revealed in the structure of yeast F_1 ATPase. *The EMBO Journal*, 25(22):5433–5442.

[26] *Kabaleeswaran V, Shen H, Symersky J, Walker JE, Leslie AGW, and Mueller DM* (2009). Asymmetric structure of the yeast F_1 ATPase in the absence of bound nucleotides. *The Journal of Biological Chemistry*, 284(16):10546–10551.

[27] *Groth G and Pohl E* (2001). The structure of the chloroplast F_1-ATPase at 3.2 Å resolution. *The Journal of Biological Chemistry*, 276(2):1345–1352.

[28] *Hausrath AC, Grüber G, Matthews BW, and Capaldi RA* (1999). Structural features of the gamma subunit of the *Escherichia coli* F_1 ATPase revealed by a 4.4Å resolution map obtained by x-ray crystallography. *Proceedings of the National Academy of Sciences of the United States of America*, 96(24):13697–13702.

[29] *Rodgers AJ and Wilce MC* (2000). Structure of the gamma-epsilon complex of ATP synthase. *Nature structural biology*, 7(11):1051–1054.

[30] *Weber J, Muharemagic A, Wilke-Mounts S, and Senior AE* (2003). F_1F_O-ATP synthase. binding of delta subunit to a 22-residue peptide mimicking the N-terminal region of alpha subunit. *The Journal of Biological Chemistry*, 278(16):13623–13626.

[31] *McLachlin DT, Bestard JA, and Dunn SD* (1998). The b and delta subunits of the *Escherichia coli* ATP synthase interact via residues in their C-terminal regions. *The Journal of Biological Chemistry*, 273(24):15162–15168.

[32] *Wilkens S, Borchardt D, Weber J, and Senior AE* (2005). Structural characterization of the interaction of the delta and alpha subunits of the *Escherichia coli* F_1F_O-ATP synthase by NMR spectroscopy. *Biochemistry*, 44(35):11786–11794.

[33] *Rao R and Senior AE* (1987). The properties of hybrid F_1-ATPase enzymes suggest that a cyclical catalytic mechanism involving three catalytic sites occurs. *The Journal of Biological Chemistry*, 262(36):17450–17454.

[34] *Duncan TM, Bulygin VV, Zhou Y, Hutcheon ML, and Cross RL* (1995). Rotation of subunits during catalysis by *Escherichia coli* F_1-ATPase. *Proceedings of the National Academy of Sciences of the United States of America*, 92(24):10964–10968.

[35] *Sabbert D, Engelbrecht S, and Junge W* (1996). Intersubunit rotation in active F-ATPase. *Nature*, 381(6583):623–625.

[36] *Hutton RL and Boyer PD* (1979). Subunit interaction during catalysis. Alternating site cooperativity of mitochondrial adenosine triphosphatase. *Journal of Biological Chemistry*, 254(20):9990–3.

[37] *Boyer PD* (1989). Perspective of the binding change mechanism for ATP synthesis. *The FASEB Journal*, 3(10):2164–78.

[38] *Boyer PD* (1997). ATP synthase–a splendid molecular machine. *Annuale Review of Biochemistry*, 66:717–49.

[39] *Noji H, Hasler K, Junge W, Kinosita KJ, Yoshida M, and Engelbrecht S* (1999). Rotation of *Escherichia coli* F_1-ATPase. *Biochemical and Biophysical Research Communications*, 260(3):597–9.

[40] *Omote H, Sambonmatsu N, Saito K, Sambongi Y, Iwamoto-Kihara A, Yanagida T, Wada Y, and Futai M* (1999). The gamma-subunit rotation and torque generation in F_1-ATPase from wild-type or uncoupled mutant *Escherichia coli*. *Proceedings of the National Academy of Sciences of the United States of America*, 96(14):7780–4.

[41] *Bilyard T, Nakanishi-Matsui M, Steel BC, Pilizota T, Nord AL, Hosokawa H, Futai M, and Berry RM* (2013). High-resolution single-molecule characterization of the enzymatic states in *Escherichia coli* F_1-ATPase. *Philosophical transactions of the Royal Society of London. Series B, Biological sciences*, 368(1611):20120023.

[42] *Hisabori T, Kondoh A, and Yoshida M* (1999). Gamma subunit in chloroplast F_1-ATPase can rotate in a unidirectional and counter-clockwise manner. *FEBS Letters*, 463(1-2):35–8.

[43] *Yasuda R, Noji H, Kinosita KJ, and Yoshida M* (1998). F_1-ATPase is a highly efficient molecular motor that rotates with discrete 120 degree steps. *Cell*, 93(7):1117–24.

[44] *Gumbiowski K, Cherepanov D, Muller M, Panke O, Promto P, Winkler S, Junge W, and Engelbrecht S* (2001). F-ATPase: forced full rotation of the rotor despite covalent cross-link with the stator. *The Journal of Biological Chemistry*, 276(45):42287–92.

[45] *Muller M, Panke O, Junge W, and Engelbrecht S* (2002). F_1-ATPase, the C-terminal end of subunit gamma is not required for ATP hydrolysis-driven rotation. *The Journal of Biological Chemistry*, 277(26):23308–13.

[46] *Yasuda R, Noji H, Yoshida M, Kinosita KJ, and Itoh H* (2001). Resolution of distinct rotational substeps by submillisecond kinetic analysis of F_1-ATPase. *Nature*, 410(6831):898–904.

[47] *Hirono-Hara Y, Noji H, Nishiura M, Muneyuki E, Hara KY, Yasuda R, Kinosita KJ, and Yoshida M* (2001). Pause and rotation of F_1-ATPase during catalysis. *Proceedings of the National Academy of Sciences of the United States of America*, 98(24):13649–54.

[48] *Nakanishi-Matsui M, Kashiwagi S, Ubukata T, Iwamoto-Kihara A, Wada Y, and Futai M* (2007). Rotational catalysis of *Escherichia coli* ATP synthase F_1 sector. Stochastic fluctuation and a key domain of the beta subunit. *The Journal of Biological Chemistry*, 282(28):20698–704.

[49] *Nakanishi-Matsui M, Kashiwagi S, Hosokawa H, Cipriano DJ, Dunn SD, Wada Y, and Futai M* (2006). Stochastic high-speed rotation of *Escherichia coli* ATP synthase F_1 sector: the epsilon subunit-sensitive rotation. *The Journal of Biological Chemistry*, 281(7):4126–31.

[50] *Pilizota T, Bilyard T, Bai F, Futai M, Hosokawa H, and Berry RM* (2007). A programmable optical angle clamp for rotary molecular motors. *Biophysical Journal*, 93(1):264–75.

[51] *Nishimura N, Araki K, Shinahara W, Nakano Y, Nishimura K, Higashio H, and Sasaki T* (2008). Interaction of Rab3b with microtubule-binding protein Gas8 in NIH 3T3 cells. *Arch Biochem Biophys*, 474(1):136–42.

[52] *Sekiya M, Nakamoto RK, Al-Shawi MK, Nakanishi-Matsui M, and Futai M* (2009). Temperature dependence of single molecule rotation of the *Escherichia coli* ATP synthase F_1 sector reveals the importance of gamma-beta subunit interactions in the catalytic dwell. *The Journal of Biological Chemistry*, 284(33):22401–10.

[53] *Adachi K, Yasuda R, Noji H, Itoh H, Harada Y, Yoshida M, and Kinosita KJ* (2000). Stepping rotation of F_1-ATPase visualized through angle-resolved single-fluorophore imaging. *Proceedings of the National Academy of Sciences of the United States of America*, 97(13):7243–7.

[54] *Yasuda R, Masaike T, Adachi K, Noji H, Itoh H, and Kinosita KJ* (2003). The ATP-waiting conformation of rotating F_1-ATPase revealed by single-pair fluorescence resonance energy transfer. *Proceedings of the National Academy of Sciences of the United States of America*, 100(16):9314–8.

[55] *Borsch M, Diez M, Zimmermann B, Reuter R, and Graber P* (2002). Stepwise rotation of the gamma-subunit of EF_OF_1-ATP synthase observed by intramolecular single-molecule fluorescence resonance energy transfer. *FEBS Letters*, 527(1-3):147–52.

[56] *Diez M, Zimmermann B, Borsch M, Konig M, Schweinberger E, Steigmiller S, Reuter R, Felekyan S, Kudryavtsev V, Seidel CA, and Graber P* (2004). Proton-powered subunit rotation in single membrane-bound F_OF_1-ATP synthase. *Nature Structural & Molecular Biology*, 11(2):135–41.

[57] *Zimmermann B, Diez M, Zarrabi N, Graber P, and Borsch M* (2005). Movements of the epsilon-subunit during catalysis and activation in single membrane-bound H^+-ATP synthase. *The EMBO Journal*, 24(12):2053–63.

[58] *Spetzler D, Ishmukhametov R, Hornung T, Day LJ, Martin J, and Frasch WD* (2009). Single molecule measurements of F_1-ATPase reveal an interdependence between the power stroke and the dwell duration. *Biochemistry*, 48(33):7979–85.

[59] *Spetzler D, York J, Daniel D, Fromme R, Lowry D, and Frasch W* (2006). Microsecond time scale rotation measurements of single F_1-ATPase molecules. *Biochemistry*, 45(10):3117–24.

[60] *Rondelez Y, Tresset G, Tabata KV, Arata H, Fujita H, Takeuchi S, and Noji H* (2005). Microfabricated arrays of femtoliter chambers allow single molecule enzymology. *Nature Biotechnology*, 23(3):361–5.

[61] *Itoh H, Takahashi A, Adachi K, Noji H, Yasuda R, Yoshida M, and Kinosita K* (2004). Mechanically driven ATP synthesis by F_1-ATPase. *Nature*, 427(6973):465–8.

[62] *Rondelez Y, Tresset G, Nakashima T, Kato-Yamada Y, Fujita H, Takeuchi S, and Noji H* (2005). Highly coupled ATP synthesis by F_1-ATPase single molecules. *Nature*, 433(7027):773–7.

[63] *Sone N, Yoshida M, Hirata H, and Kagawa Y* (1975). Purification and properties of a dicyclohexylcarbodiimide-sensitive adenosine triphosphatase from a thermophilic bacterium. *Journal of Biological Chemistry*, 250(19):7917–23.

[64] *Yoshida M, Sone N, Hirata H, and Kagawa Y* (1975). A highly stable adenosine triphosphatase from a thermophillie bacterium. purification, properties, and reconstitution. *The Journal of Biological Chemistry*, 250(19):7910–7916.

[65] *Sakaki N, Shimo-Kon R, Adachi K, Itoh H, Furuike S, Muneyuki E, Yoshida M, and Kinosita KJ* (2005). One rotary mechanism for F_1-ATPase over ATP concentrations from millimolar down to nanomolar. *Biophysical Journal*, 88(3):2047–56.

[66] *Shimabukuro K, Yasuda R, Muneyuki E, Hara KY, Kinosita KJ, and Yoshida M* (2003). Catalysis and rotation of F_1 motor: cleavage of ATP at the catalytic site occurs in 1 ms before 40 degree substep rotation. *Proceedings of the National Academy of Sciences of the United States of America*, 100(25):14731–6.

[67] *Nishizaka T, Oiwa K, Noji H, Kimura S, Muneyuki E, Yoshida M, and Kinosita KJ* (2004). Chemomechanical coupling in F_1-ATPase revealed by simultaneous observation of nucleotide kinetics and rotation. *Nature Structural & Molecular Biology*, 11(2):142–8.

[68] *Adachi K, Oiwa K, Nishizaka T, Furuike S, Noji H, Itoh H, Yoshida M, and Kinosita KJ* (2007). Coupling of rotation and catalysis in F_1-ATPase revealed by single-molecule imaging and manipulation. *Cell*, 130(2):309–21.

[69] *Watanabe R, Iino R, Shimabukuro K, Yoshida M, and Noji H* (2008). Temperature-sensitive reaction intermediate of F_1-ATPase. *EMBO reports*, 9(1):84–90.

[70] *Watanabe R, Iino R, and Noji H* (2010). Phosphate release in F_1-ATPase catalytic cycle follows ADP release. *Nat Chem Biol*, 6(11):814–20.

[71] *Jault JM, Matsui T, Jault FM, Kaibara C, Muneyuki E, Yoshida M, Kagawa Y, and Allison WS* (1995). The alpha 3 beta 3 gamma complex of the F_1-ATPase from thermophilic *Bacillus* PS3 containing the alpha D261N substitution fails to dissociate inhibitory MgADP from a catalytic site when ATP binds to non-catalytic sites. *Biochemistry*, 34(50):16412–16418.

[72] *Hirono-Hara Y, Ishizuka K, Kinosita KJ, Yoshida M, and Noji H* (2005). Activation of pausing F_1 motor by external force. *Proceedings of the National Academy of Sciences of the United States of America*, 102(12):4288–93.

[73] *Jault JM, Dou C, Grodsky NB, Matsui T, Yoshida M, and Allison WS* (1996). The alpha3beta3gamma subcomplex of the F_1-ATPase from the thermophilic Bacillus PS3 with the betaT165S substitution does not entrap inhibitory MgADP in a catalytic site during turnover. *The Journal of Biological Chemistry*, 271(46):28818–28824.

[74] *Furuike S, Adachi K, Sakaki N, Shimo-Kon R, Itoh H, Muneyuki E, Yoshida M, and Kinosita KJ* (2008). Temperature dependence of the rotation and hydrolysis activities of F_1-ATPase. *Biophysical Journal*, 95(2):761–70.

[75] *Ariga T, Muneyuki E, and Yoshida M* (2007). F_1-ATPase rotates by an asymmetric, sequential mechanism using all three catalytic subunits. *Nature Structural & Molecular Biology*, 14(9):841–6.

[76] *Shimo-Kon R, Muneyuki E, Sakai H, Adachi K, Yoshida M, and Kinosita K* (2010). Chemo-mechanical coupling in F_1-ATPase revealed by catalytic site occupancy during catalysis. *Biophysical Journal*, 98(7):1227–1236.

[77] *Iino R and Noji H* (2013). Operation mechanism of F_O F_1-adenosine triphosphate synthase revealed by its structure and dynamics. *IUBMB Life*, 65(3):238–246.

[78] *Panke O, Cherepanov DA, Gumbiowski K, Engelbrecht S, and Junge W* (2001). Viscoelastic dynamics of actin filaments coupled to rotary F-ATPase: angular torque profile of the enzyme. *Biophysical Journal*, 81(3):1220–33.

[79] *Cherepanov DA and Junge W* (2001). Viscoelastic dynamics of actin filaments coupled to rotary f-ATPase: curvature as an indicator of the torque. *Biophysical journal*, 81(3):1234–1244.

[80] *Berg JM, Tymoczko JL, and Stryer L* (2002). *Biochemistry*. W. H. Freeman, 5th edition.

[81] *Hackney DD, Rosen G, and Boyer PD* (1979). Subunit interaction during catalysis: alternating site cooperativity in photophosphorylation shown by substrate modulation of [18O]ATP species formation. *Proceedings of the National Academy of Sciences of the United States of America*, 76(8).

[82] *Elston T, Wang H, and Oster G* (1998). Energy transduction in ATP synthase. *Nature*, 391(6666):510–3.

[83] *Oster G and Wang H* (2000). Reverse engineering a protein: the mechanochemistry of ATP synthase. *Biochimica et biophysica acta*, 1458(2-3):482–510.

[84] *Kinosita KJ, Adachi K, and Itoh H* (2004). Rotation of F_1-ATPase: how an ATP-driven molecular machine may work. *Annual Review of Biophysics and Biomolecular Structure*, 33:245–68.

[85] *Berg HC and Anderson RA* (1973). Bacteria swim by rotating their flagellar filaments. *Nature*, 245(5425):380–2.

[86] *Silverman M and Simon M* (1974). Flagellar rotation and the mechanism of bacterial motility. *Nature*, 249(452):73–4.

[87] *Berry RM and Armitage JP* (1999). The bacterial flagella motor. *Advances in Microbial Physiology*, 41:291–337.

[88] *Macnab RM* (1996). *Eschericia coli and Salmonella: Cellular and Molecular Biology*, chapter Flagella and motility, pages 123–45. American Society for Microbiology, Washington, D.C.

[89] *Blair DF* (1995). How bacteria sense and swim. *Annual Review of Microbiology*, 49:489–522.

[90] *Falke JJ, Bass RB, Butler SL, Chervitz SA, and Danielson MA* (1997). The two-component signaling pathway of bacterial chemotaxis: a molecular view of signal transduction by receptors, kinases, and adaptation enzymes. *Annual Review of Cell and Developmental Biology*, 13:457–512.

[91] *Wadhams GH and Armitage JP* (2004). Making sense of it all: bacterial chemotaxis. *Nature Reviews Molecular Cell Biology*, 5(12):1024–37.

[92] *Baker MD, Wolanin PM, and Stock JB* (2006). Signal transduction in bacterial chemotaxis. *BioEssays*, 28(1):9–22.

[93] *Fukuoka H, Inoue Y, Terasawa S, Takahashi H, and Ishijima A* (2010). Exchange of rotor components in functioning bacterial flagellar motor. *Biochemical Biophysical Research Communications*, 394(1):130–5.

[94] *Berg HC and Brown DA* (1972). Chemotaxis in *Escherichia coli* analysed by three-dimensional tracking. *Nature*, 239(5374):500–4.

[95] *Turner L, Ryu WS, and Berg HC* (2000). Real-time imaging of fluorescent flagellar filaments. *Journal of Bacteriology*, 182(10):2793–801.

[96] *Darnton NC, Turner L, Rojevsky S, and Berg HC* (2007). On torque and tumbling in swimming *Escherichia coli*. *Journal of Bacteriology*, 189(5):1756–64.

[97] *Kim M, Bird JC, Van Parys AJ, Breuer KS, and Powers TR* (2003). A macroscopic scale model of bacterial flagellar bundling. *Proceedings of the National Academy of Sciences of the United States of America*, 100(26):15481–5.

[98] *Berg HC and Brown DA* (1974). Chemotaxis in *Escherichia coli* analyzed by three-dimensional tracking. *Antibiotics and Chemotherapy*, 19:55–78.

[99] *Berg HC and Tedesco PM* (1975). Transient response to chemotactic stimuli in *Escherichia coli*. *Proceedings of the National Academy of Sciences of the United States of America*, 72(8):3235–3239.

[100] *Berg HC* (2003). *E. coli in Motion*. Springer, New York, 1st edition.

[101] *Sourjik V* (2004). Receptor clustering and signal processing in *E. coli* chemotaxis. *Trends in Microbiology*, 12(12):569–76.

[102] *Hazelbauer GL, Falke JJ, and Parkinson JS* (2008). Bacterial chemoreceptors: high-performance signaling in networked arrays. *Trends in Biochemical Sciences*, 33(1):9–19.

[103] *Bai F, Branch RW, Nicolau DV, Pilizota T, Steel BC, Maini PK, and Berry RM* (2010). Conformational spread as a mechanism for cooperativity in the bacterial flagellar switch. *Science (New York, N.Y.)*, 327(5966):685–689.

[104] *Berg HC* (2003). Rotary motor of bacterial flagella. *Annual Review of Biochemistry*, 72(1):19–54.

[105] *DePamphilis ML and Adler J* (1971). Attachment of flagellar basal bodies to the cell envelope: specific attachment to the outer, lipopolysaccharide membrane and the cyoplasmic membrane. *Journal of Bacteriology*, 105(1):396–407.

[106] *DePamphilis ML and Adler J* (1971). Fine structure and isolation of the hook-basal body complex of flagella from *Escherichia coli* and *Bacillus subtilis*. *Journal of Bacteriology*, 105(1):384–95.

[107] *Ueno T, Oosawa K, and Aizawa S* (1992). M ring, S ring and proximal rod of the flagellar basal body of *Salmonella typhimurium* are composed of subunits of a single protein, FliF. *Journal of Molecular Biology*, 227(3):672–7.

[108] *Ueno T, Oosawa K, and Aizawa S* (1994). Domain structures of the MS ring component protein FliF of the flagellar basal body of *Salmonella typhimurium*. *Journal of Molecular Biology*, 236(2):546–55.

[109] *Suzuki H, Yonekura K, and Namba K* (2004). Structure of the rotor of the bacterial flagellar motor revealed by electron cryomicroscopy and single-particle image analysis. *Journal of Molecular Biology*, 337(1):105–13.

[110] *Aizawa SI* (1996). Flagellar assembly in *Salmonella typhimurium*. *Molecular Microbiology*, 19(1):1–5.

[111] *Macnab RM* (2003). How bacteria assemble flagella. *Annual Review of Microbiology*, 57:77–100.

[112] *Kubori T, Yamaguchi S, and Aizawa S* (1997). Assembly of the switch complex onto the MS ring complex of *Salmonella typhimurium* does not require any other flagellar proteins. *Journal of Bacteriology*, 179(3):813–817.

[113] *Fan F, Ohnishi K, Francis NR, and Macnab RM* (1997). FliP and FliR proteins of *Salmonella typhimurium*, putative components of the type III flagellar export apparatus, are located in the flagellar basal body. *Molecular Microbiology*, 26(5):1035–1046.

[114] *Ohnishi K, Fan F, Schoenhals GJ, Kihara M, and Macnab RM* (1997). FliO, FliP, FliQ, and FliR proteins of *Salmonella typhimurium*: putative components for flagellar assembly. *Journal of Bacteriology*, 179(19):6092–6099.

[115] *Minamino T and MacNab RM* (2000). Interactions among components of the-salmonellaflagellar export apparatus and its substrates. *Molecular Microbiology*, 35(5):1052–64.

[116] *Minamino T and Macnab RM* (1999). Components of the *Salmonella* flagellar export apparatus and classification of export substrates. *Journal of Bacteriology*, 181(5):1388–94.

[117] *Kihara M, Minamino T, Yamaguchi S, and Macnab RM* (2001). Intergenic suppression between the flagellar MS ring protein FliF of *Salmonella* and FlhA, a membrane component of its export apparatus. *Journal of Bacteriology*, 183(5):1655–62.

[118] *Kubori T, Shimamoto N, Yamaguchi S, Namba K, and Aizawa S* (1992). Morphological pathway of flagellar assembly in *Salmonella typhimurium*. *Journal of Molecular Biology*, 226(2):433–46.

[119] *Katayama E, Shiraishi T, Oosawa K, Baba N, and Aizawa S* (1996). Geometry of the flagellar motor in the cytoplasmic membrane of *Salmonella typhimurium* as determined by stereo-photogrammetry of quick-freeze deep-etch replica images. *Journal of Molecular Biology*, 255(3):458–75.

[120] *Lloyd SA, Whitby FG, Blair DF, and Hill CP* (1999). Structure of the C-terminal domain of FliG, a component of the rotor in the bacterial flagellar motor. *Nature*, 400(6743):472–5.

[121] *Irikura VM, Kihara M, Yamaguchi S, Sockett H, and Macnab RM* (1993). *Salmonella typhimurium* FliG and FliN mutations causing defects in assembly, rotation, and switching of the flagellar motor. *Journal of Bacteriology*, 175(3):802–10.

[122] *Thomas DR, Francis NR, Xu C, and DeRosier DJ* (2006). The three-dimensional structure of the flagellar rotor from a clockwise-locked mutant of *Salmonella entericaserovar Typhimurium*. *Journal of Bacteriology*, 188(20):7039–48.

[123] *Morimoto YV, Nakamura S, Hiraoka KD, Namba K, and Minamino T* (2013). Distinct roles of highly conserved charged residues at the MotA-FliG interface in bacterial flagellar motor rotation. *Journal of Bacteriology*, 195(3):474–481.

[124] *Jones CJ, Macnab RM, Okino H, and Aizawa S* (1990). Stoichiometric analysis of the flagellar hook-basal-body complex of *Salmonella typhimurium*. *Journal of Molecular Biology*, 212(2):377–87.

[125] *Thomas D, Morgan DG, and DeRosier DJ* (2001). Structures of bacterial flagellar motors from two FliF-FliG gene fusion mutants. *Journal of Bacteriology*, 183(21):6404–12.

[126] *Francis NR, Irikura VM, Yamaguchi S, DeRosier DJ, and Macnab RM* (1992). Localization of the *Salmonella typhimurium* flagellar switch protein FliG to the cytoplasmic M-ring face of the basal body. *Proceedings of the National Academy of Sciences of the United States of America*, 89(14):6304–8.

[127] *Marykwas DL, Schmidt SA, and Berg HC* (1996). Interacting components of the flagellar motor of *Escherichia coli* revealed by the two-hybrid system in yeast. *Journal of Molecular Biology*, 256(3):564–76.

[128] *Oosawa K, Ueno T, and Aizawa S* (1994). Overproduction of the bacterial flagellar switch proteins and their interactions with the MS ring complex in vitro. *Journal of Bacteriology*, 176(12):3683–91.

[129] *Kihara M, Miller GU, and Macnab RM* (2000). Deletion analysis of the flagellar switch protein FliG of *Salmonella*. *Journal of Bacteriology*, 182(11):3022–8.

[130] *Levenson R, Zhou H, and Dahlquist FW* (2012). Structural insights into the interaction between the bacterial flagellar motor proteins FliF and FliG. *Biochemistry*, 51(25):5052–5060.

[131] *Thomas DR, Morgan DG, and DeRosier DJ* (1999). Rotational symmetry of the C ring and a mechanism for the flagellar rotary motor. *Proceedings of the National Academy of Sciences of the United States of America*, 96(18):10134–9.

[132] *Zhao R, Pathak N, Jaffe H, Reese TS, and Khan S* (1996). FliN is a major structural protein of the C-ring in the *Salmonella typhimurium* flagellar basal body. *Journal of Molecular Biology*, 261(2):195–208.

[133] *Toker AS and Macnab RM* (1997). Distinct regions of bacterial flagellar switch protein FliM interact with FliG, FliN and CheY. *Journal of Molecular Biology*, 273(3):623–34.

[134] *Tang H, Braun TF, and Blair DF* (1996). Motility protein complexes in the bacterial flagellar motor. *Journal of Molecular Biology*, 261(2):209–21.

[135] *Brown PN, Mathews MA, Joss LA, Hill CP, and Blair DF* (2005). Crystal structure of the flagellar rotor protein FliN from *Thermotoga maritima. Journal of Bacteriology*, 187(8):2890–902.

[136] *Brown PN, Terrazas M, Paul K, and Blair DF* (2007). Mutational analysis of the flagellar protein FliG: sites of interaction with FliM and implications for organization of the switch complex. *Journal of Bacteriology*, 189(2):305–12.

[137] *Lee LK, Ginsburg MA, Crovace C, Donohoe M, and Stock D* (2010). Structure of the torque ring of the flagellar motor and the molecular basis for rotational switching. *Nature*, 466(7309):996–1000.

[138] *Vartanian AS, Paz A, Fortgang EA, Abramson J, and Dahlquist FW* (2012). Structure of flagellar motor proteins in complex allows for insights into motor structure and switching. *The Journal of Biological Chemistry*, 287(43):35779–35783.

[139] *Young HS, Dang H, Lai Y, DeRosier DJ, and Khan S* (2003). Variable symmetry in *Salmonella typhimurium* flagellar motors. *Biophysical Journal*, 84(1):571–7.

[140] *Chen S, Beeby M, Murphy GE, Leadbetter JR, Hendrixson DR, Briegel A, Li Z, Shi J, Tocheva EI, Müller A, Dobro MJ, and Jensen GJ* (2011). Structural diversity of bacterial flagellar motors. *The EMBO Journal*, 30(14):2972–2981.

[141] *Lee LK, Ginsburg MA, Crovace C, Donohoe M, and Stock D* (2010). Structure of the torque ring of the flagellar motor and the molecular basis for rotational switching. *Nature*, 466(7309):996–1000.

[142] *Sowa Y and Berry RM* (2008). Bacterial flagellar motor. *Quarterly reviews of biophysics*, 41(2):103–132.

[143] *Blair DF and Berg HC* (1991). Mutations in the MotA protein of *Escherichia coli* reveal domains critical for proton conduction. *Journal of Molecular Biology*, 221(4):1433–42.

[144] *Sato K and Homma M* (2000). Multimeric structure of PomA, a component of the Na$^+$-driven polar flagellar motor of *Vibrio alginolyticus*. *Journal of Biological Chemistry*, 275(26):20223–8.

[145] *Kojima S and Blair DF* (2004). Solubilization and purification of the MotA/MotB complex of *Escherichia coli*. *Biochemistry*, 43(1):26–34.

[146] *Braun TF, Al-Mawsawi LQ, Kojima S, and Blair DF* (2004). Arrangement of core membrane segments in the MotA/MotB proton-channel complex of *Escherichia coli*. *Biochemistry*, 43(1):35–45.

[147] *Sato K and Homma M* (2000). Functional reconstitution of the Na$^+$-driven polar flagellar motor component of *Vibrio alginolyticus*. *Journal of Biological Chemistry*, 275(8):5718–22.

[148] *Yorimitsu T, Kojima M, Yakushi T, and Homma M* (2004). Multimeric structure of the PomA/PomB channel complex in the Na$^+$-driven flagellar motor of *Vibrio alginolyticus*. *Journal of Biochemistry (Tokyo)*, 135(1):43–51.

[149] *Dean GE, Macnab RM, Stader J, Matsumura P, and Burks C* (1984). Gene sequence and predicted amino acid sequence of the MotA protein, a membrane-associated protein required for flagellar rotation in *Escherichia coli*. *Journal of Bacteriology*, 159(3):991–9.

[150] *Zhou J, Fazzio RT, and Blair DF* (1995). Membrane topology of the MotA protein of *Escherichia coli*. *Journal of Molecular Biology*, 251(2):237–42.

[151] *Stader J, Matsumura P, Vacante D, Dean GE, and Macnab RM* (1986). Nucleotide sequence of the *Escherichia coli* MotB gene and site-limited incorporation of its product into the cytoplasmic membrane. *Journal of Bacteriology*, 166(1):244–252.

[152] *Chun SY and Parkinson JS* (1988). Bacterial motility: membrane topology of the *Escherichia coli* MotB protein. *Science*, 239(4837):276–8.

[153] *Sharp LL, Zhou J, and Blair DF* (1995). Features of MotA proton channel structure revealed by tryptophan-scanning mutagenesis. *Proceedings of the National Academy of Sciences of the United States of America*, 92(17):7946–50.

[154] *Sharp LL, Zhou J, and Blair DF* (1995). Tryptophan-scanning mutagenesis of MotB, an integral membrane protein essential for flagellar rotation in *Escherichia coli*. *Biochemistry*, 34(28):9166–71.

[155] *Braun TF and Blair DF* (2001). Targeted disulfide cross-linking of the MotB protein ofescherichia *coli*: evidence for two H$^+$channels in the stator complex. *Biochemistry*, 40(43):13051–9.

[156] *Zhou J, Sharp LL, Tang HL, Lloyd SA, Billings S, Braun TF, and Blair DF* (1998). Function of protonatable residues in the flagellar motor of *Escherichia coli*: a critical role for Asp 32 of MotB. *Journal of Bacteriology*, 180(10):2729–35.

[157] *Garza AG, Harris-Haller LW, Stoebner RA, and Manson MD* (1995). Motility protein interactions in the bacterial flagellar motor. *Proceedings of the National Academy of Sciences of the United States of America*, 92(6):1970–4.

[158] *Lloyd SA, Tang H, Wang X, Billings S, and Blair DF* (1996). Torque generation in the flagellar motor of *Escherichia coli*: evidence of a direct role for FliG but not for FliM or FliN. *Journal of Bacteriology*, 178(1):223–31.

[159] *Garza AG, Bronstein PA, Valdez PA, Harris-Haller LW, and Manson MD* (1996). Extragenic suppression of MotA missense mutations of *Escherichia coli. Journal of Bacteriology*, 178(21):6116–22.

[160] *Garza AG, Biran R, Wohlschlegel JA, and Manson MD* (1996). Mutations in MotB suppressible by changes in stator or rotor components of the bacterial flagellar motor. *Journal of Molecular Biology*, 258(2):270–85.

[161] *Zhou J, Lloyd SA, and Blair DF* (1998). Electrostatic interactions between rotor and stator in the bacterial flagellar motor. *Proceedings of the National Academy of Sciences of the United States of America*, 95(11):6436–41.

[162] *De Mot R and Vanderleyden J* (1994). The C-terminal sequence conservation between OmpA-related outer membrane proteins and MotB suggests a common function in both gram-positive and gram-negative bacteria, possibly in the interaction of these domains with peptidoglycan. *Molecular Microbiology*, 12(2):333–4.

[163] *Berg HC* (1974). Dynamic properties of bacterial flagellar motors. *Nature*, 249(452):77–9.

[164] *Lloyd SA and Blair DF* (1997). Charged residues of the rotor protein FliG essential for torque generation in the flagellar motor of *Escherichia coli. Journal of Molecular Biology*, 266(4):733–44.

[165] *Zhou J and Blair DF* (1997). Residues of the cytoplasmic domain of MotA essential for torque generation in the bacterial flagellar motor. *Journal of Molecular Biology*, 273(2):428–39.

[166] *Yakushi T, Yang J, Fukuoka H, Homma M, and Blair DF* (2006). Roles of charged residues of rotor and stator in flagellar rotation: comparative study

using H$^+$-driven and Na$^+$-driven motors in *Escherichia coli*. *Journal of Bacteriology*, 188(4):1466–72.

[167] *Kojima S and Blair DF* (2001). Conformational change in the stator of the bacterial flagellar motor. *Biochemistry*, 40(43):13041–50.

[168] *Braun TF, Poulson S, Gully JB, Empey JC, Van Way S, Putnam A, and Blair DF* (1999). Function of proline residues of MotA in torque generation by the flagellar motor of *Escherichia coli*. *Journal of Bacteriology*, 181(11):3542–51.

[169] *Murphy GE, Leadbetter JR, and Jensen GJ* (2006). In situ structure of the complete treponema primitia flagellar motor. *Nature*, 442(7106):1062–4.

[170] *Kudryashev M, Cyrklaff M, Wallich R, Baumeister W, and Frischknecht F* (2010). Distinct in situ structures of the *Borrelia* flagellar motor. *Journal of Structural Biology*, 169(1):54–61.

[171] *Liu J, Lin T, Botkin DJ, McCrum E, Winkler H, and Norris SJ* (2009). Intact flagellar motor of *Borrelia burgdorferi* revealed by cryo-electron tomography: evidence for stator ring curvature and rotor/C-ring assembly flexion. *Journal of Bacteriology*, 191(16):5026–36.

[172] *Liu J, Howell JK, Bradley SD, Zheng Y, Zhou ZH, and Norris SJ* (2010). Cellular architecture of treponema pallidum: novel flagellum, periplasmic cone, and cell envelope as revealed by cryo electron tomography. *Journal of molecular biology*, 403(4):546–561.

[173] *Reid SW, Leake MC, Chandler JH, Lo CJ, Armitage JP, and Berry RM* (2006). The maximum number of torque-generating units in the flagellar motor of *Escherichia coli* is at least 11. *Proceedings of the National Academy of Sciences of the United States of America*, 103(21):8066–71.

[174] *Leake MC, Chandler JH, Wadhams GH, Bai F, Berry RM, and Armitage JP* (2006). Stoichiometry and turnover in single, functioning membrane protein complexes. *Nature*, 443(7109):355–8.

[175] *Morimoto YV, Nakamura S, Kami-ike N, Namba K, and Minamino T* (2010). Charged residues in the cytoplasmic loop of MotA are required for stator assembly into the bacterial flagellar motor. *Molecular Microbiology*, 78(5):1117–1129.

[176] *Block SM and Berg HC* (1984). Successive incorporation of force-generating units in the bacterial rotary motor. *Nature*, 309(5967):470–2.

[177] *Blair DF and Berg HC* (1988). Restoration of torque in defective flagellar motors. *Science*, 242(4886):1678–81.

[178] *Samatey FA, Matsunami H, Imada K, Nagashima S, Shaikh TR, Thomas DR, Chen JZ, Derosier DJ, Kitao A, and Namba K* (2004). Structure of the bacterial flagellar hook and implication for the molecular universal joint mechanism. *Nature*, 431(7012):1062–8.

[179] *Hirano T, Yamaguchi S, Oosawa K, and Aizawa S* (1994). Roles of FliK and FlhB in determination of flagellar hook length in *Salmonella typhimurium. Journal of Bacteriology*, 176(17):5439–49.

[180] *Brown MT, Steel BC, Silvestrin C, Wilkinson DA, Delalez NJ, Lumb CN, Obara B, Armitage JP, and Berry RM* (2012). Flagellar hook flexibility is essential for bundle formation in swimming *Escherichia coli* cells. *Journal of Bacteriology*, 194(13):3495–3501.

[181] *Yonekura K, Maki-Yonekura S, and Namba K* (2003). Complete atomic model of the bacterial flagellar filament by electron cryomicroscopy. *Nature*, 424(6949):643–50.

[182] *Samatey FA, Imada K, Nagashima S, Vonderviszt F, Kumasaka T, Yamamoto M, and Namba K* (2001). Structure of the bacterial flagellar protofilament and implications for a switch for supercoiling. *Nature*, 410(6826):331–7.

[183] *Asakura S* (1970). Polymerization of flagellin and polymorphism of flagella. *Advances in Biophysics*, 1:99–155.

[184] *Hasegawa K, Yamashita I, and Namba K* (1998). Quasi- and nonequivalence in the structure of bacterial flagellar filament. *Biophysical Journal*, 74(1):569–75.

[185] *Minamino T and Namba K* (2004). Self-assembly and type III protein export of the bacterial flagellum. *Journal of Molecular Microbiology and Biotechnology*, 7(1-2):5–17.

[186] *Kojima S and Blair DF* (2004). The bacterial flagellar motor: structure and function of a complex molecular machine. *International Reveiw of Cytology*, 233:93–134.

[187] *Suzuki H, Yonekura K, Murata K, Hirai T, Oosawa K, and Namba K* (1998). A structural feature in the central channel of the bacterial flagellar FliF ring complex is implicated in type III protein export. *Journal of Structural Biology*, 124(2-3):104–14.

[188] *Terashima H, Kojima S, and Homma M* (2008). Flagellar motility in bacteria structure and function of flagellar motor. *International Review of Cell and Molecular Biology*, 270:39–85.

[189] *Minamino T, Imada K, and Namba K* (2008). Molecular motors of the bacterial flagella. *Current Opinion in Structural Biology*, 18(6):693–701.

[190] *Reynolds O* (1883). An experimental investigation of the circumstances which determine whether the motion of water shall be direct or sinuous, and of the law of resistance in parallel channels. *Proceedings of the Royal Society of London*, 35(224-226):84–99.

[191] *Purcell EM* (1977). Life at low reynolds number. *American Journal of Physics.*, 45(1):3–11.

[192] *Berg HC* (1983). *Random Walks in Biology.* Princeton University Press, 2nd edition.

[193] *Manson MD, Tedesco P, Berg HC, Harold FM, and Van der Drift C* (1977). A protonmotive force drives bacterial flagella. *Proceedings of the National Academy of Sciences of the United States of America*, 74(7):3060–4.

[194] *Matsuura S, Shioi J, and Imae Y* (1977). Motility in *Bacillus subtilis* driven by an artificial protonmotive force. *FEBS Letters*, 82(2):187–90.

[195] *Fung DC and Berg HC* (1995). Powering the flagellar motor of *Escherichia coli* with an external voltage source. *Nature*, 375(6534):809–12.

[196] *Gabel CV and Berg HC* (2003). Speed of the flagellar rotary motor of *Escherichia coli* varies linearly with protonmotive force. *Proceedings of the National Academy of Sciences of the United States of America*, 100(15):8748–51.

[197] *Imae Y and Atsumi T* (1989). Na^+-driven bacterial flagellar motors. *Journal of Bioenergetic and Biomembranes*, 21(6):705–16.

[198] *Yorimitsu T and Homma M* (2001). Na^+-driven flagellar motor of *Vibrio*. *Biochim Biophys Acta*, 1505(1):82–93.

[199] *Khan S and Macnab RM* (1980). Proton chemical potential, proton electrical potential and bacterial motility. *Journal of Molecular Biology*, 138(3):599–614.

[200] *Khan S and Macnab RM* (1980). The steady-state counterclockwise/clockwise ratio of bacterial flagellar motors is regulated by protonmotive force. *Journal of Molecular Biology*, 138(3):563–97.

[201] *Ravid S and Eisenbach M* (1984). Minimal requirements for rotation of bacterial flagella. *Journal of Bacteriology*, 158(3):1208–10.

[202] *Asai Y, Kojima S, Kato H, Nishioka N, Kawagishi I, and Homma M* (1997). Putative channel components for the fast-rotating sodium-driven flagellar motor of a marine bacterium. *Journal of Bacteriology*, 179(16):5104–10.

[203] *Magariyama Y, Sugiyama S, Muramoto K, Maekawa Y, Kawagishi I, Imae Y, and Kudo S* (1994). Very fast flagellar rotation. *Nature*, 371(6500):752.

[204] *Muramoto K, Kawagishi I, Kudo S, Magariyama Y, Imae Y, and Homma M* (1995). High-speed rotation and speed stability of the sodium-driven flagellar motor in *Vibrio alginolyticus*. *Journal of Molecular Biology*, 251(1):50–8.

[205] *Asai Y, Yakushi T, Kawagishi I, and Homma M* (2003). Ion-coupling determinants of Na^+-driven and H^+-driven flagellar motors. *Journal of Molecular Biology*, 327(2):453–63.

[206] *Lo CJ, Leake MC, Pilizota T, and Berry RM* (2007). Nonequivalence of membrane voltage and ion-gradient as driving forces for the bacterial flagellar motor at low load. *Biophysical Journal*, 93(1):294–302.

[207] *Lo CJ, Leake MC, and Berry RM* (2006). Fluorescence measurement of intracellular sodium concentration in single *Escherichia coli* cells. *Biophysical Journal*, 90(1):357–65.

[208] *Sowa Y, Rowe AD, Leake MC, Yakushi T, Homma M, Ishijima A, and Berry RM* (2005). Direct observation of steps in rotation of the bacterial flagellar motor. *Nature*, 437(7060):916–9.

[209] *Sowa Y, Hotta H, Homma M, and Ishijima A* (2003). Torque-speed relationship of the Na$^+$-driven flagellar motor of *Vibrio alginolyticus*. *Journal of Molecular Biology*, 327(5):1043–51.

[210] *Lo CJ, Sowa Y, Pilizota T, and Berry RM* (2013). Mechanism and kinetics of a sodium-driven bacterial flagellar motor. *Proceedings of the National Academy of Sciences*.

[211] *Fukuoka H, Wada T, Kojima S, Ishijima A, and Homma M* (2009). Sodium-dependent dynamic assembly of membrane complexes in sodium-driven flagellar motors. *Molecular Microbiology*, 71(4):825–35.

[212] *Meister M and Berg HC* (1987). The stall torque of the bacterial flagellar motor. *Biophysical Journal*, 52(3):413–9.

[213] *Berg HC and Turner L* (1979). Movement of microorganisms in viscous environments. *Nature*, 278(5702):349–351.

[214] *Berry RM and Berg HC* (1997). Absence of a barrier to backwards rotation of the bacterial flagellar motor demonstrated with optical tweezers. *Proceedings of the National Academy of Sciences of the United States of America*, 94(26):14433–7.

[215] *Berry RM and Berg HC* (1999). Torque generated by the flagellar motor of *Escherichia coli* while driven backward. *Biophysical Journal*, 76(1 Pt 1):580–7.

[216] *Yuan J and Berg HC* (2008). Resurrection of the flagellar rotary motor near zero load. *Proceedings of the National Academy of Sciences of the United States of America*, 105(4):1182–5.

[217] *Inoue Y, Lo CJ, Fukuoka H, Takahashi H, Sowa Y, Pilizota T, Wadhams GH, Homma M, Berry RM, and Ishijima A* (2008). Torque-speed relationships of Na$^+$-driven chimeric flagellar motors in *Escherichia coli*. *Journal of Molecular Biology*, 376(5):1251–9.

[218] *Chen X and Berg HC* (2000). Solvent-isotope and pH effects on flagellar rotation in *Escherichia coli*. *Biophysical Journal*, 78(5):2280–4.

187

[219] *Berg HC and Turner L* (1993). Torque generated by the flagellar motor of *Escherichia coli. Biophysical Journal*, 65(5):2201–16.

[220] *Washizu M, Kurahashi Y, Iochi H, Kurosawa O, Aizawa S, Kudo S, Magariyama Y, and Hotani H* (1993). Dielectrophoretic measurement of bacterial motor characteristics. *IEEE Transactions on Industrial Applications*, 29:286–94.

[221] *Baker MAB and Berry RM* (2009). An introduction to the physics of the bacterial flagellar motor: a nanoscale rotary electric motor. *Contemporary Physics*, 50(6):617–632.

[222] *Chen X and Berg HC* (2000). Torque-speed relationship of the flagellar rotary motor of *Escherichia coli. Biophysical Journal*, 78(2):1036–41.

[223] *Manson MD, Tedesco PM, and Berg HC* (1980). Energetics of flagellar rotation in bacteria. *Journal of Molecular Biology*, 138(3):541–61.

[224] *Yuan J and Berg HC* (2010). Thermal and solvent-isotope effects on the flagellar rotary motor near zero load. *Biophysical journal*, 98(10):2121–2126.

[225] *Yuan J, Fahrner KA, Turner L, and Berg HC* (2010). Asymmetry in the clockwise and counterclockwise rotation of the bacterial flagellar motor. *Proceedings of the National Academy of Sciences of the United States of America*, 107(29):12846–12849.

[226] *Ryu WS, Berry RM, and Berg HC* (2000). Torque-generating units of the flagellar motor of *Escherichia coli* have a high duty ratio. *Nature*, 403(6768):444–7.

[227] *Lele PP, Hosu BG, and Berg HC* (2013). Dynamics of mechanosensing in the bacterial flagellar motor. *Proceedings of the National Academy of Sciences*.

[228] *Tipping MJ, Delalez NJ, Lim R, Berry RM, and Armitage JP* (2013). Load-dependent assembly of the bacterial flagellar motor. *mBio*, 4(4).

[229] *Yamaguchi S, Fujita H, Ishihara A, Aizawa S, and Macnab RM* (1986). Subdivision of flagellar genes of *Salmonella typhimurium* into regions responsible for assembly, rotation, and switching. *Journal of Bacteriology*, 166(1):187–93.

[230] *Yamaguchi S, Aizawa S, Kihara M, Isomura M, Jones CJ, and Macnab RM* (1986). Genetic evidence for a switching and energy-transducing complex in the flagellar motor of *Salmonella typhimurium. Journal of Bacteriology*, 168(3):1172–9.

[231] *Dyer CM, Vartanian AS, Zhou H, and Dahlquist FW* (2009). A molecular mechanism of bacterial flagellar motor switching. *Journal of Molecular Biology*, 388(1):71–84.

[232] *Welch M, Oosawa K, Aizawa S, and Eisenbach M* (1993). Phosphorylation-dependent binding of a signal molecule to the flagellar switch of bacteria. *Proceedings of the National Academy of Sciences of the United States of America*, 90(19):8787–91.

[233] *Lee SY, Cho HS, Pelton JG, Yan D, Henderson RK, King DS, Huang L, Kustu S, Berry EA, and Wemmer DE* (2001). Crystal structure of an activated response regulator bound to its target. *Nature Structural and Molecular Biology*, 8(1):52–6.

[234] *Bren A and Eisenbach M* (1998). The N terminus of the flagellar switch protein, FliM, is the binding domain for the chemotactic response regulator, CheY. *Journal of Molecular Biology*, 278(3):507–14.

[235] *Parkinson JS, Ames P, and Studdert CA* (2005). Collaborative signaling by bacterial chemoreceptors. *Current Opinion in Microbiology*, 8(2):116–21.

[236] *Togashi F, Yamaguchi S, Kihara M, Aizawa SI, and Macnab RM* (1997). An extreme clockwise switch bias mutation in FliG of *Salmonella typhimurium* and its suppression by slow-motile mutations in MotA and MotB. *Journal of Bacteriology*, 179(9):2994–3003.

[237] *Mathews MA, Tang HL, and Blair DF* (1998). Domain analysis of the FliM protein of *Escherichia coli*. *Journal of Bacteriology*, 180(21):5580–90.

[238] *Brown PN, Hill CP, and Blair DF* (2002). Crystal structure of the middle and C-terminal domains of the flagellar rotor protein FliG. *The EMBO Journal*, 21(13):3225–34.

[239] *Van Way SM, Millas SG, Lee AH, and Manson MD* (2004). Rusty, jammed, and well-oiled hinges: Mutations affecting the interdomain region of FliG, a rotor element of the *Escherichia coli* flagellar motor. *Journal of Bacteriology*, 186(10):3173–81.

[240] *Park SY, Lowder B, Bilwes AM, Blair DF, and Crane BR* (2006). Structure of FliM provides insight into assembly of the switch complex in the bacterial flagella motor. *Proceedings of the National Academy of Sciences of the United States of America*, 103(32):11886–91.

[241] *Alon U, Camarena L, Surette MG, Aguera y Arcas B, Liu Y, Leibler S, and Stock JB* (1998). Response regulator output in bacterial chemotaxis. *The EMBO Journal*, 17(15):4238–48.

[242] *Kudo S, Magariyama Y, and Aizawa S* (1990). Abrupt changes in flagellar rotation observed by laser dark-field microscopy. *Nature*, 346(6285):677–80.

[243] *Block SM, Segall JE, and Berg HC* (1983). Adaptation kinetics in bacterial chemotaxis. *Journal of Bacteriology*, 154(1):312–23.

[244] *Scharf BE, Fahrner KA, Turner L, and Berg HC* (1998). Control of direction of flagellar rotation in bacterial chemotaxis. *Proceedings of the National Academy of Sciences of the United States of America*, 95(1):201–6.

[245] *Cluzel P, Surette M, and Leibler S* (2000). An ultrasensitive bacterial motor revealed by monitoring signaling proteins in single cells. *Science*, 287(5458):1652–5.

[246] *Bray D* (2002). Bacterial chemotaxis and the question of gain. *Proceedings of the National Academy of Sciences of the United States of America*, 99(1):7–9.

[247] *Sourjik V and Berg HC* (2002). Binding of the *Escherichia coli* response regulator CheY to its target measured *in vivo* by fluorescence resonance energy transfer. *Proceedings of the National Academy of Sciences of the United States of America*, 99(20):12669–74.

[248] *Sourjik V, Vaknin A, Shimizu TS, and Berg HC* (2007). *In vivo* measurement by fret of pathway activity in bacterial chemotaxis. *Methods in Enzymology*, 423:363–91.

[249] *Sagi Y, Khan S, and Eisenbach M* (2003). Binding of the chemotaxis response regulator CheY to the isolated, intact switch complex of the bacterial flagellar motor: lack of cooperativity. *Journal of Biological Chemistry*, 278(28):25867–71.

[250] *Duke TA, Le Novere N, and Bray D* (2001). Conformational spread in a ring of proteins: a stochastic approach to allostery. *Journal of Molecular Biology*, 308(3):541–53.

[251] *Eisenbach M, Wolf A, Welch M, Caplan SR, Lapidus IR, Macnab RM, Aloni H, and Asher O* (1990). Pausing, switching and speed fluctuation of the bacterial flagellar motor and their relation to motility and chemotaxis. *Journal of Molecular Biology*, 211(3):551–63.

[252] *Berg HC* (1976). *Cell motility*, chapter Does the flagellar rotary motor step?, pages 47–56. Cold Spring Harbor Conferences on Cell Proliferation. Cold Spring Harbor Laboratory, NY.

[253] *Svoboda K, Schmidt CF, Schnapp BJ, and Block SM* (1993). Direct observation of kinesin stepping by optical trapping interferometry. *Nature*, 365(6448):721–7.

[254] *Hirakawa E, Higuchi H, and Toyoshima YY* (2000). Processive movement of single 22S dynein molecules occurs only at low ATP concentrations. *Proceedings of the National Academy of Sciences of the United States of America*, 97(6):2533–2537.

[255] *Veigel C, Coluccio LM, Jontes JD, Sparrow JC, Milligan RA, and Molloy JE* (1999). The motor protein myosin-I produces its working stroke in two steps. *Nature*, 398(6727):530–533.

[256] *Samuel AD and Berg HC* (1995). Fluctuation analysis of rotational speeds of the bacterial flagellar motor. *Proceedings of the National Academy of Sciences of the United States of America*, 92(8):3502–6.

[257] *Samuel AD and Berg HC* (1996). Torque-generating units of the bacterial flagellar motor step independently. *Biophysical Journal*, 71(2):918–23.

[258] *Block SM, Blair DF, and Berg HC* (1989). Compliance of bacterial flagella measured with optical tweezers. *Nature*, 338(6215):514–8.

[259] *Nakamura S, Kami-ike N, Yokota JiP, Minamino T, and Namba K* (2010). Evidence for symmetry in the elementary process of bidirectional torque generation by the bacterial flagellar motor. *Proceedings of the National Academy of Sciences*, 107(41):17616–17620.

[260] *Pilizota T, Brown MT, Leake MC, Branch RW, Berry RM, and Armitage JP* (2009). A molecular brake, not a clutch, stops the rhodobacter sphaeroides flagellar motor. *Proceedings of the National Academy of Sciences of the United States of America*, 106(28):11582–7.

[261] *Bai F, Lo CJ, Berry RM, and Xing J* (2009). Model studies of the dynamics of bacterial flagellar motors. *Biophysical Journal*, 96(8):3154–67.

[262] *Berry RM* (2000). Theories of rotary motors. *Philosophical Transactions of the Royal Soceiety B: Biological Sciences*, 355(1396):503–9.

[263] *Khan S and Berg HC* (1983). Isotope and thermal effects in chemiosmotic coupling to the flagellar motor of streptococcus. *Cell*, 32(3):913–9.

[264] *Meister M, Caplan SR, and Berg HC* (1989). Dynamics of a tightly coupled mechanism for flagellar rotation. Bacterial motility, chemiosmotic coupling, protonmotive force. *Biophysical Journal*, 55(5):905–14.

[265] *Vik SB and Antonio BJ* (1994). A mechanism of proton translocation by F_1F_OATP synthases suggested by double mutants of the a subunit. *The Journal of Biological Chemistry*, 269(48):30364–9.

[266] *Läuger P* (1977). Ion transport and rotation of bacterial flagella. *Nature*, 268(5618):360–2.

[267] *Berry RM* (1993). Torque and switching in the bacterial flagellar motor. An electrostatic model. *Biophysical Journal*, 64(4):961–73.

[268] *Elston TC and Oster G* (1997). Protein turbines. I: The bacterial flagellar motor. *Biophysical Journal*, 73(2):703–21.

[269] *Walz D and Caplan SR* (2000). An electrostatic mechanism closely reproducing observed behavior in the bacterial flagellar motor. *Biophysical Journal*, 78(2):626–51.

[270] *Läuger P* (1988). Torque and rotation rate of the bacterial flagellar motor. *Biophysical journal*, 53(1):53–65.

[271] *Xing J, Bai F, Berry R, and Oster G* (2006). Torque-speed relationship of the bacterial flagellar motor. *Proceedings of the National Academy of Sciences of the United States of America*, 103(5):1260–5.

[272] *Mora T, Yu H, and Wingreen NS* (2009). Modeling torque versus speed, shot noise, and rotational diffusion of the bacterial flagellar motor. *Phys Rev Lett*, 103(24):248102.

[273] *Langevin M* (1905). Recombination and diffusion of gaseous ions (recombinaison et diffusion des ions gazeux). *Journal de Physique Theorique et Applique*, (4):322–333.

[274] *Mora T, Yu H, Sowa Y, and Wingreen NS* (2009). Steps in the bacterial flagellar motor. *PLOS Computational Biology*, 5(10):1000540.

[275] *Meacci G and Tu Y* (2009). Dynamics of the bacterial flagellar motor with multiple stators. *Proceedings of the National Academy of Sciences of the United States of America*, 106(10):3746–51.

[276] *Meacci G, Lan G, and Tu Y* (2011). Dynamics of the bacterial flagellar motor: The effects of stator compliance, back steps, temperature, and rotational asymmetry. *Biophysical Journal*, 100(8):1986–1995.

[277] *Kato-Yamada Y, Noji H, Yasuda R, Kinosita KJ, and Yoshida M* (1998). Direct observation of the rotation of epsilon subunit in F_1-ATPase. *Journal of Biological Chemistry*, 273(31):19375–7.

[278] *York J, Spetzler D, Hornung T, Ishmukhametov R, Martin J, and Frasch WD* (2007). Abundance of *Escherichia coli* F_1-ATPase molecules observed to rotate via single-molecule microscopy with gold nanorod probes. *Journal of bioenergetics and biomembranes*, 39(5-6):435–439.

[279] *Reid SW* (2006). *Torque generation in the bacterial flagellar motor*. Ph.D. thesis.

[280] *Gibbons C, Montgomery MG, Leslie AG, and Walker JE* (2000). The structure of the central stalk in bovine F_1-ATPase at 2.4 Å resolution. *Nature structural biology*, 7(11):1055–1061.

[281] *Menz RI, Walker JE, and Leslie AG* (2001). Structure of bovine mitochondrial F_1-ATPase with nucleotide bound to all three catalytic sites: implications for the mechanism of rotary catalysis. *Cell*, 106(3):331–341.

[282] *Bowler MW, Montgomery MG, Leslie AGW, and Walker JE* (2007). Ground state structure of F_1-ATPase from bovine heart mitochondria at 1.9 Å resolution. *The Journal of Biological Chemistry*, 282(19):14238–14242.

[283] *O'Neill J and Roujeinikova A* (2008). Cloning, purification and crystallization of MotB, a stator component of the proton-driven bacterial flagellar motor. *Acta Crystallographica. Secttion F, Structural Biology and Crystallization Communications*, 64(Pt 6):561–3.

[284] *Roujeinikova A* (2008). Crystal structure of the cell wall anchor domain of MotB, a stator component of the bacterial flagellar motor: implications for peptidoglycan recognition. *Proceedings of the National Academy of Sciences of the United States of America*, 105(30):10348–53.

[285] *Lam KH, Ling TK, and Au SW* (2010). Crystal structure of activated CheY1 from *Helicobacter pylori. Journal of Bacteriology*, 192(9):2324–34.

[286] *Mimori Y, Yamashita I, Murata K, Fujiyoshi Y, Yonekura K, Toyoshima C, and Namba K* (1995). The structure of the R-type straight flagellar filament of *Salmonella* at 9 resolution by electron cryomicroscopy. *Journal of Molecular Biology*, 249(1):69–87.

[287] *Mimori-Kiyosue Y, Yamashita I, Fujiyoshi Y, Yamaguchi S, and Namba K* (1998). Role of the outermost subdomain of salmonella flagellin in the filament structure revealed by electron cryomicroscopy. *Journal of Molecular Biology*, 284(2):521–30.

[288] *Yonekura K, Maki-Yonekura S, and Namba K* (2005). Building the atomic model for the bacterial flagellar filament by electron cryomicroscopy and image analysis. *Structure*, 13(3):407–12.

[289] *Yonekura K, Yakushi T, Atsumi T, Maki-Yonekura S, Homma M, and Namba K* (2006). Electron cryomicroscopic visualization of PomA/B stator units of the sodium-driven flagellar motor in liposomes. *Journal of Molecular Biology*, 357(1):73–81.

[290] *Lucić V, Förster F, and Baumeister W* (2005). Structural studies by electron tomography: from cells to molecules. *Annual Review of Biochemistry*, 74:833–865.

[291] *Hosogi N, Shigematsu H, Terashima H, Homma M, and Nagayama K* (2011). Zernike phase contrast cryo-electron tomography of sodium-driven flagellar hook-basal bodies from *Vibrio alginolyticus. Journal of Structural Biology*, 173(1):67–76.

[292] *Zhao X, Zhang K, Boquoi T, Hu B, Motaleb MA, Miller KA, James ME, Charon NW, Manson MD, Norris SJ, Li C, and Liu J* (2013). Cryoelectron tomography reveals the sequential assembly of bacterial flagella in *Borrelia burgdorferi. Proceedings of the National Academy of Sciences of the United States of America*, 110(35):14390–14395.

[293] *Sowa Y, Steel BC, and Berry RM* (2010). Simple backscattering microscope for fast tracking of biological molecules. *The Review of Scientific Instruments*, 81(11):113704.

[294] *Haynes CL, McFarland AD, Zhao L, Van Duyne RP, Schatz GC, Gunnarsson L, Prikulis J, Kasemo B, and Käll M* (2003). Nanoparticle optics: the importance of radiative dipole coupling in two-dimensional nanoparticle arrays. *The Journal of Physical Chemistry B*, 107(30):7337–7342.

[295] *Jain PK, Lee KS, El-Sayed IH, and El-Sayed MA* (2006). Calculated absorption and scattering properties of gold nanoparticles of different size, shape, and composition: applications in biological imaging and biomedicine. *The Journal of Physical Chemistry B*, 110(14):7238–7248.

[296] *Masaike T, Koyama-Horibe F, Oiwa K, Yoshida M, and Nishizaka T* (2008). Cooperative three-step motions in catalytic subunits of F_1-ATPase correlate with 80 degrees and 40 degrees substep rotations. *Nature Structural and Molecular Biology*, 15(12):1326–33.

[297] *Kim S, Blainey PC, Schroeder CM, and Xie XS* (2007). Multiplexed single-molecule assay for enzymatic activity on flow-stretched DNA. *Nat Methods*, 4(5):397–9.

[298] *Nan X, Sims PA, and Xie XS* (2008). Organelle tracking in a living cell with microsecond time resolution and nanometer spatial precision. *ChemPhysChem*, 9(5):707–12.

[299] *Dunn AR and Spudich JA* (2007). Dynamics of the unbound head during myosin V processive translocation. *Nature Structural and Molecular Biology*, 14(3):246–8.

[300] *Stokes GG* (1852). On the change of refrangibility of light. *Philosophical Transactions of the Royal Society*, (142):463:562.

[301] *Kasha M* (1950). Characterization of electronic transitions in complex molecules. *Discussions of the Faraday Society*, (9):14–19.

[302] *Baker MAB, Inoue Y, Takeda K, Ishijima A, and Berry RM* (2011). Two methods of temperature control for single-molecule measurements. *European biophysics journal : EBJ*.

[303] *Berry RM and Berg HC* (1996). Torque generated by the bacterial flagellar motor close to stall. *Biophysical Journal*, 71(6):3501–10.

[304] *Strick TR, Allemand JF, Bensimon D, and Croquette V* (2000). Stress-induced structural transitions in DNA and proteins. *Annual review of biophysics and biomolecular structure*, 29:523–543.

[305] *Strick T, Allemand J, Croquette V, and Bensimon D* (2000). Twisting and stretching single dna molecules. *Progress in biophysics and molecular biology*, 74(1-2):115–140.

[306] *Lionnet T, Allemand JF, Revyakin A, Strick TR, Saleh OA, Bensimon D, and Croquette V* (2012). Single-molecule studies using magnetic traps. *Cold Spring Harbor protocols*, 2012(1):34–49.

[307] *Shu YG, Yue JC, and Ou-Yang ZC* (2010). $F_O F_1$-ATPase, rotary motor and biosensor. *Nanoscale*, 2(8):1284–1293.

[308] *Saxl TE* (2007). *Electrorotation of the bacterial flagellar motor*. Ph.D. thesis.

[309] *Wang Y, Singh U, and Mueller DM* (2007). Mitochondrial genome integrity mutations uncouple the yeast *Saccharomyces cerevisiae* ATP synthase. *The Journal of Biological Chemistry*, 282(11):8228–8236.

[310] *Thompson RE, Larson DR, and Webb WW* (2002). Precise nanometer localization analysis for individual fluorescent probes. *Biophysical Journal*, 82(5):2775–83.

[311] *Fitzgibbon A, Pilu M, and Fisher RB* (1999). Direct least square fitting of ellipses. *IEEE Transactions on Pattern Analysis and Machine Intelligence*, 21(5):476–480.

[312] *Little MA, Steel BC, Bai F, Sowa Y, Bilyard T, Mueller DM, Berry RM, and Jones NS* (2011). Steps and bumps: precision extraction of discrete states of molecular machines. *Biophysical journal*, 101(2):477–485.

[313] *Einicke G*, ed. (2012). *Smoothing, Filtering and Prediction - Estimating the Past, Present and Future*. InTech.

[314] *Schwarz and Gideon* (1978). Estimating the dimension of a model. *The Annals of Statistics*, 6(2):461–464.

[315] *Bobroff N* (1986). *Review of Scientific Instruments*, volume 57, chapter Position measurement with a resolution and noiselimited instrument, pages 1152–1157. AIP Publishing.

[316] *Asai Y, Kawagishi I, Sockett RE, and Homma M* (2000). Coupling ion specificity of chimeras between H^+- and Na^+-driven motor proteins, MotB and PomB, in *Vibrio* polar flagella. *The EMBO Journal*, 19(14):3639–48.

[317] *Datsenko KA and Wanner BL* (2000). One-step inactivation of chromosomal genes in *Escherichia coli* k-12 using PCR products. *Proceedings of the National Academy of Sciences of the United States of America*, 97(12):6640–5.

[318] *Kuwajima G* (1988). Flagellin domain that affects H antigenicity of *Escherichia coli* K-12. *Journal of Bacteriology*, 170(1):485–8.

[319] *Liao H and Hafner JH* (2005). Gold nanorod bioconjugates. *Chemistry of Materials*, 17(18):4636–4641.

[320] *Bradford MM* (1976). A rapid and sensitive method for the quantitation of microgram quantities of protein utilizing the principle of protein-dye binding. *Analytical Biochemistry*, 72:248–254.

[321] *Lee KS and El-Sayed MA* (2005). Dependence of the enhanced optical scattering efficiency relative to that of absorption for gold metal nanorods on aspect ratio, size, end-cap shape, and medium refractive index. *The Journal of Physical Chemistry B*, 109(43):20331–20338.

[322] *Marchuk K, Ha JW, and Fang N* (2013). Three-dimensional high-resolution rotational tracking with superlocalization reveals conformations of surface-bound anisotropic nanoparticles. *Nano letters*, 13(3):1245–1250.

[323] *Scanlon JA, Al-Shawi MK, Le NP, and Nakamoto RK* (2007). Determination of the partial reactions of rotational catalysis in F_1-ATPase. *Biochemistry*, 46(30):8785–97.

[324] *Mueller DM, Puri N, Kabaleeswaran V, Terry C, Leslie AGW, and Walker JE* (2004). Ni-chelate-affinity purification and crystallization of the yeast mitochondrial F_1-ATPase. *Protein Expression and Purification*, 37(2):479–485.

[325] *Mueller DM, Puri N, Kabaleeswaran V, Terry C, Leslie AGW, and Walker JE* (2004). Crystallization and preliminary crystallographic studies of the mitochondrial F_1-ATPase from the yeast *Saccharomyces cerevisiae*. *Acta Crystallographica. Section D, Biological Crystallography*, 60(Pt 8):1441–1444.

[326] *Pu J and Karplus M* (2008). How subunit coupling produces the gamma-subunit rotary motion in F_1-ATPase. *Proceedings of the National Academy of Sciences of the United States of America*, 105(4):1192–1197.

[327] *Vagin A and Teplyakov A* (2010). Molecular replacement with MOLREP. *Acta Crystallographica. Section D, Biological Crystallography*, 66(Pt 1):22–25.

[328] *Murshudov GN, Vagin AA, and Dodson EJ* (1997). Refinement of macromolecular structures by the maximum-likelihood method. *Acta Crystallographica. Section D, Biological Crystallography*, 53(Pt 3):240–255.

[329] *Chen XJ and Clark-Walker GD* (1993). Mutations in MGI genes convert *Kluyveromyces lactis* into a petite-positive yeast. *Genetics*, 133(3):517–525.

[330] *Chen XJ and Clark-Walker GD* (1995). Specific mutations in alpha- and gamma-subunits of F_1-ATPase affect mitochondrial genome integrity in the petite-negative yeast *Kluyveromyces lactis*. *The EMBO Journal*, 14(13):3277–3286.

[331] *Clark-Walker GD and Chen XJ* (1996). A vital function for mitochondrial DNA in the petite-negative yeast *Kluyveromyces lactis*. *Molecular & General Genetics*, 252(6):746–750.

[332] *Chen XJ, Hansbro PM, and Clark-Walker GD* (1998). Suppression of rho0 lethality by mitochondrial ATP synthase F_1 mutations in kluyveromyces lactis occurs in the absence of F_O. *Molecular & general genetics : MGG*, 259(5):457–467.

[333] *Arsenieva D, Symersky J, Wang Y, Pagadala V, and Mueller DM* (2010). Crystal structures of mutant forms of the yeast F_1 ATPase reveal two modes of uncoupling. *The Journal of Biological Chemistry*, 285(47):36561–36569.

[334] *Hossain MD, Furuike S, Maki Y, Adachi K, Ali MY, Huq M, Itoh H, Yoshida M, and Kinosita K* (2006). The rotor tip inside a bearing of a thermophilic F_1-ATPase is dispensable for torque generation. *Biophysical journal*, 90(11):4195–4203.

[335] *Walz D and Caplan SR* (2005). A kinetic and stochastic analysis of crossbridge-type stepping mechanisms in rotary molecular motors. *Biophysical Journal*, 89(3):1650–6.

[336] *Schnitzer MJ and Block SM* (1995). Statistical kinetics of processive enzymes. *Cold Spring Harbor Symposia on Quantitative Biology*, 60:793–802.

[337] *Block SM, Blair DF, and Berg HC* (1991). Compliance of bacterial polyhooks measured with optical tweezers. *Cytometry*, 12(6):492–6.

[338] *Marchuk K and Fang N* (2013). Three-dimensional orientation determination of stationary anisotropic nanoparticles with sub-degree precision under total internal reflection scattering microscopy. *Nano letters*, 13(11):5414–5419.

[339] *von Ballmoos C, Wiedenmann A, and Dimroth P* (2009). Essentials for ATP synthesis by F_1F_O ATP synthases. *Annual Review of Biochemistry*, 78:649–672.

[340] *Youle M, Rohwer F, Stacy A, Whiteley M, Steel BC, Delalez NJ, Nord AL, Berry RM, Armitage JP, Kamoun S, Hogenhout S, Diggle SP, Gurney J, Pollitt EJG, Boetius A, and Cary SC* (2012). Microbial olympics. *Nature reviews. Microbiology*, 10(8):583–588.

Appendix A

Full Protocols

Cell growth

1. Add the appropriate inducers and antibiotics to 5mL of tryptone broth (TB, 1% BD bacto tryptone, 85mM EMD sodium chloride) in an Erlenmeyer Flask. Typical concentrations to preserve plasmids were 100μM for ampicillin and 50μM of chloramphenicol. Typical concentrations to induce plasmids were 50μM IPTG and 1mM arabinose. Low induction for IPTG was 5μM.

2. Add the appropriate amount of cells from a frozen stock (typically 10-100μL) such that the OD_{600} is 0.5-0.7 after growing.

3. Partially screw the lid on to allow aerobic conditions. Place in the incubator for 5.5 hours at 33°C, shaking at 200rpm.

4. Remove from the incubator and use immediately.

Cell preparation

1. Wash the cells by spinning in the centrifuge for 2 minutes at 3000g. Carefully remove the supernatant with a pipette. Gently resuspend the cells with a pipette into 1mL motility broth (MB, 10mM potassium phosphate, 0.1mM EDTA, 10mM lactate, 0-70mM NaCL, pH 7.0).

2. Repeat this washing two more times, with a final suspension of 400μL.

Preparing primary antibody

1. Purify 50μL of rabbit anti-hook antibody (gift from Howard Berg), using IgG purification kit-A (Dojin-Do), following kit instructions.

2. Measure the purified antibody using the Bradford Method. BSA or IgG can be used for a standard calibration curve. The purified antibody should be about 0.1-$0.25\frac{mg}{mL}$

3. Pre-adsorb the antibody before freezing.

Pre-adsorption of the primary antibody

1. Grow the hook-less strain (HCB137) as per the regular protocol.

2. Follow the cell preparation protocol, but with a final resuspension of 1mL of MB. Leave on ice for 10 minutes.

3. Wash again, resuspending in 100μL MB, and add 40μg of antibody. Leave on ice for 20 minutes.

4. Spin down the cells and collect the supernatant (about 250μL of purified antibody).

5. Use the Bradford Method to measure the concentration. The concentration is typically about $0.1\frac{mg}{mL}$.

6. Fast freeze aliquots of 2.5μL with liquid nitrogen and store at -80°C.

Preparing secondary antibody

This protocol is per the manufactruer's (Pierce) instructions:

1. Allow the vial of SPDP to come to room temperature before opening.

2. Dissolve 2mg LC-SPDP in 235μL of DMSO, for immediate use.

3. Add 25μL of the 20mM LC-SPDP solution to 2-5mgIgG dissolved in 1.0ml of PBS-EDTA

4. Incubate for 30 minutes at room temperature.

5. Equilibrate a desalting column with PBS-EDTA, and buffer exchange the LC-SPDP-modified IgG to remove reaction byproducts and excess nonreated LC-SPDP reagent.

6. Add 1-3mg of β-galactosidase to the IgG solution and incubate the reation mixture overnight at room temperature.

7. Fast freeze aliquots of 2.5μL with liquid nitrogen and store at -80°C.

Preparing secondary antibody conjugated gold nanoparticles

1. Sonicate 500μL of gold nanoparticles, stored at 4°C, for 5 minutes.

2. Add 2.5μL of IgG LC-SPDP to the gold nanoparticles. Incubate at room temperature for 2 hours.

3. Add 1mM MPEG-SH in DMSO to the gold solution. Incubate at room temperature overnight.

4. Store at 4°C, and use within 2 weeks.

Antibody assay

1. After growing and preparing the cells, combine 100μL cell culture to 2.5mL of $0.1\frac{mg}{mL}$ primary antibody. Incubate at room temperature for 25 minutes on a tabletop spinner.

2. Wash twice in 300μL and gently resuspend in 40μL of MB.

3. Centrifuge 100μL of gold solution at 1100g for 3 minutes and gently remove the supernatant.

4. Conbine 40μL of the cell culture to the remaining gold pellet and incubate at room temperature for 25 minutes on a tabletop spinner.

5. Centrifuge for 45 seconds at 1800g, decant, and resuspend in 300μL of MB.

6. Add 0.01% poly-L-lysine to a tunnel slide, place the slide with the coverslip down, and incubate for 5 minutes.

7. Rinse the tunnel slide with 100μL MB twice.

8. Add 30μL of the cell suspension and incubate at room temperature for 5 minutes with the coverslip down and within a humidity chamber.

9. Rinse the tunnel slide with 100μL of a solution of 90% MB and 10% TB.

Biotin hook assay

1. After growing and preparing the cells, add 0.01% poly-L-lysine to a tunnel slide, place the slide with the coverslip down, and incubate for 5 minutes.

2. Rinse the tunnel slide with 100μL MB twice.

3. Add 30μL of the cell suspension and incubate at room temperature for 5 minutes with the coverslip down and within a humidity chamber.

4. Rinse the tunnel slide with 100μL of MB.

5. Add 30μL of 4μM streptavidin in MB. Incubate for 5 minutes with the coverslip down in a humidity chamber.

6. Rinse the tunnel slide with 100μL MB twice.

7. Add 2μL biotin conjugated gold beads or rods to 50μL MB, and add the solution to the tunnel slide. Incubate for 8 minutes in a humidity chamber.

8. Rinse the tunnel slide with 100μL of a solution of 90% MB and 10% TB.

Appendix B

Microbial Olympics

In an essay published near the time and in the spirit of the London 2012 Olympic games, a number of BFMs from different species of bacteria were put to the test in a 100 μm 'freestyle' swim. As in the early human Olympic Games, contestants were chosen by their ability to travel to the venue; for these games, contestents were chosen from the frozen stocks within the lab. The only criterion for qualification was a body length of around one micron. Of the eight contestants, there was a mix of sodium and proton driven motors, switching and non-switching motors, and single and multiple flagellar propulsion.

Each strain of bacteria was grown and raced under its own ideal conditions. Each strain was recorded separately, and the single bacterium demonstrating a trajectory that mostly closely fit within a defined lane line was chosen for the final video. The final video, consisting of a compilation of eight individual videos spliced to start at the same time and position, can be found in the Supplementary Information of [340].

As seen in Figure B.1, the race came down to a photo-finish with *R. shaeroides* winning by a body length (2.02 s) to the chimeric *E. coli* (2.08 s). Third and fourth places went to *P. aeruginosa* and *V. alginolyticus* (pusher) respectively, followed by the proton driven *E. coli* and *Y. enterocolitica*. Bringing up the back, taking over 15 s

to swim the distance, was *R. rubrum*. Ten micrometers into the race, *V. alginolyticus* (puller) began swimming in circles, failing to finish the race.

These contestants represent a very small portion of bacterial species, a large quantity of which are uncharacterized. With widening access and more rigorous selection, not to mention the potential for synthetic biology, there is no doubt that the times of the 100 μm Microbial freestyle will improve in future Olympic games.
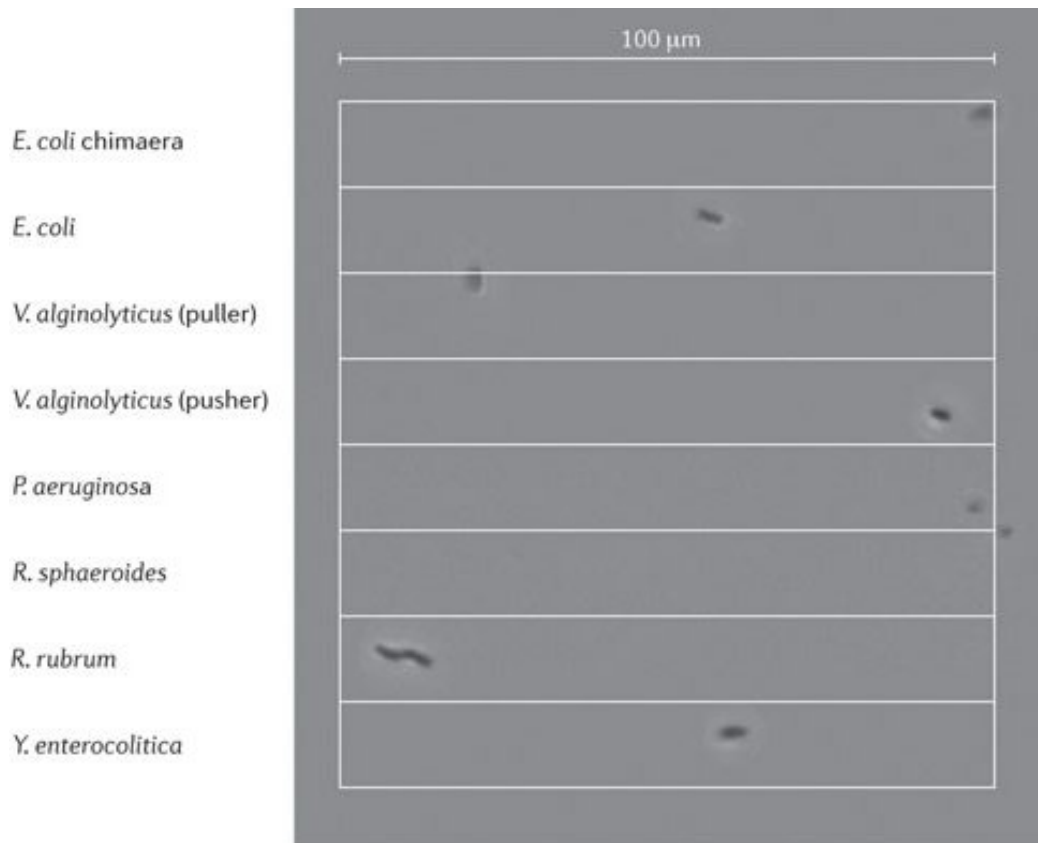
Figure B.1: Contestants (and country of origin) by lane: (1) sodium-driven chimeric *E. coli*, with multiple flagella (Japan); (2) proton-driven *E. coli*, with multiple flagella (USA); (3) sodium-driven *Vibrio alginolyticus*, with a single polar, clockwise locked puller flagellum (that is, the flagellum pulls the cell body along behind it; Japan); (4) sodium-driven *V. alginolyticus* with a single polar, anticlockwise locked pusher flagellum (that is, the flagellum pushes the cell body along in front of it; Japan); (5) proton-driven *Pseudomonas aeruginosa*, with a single polar flagellum (Australia); (6) proton-driven *Rhodobacter sphaeroides*, with a single subpolar flagellum (USA); (7) proton-driven *Rhodospirillum rubrum*, a spiral-shaped bacterium with multiple flagella at each pole to both push and pull (USA); and (8) proton-driven *Yersinia enterocolitica*, with multiple flagella (Belgium). Figure and caption reproduced from [340].